Energy Features of Underground Exploitation by Fluid Circulation

Murad S. Abuaisha

SORBONNE UNIVERSITÉ

HABILITATION À DIRIGER DES RECHERCHES

Sciences de la Terre et de l'Univers

Energy Features of Underground Exploitation by Fluid Circulation

---

Author:
Murad ABUAISHA

Defended publicly on July the 10th 2024 in front of the jury composed of:

Christophe Tournassat	Professor, ISTO/CNRS/Université d'Orléans	Reporter
Nicolas Espinoza	Professor, University of Texas at Austin	Reporter
Fabrice Golfier	HDR Lecturer, Université de Lorraine	Reporter
Laetitia Le Pourhiet	Professor, ISTeParis, Sorbonne Université	Examiner
Élie Hachem	Professor, MINES Paris - PSL	Examiner
Christophe Coquelet	Professor, IMT MINES Albi-Carmaux	Examiner
Ahmed Rouabhi	HDR Teacher-Reasercher, MINES Paris - PSL	Examiner

Centre de Géosciences
MINES Paris - PSL

إِلَيْكِ: إِلَيْكِ يَا أُمِّي ...
إِلَيْكِ يَا أُمِّي, يَا آيَتِي الَّتِي لَمْ يَجْعَلْهَا اللهُ لِلْعَالَمِين

"I have read, alas! through philosophy,
medicine and jurisprudence too,
and, to my grief, theology,
with ardent labour studied through.
And here I stand with all my lore,
poor fool no wiser than before."

Goethe/Faust

SORBONNE UNIVERSITÉ

Abstract

Centre de Géosciences
MINES Paris - PSL

Habilitation à Diriger des Recherches

Energy Features of Underground Exploitation by Fluid Circulation

by Murad ABUAISHA

This work presents the geomechanical and thermodynamic aspects related to the problem of exploiting underground energy resources by fluid circulation. The first chapter discusses the thermodynamics of continuous media. The two frameworks of thermodynamics of isotropic fluid mixtures and thermodynamics of multiphase compositional flows in porous media are briefly pointed out. The second chapter treats the problem of hydraulic stimulation of deep geothermal reservoirs. While considering a continuum approach, it investigates hydraulic fracturing effects on impedance and efficiency of thermal recovery from these reservoirs. The chapter continues to scrutinize the technique of hydraulic fracturing, particularly the fluid-injection related induced seismicity. In a continuum-discontinuum framework, it provides a strategy to relate induced seismicity to non-diffusive triggering fronts that encompass most of the seismic cloud.

Since renewable energy is limited to its intermittent nature, this research introduces gas storage in salt caverns as a large-scale storing technique. The increasing energy demands will, however, necessitate frequent utilization of these caverns. The fast cycling, and its subsequent severe mechanical and thermal charges, impose challenges regarding the thermodynamic state within the cavern, and the masses exchanged between the cavern phases. To have precise tracks of cycled gas quantities and to master losses, these challenges have to be considered. This work validates the mathematical models at the laboratory scale, and provides transferring techniques to real-scale applications. Each section provides a precise introduction concerning the discussed problem, and terminates by a conclusion. A general introduction and a review and perspectives are also furnished.

SORBONNE UNIVERSITÉ

Abstract

Centre de Géosciences
MINES Paris - PSL

Habilitation à Diriger des Recherches

Energy Features of Underground Exploitation by Fluid Circulation

by Murad ABUAISHA

Ce travail présente les aspects géomécaniques et thermodynamiques liés à la problématique de l'exploitation des ressources énergétiques souterraines par la circulation de fluides. Dans le premier chapitre, on traite de la thermodynamique des milieux continus. Les deux cadres de la thermodynamique des mélanges fluides isotropes et de la thermodynamique des écoulements multiphasiques et multiconstituants dans les milieux poreux sont brièvement soulignés. Dans le deuxième chapitre, on présente la problématique de la stimulation hydraulique des réservoirs géothermiques profonds. En considérant une approche continue, on étudie les effets de la fracturation hydraulique sur l'impédance et l'efficacité de la récupération de chaleur de ces réservoirs. On continue d'examiner la technique de la fracturation hydraulique, en particulier la sismicité induite liée à l'injection de fluide. Dans un cadre continu-discontinu, on propose une stratégie permettant de relier la sismicité induite aux fronts non-diffusifs englobant la majeure partie des événements sismiques.

Les énergies renouvelables étant intermittentes, cette recherche introduit le stockage des gaz dans les cavités salines comme une technique de stockage à grande échelle. Or, la demande croissante en énergie nécessitera des sollicitations fréquentes de ces cavités. Le cyclage rapide, et les charges mécaniques et thermiques sévères qui en résultent, imposent des défis concernant l'état thermodynamique de la cavité et les masses échangées entre les phases. Pour avoir une trace précise des quantités de gaz cyclées et maîtriser les pertes, ces défis doivent être relevés. Ces travaux valident les modèles mathématiques à l'échelle du laboratoire et permettent de les transférer vers des applications à l'échelle réelle. Chaque section fournit une introduction précise concernant le problème abordé et se termine par une conclusion. Une introduction générale ainsi qu'un bilan et des perspectives sont également fournis.

Acknowledgements

I cannot close these prefatory remarks without expressing a deep feeling of gratitude to Benjamin Loret. Benjamin was not only my PhD supervisor but also a friend who accompanied me during my scientific journey since 2010. I thankfully recognize the favors of all my colleagues at the Center of Geosciences, starting from fellows, to technicians, to postdocs and PhD students. I thank the members of the jury, both reporters and examiners, for having accepted to participate, your presence was much appreciated. I would like to thank our industrial partners who, with fervor, helped us put our theories into real-scale applications.

Contents

Introduction

For the last thirty years there has been a worldwide conscientiousness with regard to the consumption of available energy resources. Such concerns were also accompanied by awareness of the climate change crisis, the emergence of new economic world powers, and the geopolitical conflicts. All of these factors have caused energy prices to raise up bringing a considerable fraction of humanity to energy scarcity. Exploitation of abundant renewable energy resources is seen as the optimum solution to reply to these challenges. However, renewable energy resources are limited to their intermittent nature, and require the development and mastering of a new knowledge. This research is dedicated to studying the geomechanical and thermodynamic aspects pertaining to energy exploitation by underground fluid circulation.

Since I have started my PhD in 2011, I have chosen a research axis that focused on renewable energy exploitation. I began by using the hydraulic fracturing technique to explore its effect on thermal recovery from geothermal systems. I employed the same technique for applications related to shale gas extraction. For the last seven years, I have been working extensively on gas storage in salt caverns. The idea of this work emerged as I felt the need to put the information I collected and gained during developing this research axis in a general context. This work is divided into two main parts: the first part focuses on fluid (liquid) circulation in porous media; and the second part concerns fluid (gas) circulation (cycling) in salt caverns. Even-though the two applications may seem different, the physics behind them is similar.

Chapter one of this work presents the thermodynamic frameworks of fluid flow in continuous media. Both the thermodynamics of fluid mixtures and multi-phase compositional flows in porous media are briefly discussed. The second chapter concerns deep geothermy. Heat extraction from deep reservoirs is challenging in the sense that such reservoirs are impermeable. Hydraulic stimulation, through hydraulic fracturing or chemistry, enhances the reservoir fluid flow capacities leading to lucrative and productive utilization. This research provides a simple continuum modelling approach to perform hydraulic fracturing in a fully coupled therm-hydromechanical framework. A special emphasis is given to the nature of fracture evolution (mode I or mode II), to the used geothermal fluids, and to the impedance and efficiency of thermal recovery. However, public opinion may prevent future large-scale utilization of deep geothermal systems. This is attributed to uncontrolled induced seismicity which is perceived as an unsolicited side effect of geothermal energy exploitation. The development of geothermal systems therefore requires a better control on induced seismicity. For this reason, this work investigates induced seismicity related to fluid injection in a continuum-discontinuum (quasi-static) modelling tactic. Based on the injection information, a seismicity triggering front is predicted giving important information about the range of induced seismicity and hydraulic fracture size.

Clean energy resources are intermittent and production of geothermal energy requires storage, this necessitates the development of large-scale storage techniques. Gas storage in salt caverns is presenting a promising solution. Nevertheless, increasing energy demands entail frequent solicitations of such caverns. Fast charges, mechanical and thermal, impose several challenges that include:

– investigating the widely adopted hypothesis of a uniform thermodynamic state in the cavern, and consequently the precision of the used codes embracing this hypothesis;

– keeping good records of cycled gas quantities, which necessitates studying all possible mass exchanges between the cavern phases.

The third chapter of this work addresses the technology of gas storage in salt caverns while furnishing solutions to the two above mentioned challenges. The research approach/strategy presented in this work has many particularities, of which I may cite:

– the used/developed numerical models are validated by *in situ* or experimental data;

– the experimental setups are designed by common team reflection, and by the help of other research centers of MINES Paris, I may mention the Center of Thermodynamics of Processes (CTP);

– the transfer between laboratory and real applications is done by developing non-dimensional approaches or by adopting some physical simplifications;

– different gases are included in the performed analyses (hydrogen, helium, and carbon dioxide);

– research is conducted for different gas cycling scenarios in salt caverns (daily, weekly, and monthly). However, emphasis is given to fast cycling to reply to the increasing energy demands.

Each section of this work starts by a precise introduction that tackles the particular problem presented, and terminates by a conclusion. A general review and perspectives are offered at the end of this research.

Chapter 1

Thermodynamics of continuous media

The main objective of this chapter is to construct comprehensive thermodynamic frameworks for gas storage in salt caverns and multiphase compositional flows in porous media. Most of physical problems related to earth science and engineering require the employment of robust numerical techniques (Chen, Huan, and Ma, 2006; Kolditz et al., 2012). While improving the numerical methods is a vital topic, the mathematical and physical explanations behind the used models need to be based on thermodynamics. Unlike modelling strategies based on analogy, thermodynamics helps give theoretical and consistent foundations to the used macroscopic equations.

This work applies the principles of thermodynamics of irreversible processes to reply to problems related to the underground exploitation by fluid circulation. Macroscopic thermodynamic descriptions for such applications are explored since decades (Svendsen and Hutter, 1995; Rouabhi et al., 2017; Everett, 1975; Marle, 1982; Hassanizadeh and Gray, 1990). For its clarity, this chapter is based on the work of Rouabhi (2019). An important benefit of this approach is to avoid assuming specific processes at the microscale, only that the studied system is close to equilibrium. This framework is sufficient to introduce macroscopic constitutive laws that verify the second principle of thermodynamics. Physical assumptions can be also expanded to include additional processes.

1.1 Introduction

Let us consider a fluid mixture of q constituents. The total mass of this mixture $\mathcal{M}$ occupying a total volume $\mathcal{V}$ can be written as the sum of the constituent masses $\mathcal{M} = \sum \mathcal{M}_k$. Let $\mathcal{U}$ and $\mathcal{S}$ be the internal energy and entropy of the material in $\mathcal{V}$. If the studied system is closed, the first law of thermodynamics (Gibbs relation) takes the form $d\mathcal{U} = -pd\mathcal{V} + Td\mathcal{S}$. This relation is valid for any infinitesimal transformation of the system, in which the mixture thermodynamic pressure is $p = -\partial_{\mathcal{V}}\mathcal{U}$, and its absolute temperature is $T = \partial_{\mathcal{S}}\mathcal{U}$. If a thermodynamic system changes material with the surrounding, it becomes thermodynamically open which allows us to write the previous law as $d\mathcal{U} = -pd\mathcal{V} + Td\mathcal{S} + \sum \mu_k d\mathcal{M}_k$, where μ_k is the chemical potential of the k constituent in the mixture. All the quantities $\mathcal{U}$, $\mathcal{S}$, $\mathcal{V}$, $\mathcal{M}$ are extensive and do not depend on the size of the considered system. However, the partial derivatives of the internal energy with respect to its variables are intensive quantities that depend on the system size. By applying the Euler's homogeneous function theorem to the Gibbs relation, it is found that $\mathcal{U} = -p\mathcal{V} + T\mathcal{S} + \sum \mu_k \mathcal{M}_k$. By introducing the specific free enthalpy $\mathcal{G} = \mathcal{U} + p\mathcal{V} - T\mathcal{S}$, it is concluded that $\mathcal{G} = \sum \mu_k \mathcal{M}_k$ and $d\mathcal{G} = \mathcal{V}dp - \mathcal{S}dT + \sum \mu_k d\mathcal{M}_k$.

The homogeneous function theorem can be used as well to write the internal energy in terms of its specific quantities $u = -pv + Ts + \sum c_k \mu_k$, with $v = \mathcal{V}/\mathcal{M}$, $s = \mathcal{S}/\mathcal{M}$, and $c_k = \mathcal{M}_k/\mathcal{M}$ being the specific volume, the specific entropy, and the mass concentration of the constituent k. By definition $\sum c_k = 1$ and only $q-1$ concentrations are independent, therefore $\boldsymbol{c} = (c_1, c_2, ..., c_{q-1})$. Equivalently, the specific free enthalpy is $g = \sum \mu_k c_k$. With some manipulation, the Gibbs-Duhem relation is reached $vdp - sdT - \sum c_k d\mu_k = 0$. This relation shows that

when the extensive quantities $\mathcal{S}$, $\mathcal{V}$, $\mathcal{M}_k$ are fixed, the intensive quantities p, T, and μ_k become dependent. Establishing a relation between an extensive quantity and its density is interesting. For any extensive quantity, function of the thermodynamic state, $\Phi(p,T,\mathcal{M}_1,...,\mathcal{M}_q) = \mathcal{M}\varphi$ of the specific density $\varphi(p,T,\boldsymbol{c})$, it is written (Rouabhi, 2019),

$$\varphi(p,T,\boldsymbol{c}) = \sum c_k \bar{\varphi}_k(p,T,\boldsymbol{c}), \tag{1.1}$$

with $\bar{\varphi}_k(p,T,\boldsymbol{c}) = \partial_{\mathcal{M}_k}\Phi(p,T,\mathcal{M}_1,...,\mathcal{M}_q)$.

The first part of this section presents the thermodynamics framework of mixtures of isotropic fluids. The second part discusses the thermodynamics framework of fluid circulation in porous media.

1.2 Thermodynamics framework of mixtures of isotropic fluids

This work proposes a derivation of macroscopic equations for isotropic fluid flows in a continuous medium. It is assumed that local equilibrium applies at an elemental volume (Kondepudi and Prigogine, 2014). A mixture of isotropic fluid contains different phases. To construct thermodynamically compatible relations for any phase, the strategy adopted in this research introduces its thermodynamic potential. Consequently, all remaining state functions can be derived from this potential by using appropriate partial derivatives. For a thermodynamic state characterized by the independent variables $(p,T,\boldsymbol{c})$, the thermodynamic potential is the free enthalpy g, other state functions derive as (Rouabhi et al., 2017),

$$\begin{aligned} v = \partial_p g, \quad C_p = -T\partial_T^2 g, \quad s = -\partial_T g, \\ \mu_q = g - \sum_{j=1}^{q-1} c_j \partial_{c_j} g, \quad \mu_{k\neq q} = \mu_q + \partial_{c_k} g, \end{aligned} \tag{1.2}$$

with C_p being the mixture heat capacity.

The behavior of the mixture is described by its mass density $\rho = \sum c_k \rho_k$, its barycentric velocity $\boldsymbol{v} = \sum c_k \boldsymbol{v}_k$, its temperature T, and its constituent concentrations c_k. The conservation laws that govern the evolution of these fields are expressed macroscopically (Fer, 1971) by the following field equations:

$$\begin{array}{lllll} \text{total mass conservation:} & \dot{\rho} + \rho\,\boldsymbol{\nabla}\cdot\boldsymbol{v} & = & 0; & \text{completed by,} \\ k\text{-component mass conservation:} & \rho\dot{c}_k + \boldsymbol{\nabla}\cdot(\rho\boldsymbol{J}_k) & = & \pi_k; & \forall k = 1,\ldots,q-1, \\ \text{momentum conservation:} & \rho\,\dot{\boldsymbol{v}} - \boldsymbol{\nabla}\cdot\underline{\underline{\boldsymbol{\sigma}}} & = & \rho\,\boldsymbol{g}; & \\ \text{internal energy conservation:} & \rho\,\dot{u} + \boldsymbol{\nabla}\cdot\boldsymbol{\Psi}_u & = & \underline{\underline{\boldsymbol{\sigma}}} : \underline{\underline{\boldsymbol{\nabla}}}\boldsymbol{v} + Q_r; & \\ \text{entropy conservation:} & \rho\,\dot{s} + \boldsymbol{\nabla}\cdot(\boldsymbol{\Psi}_s/T) & = & (Q_r + \varpi)/T; & \end{array} \tag{1.3}$$

where $\boldsymbol{J}_k$ is the diffusive flux of constituent k, π_k is the mass production rate of component k per unit volume due to chemical reactions with the condition $\sum \pi_k = 0$, $\underline{\underline{\boldsymbol{\sigma}}}$ is the mixture stress tensor, $\boldsymbol{g}$ is the gravitational acceleration vector, $\boldsymbol{\Psi}_u$ is the internal energy flux vector, Q_r is the heating source per unit volume, $\boldsymbol{\Psi}_s$ is the entropy flux vector, and ϖ is the volumetric dissipation. For any physical quantity $\mathcal{F}(\boldsymbol{x},t)$, $\dot{\mathcal{F}} = d\mathcal{F}/dt = \partial_t\mathcal{F} + \boldsymbol{v}\cdot\boldsymbol{\nabla}\mathcal{F}$ is the material derivative of $\mathcal{F}$ following the motion of the mixture. The volumetric dissipation can be further expressed as,

$$\varpi = (\underline{\underline{\boldsymbol{\sigma}}} + p\underline{\underline{\boldsymbol{\delta}}}) : \underline{\underline{\boldsymbol{\nabla}}}\boldsymbol{v} - \boldsymbol{\Psi}_s\cdot\boldsymbol{\nabla}T/T - \sum \pi_k\,\bar{\mu}_k - \sum \rho\boldsymbol{J}_k\cdot\boldsymbol{\nabla}\bar{\mu}_k, \tag{1.4}$$

with $\bar{\mu}_k = \mu_k - \mu_q$ ($\bar{\mu}_q = 0$), and,

$$\boldsymbol{\Psi}_s = \boldsymbol{\Psi}_u - \sum \rho \bar{\mu}_k \boldsymbol{J}_k. \tag{1.5}$$

The mathematical relation between the two energy flux vectors $\boldsymbol{\Psi}_s$ and $\boldsymbol{\Psi}_u$ is very important to give a physical meaning to all the physical quantities presented in the fields of the system 1.3. For instance, in case of non-reacting components/no mass production and no diffusion ($\pi_k = 0$ and $\boldsymbol{J}_k = \boldsymbol{0}$), the system behaves as a closed system of a single phase component, and we can simply write $\boldsymbol{\Psi}_u = \boldsymbol{\Psi}_s = \boldsymbol{\psi}$, with $\boldsymbol{\psi} = -\Lambda \boldsymbol{\nabla} T$ being the heat flux vector and Λ is the mixture thermal conductivity (Fer, 1970). Furthermore, the volumetric dissipation becomes $\varpi = (\underline{\underline{\boldsymbol{\sigma}}} + p\underline{\underline{\boldsymbol{\delta}}}) : \underline{\underline{\boldsymbol{\nabla}}} \boldsymbol{v} - \boldsymbol{\psi} \cdot \boldsymbol{\nabla} T / T$ with irreversibilities related only to the presence of velocity and temperature gradients.

Even-though this approach sounds straight forward in the case of a closed system, ensuring a continuous production of entropy ($\varpi \geqslant 0$) becomes more complicated in the case of an open system. In this case, it is convenient to partition the volumetric dissipation into separate irreversibility sources (Rouabhi, 2019; Gelet, Loret, and Khalili, 2012a; Loret and Simões, 2017), where each inequality ($\varpi_n \geqslant 0$) is demanded. The first two dissipation partitions are simple and comparable to the case of a closed system. When the velocity field and the thermodynamic state are homogeneous ($\underline{\underline{\boldsymbol{\nabla}}} \boldsymbol{v} = \underline{\underline{\boldsymbol{0}}}$, $\boldsymbol{\nabla} T = \boldsymbol{0}$, and $\boldsymbol{\nabla} \bar{\mu}_k = \boldsymbol{0}$), the only irreversibility source is attributed to chemical interactions between the constituents $\varpi = \varpi_c = -\sum \pi_k \bar{\mu}_k$. When the thermodynamic state is only homogeneous ($\boldsymbol{\nabla} T = \boldsymbol{0}$ and $\boldsymbol{\nabla} \bar{\mu}_k = \boldsymbol{0}$) without any chemical interactions, the left irreversibility source is intrinsic and related to the viscous dissipation $\varpi = \varpi_i = (\underline{\underline{\boldsymbol{\sigma}}} + p\underline{\underline{\boldsymbol{\delta}}}) : \underline{\underline{\boldsymbol{\nabla}}} \boldsymbol{v}$. However, if the velocity filed is homogeneous without any chemical interactions between constituents ($\underline{\underline{\boldsymbol{\nabla}}} \boldsymbol{v} = \underline{\underline{\boldsymbol{0}}}$ and $\boldsymbol{\nabla} \bar{\mu}_k = \boldsymbol{0}$), the volumetric dissipation of Eq. 1.4 becomes $\varpi = -\boldsymbol{\Psi}_s \cdot \boldsymbol{\nabla} T / T - \sum \rho \boldsymbol{J}_k \cdot \boldsymbol{\nabla} \bar{\mu}_k$. If we consider that the temperature variations between constituents are attributed to pure heat conduction, then we may write,

$$\varpi = \underbrace{-\boldsymbol{\psi} \cdot \boldsymbol{\nabla} T / T}_{\varpi_\psi} \underbrace{- \sum \rho \boldsymbol{J}_k \cdot \boldsymbol{\nabla}_T \bar{\mu}_k}_{\varpi_J}, \tag{1.6}$$

where $\boldsymbol{\nabla}_T$ is the isothermal gradient operator. The introduction of this operator implies that the diffusion velocities contribute to the conjugate heat flux between constituents. Knowing that $\bar{\mu}_k = \partial_{c_k} g(p, T, \boldsymbol{c})$, it is concluded that:

$$\begin{aligned} \boldsymbol{\Psi}_s &= \boldsymbol{\psi} + \sum_{k=1}^{q-1} \rho T \partial_{c_k} s(p, T, \boldsymbol{c}) \boldsymbol{J}_k; \\ \boldsymbol{\Psi}_u &= \boldsymbol{\psi} + \sum_{k=1}^{q-1} \rho \partial_{c_k} h(p, T, \boldsymbol{c}) \boldsymbol{J}_k, \end{aligned} \tag{1.7}$$

with,

$$\varpi = \varpi_c + \varpi_i + \varpi_\psi + \varpi_J, \quad \text{restricted to,} \quad \varpi_c \geq 0,\ \varpi_i \geq 0,\ \varpi_\psi \geq 0,\ \varpi_J \geq 0, \tag{1.8}$$

with these definitions in mind, the internal energy and entropy conservation equations become equivalent. The mathematical problem is to be completed by initial and boundary conditions, and by constitutive laws that relate the secondary unknowns $\{\underline{\underline{\boldsymbol{\zeta}}},\ \pi_k,\ \boldsymbol{\psi},\ \boldsymbol{J}_k\}$ to the primary unknowns $\{\boldsymbol{v},\ \rho,\ T,\ \boldsymbol{c}\}$ while abiding to the second principle of thermodynamics.

The Fourier's heat conduction has been defined earlier, it relates the heat flux vector to the negative temperature gradient through the mixture thermal conductivity ($\boldsymbol{\psi} = -\Lambda \boldsymbol{\nabla} T$). The diffusive flux can be written in terms of the diffusion velocity of the constituent $\boldsymbol{J}_k = -D_k \boldsymbol{\nabla} c_k = c_k(\boldsymbol{v}_k - \boldsymbol{v})$, with D_k being the diffusion coefficient of the constituent k. The Stockes law is used to calculate the stress tensor in the moving mixture undergoing external effects,

$$\underline{\underline{\boldsymbol{\sigma}}} = \underline{\underline{\boldsymbol{\zeta}}} - p\,\underline{\underline{\boldsymbol{\delta}}}, \quad \text{with,} \quad \underline{\underline{\boldsymbol{\zeta}}} = 2\mu\,\underline{\underline{\boldsymbol{\mathcal{E}}}}^d, \tag{1.9}$$

where μ is the mixture dynamic viscosity, and $\underline{\underline{\boldsymbol{\mathcal{E}}}}^d$ is the deviatoric part of the rate of strain tensor $\underline{\underline{\boldsymbol{\mathcal{E}}}} = (1/2)\left(\underline{\underline{\boldsymbol{\nabla}}}\boldsymbol{v} + \underline{\underline{\boldsymbol{\nabla}}}\boldsymbol{v}^{\mathrm{T}}\right)$. The deviatoric part is calculated as $\underline{\underline{\boldsymbol{\mathcal{E}}}}^d = \underline{\underline{\boldsymbol{\mathcal{E}}}} - (1/3)\,\mathrm{tr}(\underline{\underline{\boldsymbol{\mathcal{E}}}})\,\underline{\underline{\boldsymbol{\delta}}}$. If the volumetric dissipation is caused only by a deviatoric mechanism, then $\underline{\underline{\boldsymbol{\mathcal{E}}}}^d = (1/2)\left(\underline{\underline{\boldsymbol{\nabla}}}\boldsymbol{v} + \underline{\underline{\boldsymbol{\nabla}}}\boldsymbol{v}^{\mathrm{T}}\right) - (1/3)(\boldsymbol{\nabla}\cdot\boldsymbol{v})\,\underline{\underline{\boldsymbol{\delta}}}$. Thus, the viscosity stress tensor is defined as,

$$\underline{\underline{\boldsymbol{\zeta}}} = \mu\left(\underline{\underline{\boldsymbol{\nabla}}}\boldsymbol{v} + \underline{\underline{\boldsymbol{\nabla}}}\boldsymbol{v}^{\mathrm{T}}\right) - (2/3)\mu(\boldsymbol{\nabla}\cdot\boldsymbol{v})\,\underline{\underline{\boldsymbol{\delta}}}. \tag{1.10}$$

1.3 Thermodynamics framework of multiphase compositional flows in porous media

There are several thermodynamic approaches that treat multiphase compositional flows in porous media. Generally, such approaches use the same strategy of developing a thermodynamic description at the pore level, and subsequently derive the macroscopic description from it. Linking properly the descriptions at the two levels is challenging. Though most studies use the notion of a length scale to relate the two levels, this length scale appears independently in porous media and continuum thermodynamics. In porous media, it is convenient to consider that the length scale corresponds to the Representative Elementary Volume (REV) (Bear, 1972). In the case of continuum thermodynamics, an elemental volume, that separates between uniform and non-uniform descriptions of the continuum, is used (Kondepudi and Prigogine, 2014). These two scales can be defined differently depending on the structure of the porous medium and the processes taking place inside it. Applying the thermodynamic principles to porous media involves using both length scales, and the way they relate has a considerable effect on the developed macroscopic description.

A porous medium is composed primarily of a deformable solid skeleton in which different fluid species circulate. Indeed, these fluids are composed of several immiscible phases. In this research, the concept of a REV is used. At this macroscale level, it is assumed that the thermodynamic quantities are uniform and that the porous medium is seen as a smooth continuum. At each point of this continuum, the different parts of the porous medium are independently at local equilibrium (or very close to it) and governed by their own equations of state (Gray and Miller, 2014). Let us consider a REV that occupies at time t the domain $\delta\Omega(t)$ with volume $\delta\mathcal{V}$ and mass $\delta\mathcal{M}$. It can be attributed to each phase α in this domain an apparent density ρ^α and a velocity $\boldsymbol{v}^\alpha$. The elementary mass of this phase in $\delta\mathcal{V}$ is $\delta\mathcal{M}_\alpha = \rho^\alpha\delta\mathcal{V} = \rho_\alpha n_\alpha \delta\mathcal{V}$ with $n_\alpha = \delta\mathcal{V}_\alpha/\delta\mathcal{V}$. Consequently, $\delta\mathcal{M} = \sum\delta\mathcal{M}_\alpha$ and $\rho = \sum\rho^\alpha$, with $\rho^\alpha = \rho_\alpha n_\alpha$. Knowing that each phase α is composed of q_α constituents, it can be assigned to each constituent k a density $\rho_{k\alpha}$ and a velocity $\boldsymbol{v}_{k\alpha}$. Thus, it is written that $\rho_\alpha = \sum\rho_{k\alpha}$ and $\boldsymbol{v}_\alpha = \sum\boldsymbol{v}_{k\alpha}$. If the mass of the k constituent in the phase α is $\delta\mathcal{M}_{k\alpha}$, then $\rho_{k\alpha} = \delta\mathcal{M}_{k\alpha}/\delta\mathcal{V}_\alpha$ and $c_{k\alpha} = \delta\mathcal{M}_{k\alpha}/\delta\mathcal{M}_\alpha = \rho_{k\alpha}/\rho_\alpha$ being the mass concentration of the constituent k in the phase α. With these definitions in mind, the conservation equations can be derived.

1.3.1 Conservation equations

The skeleton of the porous medium is considered deformable. For a solid particle initially at the position $\boldsymbol{x}_0$, deformation brings the particle to its a new position $\boldsymbol{x} = \boldsymbol{x}(\boldsymbol{x}_0, t)$ with velocity $\boldsymbol{v}_\sigma = \partial_t\boldsymbol{x}$. The evolution of the volume occupied by this particle through this position change is defined through the transformation Jacobian $\mathcal{J} = \delta\mathcal{V}/\delta\mathcal{V}_0$. All conservation equations are derived while taking the movement of the solid skeleton $\boldsymbol{v}_\sigma$ as a reference. For any physical quantity $\mathcal{F}(\boldsymbol{x}, t)$, $\dot{\mathcal{F}} = d\mathcal{F}/dt = \partial_t\mathcal{F} + \boldsymbol{v}_\sigma\cdot\boldsymbol{\nabla}\mathcal{F}$. For simplicity, in the coming descriptions the following notation is used $\boldsymbol{v}_\sigma = \boldsymbol{v}$. While the phase α is crossing through the elementary area

$\delta\mathcal{A}$ with normal vector $\boldsymbol{n}$, its mass flux is decomposed into two components,

$$\rho^\alpha \boldsymbol{v}_\alpha \cdot \boldsymbol{n}\delta\mathcal{A} = \underbrace{\rho^\alpha \boldsymbol{v}\cdot\boldsymbol{n}\,\delta\mathcal{A}}_{\text{due to solid movement}} + \underbrace{\rho^\alpha(\boldsymbol{v}_\alpha-\boldsymbol{v})\cdot\boldsymbol{n}\,\delta\mathcal{A}}_{\text{due to reltive movement}}, \tag{1.11}$$

which leads to the definition of filtration velocity $\boldsymbol{\omega}^\alpha = n_\alpha(\boldsymbol{v}_\alpha - \boldsymbol{v})$ of the phase α in the porous medium.

All the subsequent conservation laws are written in the Lagrangian form, i.e. with respect to the reference configuration of the solid phase. A local thermal equilibrium is assumed between all phases. The equation of mass conservation takes the form,

$$\bar{\mathcal{J}}\dot{m}^\alpha + \boldsymbol{\nabla}\cdot(\rho_\alpha\boldsymbol{\omega}^\alpha) = \bar{\pi}^\alpha, \quad \text{with,} \quad m^\alpha = \rho^\alpha\mathcal{J}, \tag{1.12}$$

while $\bar{\mathcal{J}} = 1/\mathcal{J}$, and $\bar{\pi}^\alpha$ being the total mass rate of all constituents exchanged through the interfaces of the phase α. If we consider only the solid skeleton of the porous media, Eq. 1.12 becomes $\bar{\mathcal{J}}\dot{m}^\sigma = \bar{\pi}^\sigma$. This indicates that the mass conservation of the solid phase is only verified when there are no chemical reactions contributing to the creation of a solid matter. Equation 1.12 has to be completed with the mass conservation equation of the constituent k,

$$\bar{\mathcal{J}}\dot{m}_k^\alpha + \boldsymbol{\nabla}\cdot(\rho_\alpha c_{k\alpha}\boldsymbol{\omega}^\alpha + \rho_\alpha \boldsymbol{J}_k^\alpha) = \pi_k^\alpha + \bar{\pi}_k^\alpha, \quad \text{with,} \quad m_k^\alpha = c_{k\alpha}m^\alpha, \tag{1.13}$$

and that $\sum_k \pi_k^\alpha = 0$ and $\bar{\pi}^\alpha = \sum_k \bar{\pi}_k^\alpha$.

The momentum conservation equation in the Lagrangian form is expressed as,

$$\sum(\rho^\alpha\dot{\boldsymbol{v}}_\alpha + \bar{\pi}^\alpha\boldsymbol{v}_\alpha) = \boldsymbol{\nabla}\cdot\underline{\underline{\boldsymbol{\sigma}}} + \rho\,\mathfrak{g}, \quad \text{with,} \quad \underline{\underline{\boldsymbol{\sigma}}} = \sum\underline{\underline{\boldsymbol{\sigma}}}^\alpha, \tag{1.14}$$

indicating that forces applied to the porous medium accelerate phase flow and mass convection that results from constituent exchanges on boundaries.

At interfaces, the surface tension between two phases α and β contributes to the conservation of momentum. According to Class, Helmig, and Bastian (2002), Forsyth and Simpson (2012), and Rouabhi (2019), the following macroscopic relation can be used,

$$\langle p_{|\alpha}\rangle_{\mathcal{S}_{\alpha\beta}} - \langle p_{|\beta}\rangle_{\mathcal{S}_{\alpha\beta}} = \langle \pm 2H_{\alpha\beta}\,\gamma_{\alpha\beta}\rangle_{\mathcal{S}_{\alpha\beta}}, \tag{1.15}$$

where $H_{\alpha\beta} = \pm(1/2)\boldsymbol{n}\cdot\boldsymbol{\nabla}_s\cdot(\underline{\underline{\boldsymbol{\delta}}} - \boldsymbol{n}\otimes\boldsymbol{n})$, the surface gradient operator $\boldsymbol{\nabla}_s$ is such that for any function ϕ we get $\boldsymbol{\nabla}_s\phi = (\underline{\underline{\boldsymbol{\delta}}} - \boldsymbol{n}\otimes\boldsymbol{n})\cdot\boldsymbol{\nabla}\phi$, and $\gamma_{\alpha\beta}$ is the surface tension between the two phases α and β. The numerical application of Eq. 1.15 is exhaustive. Usually the surface averaged quantities are replaced by their volume averaged equivalents ($\langle p\rangle_\alpha$ and $\langle p\rangle_\beta$) using a heuristic analogy completed by empirical relations that take temperature and volume fractions into consideration (Rouabhi, 2019).

The internal energy conservation equation is cast in the following form,

$$\bar{\mathcal{J}}\dot{\mathsf{U}} + \boldsymbol{\nabla}\cdot\left(\boldsymbol{\Psi}_u + \sum(\rho_\alpha u_\alpha\underline{\underline{\boldsymbol{\delta}}} - \underline{\underline{\boldsymbol{\sigma}}}_\alpha)\boldsymbol{\omega}^\alpha\right) = Q_r + \underline{\underline{\boldsymbol{\sigma}}} : \underline{\underline{\boldsymbol{\nabla}}}\boldsymbol{v} - \sum\rho_\alpha\boldsymbol{\omega}^\alpha\cdot(\dot{\boldsymbol{v}}_\alpha - \mathfrak{g}), \tag{1.16}$$

with $\underline{\underline{\boldsymbol{\sigma}}}_\alpha = \langle\underline{\underline{\boldsymbol{\sigma}}}\rangle_\alpha$, $\mathsf{U} = \sum\mathsf{U}^\alpha = \sum m^\alpha u_\alpha$, $\boldsymbol{\Psi}_u = \sum\boldsymbol{\Psi}_u^\alpha$, and $Q_r = \sum Q_r^\alpha$. The internal energy density U contained in the REV of the porous medium at time t can be expressed as $\mathcal{U} = \int_{\Omega(t)}\rho^\alpha u_\alpha\,d\mathcal{V} = \int_{\Omega(t=0)}\mathsf{U}\,d\mathcal{V}_0$.

While assuming local thermal equilibrium, the entropy conservation equation takes the form,

$$\bar{\mathcal{J}}\dot{\mathsf{S}} + \boldsymbol{\nabla}\cdot\left(\boldsymbol{\Psi}_s/T + \sum\rho_\alpha s_\alpha\boldsymbol{\omega}^\alpha\right) = (Q_r + \varpi)/T, \tag{1.17}$$

with $\mathsf{S} = \sum\mathsf{S}^\alpha = \sum m^\alpha s_\alpha$, $\boldsymbol{\Psi}_s = \sum\boldsymbol{\Psi}_s^\alpha$, $Q_r = \sum Q_r^\alpha$, and $\varpi = \sum\varpi^\alpha$. The entropy density S

contained in the REV of the porous medium at time t can be expressed as $\mathcal{S} = \int_{\Omega(t)} \rho^\alpha s_\alpha \, d\mathcal{V} = \int_{\Omega(t=0)} \mathsf{S} \, d\mathcal{V}_0$.

1.3.2 Constitutive laws

To verify the second principle of thermodynamics, a clear relation between the two fluxes ($\boldsymbol{\Psi}_u$ and $\boldsymbol{\Psi}_s$) needs to be established. The definition introduced in Sect. 1.2 can not be used directly here due to complexities related to the thermodynamic state of the solid phase. If it is assumed that the solid phase represents a closed system ($\boldsymbol{J}_k^\sigma = \boldsymbol{0}$ and $\bar{\pi}^\sigma = 0$), then the following expressions are reached,

$$\boldsymbol{\Psi}_s^\alpha = \boldsymbol{\Psi}_u^\alpha - \sum \rho_\alpha \bar{\mu}_{k\alpha} \boldsymbol{J}_k^\alpha \;\; (\alpha \neq \sigma), \quad \text{and,} \quad \boldsymbol{\Psi}_s^\sigma = \boldsymbol{\Psi}_u^\sigma. \tag{1.18}$$

If phases flow velocities are very small in the porous medium, viscous stresses can be neglected and the following expression is obtained for phase stresses $\underline{\underline{\boldsymbol{\sigma}}}_\alpha = -p_\alpha \underline{\underline{\boldsymbol{\delta}}} \;\; (\alpha \neq \sigma)$. The macroscopic state variables are used as defined previously (Sect. 1.2), therefore the partial derivatives of the free energy $f_\alpha(\nu_\alpha, T, \boldsymbol{c}_\alpha)$ give,

$$p_\alpha = -\partial_{\nu_\alpha} f_\alpha(\nu_\alpha, T, \boldsymbol{c}_\alpha), \quad s_\alpha = -\partial_T f_\alpha(\nu_\alpha, T, \boldsymbol{c}_\alpha), \quad \text{and,} \quad \bar{\mu}_{k\alpha} = \partial_{c_{k\alpha}} f_\alpha(\nu_\alpha, T, \boldsymbol{c}_\alpha), \tag{1.19}$$

with a rigorous assumption that mass is conserved for the α-phase. Even-though this assumption is correct in the case of an isotropic fluid flow, it is not necessarily the case in porous media (term $\bar{\pi}^\alpha$ of Eq. 1.12).

With these definitions in mind, the two energy equations can be combined to get the partitions of the volumetric dissipation,

$$\varpi = \varpi_c + \varpi_i + \varpi_\psi + \varpi_J + \varpi_\omega, \quad \text{restricted to,} \quad \varpi_c \geq 0, \; \varpi_i \geq 0, \; \varpi_\psi \geq 0, \; \varpi_J \geq 0, \; \varpi_\omega \geq 0. \tag{1.20}$$

This combination indicates that irreversibility sources are mostly due to chemical reactions, volumetric intrinsic dissipation, thermal conduction, constituents diffusion in phases, and phases transport with respect to the solid skeleton. These irreversibility sources can be expressed mathematically as,

$$\begin{aligned}
\varpi_c &= -\sum\!\!\!\!\!\!\diagup \sum \pi_k^\alpha \bar{\mu}_{k\alpha} - \sum\!\!\!\!\!\!\diagup \left(\bar{\pi}^\alpha \left(g_\alpha - \sum c_{k\alpha} \bar{\mu}_{k\alpha} \right) + \sum \bar{\pi}_k^\alpha \bar{\mu}_{k\alpha} \right); \\
\varpi_i &= \bar{\mathcal{J}} \left(T\dot{\mathsf{S}} - \dot{\mathsf{U}} + \mathcal{J} \underline{\underline{\boldsymbol{\sigma}}} : \underline{\underline{\boldsymbol{\nabla}}} \boldsymbol{v} + \sum\!\!\!\!\!\!\diagup g_\alpha \dot{m}^\alpha + \sum\!\!\!\!\!\!\diagup \sum m^\alpha \bar{\mu}_{k\alpha} \dot{c}_{k\alpha} \right); \\
\varpi_\psi &= -\boldsymbol{\psi} \cdot \boldsymbol{\nabla} T / T; \\
\varpi_J &= -\sum\!\!\!\!\!\!\diagup \sum \rho_\alpha \boldsymbol{J}_k^\alpha \cdot \boldsymbol{\nabla}_T \bar{\mu}_{k\alpha}, \quad \text{and;} \\
\varpi_\omega &= -\sum\!\!\!\!\!\!\diagup \rho_\alpha \boldsymbol{\omega}^\alpha \cdot \left(\boldsymbol{\nabla} g_\alpha + s_\alpha \boldsymbol{\nabla} T - \sum \bar{\mu}_{k\alpha} \boldsymbol{\nabla} c_{k\alpha} + \dot{\boldsymbol{v}}_\alpha - \boldsymbol{\mathfrak{g}} \right),
\end{aligned} \tag{1.21}$$

with $\boldsymbol{\psi} = \boldsymbol{\Psi}_s + \sum\!\!\!\!\!\!\diagup \sum \rho_\alpha T \partial_T \bar{\mu}_{k\alpha} \boldsymbol{J}_k^\alpha$ and $g_\alpha(p_\alpha, T, \boldsymbol{c}_\alpha)$ being the specific free enthalpy of the α-phase.

These volumetric dissipations can be used to derive the needed constitutive laws while ensuring a continuous production of entropy (Eq. 1.20). The Fourier's law of heat conduction is adopted to ensure the positivity of ϖ_ψ,

$$\boldsymbol{\psi} = -\underline{\underline{\boldsymbol{\Lambda}}} \cdot \boldsymbol{\nabla} T, \tag{1.22}$$

with $\underline{\underline{\boldsymbol{\Lambda}}}$ being the effective thermal conductivity tensor of the porous medium.

The positivity of ϖ_ω is ensured through the generalization of the Darcy's law for every phase α,

$$\boldsymbol{\omega}^\alpha = -\frac{\underline{\underline{\boldsymbol{k}}}_\alpha}{\mu_\alpha} \cdot \Big(\boldsymbol{\nabla} p_\alpha + \rho_\alpha (\dot{\boldsymbol{v}} - \mathfrak{g}) \Big), \tag{1.23}$$

with $\underline{\underline{\boldsymbol{k}}}_\alpha$ being the permeability tensor of the porous medium occupied by the α-phase, and μ_α is the dynamic viscosity of the α-phase.

For a binary mixture, the positivity of ϖ_J can be assured if the dissolved constituent has a poor concentration that it does not affect the specific volume of the α-phase ($\partial_c \nu_\alpha \approx 0$). Consequently, a relation similar to the Fickian diffusion in binary mixtures can be used where the reference velocity is the barycentric,

$$\boldsymbol{J} = -\underline{\underline{\boldsymbol{D}}}_\alpha \cdot \boldsymbol{\nabla} c, \tag{1.24}$$

with $\underline{\underline{\boldsymbol{D}}}_\alpha$ being the diffusion coefficient of the constituent k in the α-phase.

The positivity of ϖ_c is assured by considering the case of two phases α and β that exchange a single constituent k,

$$\varpi_c = \bar{\pi}_k^\alpha (\mu_{k\beta} - \mu_{k\alpha}), \tag{1.25}$$

indicating the difference between chemical potentials of this constituent in the two phases. By introducing a coefficient $\varrho_k^{\alpha\beta} \geq 0$ such that Eq. 1.25 is written as $\varrho_k^{\alpha\beta} \bar{\pi}_k^\alpha = \mu_{k\beta} - \mu_{k\alpha}$, the positivity of ϖ_c is ensured. When the two chemical potentials are equal $\varrho_k^{\alpha\beta} = 0$, a phase change without volumetric dissipation takes place.

The positivity of the volumetric intrinsic dissipation ϖ_i is ensured through the development of the solid skeleton state laws. If the solid skeleton deforms elastically, neglecting the volumetric intrinsic dissipation $\varpi_i = 0$ leads us to the following definition,

$$\dot{\mathsf{G}}^\sigma = \underline{\underline{\boldsymbol{\Pi}}} : \dot{\underline{\underline{\boldsymbol{\Delta}}}} - \mathsf{S}^\sigma \dot{T} - \sum n_\alpha \mathcal{J} \dot{p}_\alpha, \tag{1.26}$$

where the term $\underline{\underline{\boldsymbol{\Pi}}} : \dot{\underline{\underline{\boldsymbol{\Delta}}}}$ reflects the contribution of $\mathcal{J} \underline{\underline{\boldsymbol{\sigma}}} : \underline{\underline{\boldsymbol{\nabla}}} \boldsymbol{v}$ in Eq. 1.21_2. The symmetric Piola-Kirchoff tensor is $\underline{\underline{\boldsymbol{\Pi}}} = \mathcal{J} \underline{\underline{\boldsymbol{F}}}^{-1} \underline{\underline{\boldsymbol{\sigma}}} \underline{\underline{\boldsymbol{F}}}^{-T}$, the Cauchy Green tensor is $\underline{\underline{\boldsymbol{\Delta}}} = (\underline{\underline{\boldsymbol{F}}}^T \underline{\underline{\boldsymbol{F}}} - \underline{\underline{\boldsymbol{\delta}}})/2$, with $\underline{\underline{\boldsymbol{F}}}$ being the macroscopic transformation gradient of the solid skeleton. The free enthalpy of the solid skeleton is $\mathsf{G}^\sigma = \mathsf{F}^\sigma - \sum n_\alpha \mathcal{J} p_\alpha$, with $\mathsf{F}^\sigma = m^\sigma f_\sigma$ being the free energy density of the solid skeleton.

A thermodynamic potential $\mathsf{G}^\sigma(\underline{\underline{\boldsymbol{\Delta}}}, T, \boldsymbol{P})$ can be defined with the following set of independent state variables $(\underline{\underline{\boldsymbol{\Delta}}}, T, \boldsymbol{P})$, with $\boldsymbol{P} = (p_\alpha, p_\beta, ..., p_\omega)$ being the set of present fluid phase pressures. Therefore, Eq. 1.26 should be satisfied for every variation of the thermodynamic state,

$$\underline{\underline{\boldsymbol{\Pi}}} = \partial_{\underline{\underline{\boldsymbol{\Delta}}}} \mathsf{G}^\sigma(\underline{\underline{\boldsymbol{\Delta}}}, T, \boldsymbol{P}), \quad \mathsf{S}^\sigma = -\partial_T \mathsf{G}^\sigma(\underline{\underline{\boldsymbol{\Delta}}}, T, \boldsymbol{P}), \quad n_\alpha \mathcal{J} = -\partial_{p_\alpha} \mathsf{G}^\sigma(\underline{\underline{\boldsymbol{\Delta}}}, T, \boldsymbol{P}). \tag{1.27}$$

The macroscopic state laws of the solid skeleton are defined through the two Eqs 1.19 and 1.27, that relate the state variables $(\nu_\alpha, T, \boldsymbol{c}_\alpha)$ and $(\underline{\underline{\boldsymbol{\Delta}}}, T, \boldsymbol{P})$ to their associate equivalents $(p_\alpha, s_\alpha, \bar{\mu}_{k\alpha})$ and $(\underline{\underline{\boldsymbol{\Pi}}}, \mathsf{S}^\sigma, n_\alpha \mathcal{J})$.

The heat equation (Eq. 1.17) can be written in an explicit form ready to be used in the engineering applications. According to Rouabhi (2019), the heat equation of multiphase compositional flows in elastically deformable porous media is cast in the following form,

$$\begin{aligned} &\rho C_p \dot{T} + \sum \left[\left(\frac{\rho^\sigma}{\rho_0^\sigma} (\underline{\underline{\boldsymbol{\chi}}} : \underline{\underline{\boldsymbol{\kappa}}}_\alpha - \chi_{n\alpha}) - \frac{\rho^\alpha}{\rho_\alpha} \chi_{p\alpha} \right) T \dot{p}_\alpha + \boldsymbol{\omega}^\alpha \cdot \left(\rho_\alpha C_{p\alpha} \boldsymbol{\nabla} T - \chi_{p\alpha} T \boldsymbol{\nabla} p \right) \right] \\ &+ \frac{\rho^\sigma}{\rho_0^\sigma} T \underline{\underline{\boldsymbol{\chi}}} : \dot{\underline{\underline{\boldsymbol{\Pi}}}} = \varpi_\omega + Q_r + \boldsymbol{\nabla} \cdot (\underline{\underline{\boldsymbol{\Delta}}} \cdot \boldsymbol{\nabla} T) - \sum \sum \left(\bar{\pi}_k^\alpha \bar{h}_{k\alpha} + \pi_k^\alpha \partial_{c_{k\alpha}} h_\alpha + \rho_\alpha \boldsymbol{J}_k^\alpha \cdot \boldsymbol{\nabla} (\partial_{c_{k\alpha}} h_\alpha) \right), \end{aligned} \tag{1.28}$$

with:

- ρ_0^σ being the initial density of the solid skeleton;
- $\underline{\underline{\boldsymbol{\chi}}}$ being the second order tensor of volumetric thermal expansion. It relates linearly the increments of the strain tensor $\underline{\underline{\boldsymbol{\Delta}}}$ to any temperature increment at constant stresses and phase pressures;
- $\rho C_p = \rho^\sigma C_\sigma + \sum \rho^\alpha C_{p\alpha}$, where the heat capacity at constant stresses and fluid pressures is $C_\sigma = C_\Delta + (1/\rho_0^\sigma) T \underline{\underline{\boldsymbol{\chi}}} : \underset{\sim}{\boldsymbol{H}} : \underline{\underline{\boldsymbol{\chi}}}$. Noting that C_Δ is a scalar coefficient that corresponds to a mass heat capacity at constant strains and phase pressures, and $\underset{\sim}{\boldsymbol{H}}$ is the fourth order elasticity tensor of Hooke that relates linearly the increments of the stress tensor $\underline{\underline{\boldsymbol{\Pi}}}$ to any increment of the strain tensor $\underline{\underline{\boldsymbol{\Delta}}}$ at constant temperature and phase pressures (it is the drained isothermal elasticity modulus);
- $\underline{\underline{\boldsymbol{\kappa}}}_\alpha$ being the second order tensor of the hydro-mechanical coupling. It relates linearly the increments of the stress tensor $\underline{\underline{\boldsymbol{\Pi}}}$ to any α-phase pressure increment at constant temperature, strains, and phase pressure p_β ($\beta \neq \alpha$);
- $\chi_{n\alpha}$ being a scalar coefficient that relates linearly the increments of $n_\alpha \mathcal{J}$ to any increment of the temperature at constant strains and phase pressures;
- for any phase α, the specific entropy can be expressed in terms of the state variables $(p_\alpha, T, \boldsymbol{c}_\alpha)$,
$$\rho^\alpha T \dot{s}_\alpha = -\frac{\rho^\alpha}{\rho_\alpha} T \chi_{p\alpha} \dot{p}_\alpha + \rho^\alpha C_{p\alpha} \dot{T} + \sum \rho^\alpha T (\partial_{c_{k\alpha}} s_\alpha) \dot{\boldsymbol{c}}_{k\alpha}, \tag{1.29}$$
from which the heat capacity of the α-phase at constant pressure and composition is $C_{p\alpha} = T \partial_T s_\alpha(p_\alpha, T, \boldsymbol{c}_\alpha)$, and the volumetric thermal expansion at constant pressure and composition is $\chi_{p\alpha} = -\partial_T \rho_\alpha(p_\alpha, T, \boldsymbol{c}_\alpha)/\rho_\alpha$; and,
- $\bar{h}_{k\alpha}(p_\alpha, T, \boldsymbol{c}_\alpha) = h_\alpha + \partial_{c_{k\alpha}} h_\alpha - \sum c_{j\alpha} \partial_{c_{j\alpha}} h_\alpha$, with h_α being the specific enthalpy of the α-phase.

These coefficients, mostly of different tensorial nature, stem from the partial derivatives of G^σ. This heat equation is derived while considering the solid skeleton as a closed thermodynamic system ($\dot{m}^\sigma = \bar{\pi}^\sigma = 0$). The intrinsic volumetric dissipation is set equal to zero ($\varpi_i = 0$), and the Fourier's heat conduction law is adopted.

The final part of this chapter presents the Lagrangian derivatives of Eq. 1.27,

$$\begin{aligned} \dot{\underline{\underline{\boldsymbol{\Pi}}}} = \underset{\sim}{\boldsymbol{H}} : (\dot{\underline{\underline{\boldsymbol{\Delta}}}} - \underline{\underline{\boldsymbol{\chi}}} \dot{T}) + \sum \underline{\underline{\boldsymbol{\kappa}}}_\alpha \dot{p}_\alpha, \quad \dot{\mathsf{S}}^\sigma &= \underset{\sim}{\boldsymbol{H}} : \underline{\underline{\boldsymbol{\chi}}} : \dot{\underline{\underline{\boldsymbol{\Delta}}}} + \rho_0^\sigma C_\Delta \dot{T}/T - \sum \chi_{n\alpha} \dot{p}_\alpha, \\ \frac{d}{dt}(n_\alpha \mathcal{J}) &= \underline{\underline{\boldsymbol{\kappa}}}_\alpha : \dot{\underline{\underline{\boldsymbol{\Delta}}}} - \chi_{n\alpha} \dot{T} + \sum \bar{M}_{\alpha\beta} \dot{p}_\beta, \end{aligned} \tag{1.30}$$

with $\bar{M}_{\alpha\beta} = 1/M_{\alpha\beta}$ being a scalar coefficient that linearly relates an increment of $n_\alpha \mathcal{J}$ to an increment of the pressure p_β of the phase β in any evolution at constant temperature, deformation and fluid pressures p_γ ($\gamma \neq \beta$). The coefficients $M_{\alpha\beta}$ form the components of a symmetric matrix.

Chapter 2

Fluid circulation in porous media

The first part of this chapter addresses the technique of hydraulic fracturing for thermal recovery form geothermal systems. Aspects related to thermal efficiency, impedance, and effect of used geothermal fluids are briefly discussed. In the second part, hydraulic fracturing for applications related to oil an gas industry is presented, with a special emphasis on the non-diffusive induced seismicity triggering fronts.

2.1 A continuum approach to simulate fluid circulation in hydraulically stimulated geothermal reservoirs

In the context of energy transition, thermal recovery from Hot Dry Rock (HDR) reservoirs is becoming an alternative to grey energies (Turcotte and Schubert, 2002; Bruel, 1995a; Bruel, 1995b). Thermal extraction from geothermal systems is achieved by injecting cold fluids into deep reservoirs where the temperature gradient is favorable. The retrieved geothermal fluid is either used directly for heating purposes, or indirectly in generating electricity. The economic viability of the recovery process is controlled by crucial factors that include the evolution of the reservoir pressure, of the effective stresses, and of the fluid losses (Bruel, 1995a; Bruel, 1995b). Permeability changes and irreversible processes of thermo-mechanical nature may also play a significant role in the overall behavior of the HDR reservoirs (Papanastasiou, 1999).

Modern geothermal projects are nowadays focusing on enhancing the permeability of the reservoirs, the so-called Enhanced Geothermal Systems (EGS) (Jupe et al., 1995). Geothermal fluids are injected with high flow rates that the assumption of a time-independent permeability becomes improper. Extreme thermo-hydromechanical changes are expected to take place near the injection well. Indeed, such abrupt changes cause fractures to evolve and to connect and permeability to increase in a highly heterogeneous manner. The increase in HDR reservoir permeability due to hydraulic fracturing is bound to affect the thermal recovery process.

Hydraulic fracturing has been used for years to enhance oil and gas recovery (Fjaer et al., 2008). However, for heat recovery from geothermal reservoirs, a few key points should be emphasized:

- thermal effects on the fracturing process are quantitatively significant. They typically reduce the fracturing pressure by 50% or more;
- unlike simulations of drilling induced fractures, the length over which the permeability should be enhanced encompasses several hundred meters. The initial heterogeneities due to preexisting faults certainly attract and modify the enhancement that would develop in an otherwise homogeneous formation. Re-activation of these faults *alone* is to be avoided as the process would easily produce shortcuts and render the circulation paths inefficient. Therefore, even if large-scale spatial heterogeneities are unavoidable, a significant portion of the reservoir volume, where the fracture network can be considered homogeneous, should be sought;

– modeling of drilling induced fractures in petroleum engineering in a finite element context insists on creating a few fractures, typically extending over a borehole diameter, from existing singularities around the well based on numerically enhanced strain or pressure fields and cohesive fracture tricks. Such an approach is not viable in a geothermal context: indeed, as already indicated, a) the fracture network should be more homogeneously spread; b) the length scale is orders of magnitude larger; and c) critically, the width of the fractures is of capital importance for the permeability.

For these reasons, this study provides a continuum modelling approach for hydraulic fracturing in a thermo-hydromechanical framework. The Finite Element Method (FEM) is used, and fractures and their spatial evolutions are translated into spatial permeability evolutions.

2.1.1 Hydraulic fracturing in a thermo-hydromechanical framework

Hydraulic fracturing is addressed in a thermo-hydromechanical framework. As a key ingredient to this framework, a simple Hydraulic Fracturing Model (HFM) based on an opening mode of fracture evolution (Mode I), is used in a first step. The model is next modified to account for the influence of the deviatoric stress. At any time and any geometrical point, the state of fracture is embodied in a fabric that includes both the actual fracture length and actual fracture width in all directions of space. The local current anisotropic permeability tensor, which describes the evolving permeability of the fractured medium, is obtained by directional integration of the updated fracture fabric.

The fracture model is used to simulate circulation tests between an injection well and two production wells in a simplified geometrical setting. Field data from several references are collected to validate the numerical simulations. The effect of hydraulic fracturing on the designing characteristics of HDR reservoirs, primarily impedance and efficiency, is discussed based on the simulations (Grecksch et al., 2003; Jupe et al., 1995). The field record of the Soultz-sous-Forêts geothermal site presented in Bruel (1995b) indicates that hydraulic fracturing affects significantly the efficiency of the thermal extraction process. However, a minimal size of HDR reservoirs is required to ensure efficient thermal extraction and long-term low impedance (Jupe et al., 1995).

This section aims at studying the effect of hydraulic fracturing on the impedance and efficiency of HDR reservoirs using finite element simulations which are correlated to field data when available. It also discusses the effect of temperature change on the viscosity of geothermal fluids, and the subsequent implications on the hydraulic fracturing process and the resulting impedance and efficiency. The fracturing models, with and without a temperature-dependent viscosity, are implemented in a domestic Fortran 90 finite element code and the simulations, for the same reservoir, are systematically compared. Some designing considerations, in terms of injection pressure or flow rate, are included as well as issues pertaining to the stability of the wellbores.

2.1.1.1 Thermo-hydromechanical framework

The thermodynamics framework of this section features a single-phase single-constituent fluid seeping through an elastically deformed porous medium. Even-though the characteristic time of heat diffusion in the rock matrix is significantly larger than the characteristic time of heat propagation by convection in the fractures, the present study assumes Local Thermal Equilibrium (LTE). The mechanical response of a poroelastic medium undergoing thermal changes while in LTE is governed by two constitutive equations. The Biot's effective stress tensor of the mixture $\underline{\underline{\boldsymbol{\sigma}}} + \kappa \underline{\underline{\boldsymbol{\delta}}}$ expresses in terms of the strain tensor $\underline{\underline{\boldsymbol{\varepsilon}}}$ and the temperature departure

$\theta = T - T_0$ with respect to a reference T_0 as (McTigue, 1986),

$$\underline{\underline{\boldsymbol{\sigma}}} + \kappa p \underline{\underline{\boldsymbol{\delta}}} = 2G\underline{\underline{\boldsymbol{\varepsilon}}} + \frac{2G\nu}{1-2\nu}\mathrm{tr}(\underline{\underline{\boldsymbol{\varepsilon}}})\underline{\underline{\boldsymbol{\delta}}} - K\chi_{p\sigma}\theta\underline{\underline{\boldsymbol{\delta}}}, \tag{2.1}$$

where $\underline{\underline{\boldsymbol{\sigma}}}$ is the total stress tensor, p is the pore fluid pressure, $\mathrm{tr}(\underline{\underline{\boldsymbol{\varepsilon}}})\underline{\underline{\boldsymbol{\delta}}}$ is the volumetric strain, G is the shear modulus, ν is the drained Poisson's ratio, $\kappa = 1 - K/K_\sigma$ is the Biot's coefficient, K is the drained bulk modulus, K_σ is the bulk modulus of the solid constituent, and $\chi_{p\sigma}$ is the volumetric thermal expansion coefficient of the solid. Sign convention is that compressive stresses and strains are negative.

The change of the fluid mass content,

$$\tilde{m} = \kappa\mathrm{tr}(\underline{\underline{\boldsymbol{\varepsilon}}}) + \frac{p}{M} - \bar{\chi}_p\theta, \tag{2.2}$$

involves mechanical, fluid, and thermal contributions, with coefficients,

$$\frac{1}{M} = \frac{\kappa}{K_\sigma} + n_\lambda\left(\frac{1}{K_\lambda} - \frac{1}{K_\sigma}\right), \tag{2.3}$$

and $\bar{\chi}_p = \kappa\chi_{p\sigma} + n_\lambda(\chi_{p\lambda} - \chi_{p\sigma})$, that features the volumetric thermal expansion coefficient of the fluid $\chi_{p\lambda}$, the bulk modulus of the fluid K_λ, and the reference porosity of the porous medium n_λ (porous volume is full of the single phase fluid, hence $n_\sigma = 1 - n_\lambda$). The subscripts σ and λ refer to the solid and fluid phases respectively.

Two additional constitutive equations are needed to define the transport of fluid and transfer of heat. The first equation features the Darcy's law, that describes the seepage of the fluid through the porous medium. It relates the apparent fluid flux relative to the solid skeleton $\boldsymbol{\omega}$ to the effective pressure gradient $\boldsymbol{\nabla} p - \rho_\lambda \mathfrak{g}$,

$$\boldsymbol{\omega} = \boldsymbol{q} = n_\lambda(\boldsymbol{v}_\lambda - \boldsymbol{v}) = -\frac{\underline{\underline{\boldsymbol{k}}}}{\mu}\cdot(\boldsymbol{\nabla} p - \rho_\lambda \mathfrak{g}), \tag{2.4}$$

where $\underline{\underline{\boldsymbol{k}}}$ is the permeability tensor of the mixture, μ is the fluid dynamic viscosity, ρ_λ is the intrinsic fluid density, and $\mathfrak{g} = \mathfrak{g}\boldsymbol{e}$ with $\mathfrak{g}$ being the gravitational acceleration and $\boldsymbol{e}$ the unit vertical vector directed downwards. According to Fourier's law of heat conduction, the heat flux $\boldsymbol{\psi}$ is aligned with the negative of the temperature gradient $\boldsymbol{\nabla}\theta$,

$$\boldsymbol{\psi} = -\Lambda\boldsymbol{\nabla}\theta, \tag{2.5}$$

since the porous medium is in local thermal equilibrium, the effective thermal conductivity $\Lambda = n_\sigma\Lambda_\sigma + n_\lambda\Lambda_\lambda$ is obtained by volume averaging over the species. Though this analysis focuses on the evolving anisotropy of the permeability tensor, it is convenient to consider an isotropic thermal conductivity of the solid.

The displacement vector, pore pressure, and temperature satisfy three field equations:

$$\begin{aligned}
&\text{balance of momentum of the whole mixture :} && \boldsymbol{\nabla}\cdot\underline{\underline{\boldsymbol{\sigma}}} + \rho\mathfrak{g} = \boldsymbol{0};\\
&\text{balance of mass of the fluid :} && \boldsymbol{\nabla}\cdot\boldsymbol{q} + \frac{\partial\tilde{m}}{\partial t} = 0;\\
&\text{balance of energy of the whole mixture :} && \boldsymbol{\nabla}\cdot\boldsymbol{\psi} + \rho C_v\frac{\partial\theta}{\partial t} + \rho_\lambda C_{p\lambda}\boldsymbol{q}\cdot\boldsymbol{\nabla}\theta = 0.
\end{aligned} \tag{2.6}$$

Here $\rho = n_\sigma\rho_\sigma + n_\lambda\rho_\lambda$ is the mass density of the mixture. The heat storage contribution is expressed in terms of the volumetric isochoric heat capacity of the mixture, $\rho C_v = n_\sigma\rho_\sigma C_{v\sigma} +$

$n_\lambda \rho_\lambda C_{v\lambda}$, which is obtained by volume averaging over the species. The energy equation describes heat convection due to fluid seepage through the solid skeleton introduced by the isobaric heat capacity of the fluid $\rho_\lambda C_{p\lambda} = \rho_\lambda C_{v\lambda} + K_\lambda \chi_{p\lambda}^2 T$. The convective term can by no means be neglected in the context of geothermal reservoirs. Therefore, the equation of balance of energy can *not* be decoupled from the system of equations and solved independently. This thermo-hydromechanical framework is integrated into a Fortran 90 domestic finite element code. All details of matrices development, combination, and solving by several time integration schemes are documented in AbuAisha (2014) and AbuAisha, Loret, and Eaton (2016).

2.1.1.2 Mode I hydraulic fracturing model

This section provides the basic elements for a fracturing model (HFM) which is capable of ensuring a directionally stable mode I of fracture evolution in a fully coupled thermo-hydromechanical framework. Let us consider a group of penny-shaped fractures of average length ℓ and arbitrary normal direction $\boldsymbol{n}$ in the horizontal plane (x, y) around a borehole. If the borehole pressure is gradually increased to a point the normal effective stress $\sigma'_n = \boldsymbol{n} \cdot \underline{\underline{\boldsymbol{\sigma}}}' \cdot \boldsymbol{n}$ (at the fracture tip) becomes tensile and exceeds the limit of material tensile strength, the group of fractures starts propagating and consequently the average aperture increases. To track the evolution of the average length ℓ of a group of fractures in direction $\boldsymbol{n}$, a simple criterion is proposed,

$$F(\sigma'_n, \ell) = f(\ell)\, \sigma'_n \sqrt{\pi \ell} - K_{Ic} = 0, \tag{2.7}$$

where K_{Ic} is mode I fracture toughness of the rock, $f(\ell)$ is a positive scalar valued function which controls the stability of fracture propagation (Shao, Zhou, and Chau, 2005),

$$f(\ell) = \eta \begin{cases} \dfrac{\ell_f}{\ell}, & \ell < \ell_f; \\ 1, & \ell \geq \ell_f, \end{cases} \tag{2.8}$$

with ℓ_f denoting the critical fracture length for accelerated coalescence of fractures. In this study fracture healing or macroscopic damage are not considered and fracture length cannot grow beyond ℓ_f. The parameter η is the fracture growth stabilizing parameter. While $\ell < \ell_f$ fractures begin to propagate reflecting the relaxation of local tensile stresses as fractures grow away from zone of stress concentration. For $\ell \geq \ell_f$, the function $f(\ell)$ reaches an asymptotic value as fractures coalesce and damage localizes. Based on physical considerations, authors like Klimczak et al. (2010) and Shao, Zhou, and Chau (2005) and Papanastasiou and Thiercelin (1993) have related the fracture aperture to fracture face mismatch and local grain matrix interaction during fracture growth. Here, the fracture aperture w is taken as an increasing power function of the fracture length ℓ, i.e. $w(m) = 0.0002\, \ell^{0.25}$ (m) (AbuAisha, Loret, and Eaton, 2016).

The philosophy of integrating this fracture model into the developed thermo-hydromechanical framework starts by assuming that the reservoir has preexisting fractures distributed homogeneously over its volume. Once fluid injection starts, the state of effective stresses on each fracture group changes. Each Gauss point of the finite element mesh can be seen as a borehole[1] surrounded by fractures in all possible directions (Fig. 2.1). Solving for the thermo-hydromechanical framework gives the effective stresses at each Gauss point which can be substituted into the fracture criterion (Eq. 2.7) to get the updated length and aperture.

Knowing the fracture length $\ell(\boldsymbol{n})$ and aperture $w\big(\ell(\boldsymbol{n})\big)$ in the arbitrary direction $\boldsymbol{n}$, the local velocity field is calculated by implementing the Navier-Stokes equation for laminar flow between two parallel plates. The anisotropic permeability tensor, which is provided by the

[1] The radius of the borehole is assumed very small compared to the dimensions of the Boundary Value Problem (BVP).

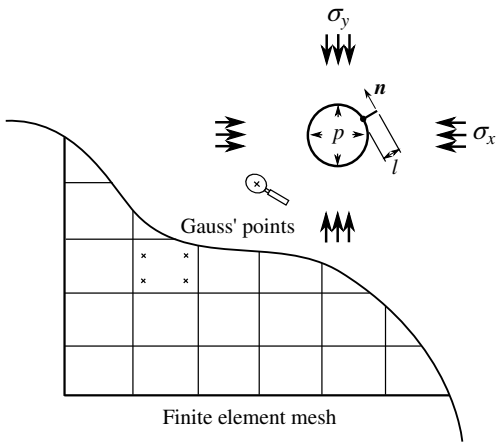

FIGURE 2.1: Integrating the fracturing model into the thermo-hydromechanical framework. Each Gauss point is seen as a borehole surrounded by preexisting fractures in all possible space directions.

fractures, is calculated by averaging the individual Poiseuille flows over all the directions of the space, i.e. by integrating over the unit sphere $\mathcal{S}$,

$$\underline{\underline{\boldsymbol{k}}}_c = \frac{1}{48}\frac{N}{\mathcal{V}}\int_{\mathcal{S}} C(\ell(\boldsymbol{n}))\, w\big(\ell(\boldsymbol{n})\big)^3\, \ell(\mathbf{n})^2\, (\underline{\underline{\boldsymbol{\delta}}} - \boldsymbol{n}\otimes\boldsymbol{n})\, d\mathcal{A}(\boldsymbol{n}), \tag{2.9}$$

where $N/\mathcal{V}$ is the fracture density (number of fractures N in the volume $\mathcal{V}$). The connectivity function $C(\boldsymbol{n})$,

$$C(\ell(\boldsymbol{n})) = c_c\,\frac{\ell(\boldsymbol{n}) - \ell_0}{\ell_f - \ell_0}, \tag{2.10}$$

indicates that connection between fractures increases as they grow in size from the initial length ℓ_0 to the final length ℓ_f, with c_c being a material constant. The overall permeability tensor of the fractured medium is composed of two parts: the initial permeability tensor denoted by $\underline{\underline{\boldsymbol{k}}}_0$ due to the initial porosity, and the fracture induced permeability tensor denoted by $\underline{\underline{\boldsymbol{k}}}_c$. The flows in the two cavities are assumed to take place in parallel and the total permeability tensor is obtained by summation $\underline{\underline{\boldsymbol{k}}} = \underline{\underline{\boldsymbol{k}}}_0 + \underline{\underline{\boldsymbol{k}}}_c$.

The method is numerically demanding that it requires an important spatial discretization to get a sufficient number of the vectors $\boldsymbol{n}$ to ensure a smooth evolution of the directional quantities. Figure 2.2 shows how the directional evolution of a fracture length is traced by spatial discretization.

Fractures are assumed to be penny-shaped and their lengths can grow in the three dimensions following the stress state evolution at each Gauss point.

2.1.1.3 Fracture initiation and wellbore stability

Once injection into the reservoir starts, the wellbore pressure increases and the rock formation cools down leading to more tensile effective stresses on the fractures. Knowing the initial geostatic conditions of the reservoir, the wellbore excess pressure needed to start hydraulic fracturing can be calculated. For a vertical borehole penetrating a rock formation with homogeneous and isotropic elastic and transport properties, the excess borehole pressure $p_b^{HF} - p_r$ to start fracturing parallel to the major principal stress depends on the presence of a mud cake and on the range of formation permeability (Fjaer et al., 2008). If a mud cake is present or if the formation is impermeable (permeability $< 10^{-18}$ m^2),

$$p_b^{HF} - p_r = -3\sigma_h + \sigma_H - p_r + \frac{E}{1-\nu}\,\frac{\chi_{p\sigma}}{3}\,\theta + \sigma_T, \tag{2.11}$$

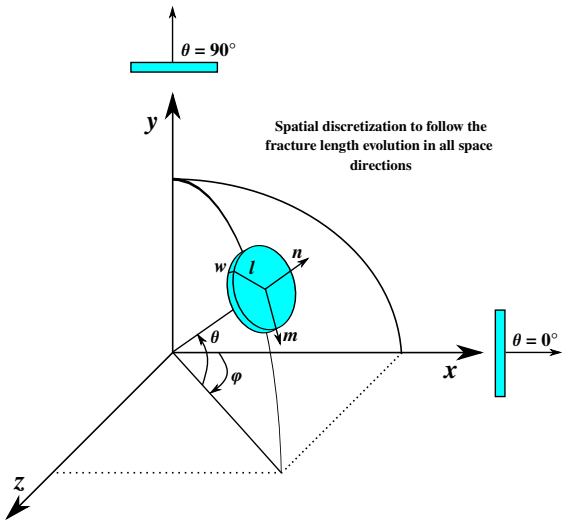

FIGURE 2.2: Directional evolution of a penny-shaped fracture length. The figure shows how space needs to be discretized to trace a smooth evolution of the directional quantities.

while if the rock formation is permeable/without a mud cake (permeability $> 10^{-18}$ m^2),

$$p_b^{HF} - p_r = (1-\nu)\Big[-3\sigma_h + \sigma_H - p_r + \frac{E}{1-\nu}\frac{\chi_{p\sigma}}{3}\theta + \sigma_T\Big] + \nu\, p_r, \tag{2.12}$$

where σ_H and σ_h are the maximum and minimum horizontal far-field stresses, p_r is the reservoir pressure just behind the wall of the borehole, $E > 0$ is the drained elastic modulus of the rock formation , $\sigma_T > 0$ its tensile strength, and θ its change of temperature after injecting the geothermal fluid. As expected, large longitudinal geological stress σ_H, formation pressure, and cooling ease fracturing. Meanwhile, large transversal confinement σ_h and high tensile strength hinder fracturing. The value of the excess pore pressure is used to parameterize the HFM, namely to calculate the stabilization parameter η (Eq. 2.8) so that hydraulic fracturing in the numerical model starts at this particular value of $p_b^{HF} - p_r$.

The other modelling aspect that needs to be considered concerns the stability of boreholes against shear failure. Shear failure of a borehole may be reached if the deviation of effective stresses around the borehole, due to the change in pore fluid pressure and temperature between the borehole and the formation, exceeds the failure criterion of the rock. To safeguard against this event, the borehole pressure p_b should not be lower than the minimum of these two values (Fjaer et al., 2008):

$$p_b^{\min} - p_r = -\frac{3\,\sigma_H - \sigma_h + 2\,p_r + \sigma_C}{1+\tan^2\beta} + \frac{1}{1+\tan^2\beta}\frac{E}{1-\nu}\frac{\chi_{p\sigma}}{3}\theta; \tag{2.13}$$

and,

$$p_b^{\min} - p_r = -\frac{\sigma_v + 2\,\nu(\sigma_H - \sigma_h) + p_r + \sigma_C}{\tan^2\beta} + \frac{1}{\tan^2\beta}\frac{E}{1-\nu}\frac{\chi_{p\sigma}}{3}\theta, \tag{2.14}$$

where σ_C is the compressive strength of the rock formation, σ_v is the vertical geostatic stress, ϑ is the angle of friction of the rock formation, and the angle $\beta = \pi/4 + \vartheta/2$ indicates the direction of the failure plane with respect to the maximum stress direction.

2.1.2 Stimulation tests: *In situ* results and simulations

This section presents numerical results for simulating heat extraction from the HDR reservoir of Soultz-sous-Forêts. It starts by validating the numerical approach by performing short time

simulations. Subsequently, simulations are conducted over the reservoir lifetime where the thermal recovery from the natural and the enhanced reservoir are compared systematically.

2.1.2.1 Stimulation tests of the Soultz-sous-Forêts HDR reservoir

A stimulation test of the well GPK1 (Fig. 2.4), between 2800 m and 3500 m, was conducted in 1993 at the Soultz-sous-Forêts HDR reservoir. Pressurized fluid led to fracture evolution which generated microseismic events. The works of Bruel (1995b) and Jupe et al. (1995) have fairly addressed this stimulation test and are used as a guiding reference for simulations.

This section is devoted to define the material data pertaining to the reservoir, the finite element mesh, and the initial and boundary conditions. In Sect. 2.1.2.2, the field flow history at the well GPK1 during a stimulation test for 17 days is simulated using the HFM implemented in the domestic finite element code, where injection is controlled by fluid volume (Fig. 2.3(a)). The time window of the simulations is next extended in Sect. 2.1.2.3 to study the permeability enhancement of the whole reservoir, where injection is controlled by fluid pressure (Fig. 2.3(b)). The effect of hydraulic fracturing on the reservoir impedance and efficiency is later highlighted.

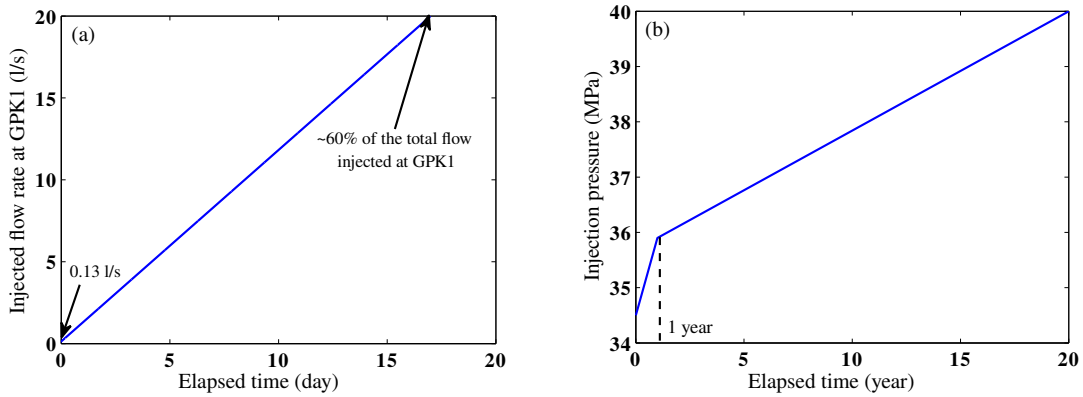

FIGURE 2.3: Two injection scenarios at the well GPK1: (a) the short period scenario is used here to validate the numerical model (Bruel, 1995b); (b) the injection scenario over the reservoir lifetime is purely numerical to serve the purpose of this research.

Based on the locations of the seismic events presented in Bruel (1995b) and on the geometrical information provided by Baumgärtner et al. (1996), the fractured zone to be stimulated (Fig. 2.4) lies at a depth that ranges between 2.8 to 2.9 km and has dimensions of 1 km and 400 m around the well GPK1 with N170 Azimuth and W70 Dip. The second well GPK2 is drilled 500 m away from GPK1 and in the direction of fracture evolution signaled by the seismic events. The initial pressure $p_0 = 28.5$ MPa, the initial temperature $T_0 = 155$ °C, and the geostatic stresses with the vertical stress being equal to the maximum horizontal stress, correspond to a typical depth of 2.85 km (Bruel, 1995b; Evans et al., 2009). The fluid is injected at $T = 50$ °C while the temperature at the outlet production well GPK2 is sought.

A mesh of 800 elements, 40 elements in x-direction and 20 elements in y-direction, is used to perform the simulations. The mesh is refined close to the inlet during the stimulation test of 17 days, otherwise, it is uniformly spread over the volume. Due to symmetry, only a quarter of the reservoir is modeled.

Table 2.1 summarizes the mechanical, the hydraulic, and thermal boundary conditions used in the stimulation process. The hydraulic boundary conditions are further discussed in Sect. 2.1.2.2. As for thermal insulation at the boundaries of the mesh, several studies (Jiang, Luo, and Chen, 2013; Gelet, Loret, and Khalili, 2013) have found that conductive heat contribution of the rock formation, external to a reservoir domain, is secondary for most of its lifetime.

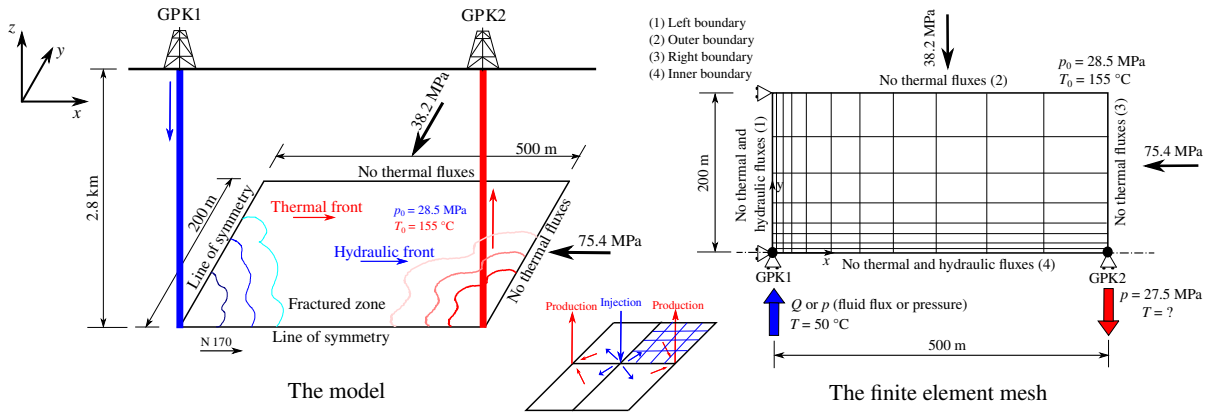

FIGURE 2.4: Schematic representation of the numerical model that is used to simulate the hydraulic fracturing tests at the HDR reservoir of Soultz-sous-Forêts. Boundary and initial conditions are displayed on the graph.

TABLE 2.1: Boundary conditions for the stimulation tests at Soultz-sous-Forêts: l=left, r=right, o=outer, and i=inner boundaries of Figure 2.4.

Type	Boundary	Condition
Displacements	l	No horizontal displacement
	i	No vertical displacement
	r and o	Calculated based on the stresses applied
Fluid flow	l, i	Impermeable
	r and o	Impermeable (scheme 1)/permeable (scheme 2)
	Injection well	Fluid flux or pressure (Fig. 2.3)
	Production well	Pore fluid pressure ($p = p_0 - 1$ MPa)
Heat flow	l, i, r and o	Thermally insulated
	Injection well	$T = 50$ °C
	Production well	Temperature is sought

The thermo-poroelastic properties of Soultz-sous-Forêts reservoir, shown in Table 2.2, are typical for the reservoir rock as reported by Evans et al. (2009).

TABLE 2.2: Material properties of Soultz-sous-Forêts HDR reservoir.

Property	Value	Unit
Drained Young's modulus E	54	GPa
Drained Poisson's ratio ν	0.25	-
Bulk modulus of solid grains K_σ	50	GPa
Bulk modulus of fluid K_λ	2.2	GPa
Dynamic viscosity of the fluid μ	3×10^{-4}	Pa×s
Initial porosity n_λ	0.1003	-
Initial permeability† k_0	2.85×10^{-14}	m^2
Solid thermal conductivity Λ_σ	2.49	W/m/K
Fluid thermal conductivity Λ_λ	0.6	W/m/K
Solid heat capacity at constant volume $C_{v\sigma}$	1000	J/kg/K
Fluid heat capacity at constant volume $C_{v\lambda}$	4200	J/kg/K
Density of solid ρ_σ	2910	kg/m^3
Volumetric thermal expansion of the solid $\chi_{p\sigma}$	7.5×10^{-6}	K^{-1}
Volumetric thermal expansion of the fluid $\chi_{p\lambda}$	1×10^{-3}	K^{-1}

The initial permeability† k_0 has been back-calculated from figure 5 of Bruel (1995b) by considering that the enhanced permeability of the reservoir has an order of magnitude of $\sim 10^{-11}$ m^2 (Evans et al., 2009). Material properties required by the HFM are listed in Table 2.3.

TABLE 2.3: Information required by the HFM to perform hydraulic stimulation

Type	Parameter	Value	Unit	Reference
Fracture	Initial length of fractures ℓ_0	0.25	m	Evans et al. (2009)
	Final length of fractures ℓ_f	0.80	m	estimated
	Toughness K_{Ic}	1.87	MPa$\sqrt{\text{m}}$	Atkinson (1991)
	Fracture stabilizing parameter η	0.2	-	calculated
	Fracture density	10^{-6}	$1/\text{m}^3$	Bruel (1995b)
Flow	Connectivity coefficient c_c	0.0001	-	calculated/parametrized

The excess borehole pressure $p_b^{HF} - p_r$ needed to start the fracturing process is provided by Eq. 2.12 since the initial permeability of the reservoir k_0 is larger than $10^{-18}\,\text{m}^2$. The rock tensile strength σ_T is taken equal to 10% of rock compressive strength $\sigma_C = 130\,\text{MPa}$ (Evans et al. (2009)). For a temperature change θ of -105 °C, the resulting casing shoe pressure at the injection well GPK1 should be around 39.15 MPa. This value is close to the actual pressure (around 40 MPa) implemented at Soultz-sous-Forêts to start hydraulic fracturing during the field tests at a depth of 2.85 km (Bruel, 1995b). Henceforth, the threshold of hydraulic fracturing is chosen to be as in the field, namely 40 MPa. It is of interest to observe that the thermal cooling eases considerably the hydraulic fracturing process. Indeed in the absence of thermal contribution, the borehole pressure required to start fracturing would be equal to 54.3 MPa.

The stabilizing parameter η is now determined by Eq. 2.7 knowing the effective normal stress σ_n' in the direction of the maximum far-field stress, the threshold of hydraulic fracturing, and the material properties of Table 2.3. The connectivity coefficient c_c is chosen so that it leads to an enhanced permeability of $\sim 10^{-11}\,\text{m}^2$ in agreement with Evans et al. (2009). In the absence of definite data, the length of fractures ℓ_f at which connectivity between fractures is complete is estimated to be a multiple of the initial fracture length ℓ_0.

Equations (2.13) and (2.14) provide the minimum borehole pressures that need to be applied to ensure the stability of the wellbore against shear failure. The friction angle ϑ of granite at 5 km depth is estimated to 42° (Cornet, Bérard, and Bourouis, 2007). For a failure angle $\beta = \pi/4 + \vartheta/2 \simeq 66°$, the minimum value of borehole pressure required to cause shear failure is 25.5 MPa by Eq. 2.13 and 12 MPa by Eq. 2.14. Since the borehole pressure is definitely larger than the initial reservoir pressure of 28.5 MPa during the fracturing process, the borehole GPK1 is not likely to fail in shear but rather in tension due to hydraulic fracturing.

2.1.2.2 Short period stimulation test: Numerical validation

The Boundary Value Problem (BVP) (Fig. 2.4) is stimulated by the HFM. The results of simulations are correlated to the flow logging injection tests performed at the well GPK1 of Soultz-sous-Forêts HDR reservoir. The most important level of the stimulation process is located at 2.85 km and absorbs about 60% of the injected fluid (Bruel, 1995b). The field test was performed by pumping geothermal fluid into the well GPK1 gradually until a total flow rate[2] of 40 l/s was reached at day 17. The *in situ* pressure curve at the injection well showed a non-linear behavior announcing the existence of turbulent flow (Grecksch et al., 2003).

Figure 2.3(a) shows the applied flow rate history at the well GPK1 as suggested by Bruel (1995b) and as applied in the simulations. The hydraulic boundaries are either impermeable (scheme 1) or permeable (scheme 2). Figure 2.5 displays the responses obtained by the numerical simulation and the *in situ* data for a period of 17 days.

When the reservoir is assumed impermeable at the outer and right boundaries (first scheme), the geothermal system reaches a pressure of 137 MPa at a flow rate 20 l/s with a plateau announcing the presence of extreme turbulent flow near the well GPK1 (Fig. 2.5(a)). This pressure value of 137 MPa is 3.5 times higher than the hydraulic fracturing pressure (40 MPa). However,

[2]The flow loss is approximately equal to 40%: the effective flow absorbed by the reservoir volume is about 60% of the total injected flow, i.e. 24 l/s. The value of 20 l/s used in the simulations is after Bruel (1995b).

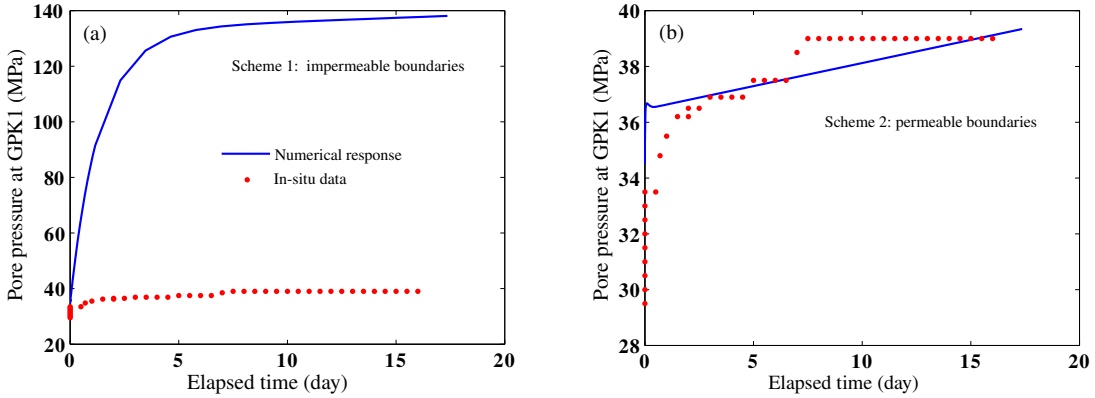

FIGURE 2.5: Injection pressure at the well GPK1 during the 1993 field injection test at Soultz-sous-Forêts. Comparison between the *in situ* data (Bruel, 1995b) and the response of the numerical model with (a) impermeable and (b) permeable boundaries.

when the outer and right boundaries of the reservoir are assumed permeable (second scheme), the geothermal system reaches the pressure of hydraulic fracturing at a flow rate of 20 l/s *almost* as applied in field. The numerical response in Fig. 2.5(b) is no longer showing an asymptotic plateau as the fluid turbulence is greatly eliminated when the outer and right boundaries are assumed permeable, i.e. smoother flow is achieved within the reservoir. As a conclusion to this section, the HFM is verified against field data and only permeable boundaries (scheme 2) are considered in next long term simulations as injection is controlled by fluid pressure (Fig. 2.3(b)).

2.1.2.3 Reservoir lifetime stimulation test: Impedance and efficiency of thermal recovery

While Sect. 2.1.2.2 presented the results of a short period stimulation test, the permeability enhancement over the whole reservoir is now addressed. The effects of the hydraulic fracturing process on the reservoir impedance and efficiency of thermal recovery are considered during the lifetime of the reservoir. In order to highlight the qualitative and quantitative effects of hydraulic fracturing, tests are run both with and without activating the HFM in the simulations.

Unlike the previous section, injection is now controlled by fluid pressure: pumping starts with 34.5 MPa and reaches 35.9 MPa at year 1. Thereafter, it continues to increase linearly but with a lower rate to reach a value of 40 MPa after 20 years of injection (Fig. 2.3(b)). Hydraulic fluxes are set to vanish on the model four boundaries. Convection of heat is treated *a priori* using the SUPG method. However, some stubborn numerical noises at the injection and production wells still require more attention (Sect. 2.1.5).

Simulations without hydraulic fracturing

The results of circulation tests in the natural/unenhanced reservoir are commented below for 5 and 10 years of simulations. Figure 2.6 shows that the pore pressure establishes in early times, in a matter of days. Therefore its contours are not showing any significant changes at subsequent times.

The fractured zone cools in x- and y-directions due to the strong fluid pressure gradients spreading all over the reservoir volume (Figs 2.7 and 2.8). These strong pressure gradients, particularly near the injection well, accompanied by thermal tensile stresses resulting from cooling help propagating and opening fractures.

Figures 2.9 and 2.10 show the contours of the effective horizontal stresses in x- and y-directions. The reservoir is relaxing faster in y-direction than in x-direction: the pace at which the stress σ'_{yy} returns to its geostatic value is faster than the stress σ'_{xx}. This effect is due to

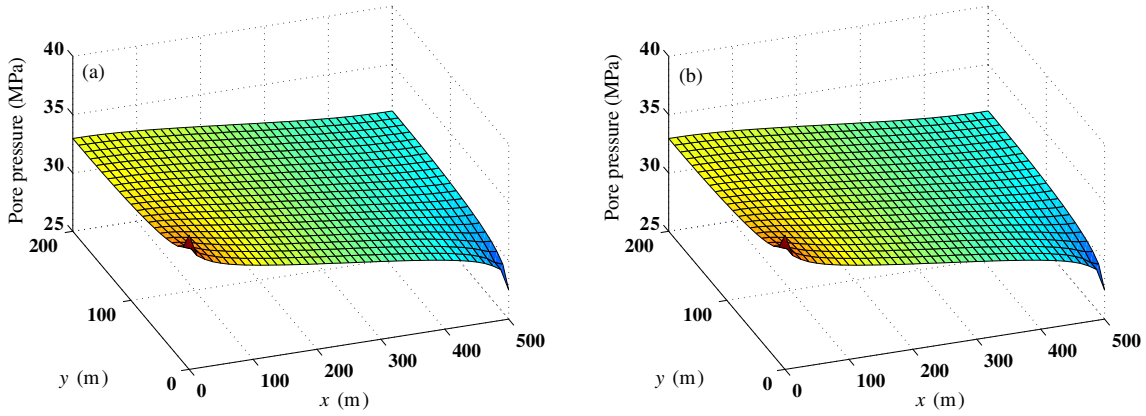

FIGURE 2.6: Contours of the unenhanced reservoir pore pressure at two times: (a) 5 years; and (b) 10 years. Contours are not showing any significant changes due to the fast hydraulic diffusion, in a matter of days.

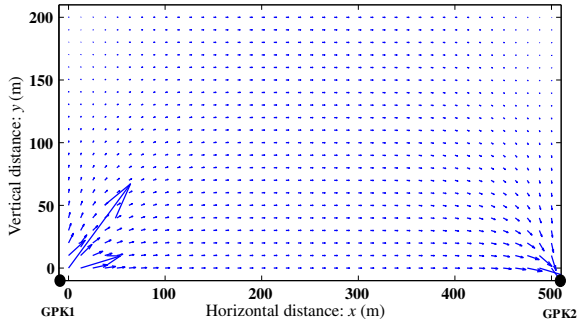

FIGURE 2.7: Scaled fluid velocity vectors spreading over the unenhanced reservoir volume.

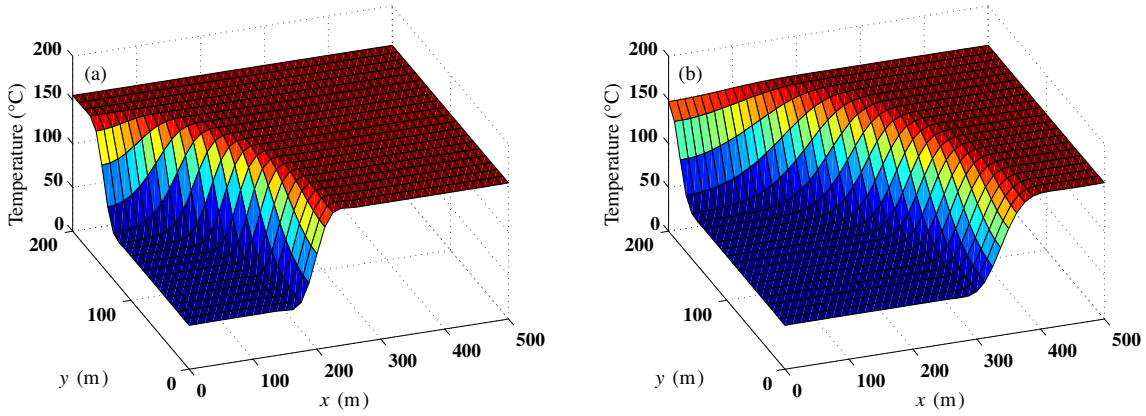

FIGURE 2.8: Contours of the unenhanced reservoir temperature at two times: (a) 5 years; and (b) 10 years.

the geologic far-field stress state which imposes smaller stresses on the outer boundary of the reservoir in the y-direction. Indeed, as expected, hydraulic fracturing is going to enhance the permeability of the HDR reservoir following the direction of the maximum far-field stress.

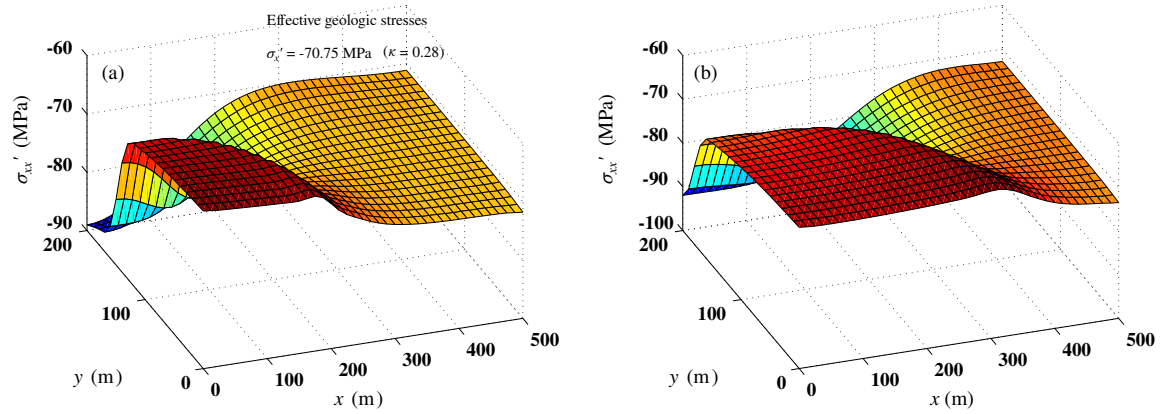

FIGURE 2.9: Contours of the unenhanced reservoir longitudinal effective stress σ'_{xx} at two times: (a) 5 years; and (b) 10 years. The Biot's coefficient $\kappa = 1 - K/K_\sigma$ is needed to calculate the effective stresses. According to Table 2.2, the drained bulk modulus K is equal to 36 GPa therefore $\kappa = 0.28$.

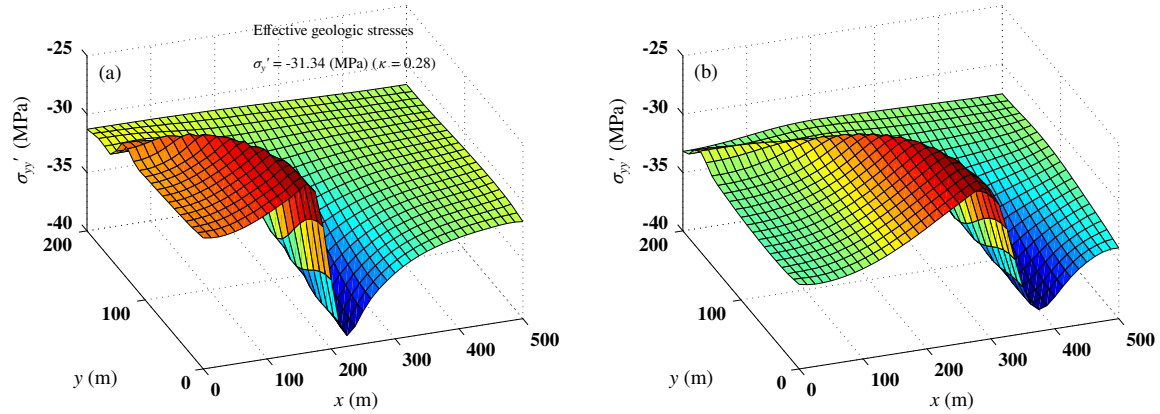

FIGURE 2.10: Contours of the unenhanced reservoir transversal effective stress σ'_{yy} at two times: (a) 5 years; and (b) 10 years.

The impedance $\mathcal{Z}$, defined as the ratio of the pressure differential between the injection and production wells required to ensure the produced flow rate Q,

$$\mathcal{Z} = \frac{p_{\text{inj}} - p_{\text{pro}}}{Q}, \tag{2.15}$$

is an important overall characteristic of a reservoir. The vertical section of the well GPK1, over which flow is taking place, is approximately 550 m extending to about 3.3 km and the radius of the well at such a depth is 15 cm (Baria et al., 2000; Bruel, 1995b). Therefore, the flow takes place over an area of $\sim$518 m^2. Assuming no leak off, the impedance of the unenhanced reservoir is obtained from the computed flux-pressure relation at the injection well GPK1 (Fig. 2.11(a)) . The time course of the injection pressure is displayed in Fig. 2.3(b) and the production pressure is maintained at $p = p_0 - 1 = 27.5$ MPa.

Impedance is seen to be virtually constant in time and greater than 1000 MPa/(m^3/s) (Fig. 2.11(b)). Such a large impedance indicates an inefficient operation where the power pumped through the reservoir exceeds a substantial fraction of the power produced by the reservoir (Murphy et al., 1999).

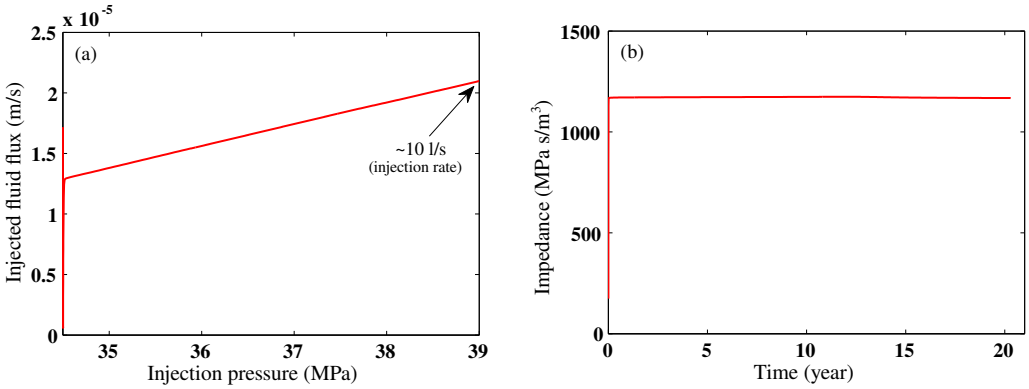

FIGURE 2.11: (a) The relation between the injected pore fluid pressure and the magnitude of created fluid flux at the injection well GPK1 of the unenhanced HDR reservoir of Soultz-sous-Forêts. Fluid flux increases linearly following the injection schedule of Fig. 2.3(b). (b) The impedance profile: impedance greater than 1000 MPa/(m^3/s) indicates inefficient operation (Murphy et al., 1999).

Simulations with hydraulic fracturing

If hydraulic fracturing is activated in the simulations, fractures are evolving in the direction of the maximum far-field stress (along the x-axis) causing the longitudinal permeability to reach its maximum value up to distances of $\simeq$80 m in y-direction and $\simeq$240 m in x-direction. The permeability contours for the enhanced HDR reservoir after 1 year of pumping at the GPK1 well are shown in Fig. 2.12. The results of these simulations are in a good agreement with the micro-seismic events diagram presented in Bruel (1995b) announcing the propagation of hydraulic front and fracture coalescence.

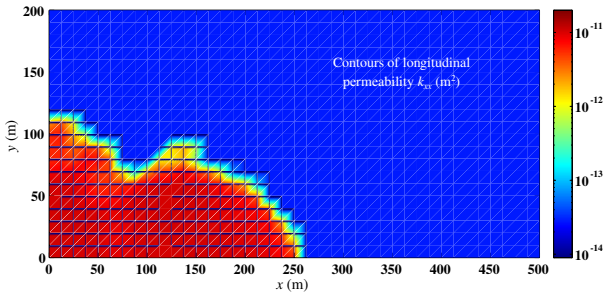

FIGURE 2.12: Contours of longitudinal permeability component k_{xx} after 1 year of pumping.

Figure 2.13 shows the projection of the contours of k_{xx}/k_{yy} in the x-y plane with some points (A, B, C, and D) where the evolution of fracture radii is studied. The degree of anisotropy between the longitudinal and the transversal permeability components remains in the range $k_{xx}/k_{yy} \in [2.5, 0.4]$ as documented by Schulze, Popp, and Kern (2001a).

Figure 2.14 shows the directional evolution of the fracture radius after 1 year of hydraulic fracturing at points A and D of Fig. 2.13. Point A represents a position very close to the injection well where the components of the permeability tensor increase rapidly and almost equally, nevertheless, with a little preference in the direction of the far-field longitudinal stress $\theta = 90°$ and $k_{xx}/k_{yy} = 1.05$. Point D is far away from the region of hydraulic enhancement and no change of the fracture radius is observed $\ell = \ell_0 = 25$ cm.

Figure 2.15 shows the directional evolution of fracture radii at points B and C. At point C, fractures evolve strongly in the longitudinal direction and slightly in the transversal direction $k_{xx}/k_{yy} = 1.7$. Meanwhile, a slighter evolution of fractures in the longitudinal direction is observed at point B which gives $k_{xx}/k_{yy} = 1.6$.

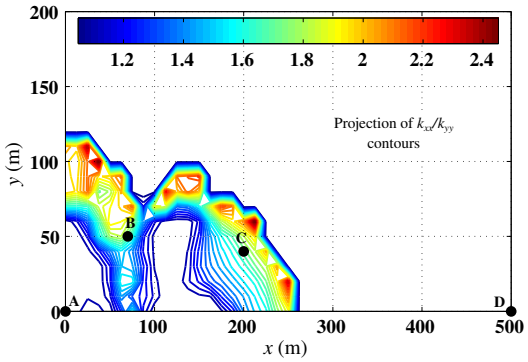

FIGURE 2.13: Projection of the contours of k_{xx}/k_{yy} in x-y plane with some points where the evolution of fracture radii is studied.

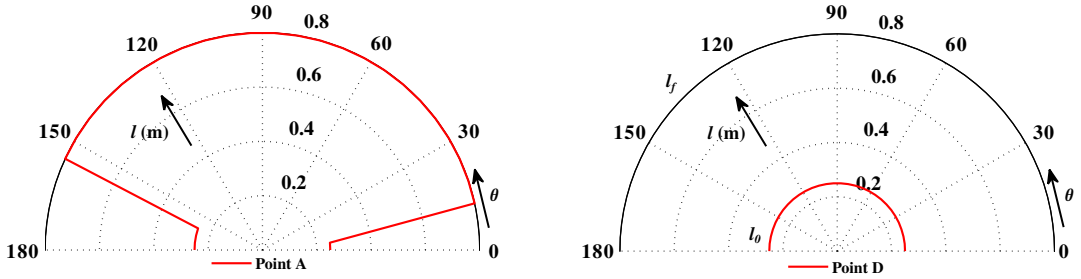

FIGURE 2.14: Directional evolution of fracture radii at points A and D after 1 year of hydraulic fracturing.

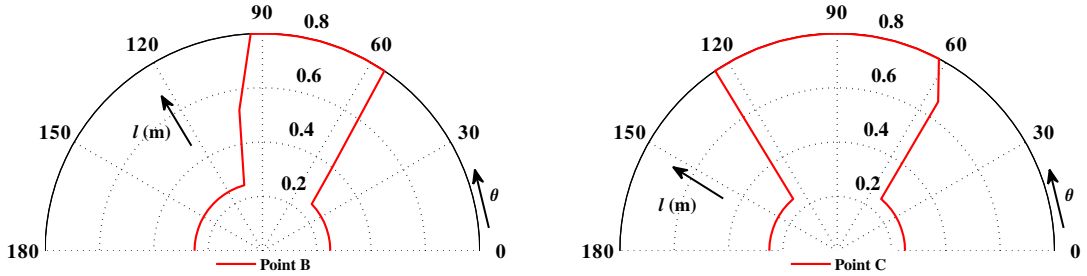

FIGURE 2.15: Directional evolution of fracture radii at points B and C after 1 year of hydraulic fracturing.

Figure 2.16 shows the evolution of the longitudinal permeability component k_{xx} at the injection well GPK1 during the hydraulic enhancement. The permeability evolution at the injection well happens very rapidly. This is due to modeling hydraulic fracturing while considering only mode I of fracture propagation.

The experimental work of Papanastasiou (1999) has proven that for every geothermal system there exists an optimum injection schedule (injection pressure and duration). Any further increase in stimulation effort, i.e. stimulation time for a given stimulation pressure, does not provide additional permeability enhancement. The injection pressure schedule (Fig. 2.3(b)) is sufficient to enhance the reservoir permeability (Fig. 2.12) up to one year. The subsequent increase in stimulation pressure over time did not enhance the reservoir permeability any more. The point N, indicated in Fig. 2.16, announces the end of hydraulic enhancement/fracturing,

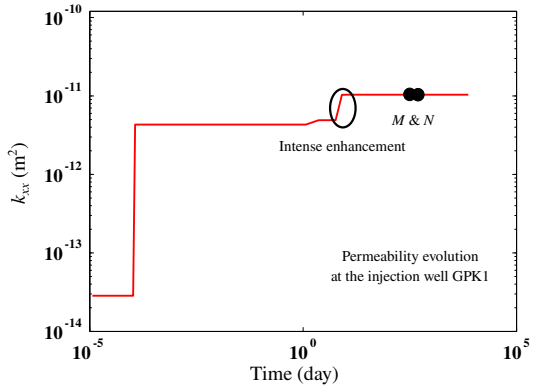

FIGURE 2.16: Longitudinal permeability k_{xx} history at the injection well GPK1.

i.e. $t = 1$ year.

Preferential cooling following the new paths of the enhanced permeability is thus expected: heat convection is dominant in the direction of the major far-field stress (direction of fracture evolution, Fig. 2.17). The numerical oscillations observed in temperature contours near the production well are related to stabilization of heat convection as fluid fluxes converge leading to high pore fluid velocity. The Subgrid Scale method (SGS) and the Discontinuity Capturing Method (DCM) have been seen to be more efficient in curing such numerical noises than the SUPG method (Sect. 2.1.5).

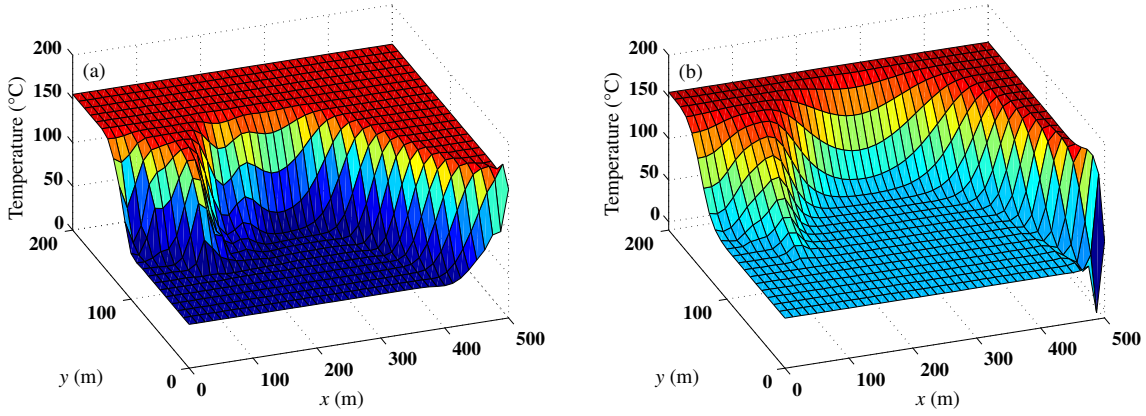

FIGURE 2.17: Contours of the enhanced reservoir temperature at two times: (a) 5 years; and (b) 10 years. Convection of heat is dominant in the direction of fracture evolution.

The velocity field at year 1 of hydraulic enhancement (Fig. 2.18) shows larger pore fluid velocity in the zone of active hydraulic enhancement, i.e. $\sim 2.75 \times 10^{-5}$ m/s against $\sim 0.62 \times 10^{-5}$ m/s in other regions.

The contours of pore fluid pressure at years 5 and 10 are shown in Fig. 2.19. The tremendous fast increase in the permeability in the zone of active enhancement makes the changes in pore fluid pressure quite small (kind of leveled up surfaces) in this zone as compared to the situation of unenhanced HDR reservoir (Fig. 2.6). This behavior of pressure distributions/contours was also observed by Lee and Ghassemi (2010) and Lee and Ghassemi (2011) for two-dimensional and three-dimensional BVPs.

The contours of the longitudinal and transversal effective stresses (Figs. 2.20 and 2.21) are following the preferential cooling derived by the hydraulic fracturing process. Compressive stresses are mitigated in the cooled regions as the reservoir is constrained to some degree on the

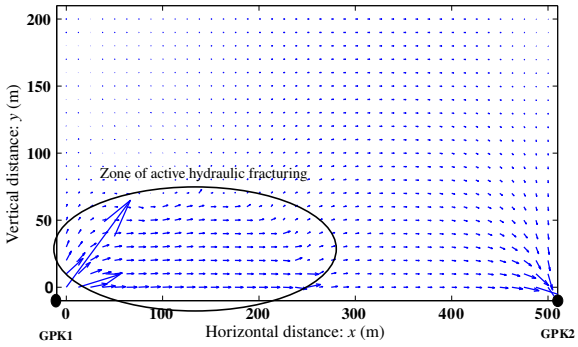

FIGURE 2.18: Scaled fluid velocity vectors spreading over the enhanced reservoir volume.

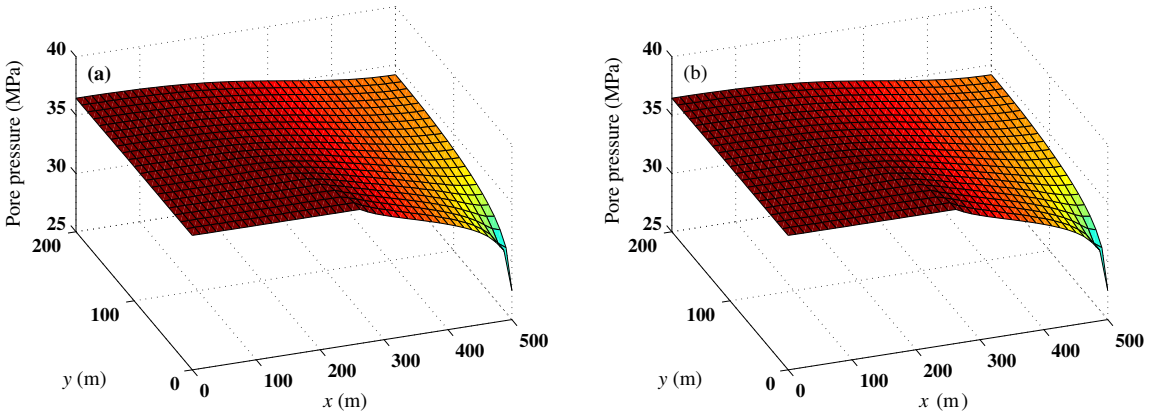

FIGURE 2.19: Contours of the enhanced reservoir pressure at two times: (a) 5 years; and (b) 10 years. The high permeability created by hydraulic fracturing levels up the contours in the regions of the enhancement.

boundaries of symmetry. The created new highly-permeable paths take most of the fluid flow in the direction of the maximum far-field stress causing increased compressive stresses near the outer boundary of the HDR reservoir. Thus, at the outer boundary, fractures are most likely closing and permeability is decreasing, unless shear dilatation copes for the reduction in the fracture aperture (Chen, Zhou, and Sheng, 2007).

The jump between the two points M and N in Fig. 2.22(a) is understood by studying the permeability history at the injection well GPK1 (Fig. 2.16). The period of intense permeability enhancement is taking place earlier at the injection well which is expected due to significant thermo-poroelastic changes at this location. However, if permeability histories are averaged over the whole reservoir, the period of intense permeability enhancement in the averaged curve corresponds to the jump M-N in Fig. 2.22(a). The process of HF, for only one year, has reduced the flow impedance of the HDR reservoir from $\sim$1170 MPa/(m^3/s) to $\sim$600 MPa/(m^3/s) (Fig. 2.22(b)). This reduction in the impedance lowers the power required to pump geothermal fluid through the reservoir and enhances its efficiency by about 49%.

Efficiency and thermal recovery

Figure 2.22(b) proves the effect of hydraulic enhancement on reducing the impedance of thermal recovery from HDR reservoirs. Besides, the profiles of the reservoir produced fluid temperatures with hydraulic fracturing (enhanced) (T_{hf}) and without hydraulic fracturing (natural) (T_{whf}) are displayed in Fig. 2.23(a). In most geothermal systems, the produced fluid is efficiently used as long as its temperature does not drop below 80 °C (Lund, 2009). The standard

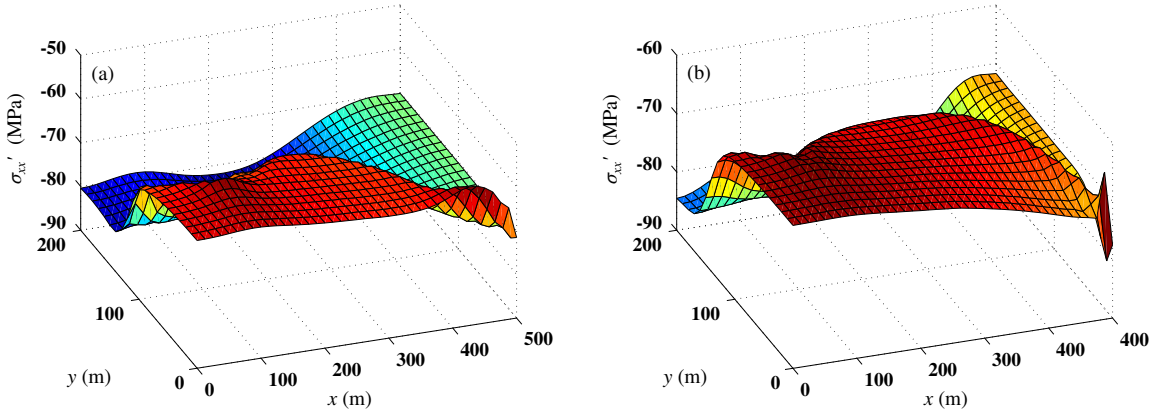

FIGURE 2.20: Contours of the enhanced reservoir longitudinal effective stress σ'_{xx} at two times: (a) 5 years; and (b) 10 years. Stresses are dawdled in compression in the cooled regions due to tensile stresses.

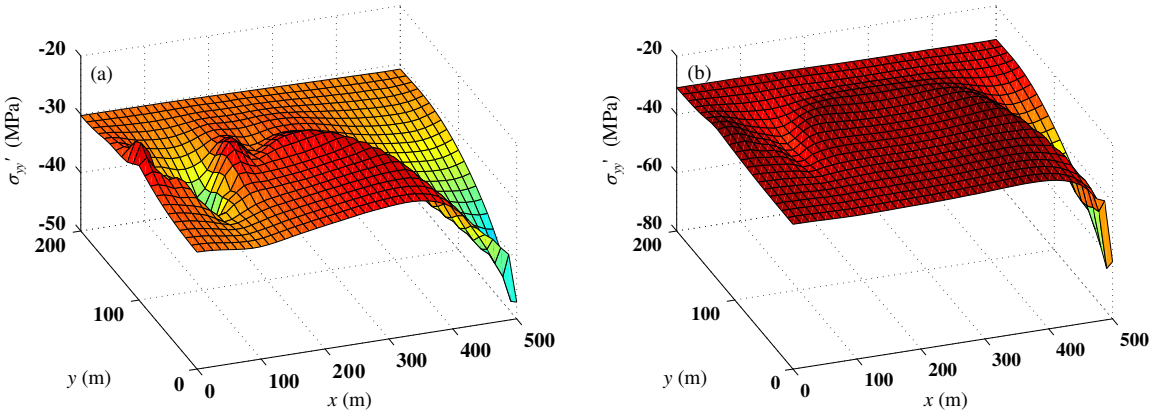

FIGURE 2.21: Contours of the enhanced reservoir transversal effective stress σ'_{yy} at two times: (a) 5 years; and (b) 10 years.

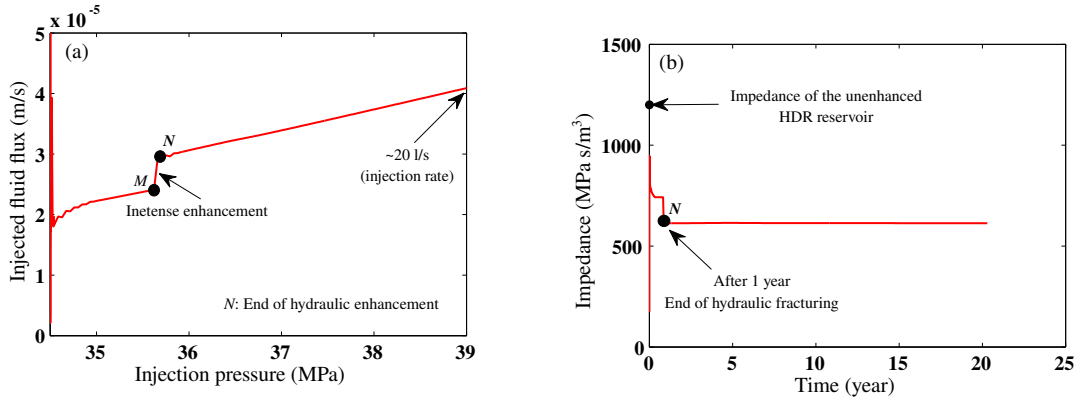

FIGURE 2.22: (a) The relation between the injected pore fluid pressure and the magnitude of created fluid flux at the injection well GPK1 of the enhanced HDR reservoir of Soultz-sous-Forêts. The non-linear behavior results from the the creation of improved connections (Bruel, 1995b). (b) the Impedance history.

mean production temperature curve (Fig. 2.23(a)) is based on the analytical solution provided by Kolditz (1995) for one-dimensional matrix heat diffusion and for 15 l/s injection flow rate.

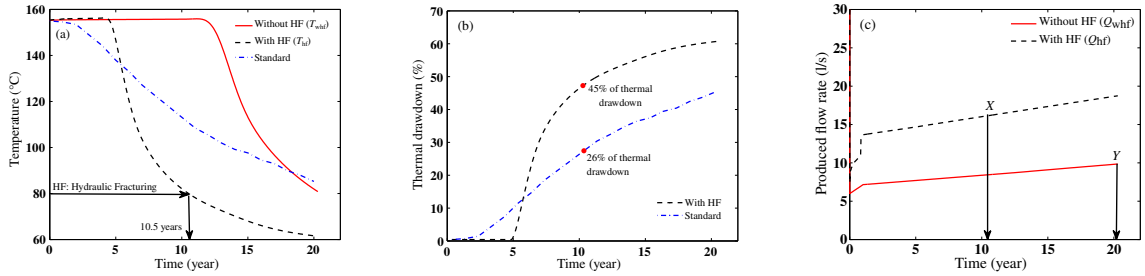

FIGURE 2.23: (a) Histories of produced fluid temperature from the enhanced reservoir (T_{hf}) compared to the natural reservoir (T_{whf}). (b) Thermal drawdown of the mean production temperature from the enhanced HDR reservoir against the standard production temperature as suggested by Kolditz (1995). (c) Profiles of produced flow rate from the enhanced reservoir (Q_{hf}) compared to the natural reservoir (Q_{whf}).

As another indicator of thermal recovery from geothermal reservoirs, Fig. 2.23(b) shows the thermal drawdown of the enhanced reservoir and the standard production curve as suggested by Kolditz (1995). Thermal drawdown $\mathcal{T}_{\mathcal{D}}$ is defined as the relative difference between initial temperature of the reservoir T_0 and production temperature T_{pro},

$$\mathcal{T}_{\mathcal{D}} = \frac{T_0 - T_{\mathrm{pro}}}{T_0}. \tag{2.16}$$

The standard solution shows a thermal drawdown of approximately 26% in 10 years, against 45% for the enhanced reservoir (Fig. 2.23(b)). In both cases, thermal drawdown exceeds the limits required by Jupe et al. (1995), namely 1% thermal drawdown per year. Still, this poor performance may be attributed in part for the fact that the present heat diffusion analysis is two- rather than three-dimensional (Kolditz, 1995).

If hydraulic fracturing is activated in the simulations, the HDR reservoir is exhausted in 10.5 years (Fig. 2.23(a)). However, without hydraulic enhancement, the HDR reservoir lasts for up to 20 years. Still, the benefit of using hydraulic fracturing is evident in terms of the energy used to pump fluid through the reservoir (Fig. 2.22(b)) and in terms of the produced flow rate (Fig. 2.23(c)).

After 1 year of hydraulic enhancement, the produced flow rate from the HDR reservoir is two-fold the produced flow rate from the natural reservoir. Considering that the stimulated reservoir operates efficiently for 10.5 years and that the unenhanced reservoir for 20 years, the volume of the produced fluid can be calculated by numerically integrating the curves of Fig. 2.23(c), to points X and Y: the volume of efficient fluid produced from the stimulated HDR reservoir over a period of 10.5 years is 4.922 Million m^3, compared to 5.364 Million m^3 from the natural reservoir over 20 years. These huge amounts of used fluids are not utterly lost; the geothermal fluids are recirculated in a closed loop. It becomes clear now that the hydraulic fracturing process has increased the efficiency of the HDR reservoir for up to 49%. Yet by the calculations of efficient fluid volume, only 7 to 8% of the total efficient fluid to be produced is lost over the entire effective life of the reservoir.

2.1.3 Influence of geothermal fluids on the thermal recovery

Fluids used usually in geothermal systems are brines with the dominance of chloride Cl^- and sodium Na^+ ions over a typical range of concentration. In most of the geothermal systems, as in Groß Schönebeck 50 km north of Berlin, the total of dissolved solids sums up to 265 g/l with a dominant mass fraction of 0.225 kg of NaCl per kg of solution corresponding to a molality of 4.968 mol of NaCl per kg of H_2O (Francke and Thorade, 2010; Battistelli, Calore, and Pruess, 1997).

This section aims at studying the effect of a temperature-dependent dynamic viscosity of geothermal fluids on the performance of natural and enhanced reservoirs.

2.1.3.1 Temperature and salinity dependence of viscosity

The dynamic viscosity of a fluid describes its resistance to gradual deformation, and hence flow. It can be thought of as a measure of fluid friction. Francke and Thorade (2010) collected experimental data from several studies to provide three models to estimate brine viscosity temperature dependence (Fig. 2.24(a)). The models, in their respective application range, resulted in very consistent values of brine viscosity with average deviation of 0.3% and maximum deviation of 0.9%. Figure 2.24(a) shows the viscosity of 0.225 kg of NaCl per kg of solution brine over a range of temperature of interest and at a constant pressure of 1.5 MPa. The brine viscosity $\mu_b = 1.57 \times 10^{-3} \times (T/293)^{-4.37}$ Pa s, with T the temperature in Kelvin, is found to represent the average of the three models of Francke and Thorade with a determination coefficient of $R^2 = 0.9957$.

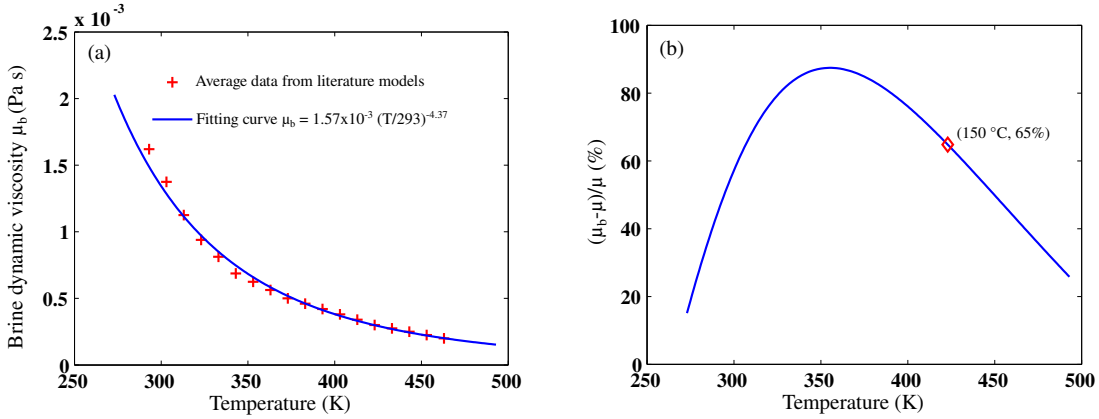

FIGURE 2.24: (a) Brine viscosity as a function of temperature while pressure and NaCl mass fraction are kept equal to 1.5 MPa and 0.225 kg of NaCl per kg of solution respectively. Solid line represents the fitting curve of the scattered data with a determination coefficient of $R^2 = 0.9957$. (b) Percentage of viscosity increase as result of using sodium chloride NaCl in a concentration of 0.225 kg of NaCl per kg of H_2O, fluid pressure is held at 1.5 MPa.

Francke and Thorade (2010) have also employed their models to study the effect of NaCl mass fraction on the viscosity of the brine. Brine viscosity has been proven to increase almost linearly by 76% for a mass fraction change from 0 to 0.25 kg of NaCl per kg of solution at a temperature of 150 °C and pressure of 1.5 MPa. On the other hand, in agreement with Likhachev (2003), the fluid pressure does not influence the brine viscosity at a temperature of 150 °C and a pressure in the range of 0.01 MPa to 50 MPa.

Figure 2.24(b) shows the percentage of increase of viscosity of the brine with respect to water as a function of temperature. The curve extends over a temperature range of 0 °C to 220 °C. This curve is built using the analytical expression of the water substance viscosity μ given by Burger, Sourieau, and Combarnous (1985) and AbuAisha (2014), yet the brine viscosity μ_b is obtained using the relation of Fig. 2.24(a).

2.1.3.2 Temperature-dependent viscosity: simulations without hydraulic fracturing

Increasing pore fluid viscosity decreases the velocity at which the hydraulic front is moving. It also increases the pressure differentials with respect to the wells and hence decreases the pore fluid pressure inside the reservoir. These phenomena are observed in Fig. 2.25 that shows pore fluid pressure profiles along the line joining the wells GPK1 and GPK2. The reduction in pore fluid pressure as result of increasing the brine viscosity hinders the process of hydraulic fracturing.

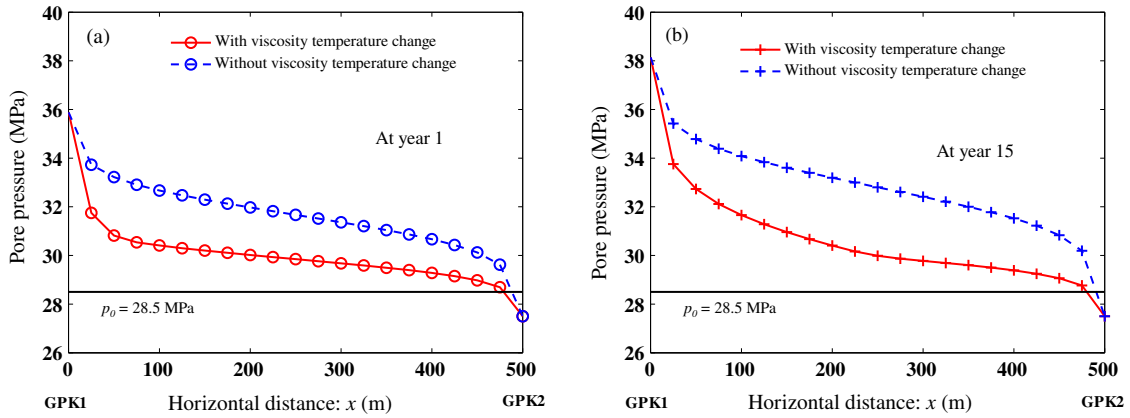

FIGURE 2.25: Pore pressure profiles along the line joining the injection and production wells, at (a) year 1 and (b) year 15. Solid lines: temperature-dependent viscosity; dashed lines: constant brine viscosity $\mu_b = 3 \times 10^{-4}$ Pa s.

Increasing brine viscosity also hinders the speed by which heat front is traveling through the reservoir: more viscous fluid moves at slower convective velocity, compare Figs 2.26 and 2.8.

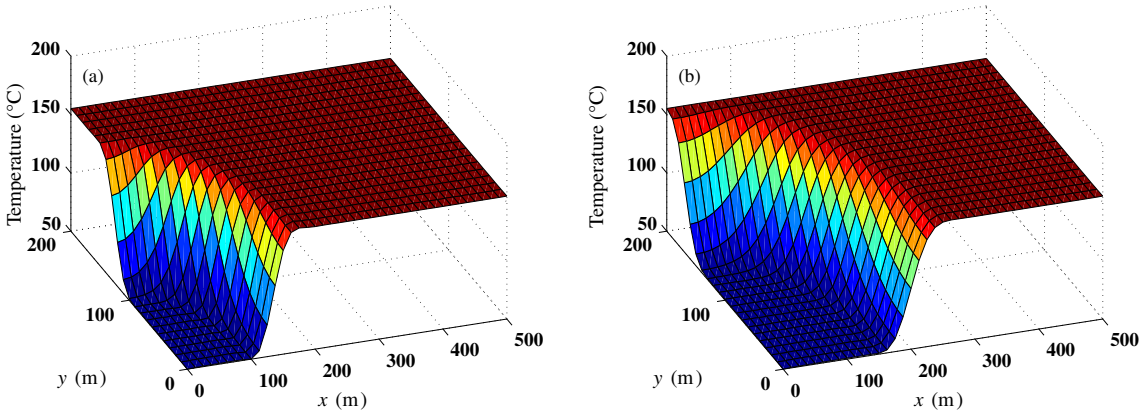

FIGURE 2.26: Contours of the natural reservoir temperature at two times: (a) 5 years; and (b) 10 years. Temperature-dependent viscosity is accounted for.

Figure 2.27(a) shows the relation between injection fluid pressure at the well GPK1 and the resulting flow rate. The relation is no longer linear (compare with Fig. 2.11(a)) even if no improved hydraulic connections are created by hydraulic fracturing. Besides, the flow rate is smaller than the value of the natural reservoir if temperature-dependent viscosity is not considered in the simulations (Fig. 2.11(a)). This non-linear relation announces a more turbulent flow near the injection well.

Figure 2.27(b) shows that increasing brine viscosity as a result of cooling increases the impedance $\mathcal{Z}$ of the unenhanced reservoir in the long range, announcing a less efficient thermal recovery from the reservoir (Murphy et al., 1999).

2.1.3.3 Temperature-dependent viscosity: simulations with hydraulic fracturing

Increasing pore fluid viscosity is expected to hinder the process of hydraulic fracturing as it reduces pore fluid pressure. Contours of the reservoir permeability at year 5 are shown in Fig 2.28. Unlike the case when constant brine viscosity is assumed, increasing viscosity by cooling

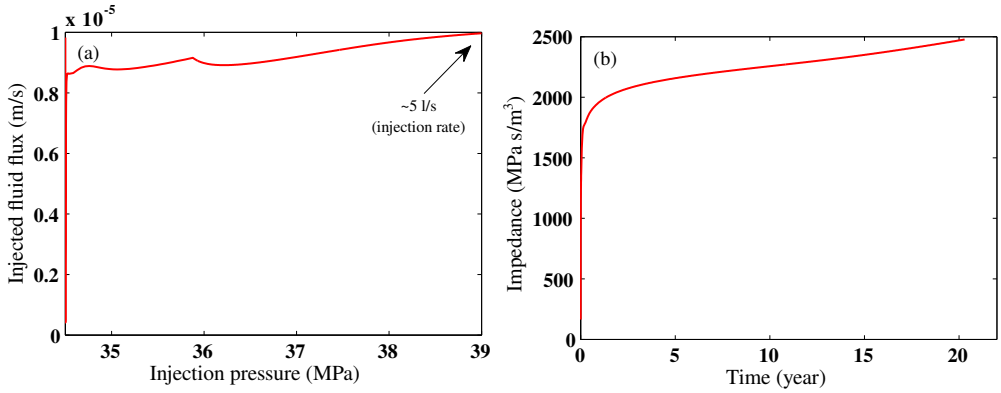

FIGURE 2.27: The relation between injection pressure and resulting flow rate at the injection well GPK1 of the natural reservoir and while accounting for a temperature-dependent viscosity. (b) The impedance profile.

tends to create high fluid pressure gradients near the injection well traveling strongly in both x- and y-directions and causing fractures to evolve and intersect. The lag in heat front, as result of increasing viscosity, renders the injection pressure schedule shown in Fig. 2.3(b) active[3] for 5 years.

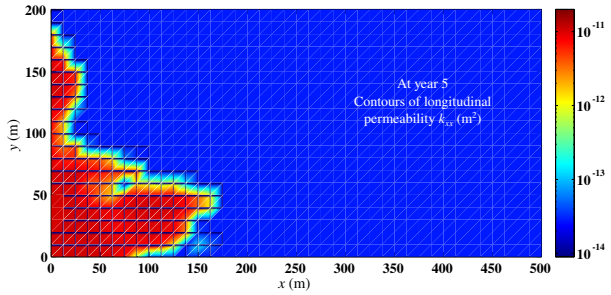

FIGURE 2.28: Contours of longitudinal permeability component k_{xx} at year 5 while accounting for a temperature-dependent viscosity. Injection pressure schedule (Fig. 2.3(b)) becomes active for 5 years.

Fractures continue to evolve following the direction of maximum far-field stress (x-direction) causing a permeability enhancement up to a distance of 170 m in x-direction in 5 years (Fig. 2.28). The reason why the injection pressure schedule (Fig. 2.3(b)) remains active for 5 years is explained by the following arguments: 1. increasing viscosity by cooling hinders the propagation of the heat front; 2. the slow propagation of the heat front gives rise to slower propagation of thermal tensile stresses; 3. which, along with the fluid pressure, keep on mitigating the geologic compressive stresses and hence helping fractures to evolve.

Figure 2.29 shows the contours of the reservoir temperature when hydraulic fracturing is activated and while accounting for viscosity increase due to brine cooling. Preferential cooling following the new paths of the enhanced permeability is obvious.

Figure 2.30(a) shows the relation between the injection pressure and the fluid flux at the injection well GPK1. During the first 5 years, while hydraulic enhancement is active, the produced fluid volume is obviously increasing even-though the viscosity of the brine fluid is increasing as result of cooling. Permeability enhancement due to hydraulic fracturing counteracts the hindrance related to viscosity increase: an approximate linear relation is observed during this period of active enhancement, compare with Fig. 2.22(a). After 5 years, hydraulic fracturing stops,

[3]Compare with Fig. 2.12 where optimum permeability enhancement is obtained after 1 year for the same injection pressure schedule.

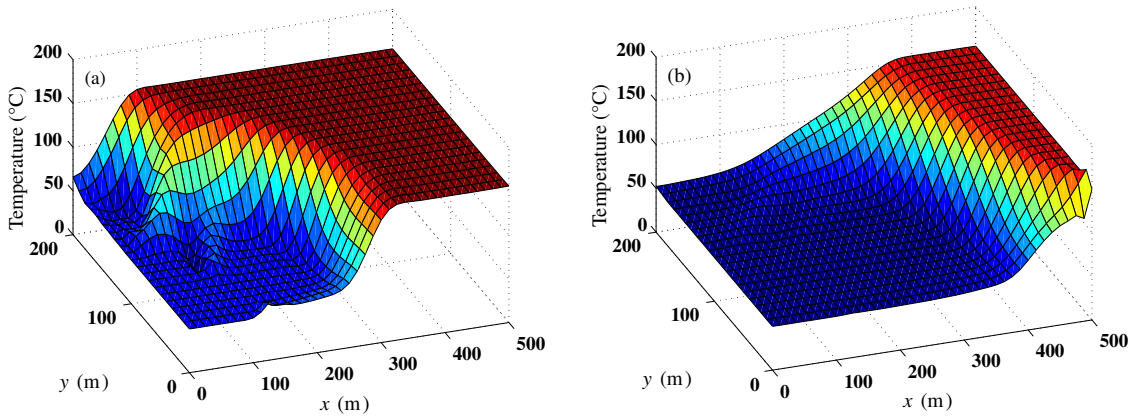

FIGURE 2.29: Contours of the enhanced reservoir temperature at two times: (a) 5 years; and (b) 10 years. Temperature-dependent viscosity is accounted for.

which eliminates the part counteracting the hindrance of viscosity increase. Subsequently, the produced fluid volume declines significantly.

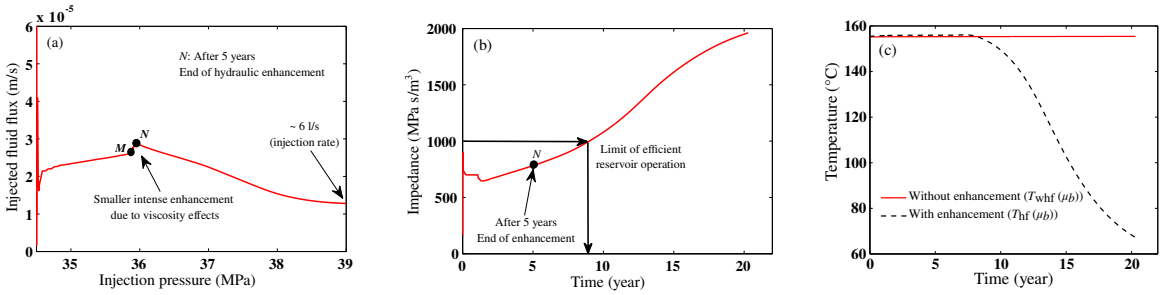

FIGURE 2.30: (a) The relation between injection pressure and resulting flow rate at the injection well GPK1 of the enhanced reservoir and while considering a temperature-dependent viscosity. An approximate linear relation is observed during the period of active hydraulic fracturing. (b) The impedance profile of the enhanced reservoir. (c) Profiles of produced fluid temperature with enhancement ($T_{\mathrm{hf}}(\mu_b)$) and without enhancement ($T_{\mathrm{whf}}(\mu_b)$).

Hydraulic fracturing reduces flow impedance of the HDR reservoir from ∼1700 MPa/(m^3/s) (Fig. 2.27(b)) when hydraulic fracturing is not activated, to ∼700 MPa/(m^3/s) (Fig. 2.30(b)). This impedance reduction should render the operation of the HDR reservoir efficient to a period of approximately 8.5 years. After 8.5 years, flow impedance becomes higher than 1000 MPa/(m^3/s) and the utilization of the reservoir becomes inefficient. This means that injection pressure must increase to a point hydraulic fracturing continues to work such that it counteracts the dragging effects of increased viscosity.

Figure 2.30(c) demonstrates that an HDR reservoir is going to last longer if the change of geothermal fluid viscosity with temperature is considered (compare with Fig. 2.23(a)). However this extended operational life is not of any importance as the impedance exceeds the limits of economic operation from the beginning if hydraulic fracturing is not activated and after ∼8.5 years when it is activated.

Before drawing a definitive conclusion, it is speculated that this disappointing performance is linked to the Newtonian constitutive behavior of the geothermal fluids. Authors like Santoyo et al. (2001) and Santoyo-Gutiérrez, Espinosa, and Amaro-Espejo (2005) have studied eleven Non-Newtonian geothermal fluids: they observed that the temperature changes associated with Non-Newtonian fluids are not as large as observed here. In other words, the Non-Newtonian character of the drilling fluids seems to counteract, at least partially, the thermal dependence of the dynamic viscosity. This statement clearly calls that future studies take into consideration

both thermal effects and Non-Newtonian nature of geothermal fluids. Possibly their effects may, in some circumstances, be cooperating rather than counteracting.

2.1.4 Combined mode I and mode II hydraulic fracturing model

The Hydraulic Fracturing Model (HFM), presented in Sect. 2.1.1.2, is developed to stand for fracture evolution which results from increasing fracture pressure to a point the minimum principal stress becomes tensile and exceeds the tensile strength of the material, and consequently normal separation of fracture surfaces (mode I) occurs. Since fractures in all spatial orientations are considered in the reservoir domain, shear displacement is expected during fracture opening by mode I (Fig. 2.31).

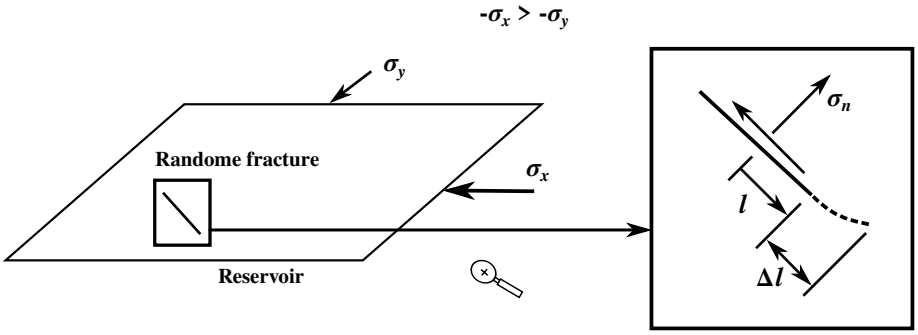

FIGURE 2.31: Fracture pinching due to deviatoric stresses (wing fracture evolution).

The modified fracturing model (HFM2) accounts for a pinching effect due to deviatoric stresses (AbuAisha, 2014; AbuAisha and Loret, 2016a),

$$F(\underline{\underline{\boldsymbol{\sigma}}}', \ell, \boldsymbol{n}) = \sqrt{\pi \ell}\left[\sigma_n' + 3f(\ell)\langle \sigma_n'^d \rangle^+\right] - C_{rc} = 0, \tag{2.17}$$

with,

$$\sigma_n' = \boldsymbol{n}\cdot\underline{\underline{\boldsymbol{\sigma}}}'\cdot\boldsymbol{n}, \quad \boldsymbol{\sigma}'^d = \underline{\underline{\boldsymbol{\sigma}}}' - \frac{\mathrm{tr}(\underline{\underline{\boldsymbol{\sigma}}}')}{3}\underline{\underline{\boldsymbol{\delta}}}, \quad \sigma_n'^d = \boldsymbol{n}\cdot\underline{\underline{\boldsymbol{\sigma}}}'^d\cdot\boldsymbol{n}, \tag{2.18}$$

and C_{rc} is the material toughness. The function $f(\ell)$ involves a fracture growth stabilizing parameter ξ in the same format as in Sect. 2.1.1.2:

$$f(\ell) = \xi \begin{cases} \dfrac{\ell_f}{\ell}, & \ell < \ell_f; \\ 1, & \ell \geq \ell_f. \end{cases} \tag{2.19}$$

The pinching effect is active only if normal deviatoric stress $\sigma_n'^d$ is positive. Consider axisymmetric loading about the axis 1, then $\sigma_n'^d = (\sigma_{11}' - \sigma_{22}')\,(n_1^2 - 1/3)$. For fractures normal to the symmetry axis ($n_1 = 1$), the term is effective if the radial stress is less tensile than the normal stress, e.g. $\sigma_{11}' = 0$ and $\sigma_{22}' < 0$. Conversely, for fractures parallel to the symmetry axis ($n_1 = 0$), the term is effective if the axial stress is less tensile than the radial stress, e.g. $\sigma_{11}' < 0$ and $\sigma_{22}' = 0$.

The same stimulation test (Sect. 2.1.2.3) is reconsidered in the following simulations. The stabilizing parameter ξ is determined such that the fracturing begins at a pressure p_b^{HF} corresponding to one of the cases demonstrated in Eqs 2.11 or 2.12 whichever applies. Material properties for hydraulic fracturing are indicated in Table 2.3, except for the stabilizing parameter $\xi = 0.0205$, which is calculated for a fracturing threshold of 40 MPa, and $C_{rc} = K_{Ic}$.

Figure 2.32 shows that the modified fracturing model requires less energy than the HFM. For the same pore fluid injection profile (Fig. 2.3(b)), hydraulic fracturing remains active for 2 years, meanwhile it is only active of a period of 1 year when the HFM is considered (Fig. 2.12).

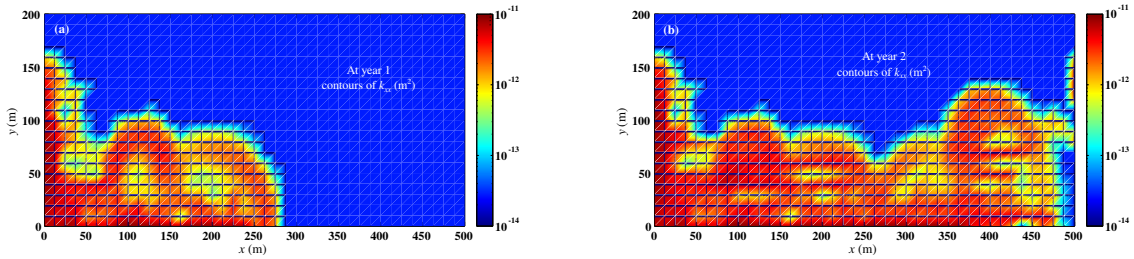

FIGURE 2.32: Contours of longitudinal permeability component k_{xx} at two times: (a) 1 year; and (b) 2 years. Fracture propagation is in the direction of maximum far-field stress. Injection pressure schedule (Fig. 2.3(b)) is sufficient to entirely enhance the reservoir in the longitudinal direction.

Clearly the HFM2 provides a more stable and a smoother evolution of porous block permeability which is translated into a slower propagation of the heat front and hence an improved hydraulic enhancement in terms of the stimulated volume.

The volume of the HDR reservoir enhanced by hydraulic fracturing, whether by applying the HFM or the HFM2, for a period of one year, shows that fractures are evolving in the direction of the maximum far-field stress (x-axis). This behavior causes an enhancement of the longitudinal permeability up to almost the same distances in x- and y-directions for both the HFM and the HFM2 (compare Figs 2.12 and 2.32(a)). These simulations are in good agreement with the microseismic events diagram presented in Bruel (1995b) after 1 year of hydraulic fracturing.

The preferential cooling following the new paths created by hydraulic fracturing is demonstrated in Fig. 2.33. The spurious oscillations on the temperature contours come from the shocks that disturb the heat front when the permeability is suddenly increased (Sect. 2.1.5).

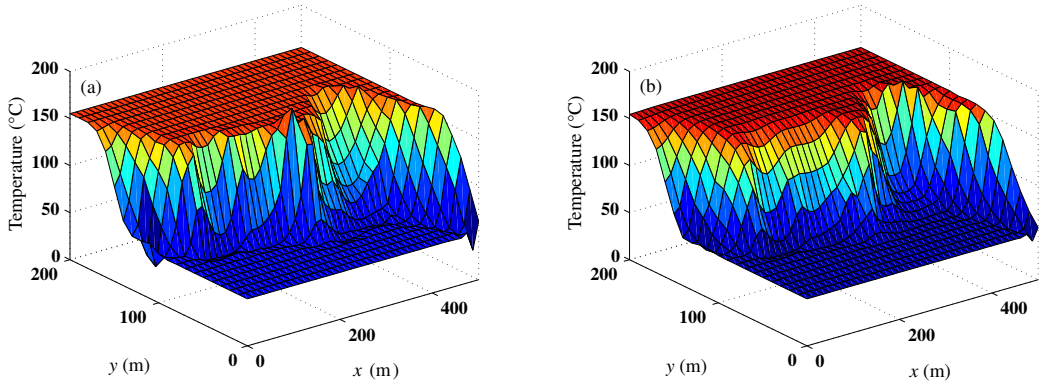

FIGURE 2.33: Contours of the enhanced reservoir temperature at two times: (a) 5 years; and (b) 10 years, and while using the HFM2.

The stabilizing effect of the modified fracturing model (HFM2) with respect to the HFM is also observed in Fig. 2.34, where the time course of the longitudinal permeability is smoother in the case of the HFM2.

The non-linear relation between the injection pressure and flow rate at the injection well GPK1 shows periods of intense enhancement during the first two years of the simulations (Fig. 2.35(a)).

Since the reservoir volume enhanced by the HFM2 is more important than in the case of the HFM for the same injection schedule, the reservoir is depleted faster (Fig. 2.36(a)).

The produced flow from the HDR reservoir when the HFM2 is used is, by average, 2.5 times higher (Fig. 2.36(b)). However, the reservoir works efficiently for 10.5 years in case of the HFM and only for 4 years when the HFM2 is employed (Fig. 2.36(a)). If flow profiles (Fig. 2.36(b)) are

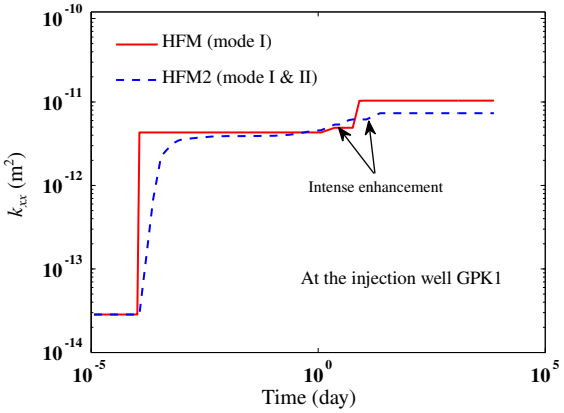

FIGURE 2.34: Longitudinal permeability k_{xx} history at the injection well GPK1 for the two models the HFM and the HFM2.

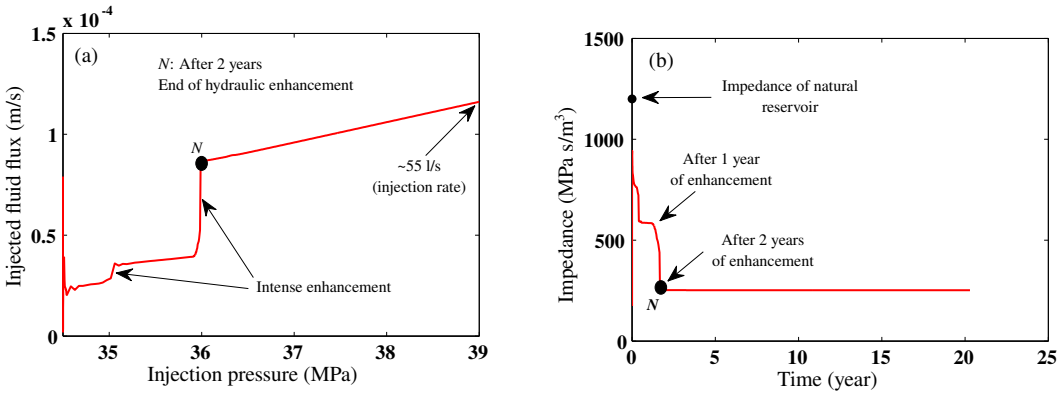

FIGURE 2.35: (a) The relation between injection pressure and resulting flow rate at the injection well GPK1 of the enhanced reservoir of Soultz-sous-Forêts and while considering the HFM2. (b) The impedance history.

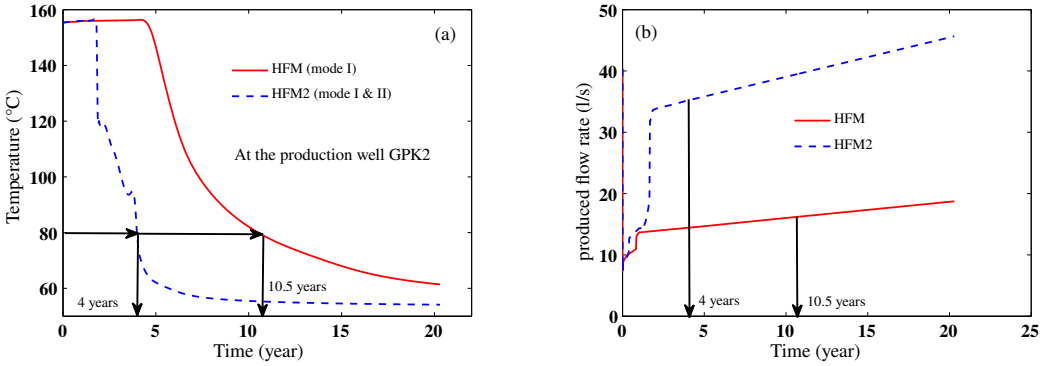

FIGURE 2.36: Time profiles of produced (a) temperatures (b) flow rates from the enhanced HDR reservoir, comparison between the HFM and the HFM2 simulation results.

numerically integrated over the efficient life of the HDR reservoir, the extracted fluid volumes are known: the volume of efficient fluid produced from the stimulated HDR reservoir by the HFM over a period of 10.5 years is 4.922 Million m^3 against 2.681 Million m^3 in the case of the HFM2.

Thus, about 45.5% of the efficient produced fluid is lost when the HFM2 is used in the simulations for the injection schedule (Fig. 2.3(b)). However, using the HFM2 has reduced the

power needed to operate the HDR reservoir by about 80% (Fig. 2.35(b)). The implementation of hydraulic fracturing is a matter of compromise: less consumption of energy requires stronger hydraulic fracturing which, regrettably, means a short effective life of the HDR reservoir and hence a reduction of the ultimate produced efficient fluid.

Murphy et al. (1999) have indicated that the ambitious goal is to enhance HDR reservoirs to a point their impedance becomes very small, i.e. $\mathcal{Z} < 100$ MPa/(m^3/s) on a consistent basis. This can be achieved numerically by applying the HFM2 and choosing such a strong injection schedule where more volume of the reservoir is enhanced. Yet, one should keep in mind that such a process strongly and regrettably reprimands the effective life of the reservoir and thus the amount of the efficient produced fluid.

2.1.5 Numerical stabilization of forced heat convection

The sudden increase of the permeability tensor at the geometrical points, where hydraulic fracturing is active, is accompanied by sudden increase in the velocity of the fluid front. Therefore, the convected heat front strongly strikes the stiff boundaries where the permeability is not yet enhanced. The reflection of the heat front is supposed to cause spurious numerical wiggles in the solution of the temperature field (Fig. 2.33). These oscillations in the temperature field result in spurious oscillations in the effective stress fields. Knowing that the effective stresses are the driving forces for fracture evolution, the numerical simulation of hydraulic fracturing cannot be trusted with such spurious oscillations.

The hydraulic fracturing stimulation tests are performed under extreme conditions where an enormous change of the reservoir pressure and temperature is expected at the injection well and at quite early stages. The commonly used stabilizing approaches for heat convection have proven to be inefficient for sudden large changes in the fluid velocity and at early stages with extreme injection conditions (AbuAisha, 2014; Yin, Dusseault, and Rothenburg, 2009). This section focuses on the computational difficulties associated with the phenomenon of forced heat convection. The disturbing spurious noises that can appear on the contours of temperature fields are healed and/or mitigated by applying multiple stabilization methods.

2.1.5.1 Limitations of the SUPG method

A method is needed to stabilize the spurious numerical oscillations in the hyperbolic solutions of the convection-dominated thermo-poroelastic BVPs. Among the several methods presented in literature to treat such oscillations, the Streamline-Upwind/Petrov-Galerkin (SUPG) method is used in the previous simulations. This method does not require to introduce additional testing functions, it nevertheless adds perturbations to the Galerkin test functions (Hughes, 2000). This advantage makes the SUPG method widely acceptable and easily implemented in the problems of heat convection.

The SUPG method originates from the upwind finite differences method which uses the artificial diffusion idea. The method taps on the work of Brooks and Hughes (1982) and the formalism of Fries and Matthies (2004). Based on the work of AbuAisha (2014), and the research of Gelet, Loret, and Khalili (2012b), Gelet, Loret, and Khalili (2013), and Gelet, Loret, and Khalili (2012a), the SUPG method is sufficient to give smooth numerical solutions except for the following cases:

- strong pumping near the injection well at early times;
- when hydraulic fracturing is activated with a strong increase in the permeability tensor components; and,
- at the production well at late times when the major part of the heat front reaches the stiff boundary.

The balance of energy of a thermo-poroelastic BVP (Eq. 2.6$_3$) with a source term f, can be written in the following format,

$$\mathcal{R}\theta - f = 0, \quad \text{with} \quad \mathcal{R}\theta = \rho C_v \frac{\partial \theta}{\partial t} + \boldsymbol{v}^{\text{conv}} \cdot \boldsymbol{\nabla}\theta - \boldsymbol{\nabla} \cdot (\Lambda \boldsymbol{\nabla}\theta)\,, \tag{2.20}$$

with $\boldsymbol{v}^{\text{conv}} = \rho_\lambda C_{p\lambda} \boldsymbol{q}$ being the convective velocity vector. The weak form associated with Eq. 2.20,

$$\int_{\mathcal{V}} \delta\theta (\mathcal{R}\theta - f)\, d\mathcal{V}, \tag{2.21}$$

uses different interpolation functions for the unknown temperature change θ and its variation $\delta\theta$:

$$\theta = \boldsymbol{N}_\theta \boldsymbol{\theta}^e; \quad \delta\theta = \boldsymbol{W}_{\boldsymbol{\theta}} \delta\boldsymbol{\theta}^e, \tag{2.22}$$

the weight function $\boldsymbol{W}_{\boldsymbol{\theta}}$ is taken as,

$$\boldsymbol{W}_{\boldsymbol{\theta}} = \boldsymbol{N}_\theta + \tau \boldsymbol{v}^{\text{conv}} \cdot \boldsymbol{\nabla} \boldsymbol{N}_\theta, \tag{2.23}$$

the stabilization parameter τ is expressed as,

$$\tau = \frac{h}{2|\boldsymbol{v}^{\text{conv}}|} \left(\coth(\text{Pe}) - \frac{1}{\text{Pe}} \right), \tag{2.24}$$

where h is the typical element length and $\text{Pe} = |\boldsymbol{v}^{\text{conv}}| h / \Lambda$ is the Péclet number.

By substituting the definition (2.23) into Eq. (2.21), the weak form of the problem is reached by discretizing the body into N_e non-overlapping generic elements of volume $\mathcal{V}^e$,

$$\sum_{e=1}^{N_e} [\delta\boldsymbol{\theta}^e]^T \int_{\mathcal{V}^e} (\boldsymbol{N}_\theta)^T \Big(\mathcal{R}\theta - f \Big)\, d\mathcal{V}^e + \underbrace{\sum_{e=1}^{N_e} [\delta\boldsymbol{\theta}^e]^T \int_{\mathcal{V}^e} \underbrace{\Big(\boldsymbol{\nabla}(\boldsymbol{N}_\theta)^T (\boldsymbol{v}^{\text{conv}})^T \Big) \tau}_{\text{Streamline perturbation}} \Big(\mathcal{R}\theta - f \Big)\, d\mathcal{V}^e}_{\text{Stabilizing part}} = 0. \tag{2.25}$$

As stated previously, the application of the SUPG method is not sufficient at small time steps. Actually, the characteristic time that weighs the stabilization of the SUPG method (Eq. 2.24) can be expressed as in Hughes, Franca, and Hulbert (1989) and Tezduyar and Park (1986),

$$\tau = \frac{1}{\sqrt{\left(\frac{2}{\Delta t}\right)^2 + \left(\frac{2|\boldsymbol{v}^{\text{conv}}|}{\rho C_v h}\right)^2 + 9\left(\frac{4\Lambda}{\rho C_v h^2}\right)^2}}, \tag{2.26}$$

for significantly small time steps ($\Delta t \to 0$), the stabilization coefficient τ becomes inefficient, i.e.,

$$\lim_{\Delta t \to 0} \tau = 0. \tag{2.27}$$

To overcome the deficiencies of the SUPG method for healing the oscillations in the numerical solutions of transient convection-diffusion problems at early times and when activating hydraulic fracturing, the Gradient Subgrid Scale GSGS method is presented in the next section. It is, henceforth, conceivable that the calculation of the stabilization parameter must take into account a time-dependent factor, where the transition between the convection-dominated and the diffusion-dominated situations in small time steps is indeed natural.

2.1.5.2 The Gradient Subgrid Scale GSGS method

The GSGS method includes two terms, an adjoint stabilization and a gradient adjoint stabilization (Harari, 2004). The two associated coefficients are tuned to attain nodal exactness for a specific one-dimensional problem. The method relies on a reactive term which may be either constitutive or resulting from a time semi-discretization scheme. For instance, it applies for the diffusion equations, the balance of mass for instance, which do not include convective terms nor constitutive reaction terms. A reaction term is exhibited by firstly discretizing in time and secondly in space. Unlike the SUPG method, the stabilizing terms vanish when the mesh gets significantly refined but not when time step is considerably reduced.

The field Eq. 2.20 is integrated at the time step $n+1$ by using a generalized trapezoidal scheme parameterized by the scalar $\beta \in]0,1]$,

$$\rho C_v \frac{\theta_{n+1}-\theta_n}{\Delta t} + \left(\boldsymbol{v}^{\text{conv}} \cdot \boldsymbol{\nabla}\theta - \boldsymbol{\nabla}\cdot(\Lambda\boldsymbol{\nabla}\theta) - f\right)_{n+\beta} = 0, \tag{2.28}$$

with the notation $a_{n+\beta} = (1-\beta)\, a_n + \beta\, a_{n+1}$. It is instrumental to define the operator $\mathcal{N}$ and its adjoint $\mathcal{N}_*$ such that,

$$\begin{aligned} \mathcal{N}\theta &= \boldsymbol{v}^{\text{conv}} \cdot \boldsymbol{\nabla}\theta - \boldsymbol{\nabla}\cdot(\Lambda\boldsymbol{\nabla}\theta) - s\theta, \\ -\mathcal{N}_*\theta &= \boldsymbol{v}^{\text{conv}} \cdot \boldsymbol{\nabla}\theta + \boldsymbol{\nabla}\cdot(\Lambda\boldsymbol{\nabla}\theta) + s\theta, \end{aligned} \tag{2.29}$$

which display the reaction coefficient $s < 0$,

$$s = -\frac{\rho C_v}{\beta \Delta t} < 0. \tag{2.30}$$

The steady convection-diffusion-reaction problem at step $n+1$ is, henceforth, cast in the following format,

$$\mathcal{N}\theta_{n+1} - F_{n+1} = 0, \tag{2.31}$$

where,

$$F_{n+1} = \frac{-(1-\beta)}{\beta}\left(\boldsymbol{v}^{\text{conv}} \cdot \boldsymbol{\nabla}\theta - \boldsymbol{\nabla}\cdot(\Lambda\boldsymbol{\nabla}\theta)\right)_n + \frac{f_{n+\beta}}{\beta} - s\theta_n. \tag{2.32}$$

For any variation w^h, the weak form of Eq. 2.31 takes the following form,

$$\begin{aligned} &\int_{\mathcal{V}} w^h \left(\mathcal{N}\theta^h_{n+1} - F_{n+1}\right) d\mathcal{V} \\ +\sum_{e=1}^{N_e} &\int_{\mathcal{V}^e} \left(-\mathcal{N}_* w^h_{n+1}\right) \tau^e_{00} \left(\mathcal{N}\theta^h_{n+1} - F_{n+1}\right) d\mathcal{V}^e \\ +\sum_{e=1}^{N_e} &\int_{\mathcal{V}^e} \boldsymbol{\nabla}\left(-\mathcal{N}_* w^h_{n+1}\right) \tau^e_{11} \boldsymbol{\nabla}\left(\mathcal{N}\theta^h_{n+1} - F_{n+1}\right) d\mathcal{V}^e = 0, \end{aligned} \tag{2.33}$$

includes the two stabilization parameters τ^e_{00} and τ^e_{11}. These parameters are defined in terms of two dimensionless coefficients t_{00} and t_{11} such that nodal exactness for a specific one-dimensional problem is assured (Hauke, Sangalli, and Doweidar, 2007),

$$\tau^e_{00} = \frac{h}{|\boldsymbol{v}^{\text{conv}}|} t_{00} \geq 0, \quad \tau^e_{11} = \frac{h^3}{|\boldsymbol{v}^{\text{conv}}|} t_{11} \leq 0, \tag{2.34}$$

with,

$$t_{00} = \left(-2\text{Da} + \frac{\text{Da}^2 \sinh(\text{Pe})}{-\cosh(\text{Pe}) + \cosh(\gamma) + \text{Da}\sinh(\text{Pe})}\right)^{-1}, \tag{2.35}$$

$$t_{11} = \frac{1}{6\mathrm{Da}^3}\left(-3-\mathrm{Da}^2+\frac{3\mathrm{Da}}{\mathrm{Pe}}+\frac{3\mathrm{Da}\cosh(\gamma)+(-3+\mathrm{Da}^2)\sinh(\mathrm{Pe})}{-2\cosh(\mathrm{Pe})+2\cosh(\gamma)+\mathrm{Da}\sinh(\mathrm{Pe})}\mathrm{Da}\right), \tag{2.36}$$

where, $\gamma = \sqrt{\mathrm{Pe}(-2\mathrm{Da}+\mathrm{Pe})}$, and Pe and Da are the Péclet and Damköhler numbers respectively,

$$\begin{aligned} \mathrm{Pe} &= \frac{|\boldsymbol{v}^{\mathrm{conv}}|h}{\Lambda} = \frac{\text{Advection}}{\text{Diffusion}} \quad \text{Péclet number;} \\ \mathrm{Da} &= \frac{s\,h}{|\boldsymbol{v}^{\mathrm{conv}}|} = \frac{\text{Reaction}}{\text{Advection}} \quad \text{Damköhler number.} \end{aligned} \tag{2.37}$$

Figure 2.37 shows the contours of the coefficients t_{00} and t_{11} as a function of Pe and Da. The first stabilizing coefficient t_{00} is always positive, whereas the coefficient t_{11} is always negative.

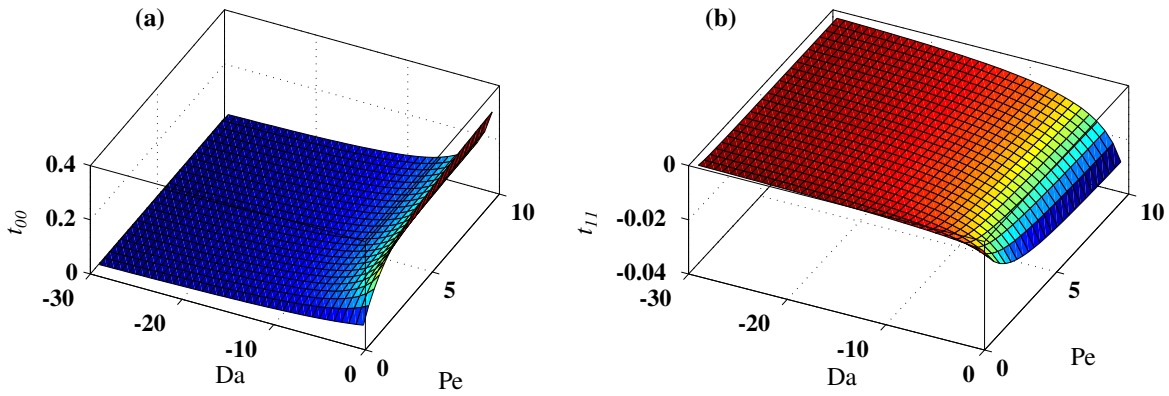

FIGURE 2.37: Dimensionless stabilizing parameters: (a) t_{00}; (b) t_{11} stemming from a one-dimensional nodal exactness of Hauke, Sangalli, and Doweidar (2007).

For linear elements in one-dimensional problems and under convective-diffusive dominant condition ($\mathrm{Da} \to 0$), the method (Eq. 2.33), produces the same modification as the SUPG method in absence of the reactive term[4],

$$\tau_{00}^e \xrightarrow{\mathrm{Da}\to 0} \frac{h}{2|\boldsymbol{v}^{\mathrm{conv}}|}\left(\coth(\mathrm{Pe})-\frac{1}{\mathrm{Pe}}\right). \tag{2.38}$$

Hauke, Sangalli, and Doweidar (2007) have provided several definitions for the stabilizing parameters τ_{00}^e and τ_{11}^e depending on the dominant limit: convective-diffusive with no reaction limit, without convection limit, reaction dominated limit, and high Péclet number limit. The only case where it is thought that the general expressions of Eqs. 2.35 and 2.36 are troublesome is when s is very small, generally less than $10^{-3} \times \rho\, C_v$. Then, the dimensionless stabilizing coefficients should be calculated as follows:

$$\begin{aligned} t_{00} &\to \frac{1}{2}\left(\coth(\mathrm{Pe})-\frac{1}{\mathrm{Pe}}\right) \xrightarrow{\mathrm{Pe}\to 0} \frac{\mathrm{Pe}}{6}; \quad \text{and,} \\ t_{11} &\to \frac{-1}{24}\left(\frac{3}{\mathrm{Pe}^3}(1-\mathrm{Pe}\coth(\mathrm{Pe}))+\coth(\mathrm{Pe})\right) \xrightarrow{\mathrm{Pe}\to 0} -\frac{\mathrm{Pe}}{60}. \end{aligned} \tag{2.39}$$

The details of the finite element formulations of both the SUPG and the GSGS methods, and the way they are integrated in the thermo-hydromechanical framework are provided in

[4]The third term of eq. (2.33) disappears as at least for linear elements in one-dimensional problems, the gradient stabilization term $\mathcal{N}_*$ disappears when $\mathrm{Da} \to 0$ since τ_{11}^e is uniformly bounded to a limit (Fig. 2.37(b)), whence $s^2\,\tau_{11}^e \to 0$. The previous remark becomes clear if the matrix form of Eq. 2.33 is derived for a one-dimensional problem with linear elements.

AbuAisha (2014) and AbuAisha and Loret (2016b). In the coming sections, the circulation tests in the Soultz-sous-Forêts HDR reservoir (Sect. 2.1.2.3) are re-performed while implementing the GSGS method in the FEM code.

2.1.5.3 The circulation test at the well GPK1 1993 without hydraulic fracturing

Simulations of the circulation test in the Soultz-sous-Forêts HDR reservoir (Sect. 2.1.2.3), and while implementing the GSGS method in the FEM code are presented. Hydraulic fracturing is not activated as this section aims at studying the stabilization of heat convection under normal circulation conditions.

Figure 2.38 compares the profiles of temperature and pressure, along the line of symmetry $y = 0$ m, for the GSGS and the SUPG methods at different times of 10 days, 6 months, and at years 1, 2, 5 and 10. The GSGS method heals quite satisfactorily the oscillations of the SUPG method even at small time interval of 10 days. The profiles of pore fluid pressure do not differ between the GSGS and the SUPG methods since hydraulic diffusion establishes quickly, i.e. in a few days. The jump in the pressure profiles at the injection well between the time intervals of 10 days and 6 months is due to the pumping schedule (Fig. 2.3(b)).

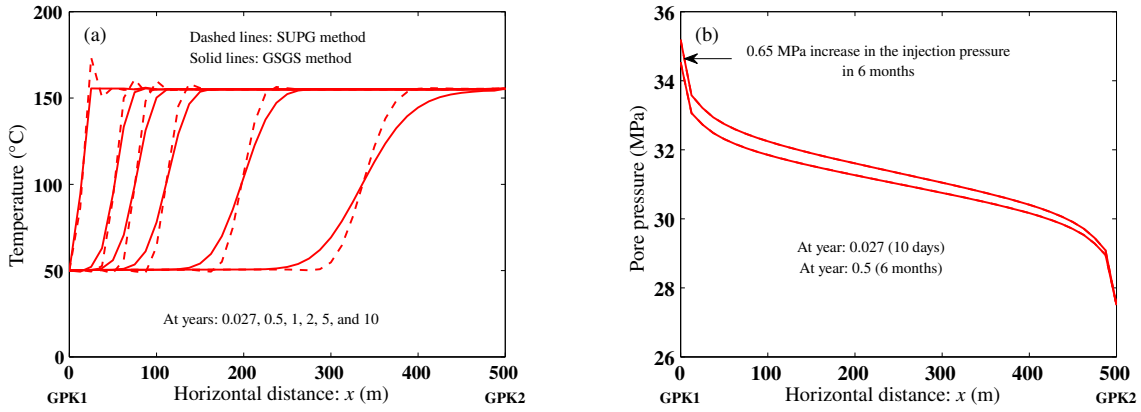

FIGURE 2.38: Temperature and pore pressure profiles along the line of symmetry $y = 0$ m: (a) heat convection oscillations near the injection well are stabilized when the GSGS method is applied; (b) pore fluid pressure profiles are not affected by the GSGS method since hydraulic diffusion establishes quickly.

Though the GSGS method is capable of circumventing the heat convection oscillations at very short and intermediate time intervals, its capacity deteriorates with time (Fig. 2.39).

At year 15 and despite mitigating the noises at the production well, the GSGS method still leaves serious temperature oscillations (Fig. 2.39). At large time intervals near the production well, the source term becomes negligible ($s \to 0$) meanwhile the convective velocity is considerably large. This causes the Damköhler number to disappear ($\mathrm{Da} \to 0$), therefore the capacity of the GSGS method is lost as a convection-dominated situation appears and the stabilizing method produces the same modification as the SUPG method.

2.1.5.4 The hydraulic fracturing test at the well GPK1 1993

The purpose of this section is to use the GSGS method to heal the numerical oscillations which appear on the contours of temperature field and hence affect the process of hydraulic fracturing. Fig. 2.40 shows the contours of the reservoir temperature during the process of stimulation at years 5 and 10, and while using the GSGS method.

The GSGS method cures almost all of heat convection oscillations, compare Figs. 2.33 and 2.40. Due to the diffusive nature of the GSGS method, the values of the contours of the enhanced

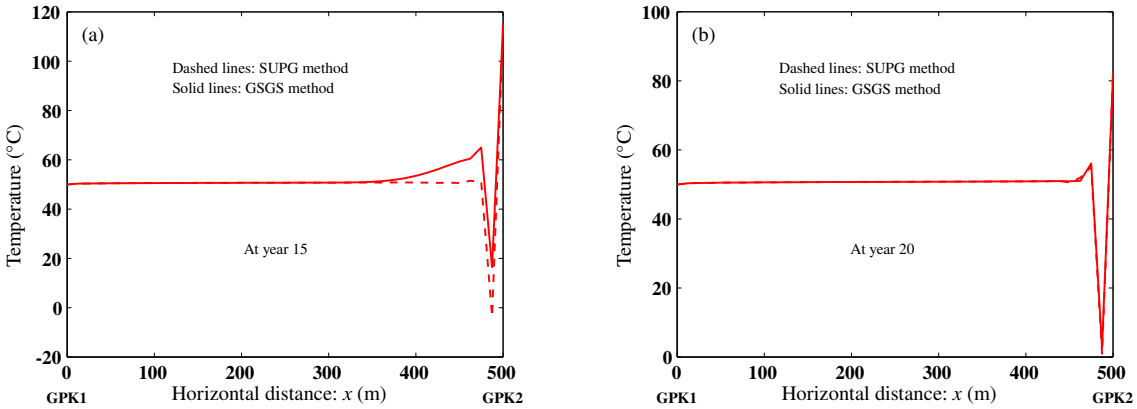

FIGURE 2.39: Temperature profiles along the line of symmetry $y = 0$ m: (a) heat convection oscillations are mitigated at the production well but still far from being healed; (b) at very large times, both the SUPG and GSGS methods are unable to stabilize oscillations near the production well.

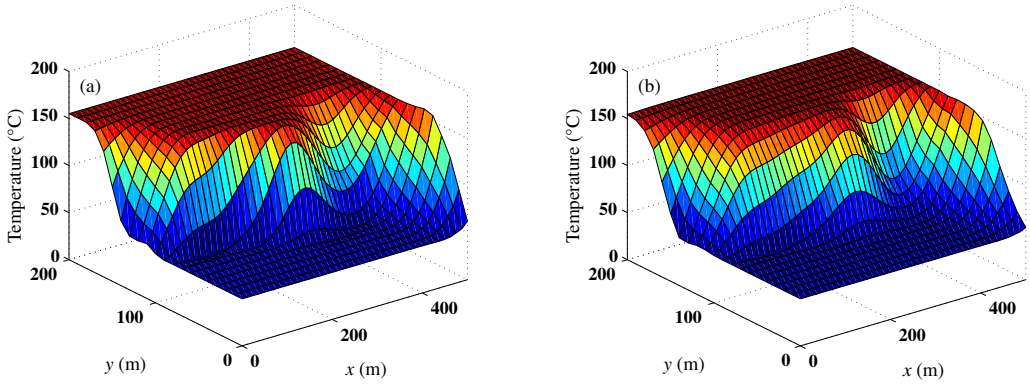

FIGURE 2.40: Contours of the enhanced reservoir temperature at two times: (a) 5 years; and (b) 10 years, heat convection is stabilized by the GSGS method

permeability of the HDR reservoir are about 0.96 less when the GSGS method is implemented. This becomes more evident when the history of the enhanced permeability is plotted at some point (Fig. 2.41). It is clear that the evolution of the longitudinal permeability is smoother in the case of the GSGS method as it provides more stabilization. Nonetheless, the same general evolution behavior is more or less obtained for both the GSGS and the SUPG methods.

The advantages and disadvantages of the GSGS method are listed as follows:

1. the GSGS method has been proven capable of efficiently healing the heat convection oscillations at very short and intermediate time intervals;

2. the GSGS method is also efficient in curing the stubborn heat convection oscillations even while tremendously enhancing the HDR reservoir permeability by hydraulic fracturing;

3. at quite large time intervals and if convection-dominated situations are present, the GSGS method loses its efficiency and the SUPG method is retrieved.

2.1.5.5 The Discontinuity Capturing Method (DCM)

Neither the GSGS method nor the SUPG method is capable of healing the numerical noises resulting from the heat front striking the stiff boundary at the production well. John and Knobloch

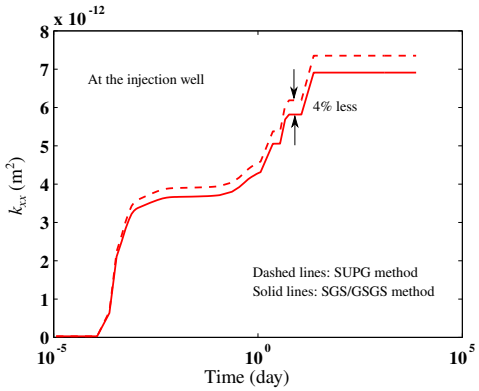

FIGURE 2.41: Longitudinal permeability k_{xx} history at the injection well: comparison between the simulations when implementing the GSGS method (solid lines) and the SUPG method (dashed lines).

(2007) have defined a modification to the SUPG method, referred to as the Discontinuity Capturing Method (DCM), such that it becomes capable of treating the spurious numerical noises at long periods.

The DCM suggests to modify the SUPG weighting function by an additional term parallel to the thermal gradient of the thermal analysis in the following format,

$$\boldsymbol{W_\theta} = \boldsymbol{N}_\theta + \tau_1 (\boldsymbol{v}^{\text{conv}})^T \cdot \boldsymbol{\nabla} N_\theta + \tau_2 (\boldsymbol{v}_{||})^T \cdot \boldsymbol{\nabla} N_\theta, \tag{2.40}$$

the projection $\boldsymbol{v}_{||}$ of $\boldsymbol{v}^{\text{conv}}$ on $\boldsymbol{\nabla}\theta$ being defined as[5],

$$\boldsymbol{v}_{||} = \begin{cases} \dfrac{(\boldsymbol{v}^{\text{conv}})^T \cdot \boldsymbol{\nabla}\theta}{|\boldsymbol{\nabla}\theta|^2} \boldsymbol{\nabla}\theta, & \boldsymbol{\nabla}\theta \neq \boldsymbol{0}, \\ \boldsymbol{0}, & \boldsymbol{\nabla}\theta = \boldsymbol{0}. \end{cases} \tag{2.41}$$

Since $(\boldsymbol{v}^{\text{conv}})^T \cdot \boldsymbol{\nabla\theta} = (\boldsymbol{v}_{||})^T \cdot \boldsymbol{\nabla\theta}$, it is concluded that,

$$\boldsymbol{W_\theta^T} (\boldsymbol{v}^{\text{conv}})^T \cdot \boldsymbol{\nabla\theta} = (\boldsymbol{N}_\theta)^T (\boldsymbol{v}^{\text{conv}})^T \cdot \boldsymbol{\nabla\theta} + \underbrace{(\boldsymbol{\nabla N}_\theta)^T \tau_1 \boldsymbol{v}^{\text{conv}} (\boldsymbol{v}^{\text{conv}})^T \cdot \boldsymbol{\nabla\theta}}_{\text{Streamline operator}} + \underbrace{(\boldsymbol{\nabla N}_\theta)^T \tau_2 \boldsymbol{v}_{||} (\boldsymbol{v}_{||})^T \cdot \boldsymbol{\nabla\theta}}_{\text{DCM operator}}. \tag{2.42}$$

While the SUPG matrix $\boldsymbol{v}^{\text{conv}} (\boldsymbol{v}^{\text{conv}})^T$ is a first-order positive semi-definite matrix acting only in the streamline direction, the discontinuity capturing matrix $\boldsymbol{v}_{||} (\boldsymbol{v}_{||})^T$ is also a first-order positive semi-definite matrix yet acting only in the direction of the discrete solution temperature gradient.

The stabilizing parameters τ_1 and τ_2 are defined such that,

$$\tau_1 = \tau, \quad (\text{of the SUPG method}) \quad \text{and,} \quad \tau_2 = \tau_{||}, \tag{2.43}$$

$\tau_{||}$ is deduced using the same strategy of calculating τ (Eq. 2.24), yet the parallel velocity $\boldsymbol{v}_{||}$ is introduced. In order to avoid the doubling of the stabilizing parameter τ when $\boldsymbol{v}^{\text{conv}} = \boldsymbol{v}_{||}$, the DCM parameter is re-defined,

$$\tau_1 = \tau, \quad \text{and,} \quad \tau_2 = \max[0, \tau_{||} - \tau]. \tag{2.44}$$

Fig. 2.42 shows that the DCM is capable of almost entirely healing the numerical oscillations at the production well, compare with Fig. 2.39.

[5]The DCM is a non-linear stabilizing method as $\boldsymbol{v}_{||} = \boldsymbol{v}_{||}(\boldsymbol{\theta}^e)$.

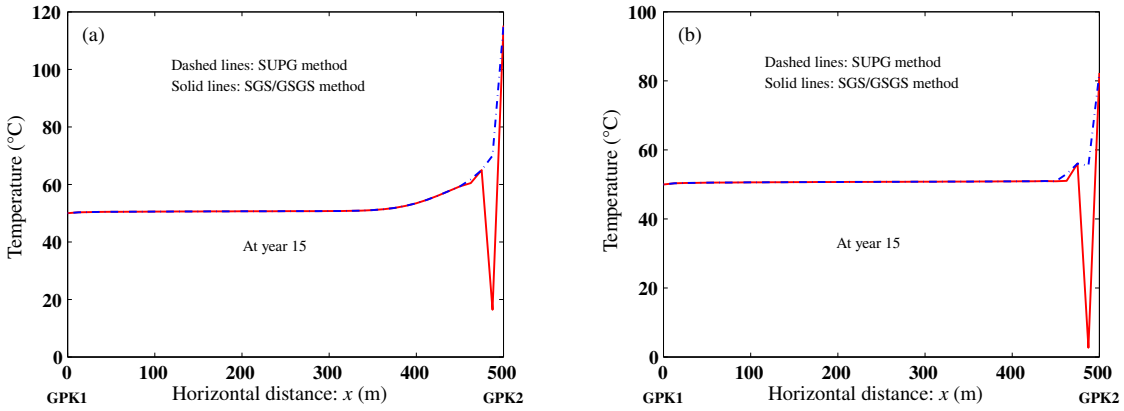

FIGURE 2.42: Temperature profiles along the line of symmetry $y = 0$ m. DCM is capable of treating the stubborn numerical oscillations at the production well where both the GSGS and SUPG methods are proven inefficient.

2.1.6 Conclusion and perspectives

The hydraulic fracturing technique is addressed in a thermo-poroelastic framework with emphasis on the impedance and efficiency of thermal recovery from HDR reservoirs. According to simulations, hydraulic fracturing is effective in a large zone adjacent to the injection well and the permeability in the direction of the production well is considerably enhanced. As a consequence, the impedance of the reservoir is improved.

A modification to the fracture model to account for both opening and pinching of fractures results in more long term positive effects on the impedance. Moreover, it displays an enlarged zone of enhanced permeability. Yet, it reduces the duration of an efficient reservoir exploitation.

The increase of viscosity in the neighborhood of the injection well hinders the hydraulic fracturing process by reducing the pressure inside the reservoir, which leads to a less enhanced permeability.

In summary, the exact zone in which the permeability enhancement is significant depends on the details of the model. In all cases, this zone is widespread so that the flow is able to collect the heat of the rock in its path to the production well. In a broader perspective, the simulations point out that non-Darcian constitutive behaviors of flow and non-Newtonian characteristics of geothermal fluids are worth of investigation. As a further extension to this work, future research should also consider the interactions between the working fluids and other techniques aiming at improving the efficiency of thermal recovery, like the chemical enhancement of HDR reservoirs as well as CO_2-based geothermal systems.

The thermo-hydromechanical framework addresses several approaches to stabilize convection of heat at all treatment stages. The commonly used SUPG method is implemented to heal the oscillations at intermediate stages. The DCM is applied to stabilize convection of heat at late stages near the production well. For instabilities at early stages, the transient advection-diffusion problem is transformed into a steady advection-diffusion-reaction problem, which takes into account the effect of the time step factor on the numerical oscillations (the GSGS method). Ultimately, this method is capable of healing the stubborn oscillations at early stages and when permeability is tremendously increased by hydraulic fracturing.

Generally, while the current developments include a single porosity and a single temperature, a double porosity approach may be worth of consideration to team up with the hydraulic fracturing models, i.e. the fracture porosity.

2.2 A continuum-discontinuum approach to simulate hydraulic fracturing and induced seismicity for oil and gas industry

Unlike the simulations of Sect. 2.1 where the entire volume of the reservoir is the goal of the hydraulic stimulation, the approach presented here focuses on developing fractures close to the borehole for applications related to *shale gas extraction* and scrutinization of *induced seismicity*.

A number of techniques that are rooted in microseismic observations have been developed to aid in the interpretation of fracturing processes. It is often assumed that the time-dependent microseismic cloud is a proxy for the growth of the hydraulic fracture. Based on this assumption, Boroumand and Eaton (2015) developed a geomechanical simulation in which model parameters for an energy-based fracture growth are tuned to fit observed microseismicity in space and time. Shapiro and Dinske (2009b) and coworkers (Shapiro and Dinske, 2009a; Shapiro, Dinske, and Rothert, 2006) have developed a poroelastic approach based on the concept of a seismicity-triggering front. This approach uses a diffusion model that is characterized by either constant diffusivity, where the triggering front has a space-time representation of a parabolic form, or pressure-dependent diffusivity, in which case a cubic-parabolic triggering front emerges under certain assumptions. Some scientists (Cornet, 2000) argued that in the presence of tensile rock failure induced by hydraulic fracturing, the simplified models underlying these approaches do not fully capture the complexity of the spatial distribution of microseismic events, where some events are activated by mechanical rather than diffusional effects.

This research uses a coupled hydro-mechanical Finite Discrete Element Modelling (FDEM) approach to investigate in more detail the link between microseismicity and hydraulic fracture propagation for petroleum applications (AbuAisha et al., 2017). The Discrete Element Method (DEM) has been used to simulate hydraulic fracturing in naturally fractured reservoir. For instance, Duan, Kwok, and Wu (2018) and Damjanac and Cundall (2016) used a DEM approach where rock mass was considered as an assembly of blocks, and contact between these blocks represented discontinuities that exhibited a non-linear mechanical behavior. Damjanac and Cundall, 2016 used lubrication theory to implement fluid flow in the rock mass and consequently hydraulic fracturing. Other authors (Sousani et al., 2015) used a DEM approach to present a solid-fluid coupled framework to investigate the effects of fluid injection on the mechanical behavior of fractured geomaterials on the particle size. Fu, Johnson, and Carrigan (2013) describe a framework that combines the finite element method for geomechanics in the rock matrix, a finite volume approach for resolving hydrodynamics, a DEM approach for joint representation and for interfacial resolution, and an adaptive re-meshing module.

The advantage of the FDEM stems from the fact that while the material is undergoing elastic deformation, only FEM calculations are performed. Calculations become more complex when fractures are initiated. The DEM permits the tracking of fracture initiation and propagation as well as the interaction with preexisting joints. The FDEM approach of this research, implemented using the *Irazu code* (Lisjak et al., 2017), enables history matching of the field-injected pressure profile until shutdown. The model also accounts for the simulated hydraulic fracturing induced microseismicity, mainly due to shear-slip of randomly distributed preexisting joints. Shear-slip takes place due to mechanical stress changes in the medium, primarily due to stress wave spread at the onset of fracturing and during the hydraulic fracture growth, i.e., opening. This chapter aims at giving insights into how the predicted evolution of the hydraulic fracture system correlates to the observed microseismic cloud and compare it to published literature.

2.2.1 An overview of the Finite-Discrete Element Method (FDEM)

The FDEM approach was first suggested by Munjiza, Owen, and Bićanić (1995). It is a hybrid technique that combines the advantages of the FEM and DEM approaches. While the medium

is undergoing elastic deformation, the behavior of intact material is explicitly modelled by the FEM. As the strength of the material is exceeded fractures are initiated, giving rise to discontinuous blocks where the interaction between these blocks is captured by the DEM. The FDEM approach is capable of tracking fracture initiation and propagation by applying the principles of non-linear elastic fracture mechanics[6] (Barenblatt, 1962). The algorithm of the Irazu code, adopted in this study, uses three interconnecting modules (Fig. 2.43) to simulate fluid-driven fractures, as follows:

1. a mechanical solver which calculates the deformation of the intact rock mass as well as the initiation, propagation and interaction of fractures;
2. a cavity volume calculator then captures the changes of the cavity volume due to fracture propagation, the elastic deformation, and fluid compressibility. It also tracks the newly created wet boundaries by checking their connection with the initial source of fluid;
3. a pump model then interacts with the previous two modules to calculate fluid pressure while considering the pumping conditions/injected flow rate.

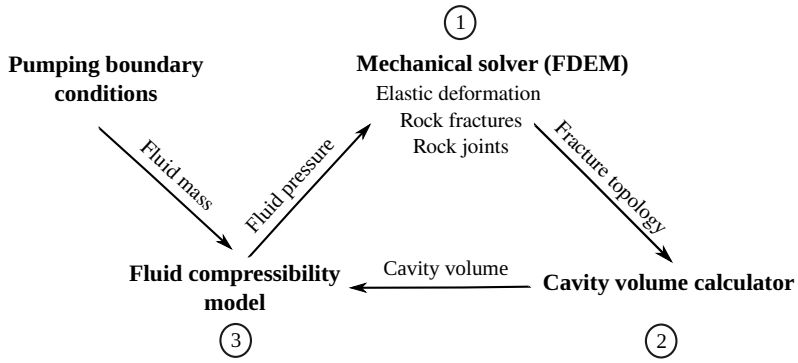

FIGURE 2.43: Interaction between computational modules of the Irazu code.

The Irazu code discretizes the modelling domain with a mesh of elastic triangular Delaunay elements connected to each other at the edges by non-dimensional rectangular cohesive fracture elements (Fig. 2.44). An explicit time integration scheme is employed to solve the equation of motion of the discretized system due to applied stresses.

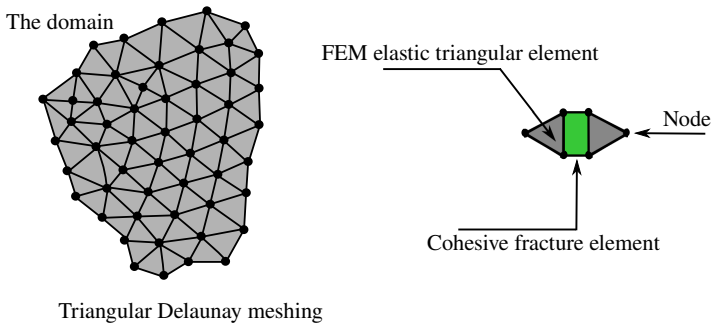

FIGURE 2.44: Triangular Delaunay meshing applied in the Irazu code. The enlarged section shows the contact nature between the elastic and the dimensionless fracture cohesive elements.

While the medium undergoes elastic loading the fracture elements are initially assigned large contact stiffness parameters (penalty parameters) to eliminate them from the elasticity

[6]The global behavior of material undergoing loading is elastic; however, non-linear means that the size of the plastic zone at the fracture tip changes as the fracture grows or as loads change, which is the common case of brittle materials.

matrix, such that all deformations occur in the triangular elements. As soon as the tensile and/or the shear strength of the material is reached, the material starts undergoing inelastic deformation (fracture process zone) that is localized within the fracture elements with the fracturing process expressed in terms of fracture energy dissipation (Lisjak, Grasselli, and Vietor, 2014). Once the fracture energies, G_{Ic} of mode I and G_{IIc} of mode II, are dissipated, the fracture elements are removed and fractures are initiated (Fig. 2.45). At this point, the positions of the separated blocks are tracked by the DEM.

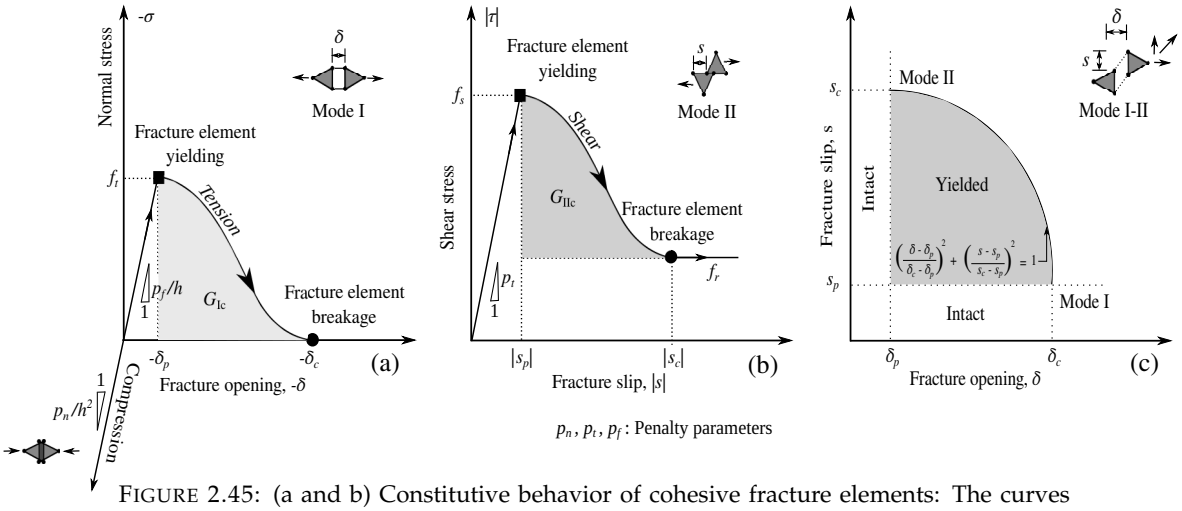

FIGURE 2.45: (a and b) Constitutive behavior of cohesive fracture elements: The curves represent a relationship between normal and tangential bonding stresses, σ and τ, versus fracture relative displacements, δ (opening) and s (sliding). G_{Ic} and G_{IIc} represent the amount of energy dissipated per unit length of fracture for mode I and mode II respectively. (c) Elliptical coupling relationship between fracture opening δ and fracture slip s for mixed-mode fracturing.

2.2.1.1 The FDEM with fluid diffusion

Fluid diffusion and fracture leakoff are implemented in the FDEM approach by considering the existence of flow channels that coincide with the edges of the triangular elements in the initial mesh. The nodes of the triangular elements represent virtual reservoirs where fluid pressure and fluid mass are sequentially calculated. The apertures of the flow channels are assigned initial values a_i that are used to reproduce/calculate the initial permeability of the porous medium using the Poiseuille flow (Fig. 2.46).

As fluid is injected at node N (Fig. 2.46), fluid pressure increases due to a fluid compressibility law (Eq. 2.45), which creates pressure gradients and causes fluid to flow to neighbor nodes (virtual reservoirs) through the flow channels. If the fluid injection rate is greater than the dissipation of fluid pressure through the flow channels, the fluid pressure eventually leads to breaking of the fracture elements and a fracture initiates. The model also accounts for true/physical fluid cavities like boreholes.

$$p^i = \begin{cases} p^{i-1} + K_\lambda \dfrac{\Delta \mathcal{M}}{\rho_\lambda \mathcal{V}^i}, & \text{change in fluid mass;} \\ p^{i-1} + K_\lambda \dfrac{\mathcal{V}^i - \mathcal{V}^{i-1}}{(\mathcal{V}^i - \mathcal{V}^{i-1})/2}, & \text{change in cavity volume;} \\ 0, & \text{for partially saturated media.} \end{cases} \tag{2.45}$$

Based on the initial flow channel aperture a_i, the initial volume of the virtual reservoir $\mathcal{V}$ is determined from the volume of conjunctive channels (Fig. 2.46) for a unity in the third dimension. The initial mass of fluid at each reservoir is calculated by adopting the same concept,

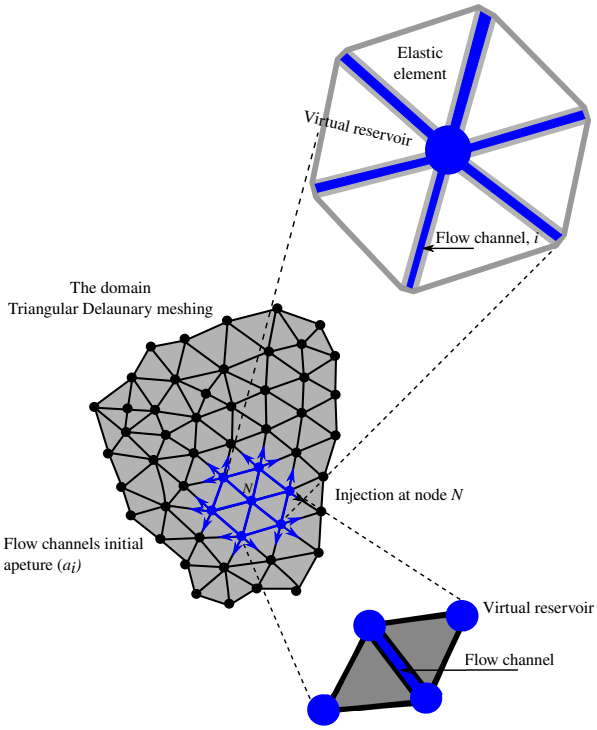

FIGURE 2.46: Conceptual graph illustrating the Delaunay triangulation with embedded fracture elements and the implementation of fluid diffusion in the Irazu code. The flow takes place in channels that are initially assigned a finite aperture (a_i) corresponding to the formation permeability. Each virtual reservoir, where fluid pressure is calculated, receives a mass of fluid from all branching channels (Lisjak et al., 2017).

yet while considering the degree of saturation S. Once the model starts undergoing the external loads and boundary conditions, the pressure and/or fluid masses at the virtual reservoirs change. Within a time step i, the fluid pressure p^i at the virtual reservoirs is calculated while considering any increase/decrease of fluid mass $\Delta\mathcal{M}$, as well as any changes in the cavity volume itself (Lisjak et al., 2017), K_λ and ρ_λ are the fluid bulk modulus and density respectively. Fluid flow in the channels is assumed viscous and laminar; henceforth, it can be described using Darcy's law. The flow q between two reservoirs, 1 and 2, within the time interval i of discretization Δt is described as,

$$q = \frac{\Delta\mathcal{M}}{\Delta t} = f(S)\frac{p_1^i - p_2^i - \rho_\lambda \mathfrak{g}(y_2 - y_1)}{R}, \tag{2.46}$$

with y_1 and y_2 being the elevations of the cavities/reservoirs 1 and 2 respectively. The dimensionless function $f(S)$ relates the permeability of the flow channel to the reservoir degree of saturation. The function $f(S)$ ranges between 0 for perfectly dry reservoirs to 1 for fully saturated reservoirs. R is the flow resistance parameter of the channel that connects the reservoirs 1 and 2, and it is calculated using the cubic law for flow between two parallel plates. While assuming that flow channel aperture varies linearly across its length, R is expressed as,

$$R = 12\frac{\mu}{\rho_\lambda}\int_{l_1}^{l_2}\frac{1}{a(l)^3}\,dl = \frac{6\mu(a_1 + a_2)}{\rho_\lambda a_1^2 a_0^2}\,L, \tag{2.47}$$

where μ is the fluid dynamic viscosity, L is the length of the flow channel, a_1 is the flow channel aperture at reservoir 1 and a_2 is the flow channel aperture at reservoir 2. The channel aperture is bounded between to limits: a_u for maximum opening; and a_l for maximum closure, beyond which further opening or closing have no meaning (Lisjak et al., 2017).

2.2.1.2 Hydromechanical coupling

There are two distinct time discretizations in the Irazu code. The first time scheme is used for the mechanical solver, i.e. deformation and fracturing. The second time scheme is used for the hydraulic solver, i.e. fluid diffusion. Both time schemes are explicit; the hydro-mechanical coupling is achieved by choosing the frequency between the mechanical and hydraulic solvers to attain the prescribed degree of saturation. For instance, the updates from the mechanical solver affect fluid pressure in the medium, and the resulting fluid pressure (from hydraulic solver) affects the mechanical calculations for the next time iteration. The stability of the mechanical solver is achieved by choosing a time step smaller than a critical value, which is proportional to the smallest element size in the model divided by the P-wave velocity of the elastic medium (Munjiza, 2004). The stability of the hydraulic solver, to attain the correct degree of saturation for all cavities and flow channels, is assured by controlling the size of the hydraulic time step (Lisjak et al., 2017),

$$\Delta t \leq \min_{m} \left(\frac{\mathcal{V}_m}{\frac{K_\lambda}{\rho_\lambda} \sum_{n} \frac{1}{R_n}} \right), \tag{2.48}$$

m and n index over all the cavities and flow channels in the boundary problem.

The FDEM method is capable of describing fracture evolution due to modes I and II of failure, as well as a combination of both fracturing modes (Fig. 2.45). Fracture opening due to fluid pressure is seen to be dominated by mode I of failure (Fjaer et al., 2008); however, mechanical deformations/pore pressure changes are expected to trigger shear-slip (mode II of failure) on preexisting joints (Bruel, 2007; Loret, 2018).

2.2.2 Simulating hydraulic fracturing test using the FDEM

The hydraulic fracturing test considered in this research was performed in the Evie member of the Horn River basin located in western Canada (Chou, Gao, and Somerwil, 2011). The Horn River basin is in the strike-slip stress regime (Roche and Baan, 2017). Consequently, the developed hydraulic fracture is vertical normal to the minimum horizontal stress. A 400×400 m horizontal cross section of the formation is simulated. This two-dimensional model represents a simplified domain where the far-field stresses are the maximum horizontal σ_H and the minimum horizontal σ_h stresses. Since the fracture length/radius is greater than its height (Chou, Gao, and Somerwil, 2011), this two-dimensional representation with a classic Perkins–Kern–Nordgren (PKN) fracture model (Adachi et al., 2007) is appropriate. Grid/model dimensions (Fig. 2.47(a)) are determined such that the 400×400 m domain includes the farthest recorded microseismic events in the σ_H-σ_h plane.

Figure 2.47 shows the setup of the two-dimensional computational grid used in this study. Fluid injection is modelled as a point source at an internal node. The mesh is intensively refined with 0.8 m elements in a area of 200×200 m around the injection point. Away from the zone of the intensive refinement, element size is gradually increased to 5.0 m. Medium parameters were assigned following a hydraulic fracturing program in the Horn River basin. Based on overburden density values, the minimum horizontal stress at the injection depth (2980 m) is $\sigma_h = -60$ MPa, while the maximum horizontal stress is $\sigma_H = -75$ MPa (Chou, Gao, and Somerwil, 2011). The initial reservoir pore pressure is 33.9 MPa (Rogers et al., 2010) and the rock permeability is 10^{-19} m^2 (Reynolds and Munn, 2010). This exceptionally low permeability value means that the formation can be treated as impermeable for the timeframe of the simulations (2.7 hr), such that flow is restricted to fractures. The injection rate used in simulations is $Q = 1.4$ l/s. This numerical injection rate is smaller than the value applied in field (0.167 m^3/s). However, considering

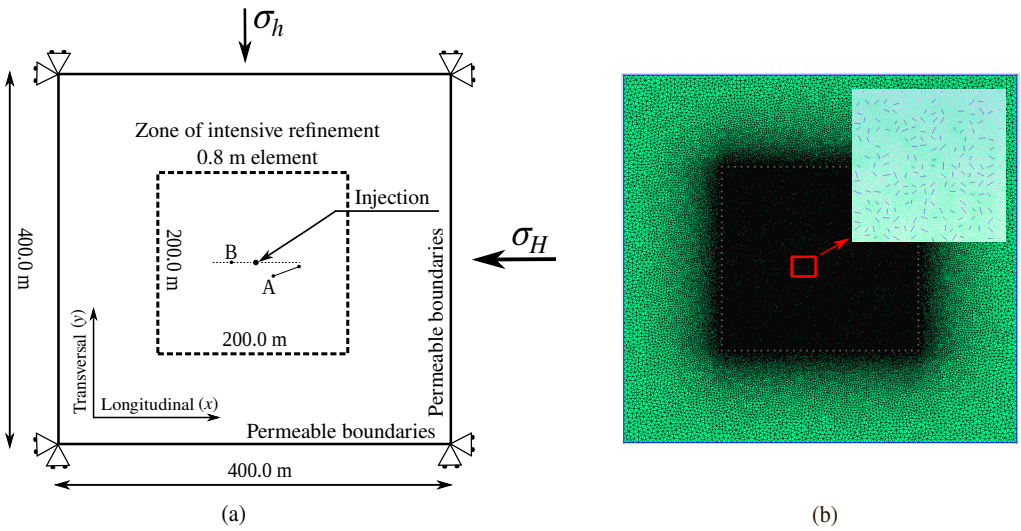

FIGURE 2.47: (a) The geometry and boundary conditions of domain chosen for the hydraulic fracturing simulations and induced seismicity. (b) Triangular Delaunay meshing of the domain showing refinement of element size approaching the wellbore: A zoom-in is displayed to show the random distribution of preexisting joints. Points A and B are displayed to investigate the loading paths during the fracturing process.

that the 3-D geometry is simplified and that no fluid loss/leakof is accounted for, this numerical injection rate is sufficient to insure stable calculations and to reproduce the field injection history (Fig. 2.48(a)).

Chou, Gao, and Somerwil (2011) reported on material and fluid properties pertaining to the rock formation of interest here, namely the Evie member of the Devonian Horn River formation (Table 2.4).

TABLE 2.4: Fluid and material properties pertaining to the porous medium of the Evie formation (Chou, Gao, and Somerwil, 2011). Fracture energy values and computational parameters are calibrated based on the recommendations of Lisjak, Grasselli, and Vietor (2014), Mahabadi et al. (2012), and Tatone and Grasselli (2015)

Nature	Parameter	Value	Unit
Elasticity	Drained Young's modulus E	24.5	GPa
	Drained Poisson's ratio ν	0.2	-
	Rock density ρ_σ	2400	kg/m^3
Fracture	Tensile strength σ_T	5.2	MPa
	Cohesion c	13.5	MPa
	Mode I fracture energy G_{Ic}	10	N/m
	Mode II fracture energy G_{IIc}	100	N/m
	Material internal friction angle ϕ_i	35.0	(°)
	Fracture friction angle ϕ_f	35.0	(°)
Fluid flow	Dynamic viscosity μ	3×10^{-3}	Pa s
	Permeability k	10^{-19}	m^2
	Compressibility K_λ	2.2	GPa
Computational	Damping coefficient η	12.3×10^6	kg/m/s
	Normal contact penalty p_n	245	GPa m
	Shear contact penalty p_t	24.5	GPa m
	Fracture penalty p_f	122.5	GPa m

The smallest element size of 0.8 m is used to avoid mesh sensitivity. Fracture energy values (Tatone and Grasselli, 2015) along with this element size are sufficient to reproduce the breakdown pressure and post-peak behavior of Fig. 2.48(a). The computational parameters (Table 2.4) are calibrated based on the recommendations of Lisjak, Grasselli, and Vietor (2014), Mahabadi et al. (2012), and Tatone and Grasselli (2015). The penalty coefficients, p_n, p_t, p_f are

set equal to $10\times$, $1\times$, and $5 \times E$, respectively. These are the largest possible values that ensured elastic response and did not necessitate a reduction in the time step size. The damping coefficient η should be larger than $0.01\eta_c$ with η_c being the critical viscous damping coefficient $\eta_c = 2h\sqrt{E\rho_\sigma}$ (Munjiza, 2004), and h the element size. For $\eta > 0.01\eta_c$, the high-frequency waves are suppressed and the resulting stress-strain curves mimic those obtained in the quasi-static laboratory tests. In these simulations, η is set equal to η_c.

A set of normally distributed joints with an average length of 1.60 m, random variation of 0.4 m, and fracture density of $0.1/\text{m}^2/\text{m}$ is created in the zone of intensive refinement (Fig. 2.47(b)). These joints are introduced in the model before meshing and they replace the cohesive fracture elements for their length and can be assigned specific hydraulic, elastic, and cohesive/friction properties. The Gmsh code is used to generate the Delaunay triangulation. In this study, joints are assigned the same hydraulic properties as the rock medium; however, they are given zero tensile strength and can only sustain shear stresses due to residual friction only (Eq. 2.49). Consequently, joints are inserted in the model to explore the distribution of microseismic events due to shear-slip induced by mechanical deformation of the medium during the growth of hydraulic fractures (AbuAisha et al., 2017). The size distribution of the joints is based on previous studies in this area (Eaton et al., 2014), whereas joint orientation is random. The maximum shear stress on these joints is determined from the Mohr-Coulomb criterion, expressed in terms of the residual/fracture friction ϕ_f angle and the normal effective stress $\sigma_n^{'}$,

$$f_r = -\sigma_n^{'} \tan(\phi_f), \tag{2.49}$$

where f_r is the maximum shear stress. As joints represent planes of weakness, while hydraulic fracture is growing, medium mechanical deformation affects the stress state on the joint tips. Depending on their random orientations, some joints are more favorable to shear-slip, and their slip gives rise to microseismic events. Fluid flow within the growing hydraulic fracture system is controlled by Darcy's law. Points A and B (Fig. 2.47(a)), at radial distances of 29.5 m and 15 m from the injection point, are recorder nodes to investigate the stress loading paths due to modes I and II of failure. Point A represents a critically stressed joint tip that fails due to mechanical deformation created by fracture growth (mode II failure). Point B is on the fracture trajectory and fails in response to a fluid pressure increase (opening/mode I).

2.2.2.1 Comparison with field data

In this section, simulations are compared with the field example from the Evie formation of the Horn River basin. As expected, simulations generated an approximately bi-wing hydraulic fracture, growing in the direction of the maximum far-field horizontal stress σ_H and perpendicular to the minimum horizontal stress σ_h. Figure 2.48(a) shows that the simulated injection pressure provides a good match to the subsurface injection pressure values. Under a constant rate of injection, the injection pressure increases until the breakdown condition is achieved. Injection pressure then gradually drops to the fracture propagation pressure equal to the minimum far-field horizontal stress (Yew and Weng, 2014).

During the numerical simulation, the calculated fracture length is determined at each time step (fracture envelope). Figure 2.48(b) shows the spatio-temporal migration of observed microseismicity, indicated by black dots, compared with the growth of the hydraulic fracture (red line). Although microseismic activity is characterized by discontinuous rates, possibly due to episodic growth of the hydraulic fracture system in the field (Boroumand and Eaton, 2015), for the most part, the fracture envelope provides an approximation to the triggering front in the sense that the time-distance locations for the majority of microseismic events plot below the curve. This relationship provides validation for the numerical approach, since the smallest element size, fracture energies, and computational parameters are calibrated to history

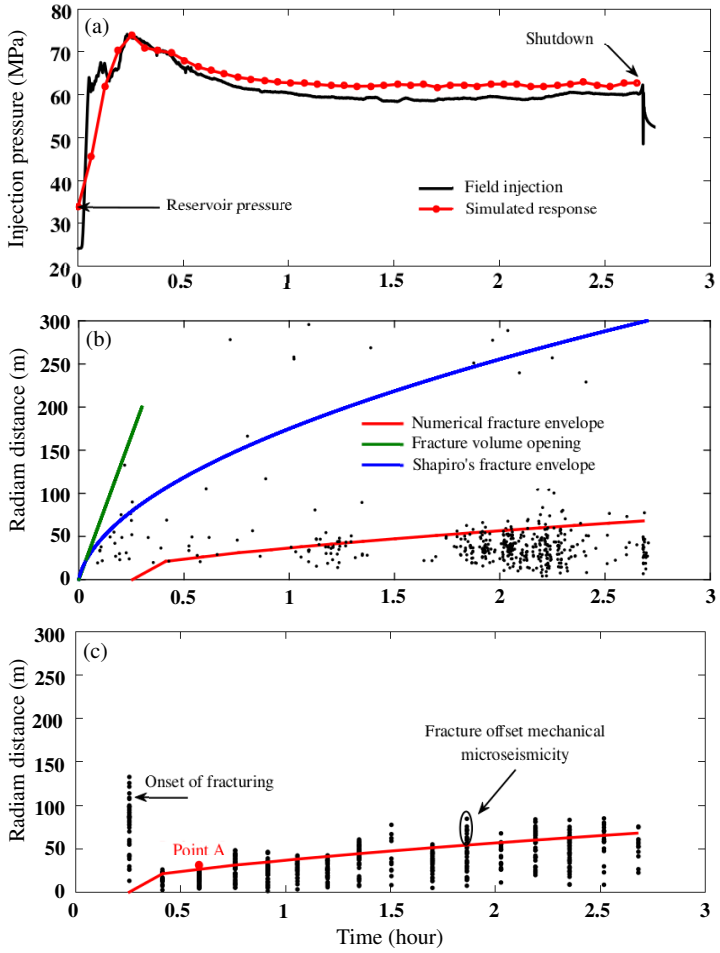

FIGURE 2.48: (a) Irazu numerical injection response correlated to the field injection history until shutdown (2.7 hr). (b) Spatio-temporal migration of the field microseismicity including the fracture envelope derived from simulations (red line), a best-fitting fracture triggering envelope (Shapiro et al. 2006) (blue line) for $\ell_f = 300$ m, and the fracture volume opening curve (Dinske et al. 2010) (green line). (c) Radial distribution of simulated microseismic events with time along with the calculated numerical fracture envelope highlighted in Fig. 2.48(b).

match the injection pressure profile rather than the time-distance behavior of the microseismicity (AbuAisha et al., 2019). Shapiro and Dinske (2009b) and coworkers Shapiro and Dinske (2009a), Shapiro, Dinske, and Rothert (2006), and Shapiro et al. (2002) suggested that the evolution of a hydraulic fracture can be treated as an end-member of a diffusional triggering front. To compare the current fracturing-microseismicity signatures with Shapiro's work, a simplified classic two-dimensional fracture geometry of a PKN fracture model is adopted (Fig. 2.49). The use of this model is appropriate since the fracture length/radius is bigger than its height and that it propagates in the rock section where the extent and concentration of microseismicity is significant (σ_H-σ_h plane) (Reynolds and Munn, 2010).

To investigate the dynamical behavior of induced microseismicity due to fracture growth, Shapiro, Dinske, and Rothert (2006) applied an approximation of the fracture growth based on the principle of volume balance, where the fracture radius ℓ is expressed in terms of injection time t,

$$\ell(t) = \frac{Q_i t}{4h_f C_L \sqrt{2t} + 2h_f w} \tag{2.50}$$

with Q_i being the injection flow rate, h_f the perforated section of the treatment well (Fig. 2.49), w

the fracture aperture, and C_L the fluid loss coefficient. Dinske and T. (2010) suggested that fluid loss overdominates fracture geometry effects over the long-term limit of injection; therefore, Eq. 2.50 reduces to the typical linear pressure diffusional front characterized by the apparent diffusivity $\mathcal{D}$, i.e. $\ell(t) = \sqrt{4\pi\mathcal{D}t}$ (Shapiro et al., 2002).

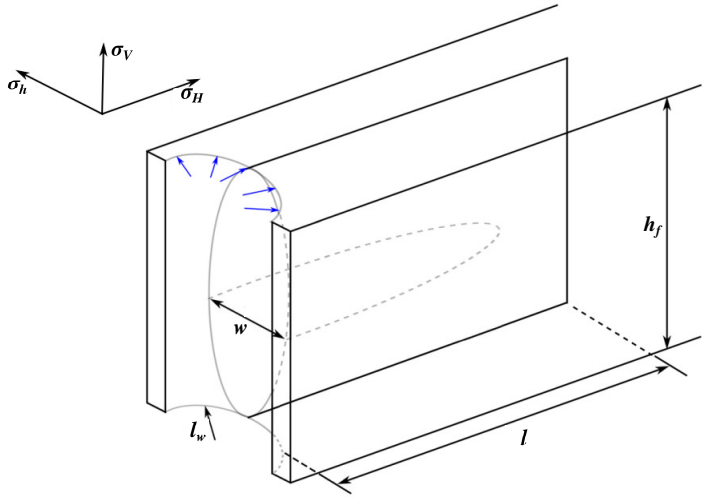

FIGURE 2.49: Schematic diagram demonstrating the PKN fracture geometry adopted in this research. w is the fracture aperture, ℓ the fracture radius, ℓ_w is the borehole radius, and h_f is the perforated section of the treatment well.

Consequently, Dinske and T. (2010) and Shapiro, Dinske, and Rothert (2006) relate the fluid loss coefficient to the apparent diffusivity that best-fits the fracture triggering front (Eq. 2.50) as,

$$C_L = \frac{Q_i}{8h_f\sqrt{2\pi\mathcal{D}}}. \tag{2.51}$$

The fluid loss coefficient can be also calculated using the fracture radius and the fracture cross-sectional area $\mathcal{A}$,

$$C_L = \frac{Q_i t - 2\ell\mathcal{A}}{4\ell h_f\sqrt{2t}}. \tag{2.52}$$

The fracture cross-sectional area is calculated by measuring the slope of the line tangent to the seismic events at time $t = 0$ (Fig. 2.48(b): fracture volume opening curve) (Dinske and T., 2010; Shapiro, Dinske, and Rothert, 2006), in this case $\mathcal{A} = 0.1853\ \mathrm{m}^2$. For a well-perforated section of length $h_f = 30$ m (Reynolds and Munn, 2010), the fracture aperture is $w = \mathcal{A}/h_f = 6.2$ mm. The numerical fracture aperture calculated by simulations is 6.6 mm. The maximum fracture opening is set to $a_u = 10$ mm; hence, the numerical aperture is still smaller than the upper limit. While considering the field injection rate ($Q_i = 0.167\ \mathrm{m}^3/\mathrm{s}$), the best-fitting of Shapiro's fracture triggering front (Eq. 2.50) and Fig. 2.48(b), blue curve), tangent to the fracture volume curve and encompassing almost all of the seismic events, is chosen for a final fracture radius $\ell_f = 300$ m, corresponding to the farthest microseismic event. In this case, an apparent diffusivity $\mathcal{D} = 0.86\ \mathrm{m}^2/\mathrm{s}$ is sufficient to match this fracture triggering front. Based on Eq. 2.51, the corresponding fluid loss coefficient is $1.13 \times 10^{-4}\ \mathrm{m}/\sqrt{\mathrm{s}}$. Dinske and T. (2010) also suggested an approach to calculate the initial reservoir permeability using the fluid loss coefficient and some typical values of the hydrocarbon in the targeted reservoir. If the hydrocarbon in the targeted shale at the Evie formation has the same properties as in the Cotton Valley tight gas reservoir (Dinske and T., 2010) (considering that the initial reservoir pressure in both locations is ~30 MPa and that the operational depth goes to ~2800 m), the following hydrocarbon properties can be assumed: dynamic viscosity $\mu = 0.03$ cP; compressibility $\chi_{T\lambda} = 3.5 \times 10^{-8}\ 1/\mathrm{Pa}$;

porosity $n_\lambda = 0.1$; and pressure difference[7] $\Delta p = 40.1$ MPa. These properties and operational conditions give an initial reservoir permeability of 2.1×10^{-19} m^2 , almost equal to the values attributed to the Evie formation shale (Reynolds and Munn, 2010).

Considering the numerical fracture envelope as a triggering front (Fig. 2.48(b), red curve), some of the observed microseismicity plots well out-side the bounds of the fracture envelope. In particular, at the onset of hydraulic fracturing at ∼0.25 hr, a cluster of microseismic events occurred up to a distance of ∼125 m from the injection location. These events are thought to occur due to the mechanical deformation of the medium/the stress wave spreading in the formation at the breakdown. Fig. 2.48(c) shows the time-distance behavior of simulated microseismicity in relation to the fracture envelope. The apparent discrete occurrence times of these events is an artifact of the numerical procedure, wherein snapshots of the simulation outputs are stored at discrete time intervals to conserve disk space. In a similar fashion to the observed pattern of field microseismicity, it is seen that the computed fracture envelope represents an approximate triggering front with the conspicuous exception of a cluster of events at the onset of fracturing to a radial distance of ∼125 m from the injection point. The events in this cluster are initiated by exceeding the Mohr-Coulomb criterion (Eq. 2.49) on the preexisting fractures/joints, due to stress changes in the medium induced by the hydraulic fracture. The similarity of these events to the early cluster of microseismicity in the observed field dataset suggests that the early cluster has the same cause (i.e. stress changes arising from the breakdown energy spreading in the medium). To see if Shapiro's envelope (Eq. 2.50) can reproduce the numerical fracture envelope, the fluid loss coefficient for the numerical fracture radius at the end of the simulation ($\ell_f = 68$ m), for the field injection rate (0.167 m^3/s), and for $t = 2.7$ hr (treatment time) is calculated, i.e. $C_L = 1.405 \times 10^{-3}$ m$/\sqrt{\text{s}}$. Implementing this value in Eq. 2.50 gives the blue curve in Fig. 2.50 shown below.

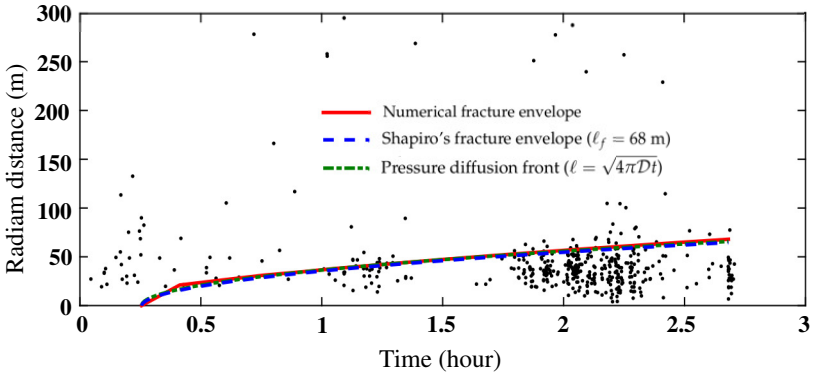

FIGURE 2.50: Spatio-temporal migration of the field microseismicity including the fracture envelope derived from simulations (red solid), Shapiro's fracture triggering envelope (blue dashed line) for $\ell_f = 68$ m, and the linear diffusion front (green dotted line).

Figure 2.50 also shows the linear diffusional front based on the apparent diffusivity calculated by Eq. 2.51, which is identical to Shapiro's fracture envelope. Though identifying triggering fronts from seismic data is far from trivial, these diffusional or non-diffusional envelope techniques compare to each other and can give information on the fluid-driven fracture geometry (ℓ and w), local stress regime, as well as on the fractured reservoir permeability and fracture conductivity (Dinske and T., 2010). The current numerical FDEM approach confirmed the validity of the diffusional envelope technique. However, it is further concluded that in impermeable media, a non-diffusive envelope, i.e., only related to the fracture geometry, can be precisely predicted by Shapiro's fracture envelope, provided that the fracture radius at the end of the treatment is known. It is also concluded that an envelope that encompasses most of the

[7]The pressure difference is calculated considering the initial reservoir pressure 33.9 MPa and the breakdown pressure 74 MPa (Fig. 2.48(a)).

radial distribution of field seismicity, and that excludes the cluster at the onset of fracturing, can give a good approximation of fluid-driven fracture radius in tight gas reservoirs.

2.2.2.2 Loading paths in the FDEM

This section aims at explaining the modes I and II of failure associated with the FDEM approach by investigating the loading paths of the two points, A and B (Fig. 2.47(a)), during the hydraulic fracturing process. Figure 2.51(a) shows the *m-s* loading paths for these two points: the joint-tip point A at a radial distance of 29.5 m and reflex orientation of 218.82° (Figs 2.47(a) and Fig. 2.48(c)) and point B at a radial distance of 15 m on the bi-wing fracture trajectory (Fig. 2.47(a)). The quantities m and s are defined as the mean of the effective principal stress tensor ($m = (\sigma_1^{'} + \sigma_2^{'})/2$) and the magnitude of the deviatoric effective principal stress tensor ($s = |\sigma_1^{'} - \sigma_2^{'}|/2$). The failure envelope (Eq. 2.49) can be expressed in terms of m and s (Fig. 2.51(a)).

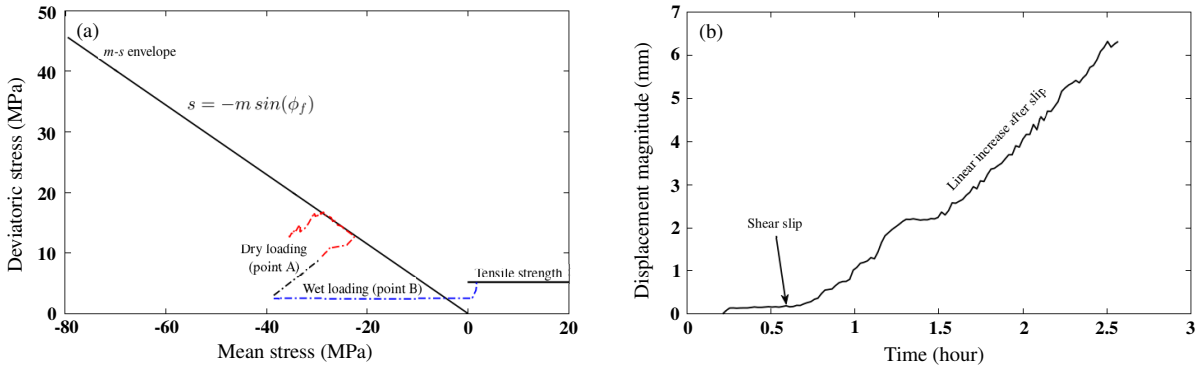

FIGURE 2.51: (a) *m-s* loading paths for two points: point A (Figs 2.47(a) and Fig. 2.48(c)) presented by dotted black and red line (shear-slip, mode II failure); and point B (Fig. 2.47(a)) on the fracture trajectory presented by dotted blue line (tensile mode I failure). (b) Displacement magnitude history at point A: the figure shows sudden increase at the onset of fracturing (∼0.25 hr) followed by slight growth before it starts to increase significantly at shear-slip.

The two loading paths start from the same point/initial effective stress state. As soon as the fluid reaches point B on the fracture trajectory, effective stresses become tensile and the loading path (blue dotted line) moves to touch the tensile failure envelope, which is characterized by mode I failure. However, for point A, and since it is located on a joint tip/weak zone, the dissipation of energy at breakdown reduces (in algebraic sense) the initial effective stress state moving the joint close to failure, which is represented by the first linear change of the dry loading path (black part). The path then continues to grow (red part) until it touches the failure envelope, which is characterized by mode II failure and shear-slip microseismic event. The path then yields to the failure envelope before it starts to show unloading behavior. However, this reduction in initial stresses depends on the orientation of joints, as some orientations, and depending on the anisotropy of the far-field stresses, are more favorable to shear-slip.

The displacement magnitude history at point A exhibits a sudden increase at breakdown (∼0.25 hr), then it continues to grow slightly before it starts to increase considerably at the onset of shear-slip (Fig. 2.51(b)).

2.2.3 Discussion and conclusion

Plotting a radial spatio-temporal distribution of field seismicity during hydraulic fracturing test reveals important dimensional information of the fluid-driven fracture. Such information includes fracture length and aperture, as well as its growth direction which helps understand the stress regime of the rock basin where the test is conducted. Most of the observed field seismicity plot under the bounds of the numerical fracture envelope, except for a cluster of

seismic events at the onset of fracturing. This cluster of seismicity at the onset of fracturing is explained numerically; upon fracture initiation, a stress wave spreads in the medium and causes critically stressed joints (to a certain distance) to slip and give rise to seismic events. These fracturing-onset seismic clusters corresponded to the breakdown peaks of the field injection history.

Chapter 3

Fluid circulation in salt caverns

Renewable energy resources are not dispatchable due to their fluctuating nature. Even-though, some of these resources are controllable, i.e. bioenergy or hydroelectricity, or represent relatively constant sources, i.e. geothermal power, using them on a large scale requires upgrades or even a redesign of the grid infrastructure. Options to absorb large shares of renewable energy into the grid include storage. Gas storage in underground salt caverns is becoming a leading technique (Klumpp, 2016; Caglayan et al., 2020). Such caverns are characterized by their large-scale storage capacities, low investment costs, and low cushion gas requirements (Matos, Carneiro, and Silva, 2019). Nevertheless, the future increasing energy demands necessitate almost daily solicitations of such caverns (AbuAisha and Rouabhi, 2019). Fast charges, mechanical and thermal, are expected to affect the mass exchange rates between the cavern phases. To keep precise tracks/accurate management of the cycled gas quantities, these mass exchanges must be quantified.

Rock salt occurs within sedimentary layers where it has formed from the evaporation of seawater or salty lakes. Rock salt is consequently deposited in cycles which affects its directional properties like the elastic modulus and the permeability. Depending on the location, the rock salt properties, mechanical and hydraulic, differ as well. Solution mining is commonly used to create large caverns in rock salt formations. In this process, a single well, drilled from the ground surface to the targeted depth (Fig. 3.1), is generally used to inject fresh water and withdraw brine through a concentric tubing system, the so called the leaching process (Charnavel, Leca, and Poulain, 1999). Once leaching is completed, the brine in the cavern is reduced to minimal quantities by a debrining phase where it is moved out by a gas injection operation.

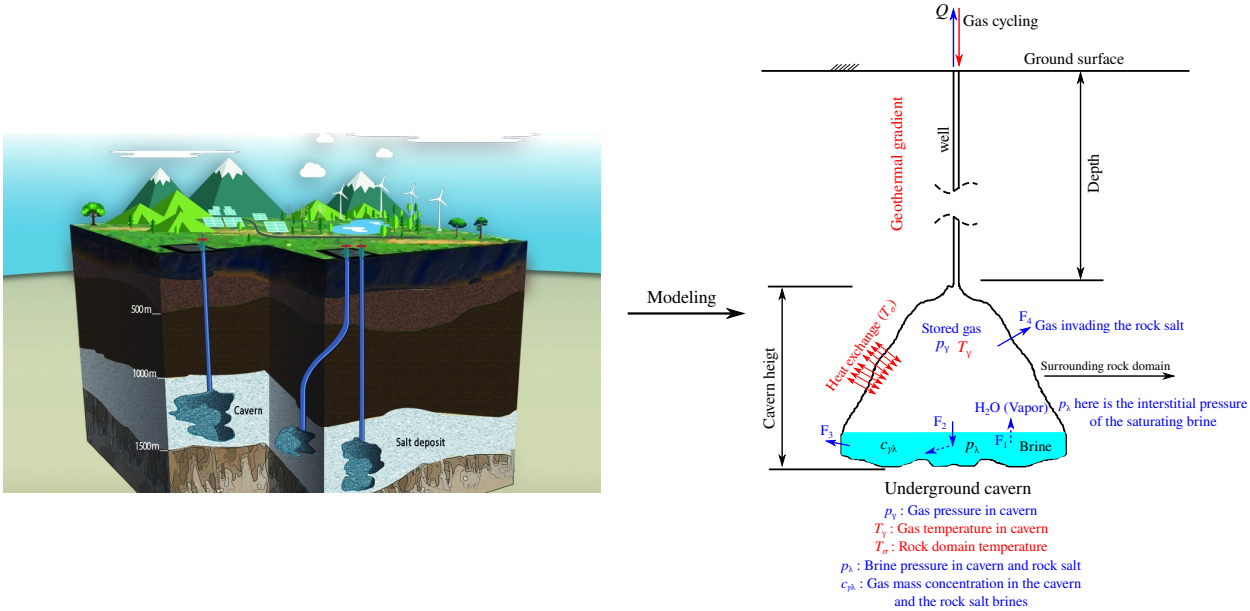

FIGURE 3.1: Schematic representation of gas storage in salt caverns and its mass exchanges between phases.

Figure 3.1 shows an underground cavern filled with gas at a certain pressure and is exchanging heat with the surrounding rock domain. The figure also depicts the amount of brine left in the cavern at the end of the debrining process. Gas within the cavern is expected to experience cycles of pressure and temperature changes according to the intended usage. During its lifetime, the cavern mainly contains, simultaneously or sequentially, two different immiscible phases: the stored humid gas and the brine. The third important phase of this storage outline is the surrounding rock salt domain. This domain is constituted of the salt mass which itself is a mixture of grains or crystals of halite and brine occupying the inter-grain spaces or present in the grains in the form of fluid inclusions. Each of the three phases is characterized by state variables which are for the humid gas: pressure, temperature, and vapor concentration; for the brine: pressure, temperature, concentration of salt and concentration of dissolved gas; and for the rock salt: stress, temperature, and interstitial fluid-phase pressures.

While the cavern is operated, the three phases are interacting as follows (Fig. 3.1): water is evaporating into the stored gas (F_1); stored gas is dissolving in the brine (F_2); brine at the cavern bottom is flowing into the rock salt (F_3); and stored gas is percolating and diffusing into the porous rock salt (F_4).

As stated earlier, in the context of energy transition gas stored within salt caverns is expected to experience fast cycles of injection and withdrawal. This chapter starts by investigating the homogeneity of the stored gas thermodynamic state during fast cycling. This investigation helps building a modelling paradigm that can be used to conduct subsequent studies concerning mass exchanges between the cavern phases.

3.1 Uniformity of the gas thermodynamic state during cycling

The rate of injected or withdrawn mass to/from caverns controls the spatial heterogeneities of the temperature and pressure fields. It also controls the magnitude of gas velocity which represents the driving force for the convective heat transfer with the surrounding rock domain. In order to consider as many industrial concerns during cycling as possible (for instance rock creep and gas percolation into the surrounding rock salt), researchers tend to simplify the cavern thermodynamic problem by neglecting the spatial variations of pressure and temperature which leads to a cavern uniform state. This reduces tremendously the simulation cost, yet it raises up a question about the validity of such assumption during fast cycling, when spatial variations of temperature and pressure are significant. The miscalculation of these variations leads to a miscalculation of the gas density field in the cavern, and consequently, for a given cavern volume, a misestimation of the stored gas mass.

To address this concern, two types of simulations are performed: simplified simulations using an in-house code where a uniform thermodynamic state is assumed within the cavern; and a Computational Fluid Dynamics (CFD) simulations using the COMSOL software. The goal is to compare the simplified simulation results with the complete simulations of COMSOL, where all complexities of the problem are considered, i.e. full mesh refinement, velocity field, convective heat transfer, and the turbulent flow modeling. The simulation results are compared for both slow (seasonal) and fast (daily) cycling where one expects a better match with regard to slow cycling and a more obvious deviation in case of fast solicitations. In both simulations the cavern is assumed full of gas with no brine or insoluble material, and only thermal conduction with the surrounding rock domain is considered.

3.1.1 Thermodynamics of gas stored in salt caverns

This section provides the mathematical problems of the simplified and the complete approaches to solve for the evolution of stored gas thermodynamics.

3.1.1.1 Complete solution of cavern thermodynamics

Injecting or withdrawing gas to/from caverns applies changes to the gas mass density ρ, velocity $\boldsymbol{v}$, and temperature T. The developments of these three fields are calculated using the general balance laws:

$$\begin{array}{lrcl} \text{mass balance:} & \dot{\rho} + \rho \boldsymbol{\nabla} \cdot \boldsymbol{v} & = & 0; \\ \text{momentum balance:} & \rho\, \dot{\boldsymbol{v}} - \boldsymbol{\nabla} \cdot \underline{\underline{\boldsymbol{\sigma}}} & = & \rho \mathfrak{g}; \\ \text{energy balance:} & \rho\, \dot{u} + \boldsymbol{\nabla} \cdot \boldsymbol{\psi} & = & \underline{\underline{\boldsymbol{\sigma}}} : \underline{\underline{\boldsymbol{\nabla}}} \boldsymbol{v}, \end{array} \tag{3.1}$$

where $\underline{\underline{\boldsymbol{\sigma}}}$ is the fluid stress tensor, $\mathfrak{g}$ is the gravitational acceleration vector, u is the specific internal energy, and $\boldsymbol{\psi}$ is the fluid heat flux. The designation of the phase subscript α is removed as the cavern is filled with a mono-component single-phase gas.

Stokes law is used to calculate the stress tensor in a moving fluid undergoing external effects,

$$\underline{\underline{\boldsymbol{\sigma}}} = 2\mu \underline{\underline{\boldsymbol{\mathcal{E}}}}^{d} - p \underline{\underline{\boldsymbol{\delta}}}, \tag{3.2}$$

where μ is the fluid dynamic viscosity, and $\underline{\underline{\boldsymbol{\mathcal{E}}}}^{d}$ is the deviatoric part of the rate of strain tensor $\underline{\underline{\boldsymbol{\mathcal{E}}}} = (1/2)\left(\underline{\underline{\boldsymbol{\nabla}}} \boldsymbol{v} + \underline{\underline{\boldsymbol{\nabla}}} \boldsymbol{v}^{\mathrm{T}}\right)$. Fourier's law is used to describe the relation between heat flux $\boldsymbol{\psi}$ and the temperature gradient $\boldsymbol{\nabla} T$ through the fluid effective thermal conductivity Λ,

$$\boldsymbol{\psi} = -\Lambda \boldsymbol{\nabla} T. \tag{3.3}$$

The fluid state equation can be completely described using two state functions; the mass density $\rho(p,\, T)$, and the heat capacity $C_p(T)$ at a given pressure. The thermodynamic variables are related to each other through the formula $p = \rho T Z$, with Z being the gas compressibility factor. Common examples are when fluid density is assumed constant in case of incompressible fluids, and when $Z = R/M_w$ in case of ideal gases, with M_w being the gas molecular weight and R the universal gas constant. In case of high pressure and low temperature, the assumption of ideal gas is weak and a real gas behavior needs to be considered.

For the relatively short-period simulations (2 months maximum) considered in this work, the mechanical behavior of the rock mass around the cavern is neglected (Labaune et al., 2019); only the thermal interaction between rock and fluid are accounted for. For a time-dependent problem, the temperature field in the surrounding rock mass verifies the following form of the heat equation,

$$\rho_\sigma C_{p\sigma} \partial_t T_\sigma = \Lambda_\sigma \boldsymbol{\nabla} \cdot (\boldsymbol{\nabla} T_\sigma), \tag{3.4}$$

with T_σ being the rock temperature, ρ_σ its density, $C_{p\sigma}$ its heat capacity, and Λ_σ its thermal conductivity.

The non-dimensional numbers of Rayleigh, Reynolds, and Péclet are needed to have an idea about the heat convection regime of cycled gas in the cavern. Most of the underground cavern operations exhibit high Reynolds Re $\sim 10^6$ and Rayleigh Ra $\sim 10^{15}$ numbers (Karimi-Jafari, 2010), which necessitates the integration of a fluid flow turbulent model to solve for velocity disturbances. When the Péclet number is large (Pe > 1), stabilization techniques are required to smooth the spurious instabilities attributed to the convection term in the energy equation (AbuAisha and Loret, 2016b).

Evolution of the thermodynamic state of the gas stored in underground caverns can be solved for by applying the finite element method on the system of Eqs 3.1 along with the proper initial and boundary conditions. However the following points need to be considered:

1. the spatial discretization should be precise and fine enough to describe properly the distribution of the velocity field;

2. adequate mesh refinement must be adopted at the solid-gas interface to account for the convective heat transfer;

3. a turbulent flow model is needed (the k-ϵ for this study) which adds another two variables, namely k and ϵ, to the list of unknowns (AbuAisha and Rouabhi, 2019).

This complete physical model with all related complexities of mesh refinement, spatial variations, convective heat transfer, and turbulent flow is validated in AbuAisha and Rouabhi (2019).

3.1.1.2 Simplified solution of cavern thermodynamics

Underground caverns have large geometries and they are utilized over long periods of time. This renders the complete CFD simulations of gas cycling over their lifetime a tremendous if not a prohibitive task. Since in most cases, underground storage necessitates seasonal/slow cycling, scientists assume that the cavern spatial variations of pressure and temperature are negligible in the main part of the cavern volume (Guo et al., 2017). Henceforth, they apply the concept of a heat transfer coefficient h_c to account for solid-gas heat exchange over the cavern surface,

$$h_c = \frac{\text{Normal thermal conduction at the solid wall}}{\text{Temperature difference between solid and gas}} = \frac{\boldsymbol{\psi} \cdot \boldsymbol{n}}{T_\sigma - T}, \tag{3.5}$$

with $\boldsymbol{n}$ being the cavern inward normal vector and T the gas temperature passing by the wall. Estimation of this coefficient is tedious, however, once *in situ* data is available, it can be precisely predicted (Raju and Khaitan, 2012). In this research, a solid-gas temperature continuity over the cavern surface is assumed. However, the well heat transfer coefficient h_w is calculated using empirical laws, as seen below.

Concerning the cavern well, the velocity and thermodynamic variables are functions of time t and the curvilinear abscissa x along the well axis, i.e. $v(x,t)$, $T(x,t)$, and $p(x,t)$. For this case, the system of Eqs 3.1 becomes:

$$\begin{aligned} \rho\dot{v} - v' &= 0; \\ \rho\dot{v} + p' &= \rho\boldsymbol{g}\cdot\boldsymbol{t} + (L_\zeta/\mathcal{A})\zeta_w; \\ \rho(\dot{u} + p\dot{v}) &= (L_w/\mathcal{A})\psi_w - v(L_\zeta/\mathcal{A})\zeta_w, \end{aligned} \tag{3.6}$$

where the prime denotes the variable derivative along the well axis, $\mathcal{A}$ is the flow cross sectional area, $\boldsymbol{t}$ is the vector tangent to the pipe wall, L_ζ is the well circumference available for fluid flow, and L_w is the well circumference available for heat transfer. These two circumferences are equal in case of simple pipe flow. ψ_w is the heat exchange across the pipe wall, and ζ_w is the friction stress. The quantities ψ_w and ζ_w are usually given by empirical laws (Kaviany, 2002). The stress ζ_w is generally expressed as $\zeta_w = -C_f\rho v|v|/2$. The term ψ_w implies the heat flux across the pipe wall, it can be expressed using the Newton's law as $\psi_w = h_w(T_\sigma - T)$. The following relations are adopted to calculate the empirical coefficients,

$$\begin{aligned} C_f &= 2\Big((8/\mathrm{Re})^{12} + (\mathrm{A}+\mathrm{B})^{-3/2}\Big)^{1/12}, \quad \text{with,} \\ A &= \left(-2.457\,\ln\Big((7/\mathrm{Re})^{0.9} + 0.27(\varepsilon L_\zeta/D_H)\Big)\right), \quad \text{and,} \quad B = (37530/\mathrm{Re})^{16}, \end{aligned} \tag{3.7}$$

and,

$$\begin{aligned} \mathrm{Nu} &= 3.66 \quad \text{for} \quad \mathrm{Re} \leq 2300, \quad \text{and,} \\ \mathrm{Nu} &= (C_f/2)(\mathrm{Re}-1000)\mathrm{Pr}/\Big(1 + 12.7\sqrt{C_f/2}(\mathrm{Pr}^{2/3}-1)\Big) \\ &\quad \text{for} \quad 2300 < \mathrm{Re} < 5\times10^6, \quad \text{and,} \quad 0.5 < \mathrm{Pr} < 2000, \end{aligned} \tag{3.8}$$

where ε is the wall roughness, $D_H = 4\mathcal{A}/L_\zeta$ is the hydraulic diameter, Nu is the Nusselt number, $\mathrm{Pr} = \mu C_p/\Lambda$ is the Prandtl number. The pipe Reynolds number takes the form $\mathrm{Re} = \rho\, v\, D_H/\mu$. The well heat transfer coefficient is expressed in terms of the Nusselt number as $h_w = \Lambda\,\mathrm{Nu}/D_T$, with $D_T = 4\mathcal{A}/L_w$ being the thermal diameter.

The problem is fully coupled in the sense that if the well variables are known, they can be used to determine the unknown parts of the boundary conditions of the cavern and the formation. Using these boundary conditions, the problem in the latest domains can be solved leading to new data that can be put for a next time step solution. With regard to the cavern itself, assuming a uniform thermodynamic state simplifies the system of Eqs 3.1 to:

$$\begin{aligned} Q_e/\mathcal{M} &= -\chi_p \dot{T} + \chi_T \dot{p}; \\ \mathcal{M} C_p \dot{T} - \mathcal{V}\chi_p T \dot{p} &= Q_e^+ (h_t^w - h^c) + \Psi, \end{aligned} \tag{3.9}$$

where $\mathcal{M}$ is the gas mass, $\chi_p = -\nu \partial_T \rho|_p$ is the isobaric volumetric thermal expansion coefficient, $\chi_T = \nu\, \partial_p \rho|_T$ is the isothermal compressibility coefficient, $\mathcal{V}$ is the cavern volume (assumed constant), $h_t^w = h^w + \boldsymbol{v}\cdot\boldsymbol{v}/2$ is the well dynamic/total specific enthalpy, h^c is the cavern specific enthalpy, Q_e is well/external flow rate, Q_e^+ is the positive/injection part of Q_e, and $\Psi = \int_S \boldsymbol{\psi}\cdot\boldsymbol{n}\, d\mathcal{A}$ is the power exchanged between gas and surrounding rock. With the assumption of solid-gas temperature continuity over the cavern surface, this power exchange is calculated using the Fourier conduction equation in the rock formation side.

The assumption of a uniform thermodynamic state leads to considerable simplifications to the mathematical problem. Considering that the time derivatives do not account for convective terms any more, and that the main variables are only functions of time, the system of Eqs 3.9 represents a system of ordinary differential equations of $p(t)$ and $T(t)$. The complexities left stem from the necessity to model a real gas behavior (when necessary and appropriate), and the discretization needed in the rock domain to solve for Eq. 3.4. However, since the cavern thermodynamic behavior is now assumed uniform in its domain (single point behavior), the surrounding rock mass is discretized into finite elements and heat conduction is assumed one-dimensional.

3.1.2 Simulations at the cavern scale

The boundary value problem represents a spherical cavern of volume $\mathcal{V} = 300{,}000\ \mathrm{m}^3$ in a surrounding rock domain. The well extends from the surface at $z = 0$ m to the cavern at $z = z_w = -910$ m. The initial cavern volume averaged temperature and pressure are 40 °C and 22 MPa respectively (Fig. 3.2). Gas is injected at $T = 40$ °C following the program shown in Fig. 3.3. The gas used in the simulations is ideal hydrogen[1] and the cavern is assumed initially full with mass $\mathcal{M}(0) = 4.52 \times 10^6$ kg.

Figure 3.3 shows the injection schemes considered in the simulations in terms of the relative mass change $\tilde{\mathcal{M}} = (\mathcal{M}/\mathcal{M}(0) - 1) \times 100\%$. The first scheme represents fast/daily cycling where the cavern is utilized extensively, and one cycle (4.5 days) leads to a relative mass change in the range [-69% to -29%]. Second scheme represents slow/seasonal cycling utilization where the cavern experiences the same relative mass change, yet over a period of 58.5 days. There are periods of standstill/rest/pause after injection and withdrawal that are marked by constant relative mass change over time. Simulations are run for 60 days to allow for the investigation of thermal exchange between the gas in the cavern and the surrounding rock mass. Points p_1 of withdrawal at ($t = 6.332, \tilde{\mathcal{M}} = -57.6$), p_2 of injection at ($t = 25.87, \tilde{\mathcal{M}} = -51.73$), and p_3 of

[1] The assumption of ideal gas simplifies calculations.

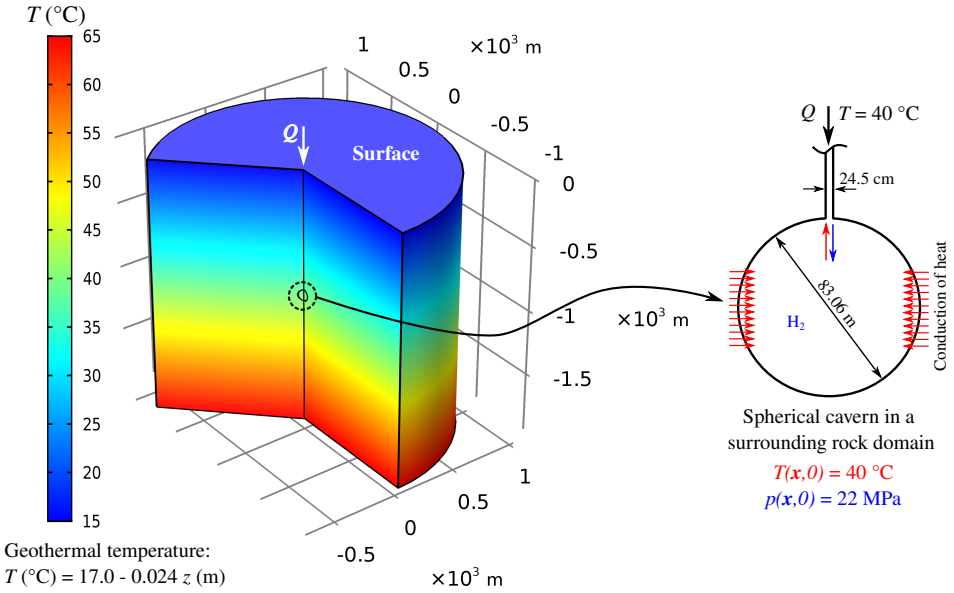

FIGURE 3.2: Schematic diagram of the boundary value problem: it represents a spherical cavern created at depth 910 m in a surrounding rock domain. The geothermal gradient causes a cavern volume averaged temperature of 40 °C. The cavern is assumed initially full of ideal hydrogen with mass $\mathcal{M}(0) = 4.52 \times 10^6$ kg at $p(\boldsymbol{x}, 0) = 22$ MPa.

pause at ($t = 35.66, \tilde{\mathcal{M}} = -29.03$) are displayed on the figure where velocity and temperature profiles analyzed in the upcoming arguments.

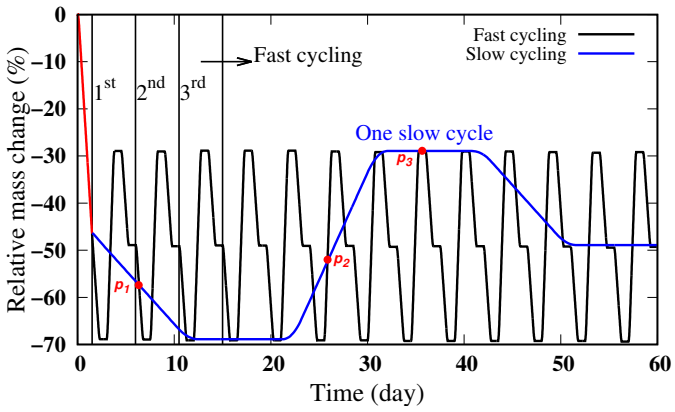

FIGURE 3.3: Two cycling schemes to run the cavern: fast/daily cycling that leads to a relative mass change of [-69% to -29%] in 4.5 days; and slow/seasonal cycling where the cavern experiences the same mass changes yet over a period of 58.5 days. Points p_1 of withdrawal, p_2 of injection, and p_3 of pause, are displayed on the figure to investigate velocity and temperature profiles in the upcoming discussions.

The gas cycling in the spherical cavern is simulated using the simplified approach and the COMSOL/complete approach, and results of the two simulations are correlated for fast and slow cycling. For the complete simulations, the boundary conditions are set as shown in Fig. 3.2. The rock formation far-field temperature boundary conditions are assumed to be of the Dirichlet type, i.e. $T = T_\infty(z)$, with $T_\infty(z)$ being the initial geothermal temperature. In case of the simplified simulations, $T_\infty(z)$ is replaced by its average value over the cavern surface. Gas is injected at $T = 40$ °C following the two schemes of Fig. 3.3. As for the initial conditions, in the complete simulations, the well and cavern are assumed in equilibrium with the surrounding rock $T(\boldsymbol{x}, 0) = T_\infty(z)$. However, in case of the simplified simulations, the cavern temperature is set to $T(0) = 40$ °C. Yet, the same temperature gradient (Fig. 3.2) is applied over the well

length.

Figure 3.4 shows the two-dimensional axisymmetric discretization of the boundary value problem for the complete simulations. The mesh consists of 445304 elements of which 24607 quadrilateral boundary elements to account for solid-gas heat transfer and turbulent flow. Aside from the boundary layer quadrilateral elements, the well is discretized into at least another 5 triangular elements to solve for possible radial variations of its thermodynamic quantities. At this level of discretization, and based on the recommendations of the k-ϵ model, the solution is not mesh dependent (Lacasse, Turgeon, and Pelletier, 2004). For the comparison purpose, a similar one-dimensional discretization with 5000 elements is used in the simplified simulations for the rock domain, and the well is discretized into 1000 elements over its length. Rock thermal diffusivity is set equal to $\mathcal{K}_\sigma = \Lambda_\sigma/(\rho_\sigma C_{p\sigma}) = 0.29 \times 10^{-5}$ m^2/s. Ideal hydrogen is assigned the following thermodynamic and flow properties: $\Lambda = 0.195$ W/m/K; $C_p = 10225$ J/kg/K; and $\mu = 8.75 \times 10^{-6}$ Pa s.

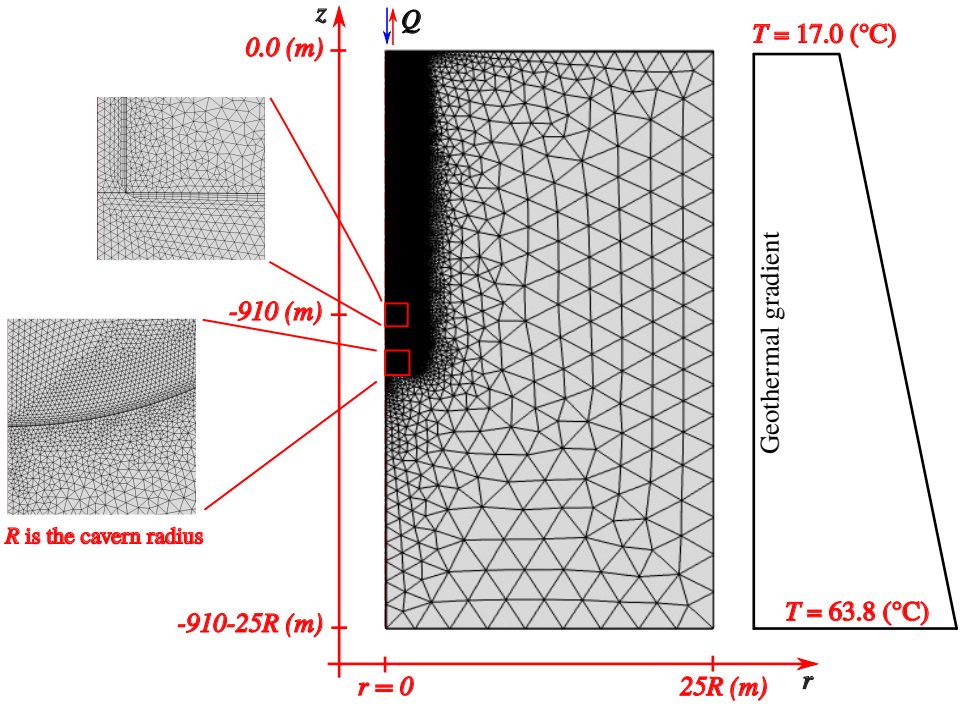

FIGURE 3.4: Two-dimensional axisymmetric discretization of the boundary value problem of Fig. 3.2 for complete simulations. A surrounding rock volume of 25R is chosen around the cavern and well to avoid the effect of far-field boundaries. Mesh is considerably refined on the solid-gas boundary with quadrilateral boundary elements based on the recommendations of the k-ϵ turbulent flow. Mesh is also heavily refined for a certain volume in the rock domain around the cavern and well to better account for the large changes happening close to them in the time-frame of our simulations (60 days). Mesh contains 445304 elements of which 24607 quadrilateral boundary elements.

Figure 3.5 shows a comparison between the simulation results of the complete and the simplified approaches for the volume averaged temperature and pressure during slow and fast cycling. Since pressure histories are mainly affected by mass changes, the simplified and complete pressure histories are quite comparable (Figs 3.5(a, c)). However, the temperature histories show very slight differences in case of slow cycling (Fig. 3.5(b)), yet these differences are noticeable in case of fast cycling and they increase with time before they stabilize eventually (Fig. 3.5(d)).

To further comment on the efficiency of the simplified approach, the temperature and the vertical gas velocity profiles along the treatment well are compared. Figures 3.6(a, b, c) show the well temperature and velocity profiles by the complete (dashed-dotted lines) and the simplified

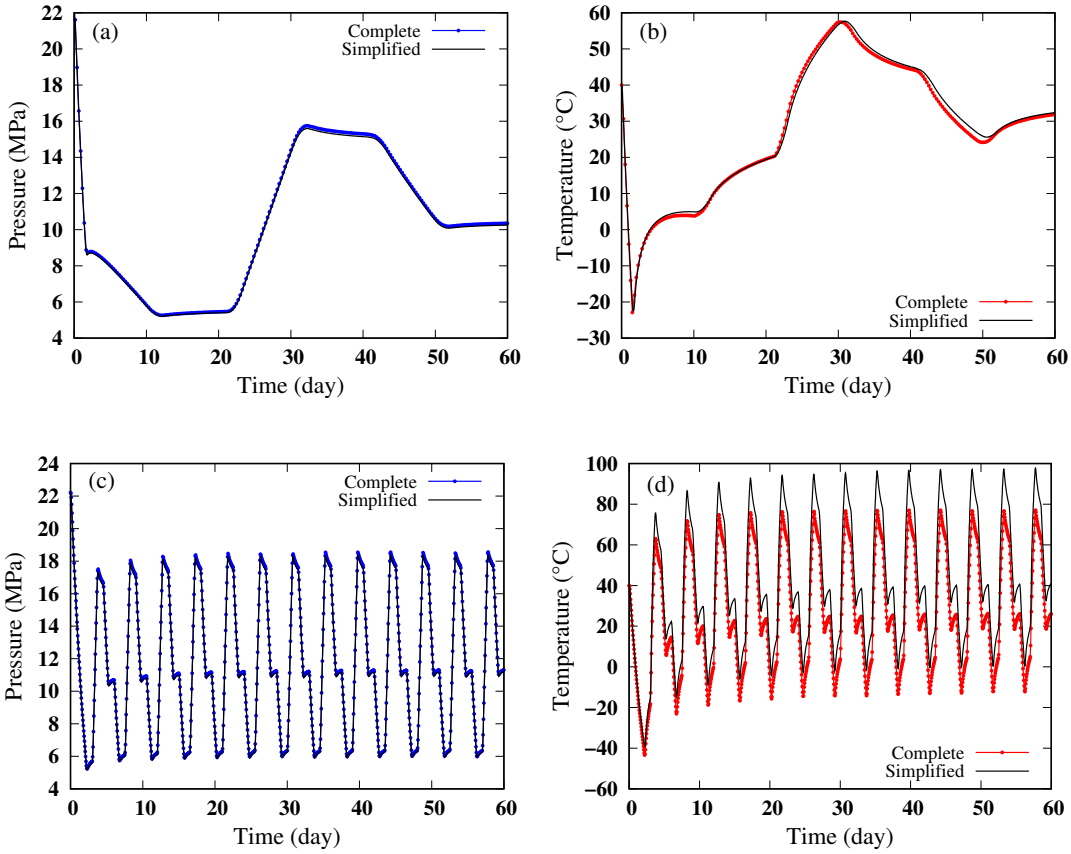

FIGURE 3.5: Development of the cavern pressure and temperature: comparison between slow/seasonal (a, b) and fast/daily (c, d) cycling of the simplified and the complete approaches.

(solid lines) approaches during slow cycling at points p_1 (withdrawal), p_2 (injection), and p_3 (standstill) of Fig. 3.3, and Figs 3.6(d, e, f) show the same profiles yet during fast cycling.

It is clear that these profiles are quite comparable in case of slow cycling, where the velocity profiles are almost vertical, meanwhile the temperature profiles show a curving behavior depending on the state of treatment (withdrawal or injection). In case of pause/standstill, the velocity is equal to zero, and the temperature profiles show linear variations and tend to resemble to the natural geothermal temperature profile. In case of fast cycling (Figs 3.6(d, e, f)), and even-though the velocity profiles are to some point comparable, the temperature profiles are considerably different and they do not show the curving variations anymore due to the fast treatment. In case of the complete approach, these profiles are calculated along the well central line, however in the simplified simulations, there are no radial variations due to the application of 1-D pipe model.

It is interesting to compare the velocity spatial heterogeneities in the cavern volume during these cycling schemes. Figure 3.7 shows the contours of gas velocity magnitude at points p_1, p_2, and p_3 for the same value range of [0 to 0.2] m/s. One can see that, regardless of the treatment stage, gas velocity is significant at the cavern wall. However, in case of injection, velocity becomes also large at the well-cavern connection and it goes all through the cavern volume for fast cycling, yet considerable values never hit the cavern bottom in case of slow cycling. It is also evident that a larger cavern volume is affected by the gas velocity spatial heterogeneities throughout the fast cycling scheme.

The spatial heterogeneities in the velocity field are expected to create corresponding spatial heterogeneities in the temperature and pressure fields. As to quantify the spatial variations of the temperature and pressure over the time course of simulations, the radial and vertical

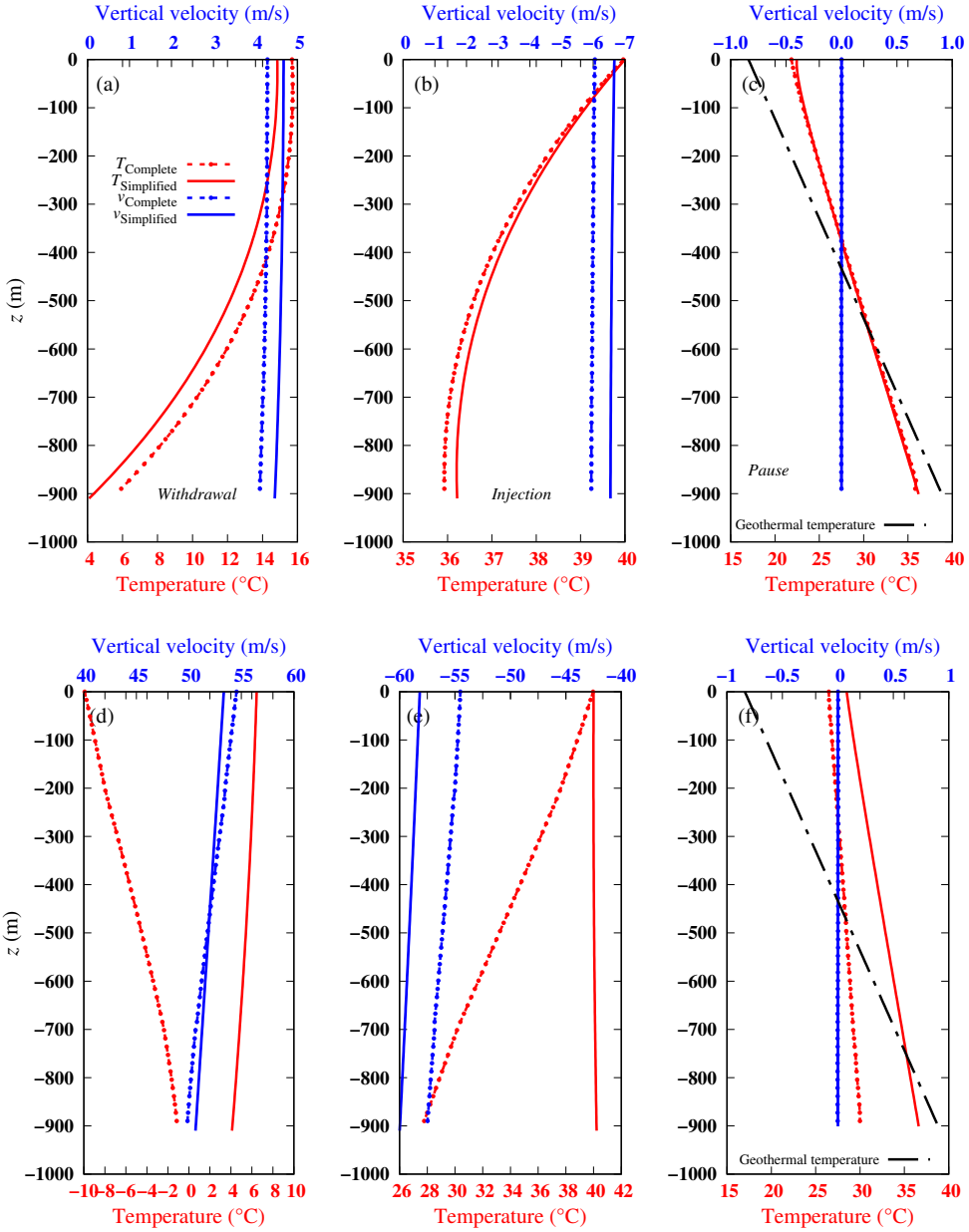

FIGURE 3.6: Development of well temperature and gas velocity profiles during slow cycling (Figs a, b, and c), and during fast cycling (Figs c, d, and e), at points p_1 of withdrawal, p_2 of injection, and p_3 of pause respectively (Fig. 3.3). The figure compares the simulation results of the complete and the simplified approaches.

components of these fields are averaged over the cavern volume (Fig. 3.8) for fast and slow cycling.

The spatial variations of the velocity field affect significantly the radial and vertical variations of the temperature field. Such variations are observed to be at least three-fold higher for fast cycling treatment (Figs 3.8(a, b)). Nonetheless, the radial variations of the pressure field are negligible, and vertical variations are almost comparable between fast and slow cycling (Figs 3.8(c, d)). Vertical pressure variations are mainly related to the gas weight and they are still negligible when compared to the volume averaged values in the range of [5 to 18] MPa. These spatial variations in the thermodynamic variables fields create the solution differences between the simplified and the complete approaches (Fig. 3.5).

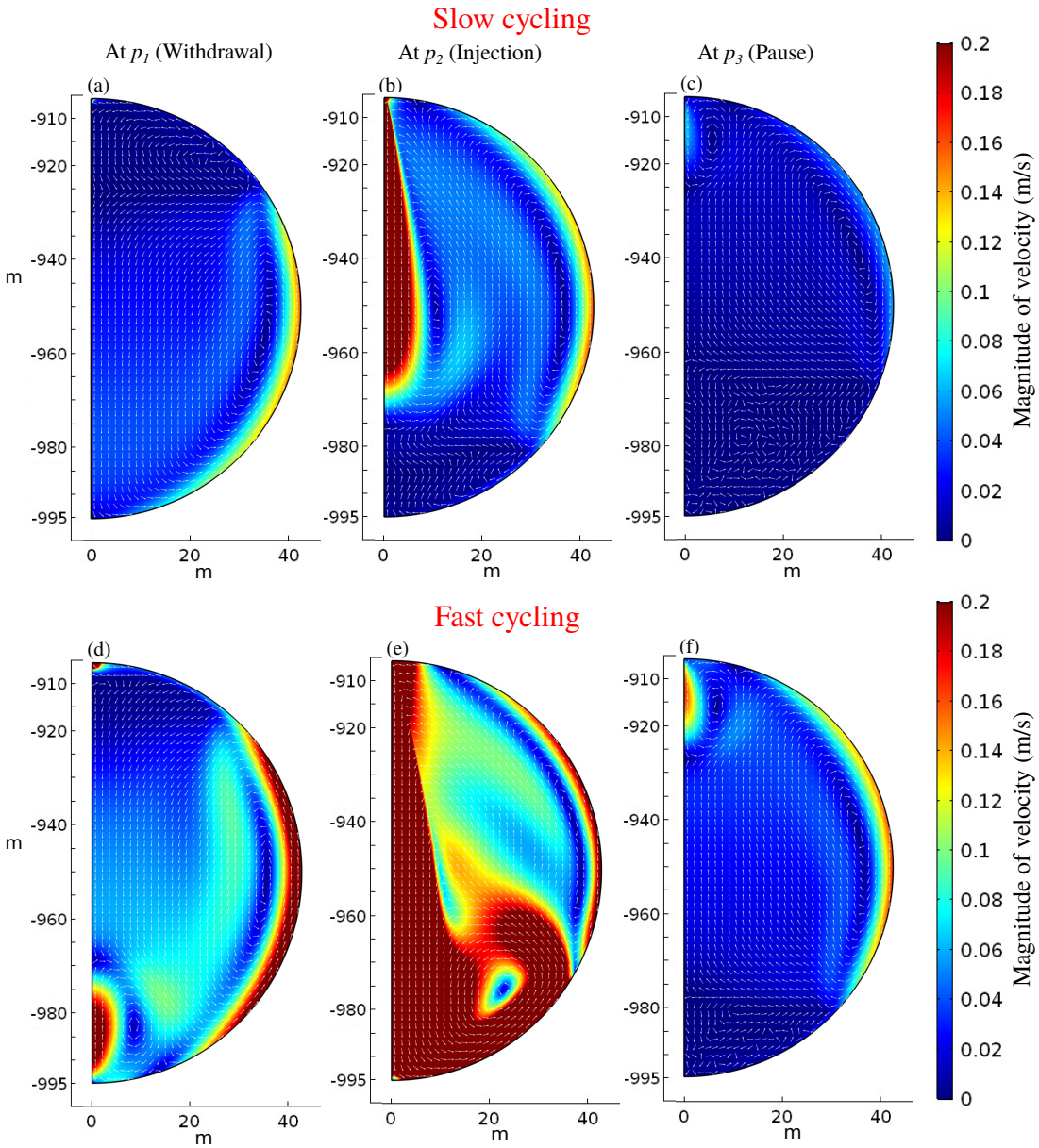

FIGURE 3.7: Contours of the magnitude of gas velocity vector $|\boldsymbol{v}|$. The figure compares the results of slow and fast cycling at points p_1, p_2, and p_3 for the same value range of [0 to 0.2] m/s. White arrows show the gas flow patterns.

3.1.3 Discussion and conclusion

The objective of this research is to know to which level the simplified uniform thermodynamic state simulations of gas storage in underground caverns (used generally) is valid, by comparing it to complete simulations that address all the complexities of the problem, i.e. mesh refinement, gas velocity field, turbulent flow model, and convective heat transfer.

Figure 3.9 shows the absolute value of the relative Kelvin temperature difference ($|1 - T_{\text{Complete}}/T_{\text{Simplified}}| \times 100\%$) between complete and simplified simulations of Figs 3.5(b, d).

Eventually, and despite considering all possible complexities of the problem, the simplified slow cycling simulations for both the well profiles (Figs 3.6(a, b, c)) and the cavern histories (Figs 3.5(a, b)), are quite close to the complete simulations with relative differences that did not exceed 1%. In terms of calculation times, simplified simulations did not last longer than 2 hours, however, complete simulations for fast cycling took approximately 60 days, and for slow cycling 45 days on parallel computation server of 16 cores. There are still more obvious

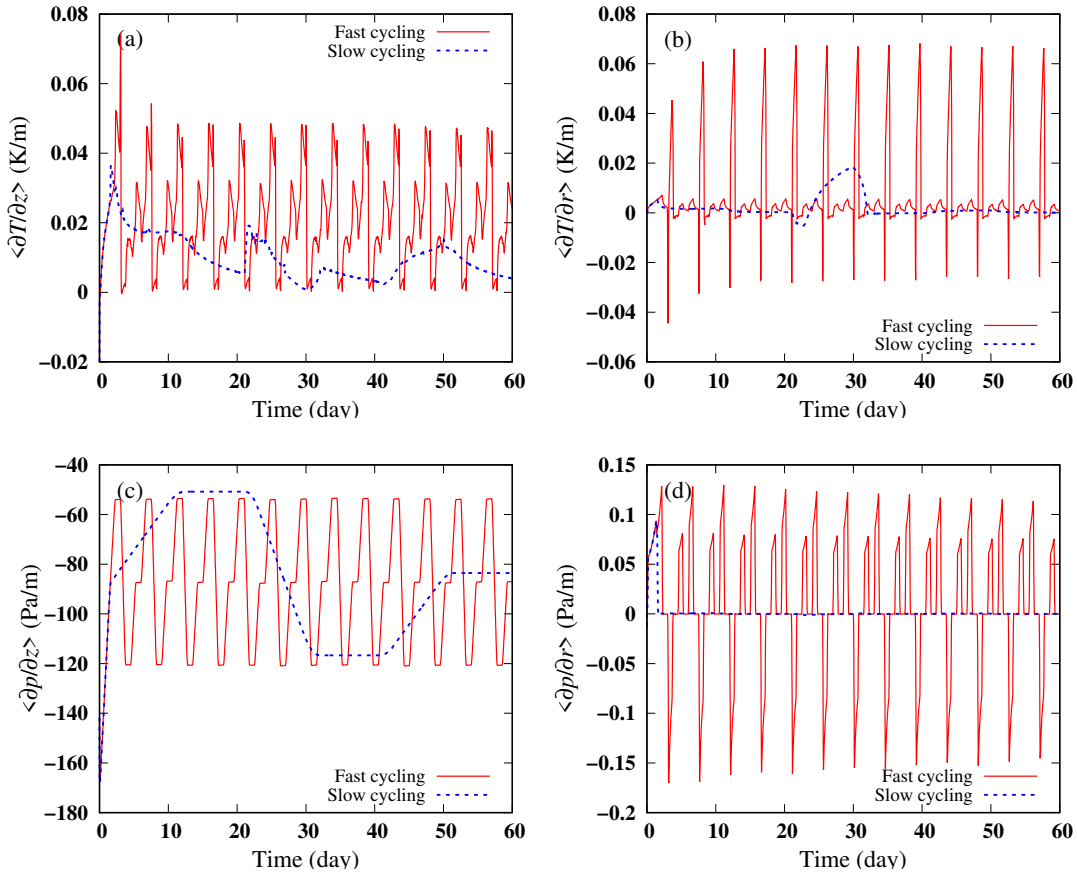

FIGURE 3.8: Volume averaged spatial variations of the gradient of the temperature field (a, b) (K/m), and of the gradient of the pressure field (c, d) (Pa/m).

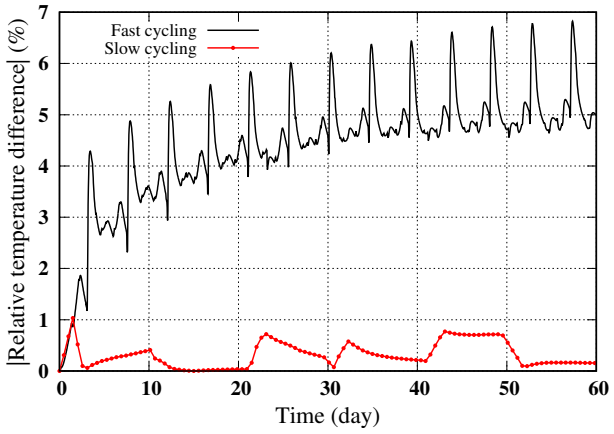

FIGURE 3.9: Relative Kelvin temperature difference $|1 - T_{\text{Complete}}/T_{\text{Simplified}}| \times 100\%$: comparison between complete and simplified simulations for fast and slow cycling of Figs 3.5(b, d).

differences between the complete and simplified simulations results in case of fast cycling that reach relative differences of 7%. Even-though the well velocity profiles are comparable, temperature profiles are considerably different, which renders the use of such simplified approaches questionable in case of fast cycling.

It is understood that a trade-off between accuracy and calculation time needs to be made. It is, until this time, still unfeasible to run complex complete simulations over the entire cavern lifetime, i.e. 30 years and maybe more. Yet, the simplified approaches can give out results in a few days. In case of seasonal utilization of underground caverns, the simplified simulations

are quite efficient in terms of results and calculation cost. In addition to that, such simplified approaches allow researchers to address other problems that are of significant importance to the industry, i..e the thermo-hydromechanical behavior of the rock mass during cycling, real gas behavior, interactions between the cavern species (gas, brine, and insoluble material), multi-phase simulations, and gas percolation into the rock mass. Still, while modern humanity demands on energy increase, the simplified approaches, to a certain level, impose a definite level of inaccuracy that might be unacceptable. The miscalculation of the cavern thermodynamic variables development lead to misestimation of the stored gas mass, as an example.

3.2 Gas migration into the surrounding rock salt

The second part of this chapter concerns the mass exchanges between the cavern phases, they are discussed in the coming three sections. This section focuses on hydrogen permeation into the rock salt during cycling in underground salt caverns (F_4 of Fig. 3.1).

During the cavern operation, hydrogen undergoes changes in its temperature and pressure. Such changes are expected to affect its migration into the surrounding rock domain. Hydrogen invasion into this embracing rock takes place either through the rock salt itself, or through the more permeable and porous interlayers (if they happen to exit). Since underground storage caverns are constructed in networks, the lost hydrogen into the surrounding rock can weaken the neighboring caverns structures. Moreover, the cost of hydrogen production as well as a good management of storage require to keep precise tracks of the injected and withdrawn hydrogen quantities.

Since rock salt contains interstitial brine and is characterized by extremely low permeability and porosity, the application of one-phase generalized Darcian flow to describe hydrogen transport is questionable. Indeed, the cavern thermodynamic state is a function of cycling. Consequently, at the cavern vicinity, both the interstitial rock salt brine pressure and temperature evolutions depend on cycling as well. These changes in the interstitial brine pressure and temperature must influence the migration of hydrogen into the rock domain. The novelty of this research stems from providing a mathematical-numerical model that couples the cavern thermodynamics with the non-isothermal transport mechanisms of hydrogen into the rock salt. Both the Darcian two-phase percolation and the Fickian diffusion are considered as well as the interaction between them. This model addresses as much as possible of the problem complex physics for good estimation of the exchanged hydrogen mass. Besides, it precisely presents the effect of cycling. The adopted van Genuchten model allows to describe the two-phase percolation of hydrogen (characterized by very low viscosity) in rock salt (characterized by very small pore size)[2]. Eventually, an overestimating scenario of model parameters, of diffusion coefficient, and of boundary conditions, is considered to estimate the amount of hydrogen migrated during a 40-year period of hydrogen cycling in a typical spherical cavern.

To quantify hydrogen migration into the rock salt, the interstitial brine pressure must be known. Due to the ambiguity with regard to the inter-grain connectivity of rock salt, the pressure of the interstitial brine is poorly defined. However, its value can be limited to two extremities (Gevantman and Lorenz, 1981):

1. the so-called halmostatic pressure, which considers that the brine occupies a totally connected space in the rock mass. Consequently, this pressure is the equivalent to the hydrostatic pressure calculated using the brine density;

2. a lithostatic pressure, which considers that the brine occupies an isolated space in the rock salt phase. Therefore, the brine pressure is assumed in equilibrium with the geologic

[2]This type of percolation is defined using the capillary and mobility numbers (Yortsos, Xu, and Salin, 1997; Lenormand et al., 1989)

stresses of the rock salt mass. This pressure extremity is calculated using the rock salt density (Bradley, 1975).

3.2.1 Mathematical and numerical model

This section presents the mathematical and numerical models needed to evaluate the quantity of hydrogen transported to the rock salt domain surrounding a typical underground cavern. Simulations are done for a seasonal cycling in a spherical cavern created at 910 m depth and for a 40-year time period (Fig. 3.2).

3.2.1.1 The mathematical model

The mathematical model couples the hydrogen thermodynamics in the cavern with the non-isothermal hydrogen transport in the saturated rock salt domain. To simplify the problem, the following assumptions are made. Some assumptions are adopted for an overestimating study:

- the underground cavern is assumed to be filled with a mono-component single-phase hydrogen;
- hydrogen cycling is seasonal/slow, consequently, a uniform thermodynamic state is assumed within the cavern (Sect. 3.1.1.2) ;
- rock salt domain is assumed saturated with brine;
- for an overestimating study, brine pressure within the rock salt domain is assumed halmostatic;
- rock salt creep due to cavern operation is neglected;
- hydrogen diffusion in the halite structure is neglected;
- hydrogen concentration is initially disregarded in the rock salt domain;
- rock salt, interstitial brine, and the invading hydrogen are assumed in thermal equilibrium;
- hydrogen invasion into the rock salt domain is assumed to follow the van Genuchten percolation model (Yortsos, Xu, and Salin, 1997; Lenormand et al., 1989);
- for an overestimating study, hydrogen entry pressure into the saturated rock salt is neglected.

As an example to model a uniform thermodynamic state within the cavern, the following system of equations is used (Sect. 3.1):

$$\begin{aligned} &\text{mass balance:} && \mathcal{M}\big(-\chi_{p\gamma}\,\dot{T}_\gamma + \chi_{T\gamma}\,\dot{p}_\gamma\big) &&= Q_e - \bar{\pi}_g^\gamma; \\ &\text{energy balance:} && \mathcal{M}\,C_{p\gamma}\,\dot{T}_\gamma - \mathcal{V}\,\chi_{p\gamma}\,T_\gamma\,\dot{p}_\gamma &&= Q_e^+\,C_{p\gamma}(T_\gamma^{\text{inj}} - T_\gamma) - \Psi, \end{aligned} \tag{3.10}$$

with $\bar{\pi}_g^\gamma$ being the exchanged mass rate between the cavern and the rock domain, and T^{inj} is the injection temperature. The well is not modelled here and the specific enthalpy is approximated by $h_\gamma = C_{p\gamma}T_\gamma$. The subscript γ is introduced to designate the gas phase.

Once the cavern thermodynamic state (p_γ and T_γ) is known, it can be used to calculate the hydrogen invasion into the surrounding rock salt domain. Figure 3.10 shows the mechanisms related to hydrogen transport in the saturated rock salt while assuming a van Genuchten two-phase percolation.

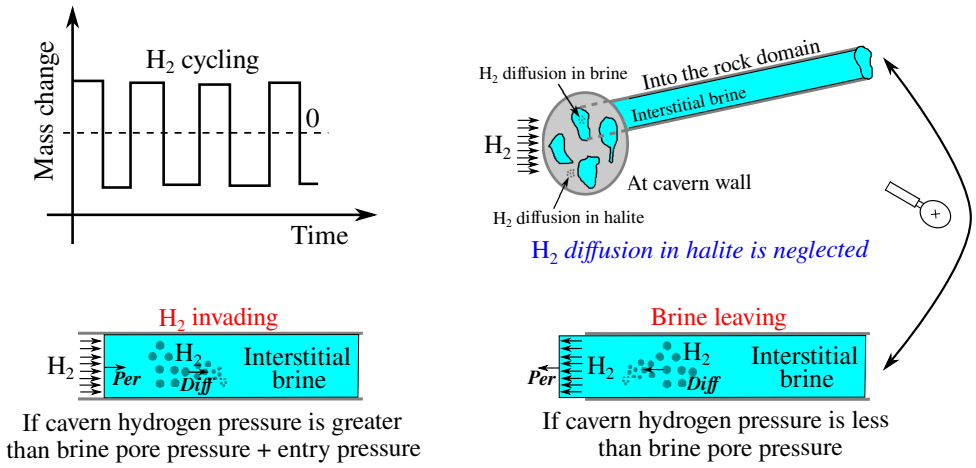

FIGURE 3.10: Schematic representation of hydrogen migration into the rock salt surrounding a slat cavern during cycling.

When hydrogen pressure within the cavern exceeds the rock salt pore pressure plus the entry pressure, hydrogen invades the rock salt in a two-phase percolation type flow. However, when hydrogen pressure becomes less than the interstitial brine pressure, brine moves towards the cavern and tends to pour down the cavern wall. Fickian diffusion of hydrogen in the rock salt interstitial brine is a function of hydrogen cycling. This diffusion is related to the hydrogen mass concentration gradient between the cavern and the rock salt domain. The temperature changes within the cavern lead to temperature changes in the rock salt domain. A temperature continuity is assumed at the cavern wall. The thermo-hydraulic coupling in the rock domain is accounted for through the pressure and temperature effects on the hydrogen and the brine densities.

As the mechanical deformation of the rock salt is neglected, the subsequent percolation-diffusion equations are established in the initial configuration of the solid matrix (Sect. 1.3). The rock salt porosity is denoted by n, and T denotes the temperature for all the phases in the rock salt domain. For each fluid phase $\alpha \in \{\lambda\,(\text{liquid}), \gamma\,(\text{gas})\}$, p_α stands for the pressure, n_α the partial porosity, $S_\alpha = n_\alpha / n$ the saturation degree, and ρ_α the density. In the liquid phase λ, $c_{g\lambda}$ denotes the mass concentration of hydrogen and $\rho_{g\lambda} = c_{g\lambda}\,\rho_\lambda$ denotes its density. For a given quantity X, the apparent value (per unit volume of the entire porous medium) is denoted X^α with $X^\alpha = n_\alpha\, X_\alpha$, where X_α is per unit volume occupied by the α-phase.

The rock salt interstitial brine density is characterized by four state variables which are the brine pressure p_λ, its temperature T, the hydrogen concentration $c_{g\lambda}$, and the salt concentration. In this study, the interstitial brine is assumed saturated with salt at any time. Besides the mass of the dissolved hydrogen is assumed very minor to affect the brine density. Therefore, the mass balance equations of the components b (brine) and g (hydrogen) of the liquid phase can be written in the following form:

$$
\begin{aligned}
\dot{m}_b^\lambda + \boldsymbol{\nabla}\cdot\left[\rho_\lambda\left(1-c_{g\lambda}\right)\boldsymbol{\omega}^\lambda - \rho_\lambda\,\boldsymbol{J}_{g\lambda}\right] &= \pi_b^\lambda;\\
\dot{m}_g^\lambda + \dot{m}^\gamma + \boldsymbol{\nabla}\cdot\left[\rho_\lambda\left(c_{g\lambda}\boldsymbol{\omega}^\lambda + \boldsymbol{J}_{g\lambda}\right) + \rho_\gamma\boldsymbol{\omega}^\gamma\right] &= \pi_g^\gamma;\\
\text{with,}\quad m^\alpha = nS_\alpha\rho_\alpha \quad \text{for} \quad \alpha &\in \{\lambda,\gamma\},\\
m_b^\lambda = (1-c_{g\lambda})\,m^\lambda, \quad \text{and,} \quad m_g^\lambda &= c_{g\lambda}\,m^\lambda,
\end{aligned}
\tag{3.11}
$$

where ρ_α is the density of the α-phase, $\boldsymbol{\omega}^\alpha$ is the filtration velocity of the α-phase, $\boldsymbol{J}_{g\lambda}$ is the Fickian diffusion flux of hydrogen in the liquid λ-phase, π_b and π_g are the total mass creation terms of the two components in the fluid phase. If heat convection in the rock salt domain is neglected, the following energy equation can be used to describe heat transfer within the rock salt domain due to cycling in the cavern,

$$\begin{aligned} m\,C_p\,\dot{T} + \boldsymbol{\nabla}\cdot\boldsymbol{\psi} = 0, \\ \text{with,} \quad m\,C_p = \sum_\alpha m^\alpha C_{p\alpha}, \quad \text{and,} \quad \boldsymbol{\psi} = -\underline{\underline{\boldsymbol{\Lambda}}}\cdot\boldsymbol{\nabla}T, \end{aligned} \tag{3.12}$$

with $\alpha \in \{\lambda,\ \gamma,\ \sigma\ (\text{solid})\}$, and $\underline{\underline{\boldsymbol{\Lambda}}}$ is the saturated rock salt domain thermal conductivity tensor. If the thermal conductivities of the three phases are assumed isotropic, the domain thermal conductivity Λ is expressed by the geometric mean of the phases thermal conductivities (Côté and Konrad, 2005),

$$\Lambda = \Lambda_\sigma^{n_\sigma}\,\Lambda_\lambda^{n_\lambda}\,\Lambda_\gamma^{n_\gamma}. \tag{3.13}$$

In a two-phase percolation flow, the liquid saturation degree S_λ can be calculated using the van Genuchten (1980) expression,

$$\tilde{S}_\lambda = \frac{S_\lambda - S_{\lambda r}}{S_{\lambda s} - S_{\lambda r}} = \left(1 + \left(\frac{p_c}{P_r}\right)^{1/(1-\ell)}\right)^{-\ell}, \tag{3.14}$$

where $p_c = p_\gamma - p_\lambda$ is the capillary pressure, $\tilde{S}_\lambda$ is the effective degree of saturation, the parameters $S_{\lambda r}$ and $S_{\lambda s}$ represent the liquid residual and maximum saturation values respectively ($S_\lambda \in [S_{\lambda r} - S_{\lambda s}]$), ℓ and P_r are model parameters. The equation does not introduce the notion of an entry pressure as it will be neglected in this research.

The hydraulic problem (Eq. 3.11) needs to be completed with constitutive and state laws. The filtration velocity vectors are assumed to follow a Darcian flow nature,

$$\boldsymbol{\omega}^\alpha = -\frac{k_{r\alpha}}{\mu_\alpha}\,\underline{\underline{\boldsymbol{k}}}\cdot\left(\boldsymbol{\nabla}p_\alpha - \rho_\alpha\mathbf{g}\right), \quad \text{for} \quad \alpha \in \{\lambda,\gamma\}, \tag{3.15}$$

where $\underline{\underline{\boldsymbol{k}}}$ is the intrinsic permeability tensor, μ_α is the dynamic viscosity of the α-phase, $\mathbf{g}$ is the gravitational acceleration vector, and $k_{r\alpha}$ is the relative permeability of the α-phase. Relative permeabilities can be calculated using the Mualem-van Genuchten model (Mualem, 1978),

$$k_{r\lambda} = \sqrt{\tilde{S}_\lambda}\left[1 - \left(1 - \tilde{S}_\lambda^{1/\ell}\right)^\ell\right]^2, \quad \text{and} \quad k_{r\gamma} = \sqrt{1-\tilde{S}_\lambda}\left(1 - \tilde{S}_\lambda^{1/\ell}\right)^{2\ell}. \tag{3.16}$$

The diffusion flux of hydrogen in the liquid phase is related to the concentration gradient through the Fick's law,

$$\boldsymbol{J}_{g\lambda} = -\underline{\underline{\boldsymbol{D}}}_{g\lambda}\cdot\boldsymbol{\nabla}c_{g\lambda} = c_{g\lambda}(\boldsymbol{v}_{g\lambda} - \boldsymbol{\omega}^\lambda), \tag{3.17}$$

where $\underline{\underline{\boldsymbol{D}}}_{g\lambda}$ and $\boldsymbol{v}_{g\lambda}$ are the diffusion coefficient tensor and the diffusive velocity of hydrogen in the λ-phase respectively. This coefficient can be determined experimentally for a given component, a phase, and a porous medium, or empirically from the plain diffusivity in the liquid phase $\bar{D}_{g\lambda}$ modified by the characteristics of the porous network (porosity, turtuosity, and constrictivity) (AbuAisha and Billiotte, 2021). A commonly used expression is $D_{g\lambda} = \bar{D}_{g\lambda}\,n^q$, where q is an empirical parameter that generally lies between 1.8 and 2.4 (Grathwohl, 2012). The exchanged hydrogen mass rate between the cavern and the surrounding rock salt (Eq. 3.10) can, therefore, be calculated as,

$$\bar{\pi}_g^\gamma = \underbrace{\int_{\mathcal{S}} \rho_\gamma\boldsymbol{\omega}^\gamma\cdot\boldsymbol{n}\,d\mathcal{A}}_{\text{Percolated mass rate}} + \underbrace{\int_{\mathcal{S}} \rho_\lambda(\boldsymbol{J}_{g\lambda} + c_{g\lambda}\boldsymbol{\omega}^\lambda)\cdot\boldsymbol{n}\,d\mathcal{A}}_{\text{Diffused mass rate}}, \tag{3.18}$$

with $\boldsymbol{n}$ being the outward unit vector normal to the cavern surface.

The hydrogen phase is assumed to behave as a real gas (AbuAisha et al., 2021). The state equation is described using two state functions; the density $\rho_\gamma(p_\gamma, T_\gamma)$, and the heat capacity $C_{p\gamma}(T_\gamma)$ at a given pressure. The thermodynamic variables are related to each other through the formula $p_\gamma = \rho_\gamma T_\gamma Z$, with Z being the gas compressibility factor. The chemical potential equality between the λ- and γ-phases leads to the definition of the Henry's law $p_\gamma = (K_H/M_w)\rho_{g\lambda} = Hc_{g\lambda}$, with K_H being the Henry's constant, M_w the hydrogen molecular weight, and $H = K_H\rho_\lambda/M_w$. The brine phase is assumed to be slightly compressible, i.e. $\dot{\rho}_\lambda/\rho_\lambda = \chi_{T\lambda}\,\dot{p}_\lambda - \chi_{p\lambda}\,\dot{T}$ with $\chi_{T\lambda}$ and $\chi_{p\lambda}$ being the isothermal compressibility and the isobaric thermal expansion coefficient respectively.

3.2.1.2 Saturated/unsaturated state transition

The set of differential equations and primary variables (Eq. 3.11) needs to be controlled to assure the transition from fully saturated state to unsaturated state, or vice versa. Only the problem of hydrogen appearance in rock salt where the brine phase is always present, is considered in this work. The proposed modeling approach consists of using the dissolution and diffusion phenomena to derive a set of differential equations applicable for both saturated and unsaturated states (Mahjoub et al., 2018).

The choice of the primary variables is crucial. The pressure p_λ can be chosen as the first primary variable because the brine phase is assumed present at any time. With regard to the second unknown, due to dissolution and diffusion phenomena, the mass concentration $c_{g\lambda}$ is a permanent unknown, whether the medium is saturated or unsaturated. Thus, it is chosen as the second primary variable. However, to assure the homogeneity in the primary variables, a pseudo-hydrogen pressure is defined as $\hat{p}_\gamma = Hc_{g\lambda}$. It represents the real hydrogen pressure only when the hydrogen phase is present ($\hat{p}_\gamma = p_\gamma$ if $S_\lambda < 1$), and it is just a definition in the saturated case. To use the same equations in the saturated case, a new pseudo-capillary pressure is introduced $\hat{p}_c = \hat{p}_\gamma - p_\lambda$. The saturation degree is expressed as a function of this pseudo-capillary pressure such that $S_\lambda(\hat{p}_c) = S_\lambda(p_c)$ when $\hat{p}_c \geq 0$ (because $\hat{p}_c = p_c$), and $S_\lambda(\hat{p}_c) = 1$ when $\hat{p}_c < 0$.

Taking these definitions into consideration, the γ-Darcy and Fick laws have to be reformulated and integrated into the conservation equations. The same equation for γ-Darcy law (Eq. 3.15) is used after replacing p_γ by $\hat{p}_\gamma$, with $\rho_\gamma(\hat{p}_\gamma, T_\gamma)$. In Fick's law (Eq. 3.17), $c_{g\lambda}$ is replaced by $\hat{p}_\gamma/H$, and the variation of H is assumed negligible compared to the variation of $\hat{p}_\gamma$. The reformulated mass conservation equations can be cast in the following system of coupled partial differential equations:

$$
\begin{aligned}
\dot{m}_b^\lambda - \boldsymbol{\nabla}\cdot\left(\underline{\underline{\boldsymbol{\mathcal{B}}}}_{b\lambda}\cdot(\boldsymbol{\nabla}p_\lambda - \rho_\lambda\boldsymbol{\mathfrak{g}}) + \underline{\underline{\boldsymbol{\mathcal{B}}}}_{b\gamma}\cdot\boldsymbol{\nabla}\hat{p}_\gamma\right) &= \pi_b^\lambda;\\
\dot{m}_g^\lambda + \dot{m}^\gamma - \boldsymbol{\nabla}\cdot\left(\underline{\underline{\boldsymbol{\mathcal{B}}}}_{g\lambda}\cdot(\boldsymbol{\nabla}p_\lambda - \rho_\lambda\boldsymbol{\mathfrak{g}}) + \underline{\underline{\boldsymbol{\mathcal{B}}^{\boldsymbol{f}}}}_{g\gamma}\cdot\boldsymbol{\nabla}\hat{p}_\gamma + \underline{\underline{\boldsymbol{\mathcal{B}}^{\boldsymbol{p}}}}_{g\gamma}\cdot(\boldsymbol{\nabla}\hat{p}_\gamma - \rho_\gamma\boldsymbol{\mathfrak{g}})\right) &= \pi_g^\gamma;\\
\text{with,}\quad \underline{\underline{\boldsymbol{\mathcal{B}}}}_{b\lambda} = \left[(1-c_{g\lambda})\rho_\lambda k_{r\lambda}/\mu_\lambda\right]\underline{\underline{\boldsymbol{k}}},&\quad \underline{\underline{\boldsymbol{\mathcal{B}}}}_{b\gamma} = (-\rho_\lambda/H)\underline{\underline{\boldsymbol{D}}}_{g\lambda},\\
\underline{\underline{\boldsymbol{\mathcal{B}}}}_{g\lambda} = (c_{g\lambda}\rho_\lambda k_{r\lambda}/\mu_\lambda)\underline{\underline{\boldsymbol{k}}},\quad \underline{\underline{\boldsymbol{\mathcal{B}}^{\boldsymbol{f}}}}_{g\gamma} = (\rho_\lambda/H)\underline{\underline{\boldsymbol{D}}}_{g\lambda},&\quad \text{and,}\quad \underline{\underline{\boldsymbol{\mathcal{B}}^{\boldsymbol{p}}}}_{g\gamma} = (\rho_\gamma k_{r\gamma}/\mu_\gamma)\underline{\underline{\boldsymbol{k}}}.
\end{aligned}
\tag{3.19}
$$

The system of Eqs 3.19 along with the energy conservation (Eq. 3.12) are written in a matrix form as follows,

$$\underbrace{\begin{bmatrix} \mathcal{C}_{b\gamma} & \mathcal{C}_{b\lambda} & \mathcal{C}_{bT} \\ \mathcal{C}_{g\gamma} & \mathcal{C}_{g\lambda} & \mathcal{C}_{gT} \\ 0 & 0 & \mathcal{C}_{T} \end{bmatrix}}_{\text{Storage matrix}} \begin{bmatrix} \dot{\hat{p}}_\gamma \\ \dot{p}_\lambda \\ \dot{T} \end{bmatrix} - \boldsymbol{\nabla} \cdot \underbrace{\begin{bmatrix} \underline{\underline{\boldsymbol{\mathcal{B}}}}_{b\gamma} & \underline{\underline{\boldsymbol{\mathcal{B}}}}_{b\lambda} & \underline{\underline{\mathbf{0}}} \\ \underline{\underline{\boldsymbol{\mathcal{B}}}}^{\boldsymbol{f}}_{g\gamma} + \underline{\underline{\boldsymbol{\mathcal{B}}}}^{\boldsymbol{p}}_{g\gamma} & \underline{\underline{\boldsymbol{\mathcal{B}}}}_{g\lambda} & \underline{\underline{\mathbf{0}}} \\ \underline{\underline{\mathbf{0}}} & \underline{\underline{\mathbf{0}}} & \underline{\underline{\boldsymbol{\Lambda}}} \end{bmatrix}}_{\text{Dispersion matrix}} \cdot \begin{bmatrix} \boldsymbol{\nabla}\hat{p}_\gamma \\ \boldsymbol{\nabla} p_\lambda \\ \boldsymbol{\nabla} T \end{bmatrix} = \underbrace{\begin{bmatrix} \mathcal{F}_{b\lambda} \\ \mathcal{F}_{g\gamma} \\ 0 \end{bmatrix}}_{\text{Body forces and source terms matrix}}, \tag{3.20}$$

with,

$$\begin{aligned} \mathcal{C}_{b\gamma} &= n\rho_\lambda \frac{\partial S_\lambda}{\partial \hat{p}_\gamma}\left(1-\frac{\hat{p}_\gamma}{H}\right) - \frac{n\rho_\lambda S_\lambda}{H}, \\ \mathcal{C}_{b\lambda} &= n\rho_\lambda \frac{\partial S_\lambda}{\partial p_\lambda}\left(1-\frac{\hat{p}_\gamma}{H}\right) + n\rho_\lambda S_\lambda \chi_{T\lambda}\left(1-\frac{\hat{p}_\gamma}{H}\right), \\ \mathcal{C}_{bT} &= -n\rho_\lambda S_\lambda \chi_{p\lambda}\left(1-\frac{\hat{p}_\gamma}{H}\right), \end{aligned} \tag{3.21}$$

and,

$$\begin{aligned} \mathcal{C}_{g\gamma} &= -n\rho_\lambda \frac{\partial S_\lambda}{\partial \hat{p}_\gamma}\left(1-\frac{\hat{p}_\gamma}{H}\right) + \frac{n\rho_\lambda S_\lambda}{H} + n\rho_\gamma(1-S_\lambda)\chi_{T\gamma}, \\ \mathcal{C}_{g\lambda} &= n\frac{\partial S_\lambda}{\partial p_\lambda}\left(\rho_\lambda \frac{\hat{p}_\gamma}{H} - \rho_\gamma\right) + n\rho_\lambda S_\lambda \chi_{T\lambda}\frac{\hat{p}_\gamma}{H}, \\ \mathcal{C}_{gT} &= -n\left(\rho_\lambda S_\lambda \chi_{p\lambda}\frac{\hat{p}_\gamma}{H} + \rho_\gamma(1-S_\lambda)\chi_{p\gamma}\right), \end{aligned} \tag{3.22}$$

and,

$$\mathcal{C}_T = m\, C_p. \tag{3.23}$$

The body forces and source terms matrix components are expressed as,

$$\begin{aligned} \mathcal{F}_{b\lambda} &= -\boldsymbol{\nabla}\cdot\left(\underline{\underline{\boldsymbol{\mathcal{B}}}}_{b\lambda}\cdot\rho_\lambda \mathfrak{g}\right) + \pi_b^\lambda, \\ \mathcal{F}_{g\gamma} &= -\boldsymbol{\nabla}\cdot\left(\underline{\underline{\boldsymbol{\mathcal{B}}}}^{\boldsymbol{p}}_{g\gamma}\cdot\rho_\gamma \mathfrak{g} + \underline{\underline{\boldsymbol{\mathcal{B}}}}_{g\lambda}\cdot\rho_\lambda \mathfrak{g}\right) + \pi_g^\gamma. \end{aligned} \tag{3.24}$$

3.2.1.3 The numerical model

The numerical model represents a spherical cavern of volume $\mathcal{V} = 300{,}000\ \mathrm{m}^3$ in a surrounding rock domain. The well extends from the surface at $z = 0$ m to the cavern top at $z = z_w = -910$ m (Fig. 3.2). The cavern has been leached (full of brine) and is initially in thermal equilibrium with the surrounding rock domain at $T = 40\ ^\circ$C. The brine pressure within the cavern is also in equilibrium with the rock salt pore pressure at the halmostatic value of $p_\lambda = -\rho_\lambda \mathfrak{g} z = 11.2$ MPa. The cavern brine is then replaced by hydrogen during a debrining/filling phase of 90 days where hydrogen pressure of 22 MPa is attained within the cavern. The cavern is later left unsolicited for a similar period of time. Consequently, after 90 days of standstill, the cavern volume averaged temperature and pressure are 46 °C and 22 MPa respectively. The cavern then undergoes seasonal cycling following the program shown in Fig. 3.11 for a 40-year time period, where hydrogen is injected at $T_\gamma^{\mathrm{inj}} = 40\ ^\circ$C.

Figure 3.11 shows the cycling scheme that will be considered in our simulations in terms of the relative mass change $\tilde{\mathcal{M}} = (\mathcal{M}/\mathcal{M}(0) - 1) \times 100\%$. The program starts with a withdrawal

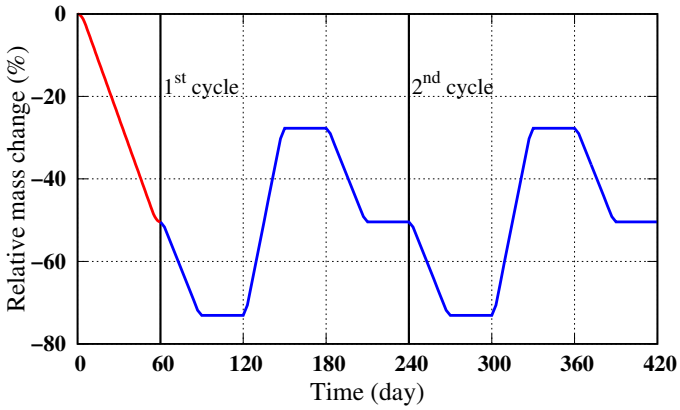

FIGURE 3.11: Imposed cavern relative mass variations. Only the first two cycles are shown, however simulations are run for 40 years.

phase of 60 days, cycling then begins where each cycle extends over a 6-month period. Only the first two cycles are shown, however, simulations are conducted for a 40-year time period, i.e. 80 cycles.

The COMSOL available general forms of the coefficient Partial Differential Equations (cPDE), of the domain Ordinary Differential Equations (dODE), and of the boundary Ordinary Differential Equations (bODE) are used to solve the previous systems of equations in a coupled thermo-hydraulic framework. COMSOL gives analytical expressions to track the evolution of the hydrogen viscosity μ_γ, thermal conductivity Λ_γ, and heat capacity $C_{p\gamma}$ as a function of temperature. Hydrogen is modelled as a real gas (AbuAisha et al., 2021). Other van Genuchten, thermal, and hydraulic parameters are detailed in Table (3.1).

TABLE 3.1: Hydraulic, thermal, and van Genuchten parameters to model hydrogen invasion into the rock salt. References: 1. (Grathwohl, 2012); 2. (Gevantman and Lorenz, 1981); 3. (Mahjoub et al., 2018); 4. (Cosenza et al., 1999); 5. (Schulze, Popp, and Kern, 2001b); 6. (Bannach et al., 2005); 7. (Poppei et al., 2006); 8. (Crozier and Yamamoto, 1974); 9. (Lopez-Lazaro et al., 2019); 10. (AbuAisha et al., 2021).

Interpretation	Parameter (unit)	Value	Reference
Rock salt permeability	k (m^2)	1×10^{-20}	[4, 5]
Rock salt porosity	n	0.01	[4, 5]
Brine density	ρ_λ (kg/m^3)	1200	[2]
Brine isothermal compressibility	$\chi_{T\lambda}$ (1/Pa)	46×10^{-11}	[2]
Brine isobaric expansivity	$\chi_{p\lambda}$ (1/K)	45×10^{-5}	[2]
Brine dynamic viscosity	μ_λ (Pa s)	1.32×10^{-3}	[2]
Brine thermal conductivity	Λ_λ (W/m/K)	0.51	[2]
Brine heat capacity	$C_{p\lambda}$ (J/kg/K)	3300	[2]
Rock salt pore pressure	p_λ (Pa)	$-\rho_\lambda \mathfrak{g} z$	Overestimating study
Rock salt density	ρ_σ (kg/m^3)	2200	[6]
Rock salt thermal conductivity	Λ_σ (W/m/K)	6	[6]
Rock salt heat capacity	$C_{p\sigma}$ (J/kg/K)	900	[6]
Maximum brine saturation	$S_{\lambda s}$	1.0	Assumed
Residual brine saturation	$S_{\lambda r}$	0.15	[3]
van Genuchten parameter	P_r (Pa)	8×10^6	[10]
van Genuchten parameter	ℓ	0.5	[7]
Mass creation terms	π_b^λ and π_g^γ ($kg/m^3/s$)	0	Assumed
Hydrogen mass concentration	$c_{g\lambda}$	$\hat{p}_\gamma / H$	Definition
Hydrogen diffusion in brine	$\tilde{D}_{g\lambda}$ (m^2/s)	5×10^{-7}	Overestimated [10]
Diffusion correction parameter	q	2.1	[1]
Henry's constant hydrogen-brine	K_H (l atm/mol)	1300	[8, 9]

3.2.2 Effects of the van Genuchten model parameters

As stated previously, and due to the absence of any literature data with regard to the entry pressure of hydrogen in the saturated rock salt, the entry pressure notion is neglected in this research. This conclusion is pessimistic as it overestimates the total amount of gas lost into the rock domain. The work of AbuAisha et al. (2021) investigated the effect of the Van Genuchten model parameters, particularly P_r and ℓ, and the diffusion coefficient on the migration of hydrogen into the saturated rock salt.

For a P_r range that resembles the hydrogen invasion into the rock salt, the Darcian percolation has a slight dependency on the value of P_r. The parameter ℓ is assigned a value of 0.5 for rock salt in a few research papers. However, possible high values ($\ell \sim 0.9$) can increase considerably the capillary pressure at full brine saturation leading to a naught percolation. A value of $\ell = 0.1$, close to the lowest limit, increases the hydrogen mass percolated into the rock salt domain by 3 folds. The value of the diffusion coefficient $\bar{D}_{g\lambda}$ does not affect directly the Darcian percolation, but rather its diffusive nature. Percolation becomes more of a piston-like for very small values (AbuAisha et al., 2021).

3.2.3 Simulations of hydrogen migration during cycling

A two-dimensional axisymmetric model is adopted to simulate heat and mass exchange with the surrounding rock domain during hydrogen cycling in the real cavern (Fig. 3.2). Figure 3.12 shows the spatial discretization of the rock domain. The cavern is not discretized since a uniform thermodynamic state is assumed within the cavern. Initial and boundary conditions are displayed on the graph.

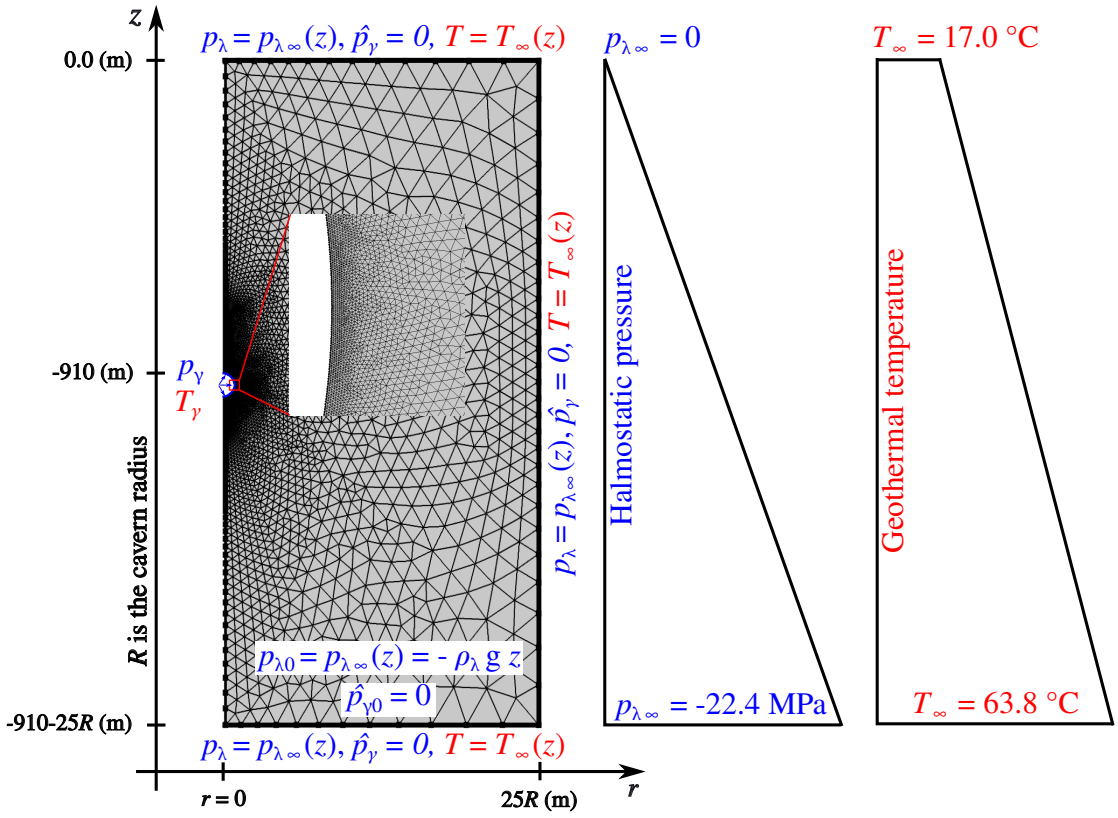

FIGURE 3.12: A two-dimensional axisymmetric discretization of the boundary value problem of Fig. 3.2. A surrounding rock volume of 25R is chosen around the cavern to avoid the effect of far-field boundaries. Mesh is considerably refined close to the cavern wall to account for abrupt changes/large gradients. Mesh contains 160113 triangular elements.

Figures 3.13(a, b) show the cavern averaged temperature and pressure as a function of cycling. Hydrogen pressure is not showing any changes during cycling as the cavern volume is assumed constant. However, temperature is showing some changes due to the energy exchanged with the surrounding rock salt domain.

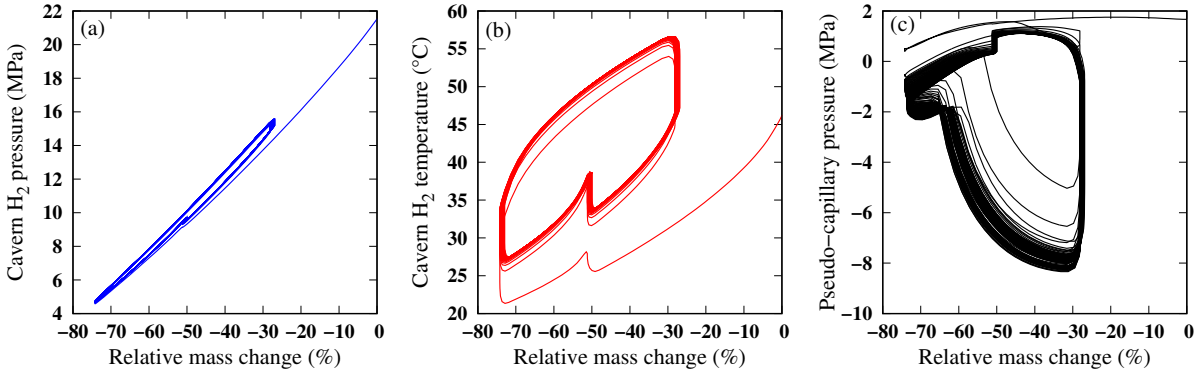

FIGURE 3.13: (a) cavern pressure, (b) cavern average temperature, and (c) hydrogen pseudo-capillary pressure averaged over the cavern surface. The three quantities are presented as a function of cycling/relative mass changes within the cavern.

Figure 3.13(c) shows the hydrogen pseudo-capillary pressure averaged over the cavern surface during cycling. The behavior of the capillary pressure becomes almost identical after five cycles. The capillary pressure does not exceed 2 MPa for the working and boundary conditions of this typical spherical cavern.

To study the hydrogen mass exchanged with the rock domain, Fig. 3.14(a) shows the brine saturation, and Fig. 3.14(b) shows the radial component of hydrogen filtration velocity averaged over the cavern surface during the first four cycles. Other cycles are not displayed due to similarity and to avoid redundant repetitions.

The debrining and the standstill phases of 180 days have led the brine saturation at the cavern wall to decrease to ∼0.981 before any cycling (Fig. 3.14(a)). The subsequent withdrawal has counteracted this reduction in the brine saturation by allowing the percolated hydrogen to leave back to the cavern volume, and again after some cycling, the full brine saturation is reached. Furthermore, hydrogen percolates into and leaves from the rock domain as a function of the cavern hydrogen pressure (Fig. 3.14(b)). This allows for a reduction in the brine saturation at the cavern wall before it sustains the full saturation state (Fig. 3.14(a) and Fig. 3.15(a)).

The Fickian diffusive velocity resembles the brine filtration velocity (Figs 3.14(c, d)). Depending on the direction of hydrogen pressure gradient, hydrogen may diffuse into the rock domain, or pour down the cavern wall along with the leaving brine. The surface averaged radial component of the brine filtration velocity is show in Fig. 3.14(d). It is observed that brine leaves the rock domain into the cavern when the percolated hydrogen leaves the rock domain as well and vice versa. Besides, the thermal effects are noticed on the behavior of the brine filtration and the Fickian diffusive velocities due to the hydro-thermal coupling, especially during the standstill phases.

To understand how the rock domain interstitial brine gets drained by the invading hydrogen, Fig. 3.15(a) shows the time variations of the brine saturation and the pseudo-capillary pressure at the cavern wall for the first four cycles. One can see that hydrogen percolates into the rock domain when the capillary pressure is positive. The brine saturation rate (increasing or decreasing) has an opposite sign to the capillary pressure rate.

To study the zone disturbed by brine pore pressure changes, and hydrogen pseudo-pressure and temperature fluctuations, Fig. 3.15(b) shows the radial profiles of these variables at the end of cycling, i.e. 40 years. The altered zone due to hydrogen invasion into the rock domain has not exceeded ∼15 m after 40 years of seasonal cycling. However, this zone extends to ∼40 m

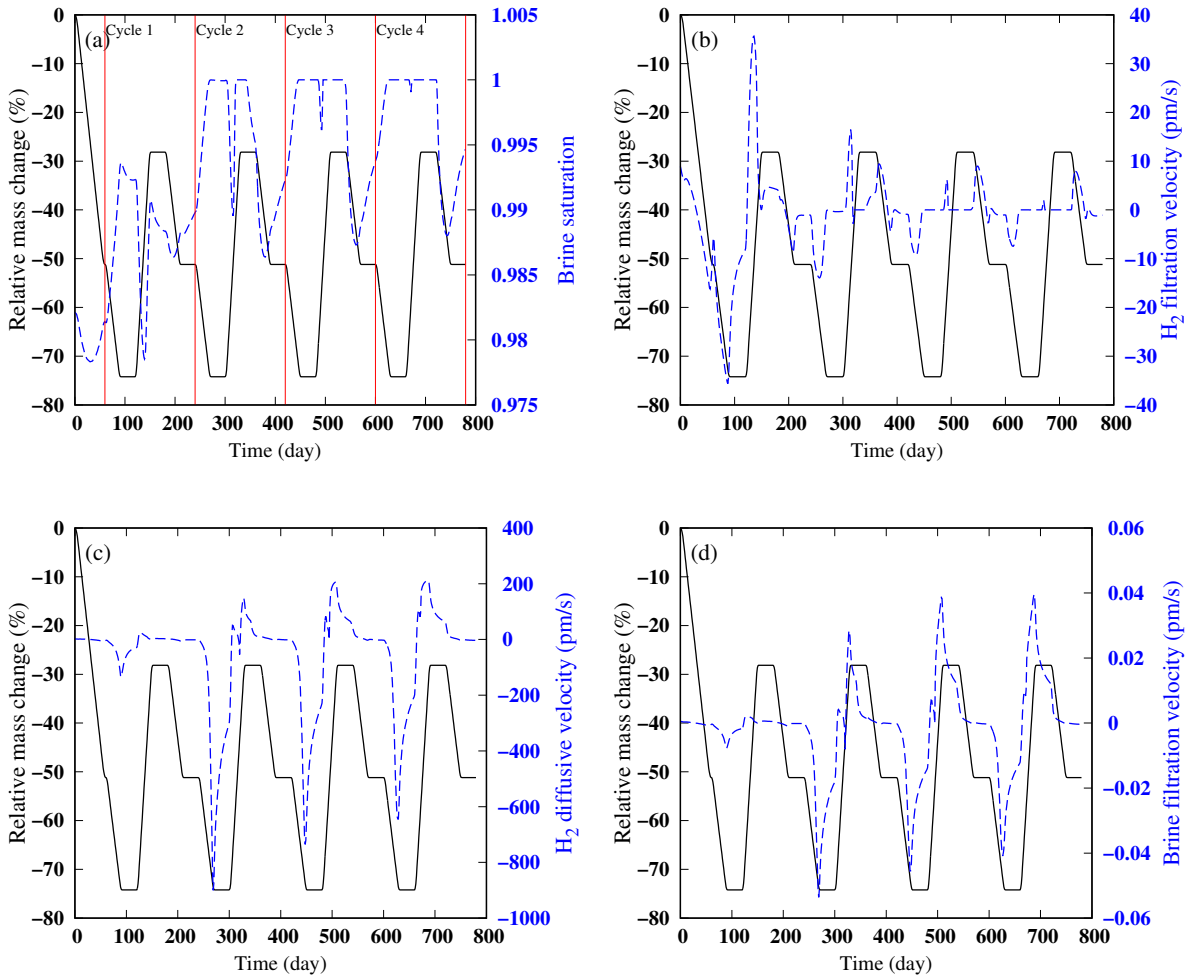

FIGURE 3.14: (a) Brine saturation at the cavern wall, as well as the surface averaged radial components of (b) the hydrogen filtration velocity, (c) the Fickian diffusive velocity, and (d) the brine filtration velocity during the first four cycles.

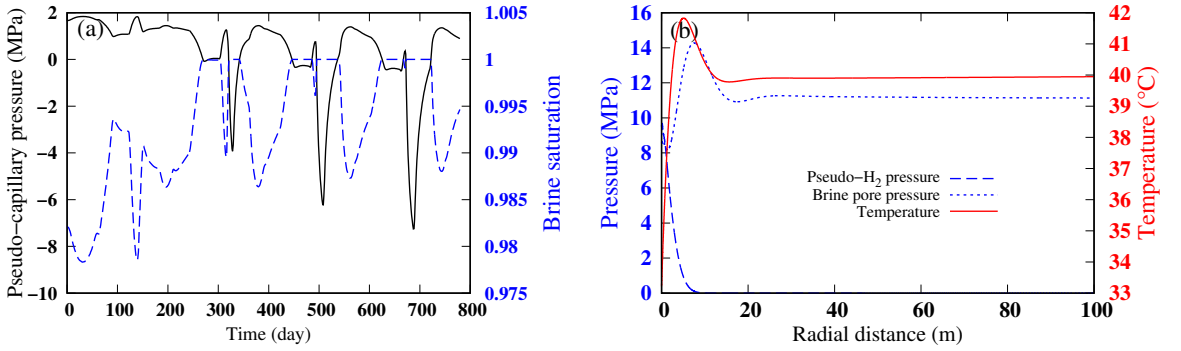

FIGURE 3.15: (a) Time variations of the cavern surface averaged brine saturation and pseudo-capillary pressure for the first four cycles. (b) Radial profiles of interstitial brine pressure, of hydrogen pseudo-pressure, and of temperature within the rock domain at the end of cycling/at 40 years.

due to brine pore pressure and rock domain temperature changes. Knowing the range of these distances helps design a network of underground caverns while avoiding harmful interactions.

Figure 3.16 shows the hydrogen mass exchanged with the surrounding rock domain due to two-phase percolation and the Fickian diffusion. Figure 3.16(a) is a zoom-in of Fig. 3.16(b) for

the first four cycles/800 days.

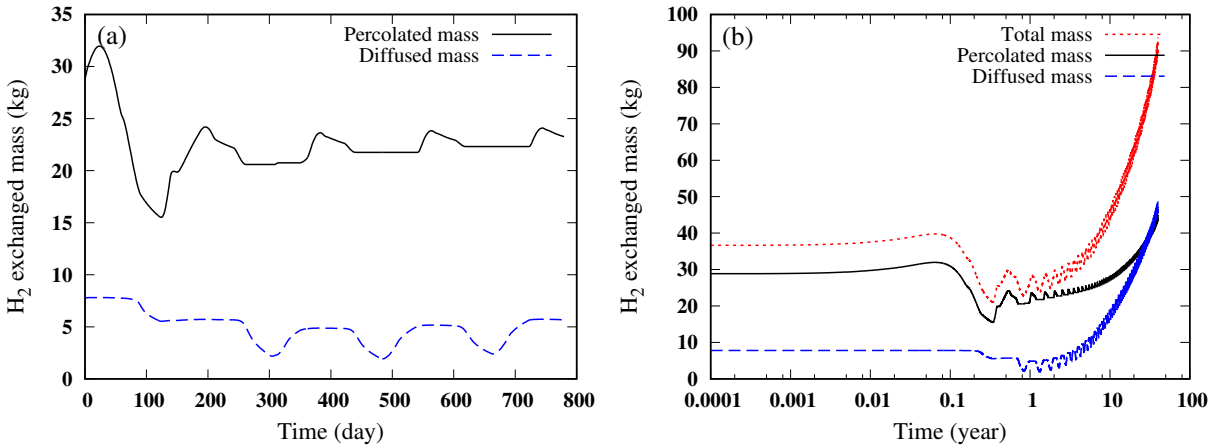

FIGURE 3.16: Darcian percolated and Fickian diffused hydrogen masses during 40 years of cycling. Figure (a) is a zoom-in of figure (b) for the first four years. The debrining and the standstill phases of 180 days have led to the initial percolated and diffused masses observed in figure (a).

Both the percolated and diffused hydrogen masses tend to reduce during withdrawal in accordance with Figs 3.14(b, c). Even-though the Fickian diffused mass is initially smaller than the percolated mass, after ∼25 years of cycling, the diffused mass becomes more significant than the two-phase percolated mass (Fig. 3.16(b)). Eventually, the percolated and the diffused hydrogen masses summed up to ∼93 kg after 40 years of the cavern operation.

3.2.4 Discussion and conclusion

The simulations on the cavern scale are performed such that an overestimating/a pessimistic scenario of lost hydrogen is considered. Therefore, while setting $\ell = 0.5$, the following values of $P_r = 8$ MPa and $\bar{D}_{g\lambda} = 5 \times 10^{-7}$ m^2/s are chosen. Cycling simulations prove that percolation happens mostly when the cavern pressure is close to the maximum cycling value, i.e. $p_\gamma \approx 16$ MPa. Yet, depending on the sign of the pressure gradient, hydrogen percolates into/leaves from the rock domain. The Fickian diffusion resembles the brine filtration, following the pressure gradient direction, hydrogen tends to diffuse into the rock domain or pours down the cavern wall along with the leaving brine. Eventually, the total mass of lost hydrogen sums up to ∼93 kg. This mass is extremely negligible compared to the hydrogen mass manipulated during one cycle ($\mathcal{M} = 2.05$ Mkg), i.e. the percentage of the lost mass to one cycle mass is ∼0.005%.

Increasing energy demands necessitate fast utilization of underground caverns. The severe utilization of salt caverns exposes them to considerable pressure and temperature changes throughout short periods, which may affect the development of the damaged zones . The introduction of a damaged zone, during cycling and at the end of leaching, can affect the total mass of the lost hydrogen. Future studies should include, in a first step, laboratory work to develop mass transport laws that would describe precisely hydrogen migration into the rock salt. In a second step, constitutive laws that quantify the permeability and porosity evolutions of rock salt due to mechanical, hydraulic and thermal charges would be needed. Once these transport and constitutive laws are developed, they can be integrated in the current framework to estimate their effect on hydrogen percolation and diffusion during rock salt damaging/severe exploitation of caverns.

3.3 Gas dissolution in the cavern brine

One promising approach for new clean energy resources is methanation, a technique used to convert carbon dioxide (CO_2) to methane using hydrogen. Methanation is supposed to reply to the energy fluctuating demand, which necessitates large storage of its production elements (H_2 and CO_2) (Mebrahtu et al., 2019). This study focuses on CO_2 dissolution kinetics in brine during storage and cycling in salt caverns in the context of clean energy transition (Zhang et al., 2022). The kinetics is strongly influenced by natural convection, which is caused by density changes related to the concentration of dissolved gas as well as thermal changes driven by gas cycling and the effects of the geothermal gradient. Based on a novel non-dimensional model that couples cavern thermodynamics with the dissolution mechanisms, this study investigates how the natural convection related to mass and thermal changes impacts dissolution kinetics. The numerical model is validated using laboratory measurements, and thereupon upscaled to typical dimensions of a salt cavern.

The effects of gas dissolution in residual brine is neglected in most of existing literature that deals with underground gas storage. It is commonly assumed that the cavern is filled with a mono-component single-phase gas. This assumption is valid if the residual brine volume is insignificant, and if the gas dissolution in the brine is insubstantial; however, residual brine may occupy up to 11% of the cavern volume (Chromik and Korzeniowski, 2021). Furthermore, some gases, especially CO_2, are soluble in brine. Therefore, gas loss due to dissolution needs to be quantified for good management of cycled quantities. This quantification becomes more important when other loss mechanisms are studied, particularly the permeation of gas into the rock domain (Sect. 3.2). Even-though this study focuses on CO_2 dissolution, the developed model is universal; it can be adapted easily to study the kinetics of dissolution of other gases.

3.3.1 The non-dimensional mathematical model

After the filling phase, the cavern brine has initially low concentration of CO_2. As CO_2 is injected into the cavern, a concentration gradient develops at the brine interface. This concentration gradient forms the driving force for the Fickian diffusion. Consequently, convection is created in the brine due to changes in the density field. A thermal convection is further developed due to cycling temperature changes at the brine interface, which interacts with the geothermal gradient of the brine. The velocity field that emerges due to both types of convection is expected to enhance the dissolution of CO_2 in the brine (F_2 of Fig. 3.1).

For each fluid phase $\alpha \in \{\lambda \text{ (liquid)}, \gamma \text{ (gas)}\}$, T_α stands for the temperature, p_α the pressure, and ρ_α the density. The subscript σ is used to designate the rock phase. Brine is assumed fully saturated with salt at any time. To simplify the mathematical problem and therefore the numerical simulations, the average gas velocity within the cavern is neglected and a uniform thermodynamic state is proposed (Sect. 3.1). This allows us to avoid the spatial discretization of the cavern domain. Consequently, the cavern thermodynamic state is used as boundary conditions for the dissolution problem in the brine domain, and for the heat transfer problem in both the brine and the rock domains. The velocity field in brine is solved for using the Navier-Stokes equation.

3.3.1.1 Fickian diffusion

At any time, a pressure equality is assumed at the gas-liquid interface $\mathcal{S}_{\gamma\lambda}$, i.e. $p_\lambda(t) = p_\gamma(t)$. The Henry law allows for calculating the mass concentration of the dissolved gas using the Henry constant H and the gas pressure, i.e. $c = c_{g\lambda} = p_\gamma / H$. In the λ-phase the barycentric movement is,

$$\rho_\lambda \boldsymbol{v}_\lambda = \rho_{g\lambda} \boldsymbol{v}_{g\lambda} + \rho_{b\lambda} \boldsymbol{v}_{b\lambda}, \tag{3.25}$$

where $\rho_{g\lambda}$ is the density of the dissolved gas in the λ-phase, $\boldsymbol{v}_{g\lambda}$ is the velocity of the dissolved gas in the λ-phase, and b is the solvent with mass concentration $1-c$. The definition of the diffusion flux $\boldsymbol{J}$ is introduced as:

$$\begin{aligned} \boldsymbol{J} = \boldsymbol{J}_{g\lambda} = c(\boldsymbol{v}_{g\lambda} - \boldsymbol{v}_{\lambda}); \quad \text{or,} \\ -\boldsymbol{J} = \boldsymbol{J}_{b\lambda} = (1-c)(\boldsymbol{v}_{b\lambda} - \boldsymbol{v}_{\lambda}). \end{aligned} \tag{3.26}$$

The gas-liquid interface is assumed still, then at $\mathcal{S}_{\gamma\lambda}$, $\boldsymbol{v}_{b\lambda} = 0$ and $\boldsymbol{v}_{\lambda} = \boldsymbol{J}/(1-c)$. Using Fick's hypothesis, the diffusion flux can be written as $\boldsymbol{J} = -D\,\boldsymbol{\nabla} c$, with D being the intrinsic diffusion coefficient.

3.3.1.2 Fluid state law

The development of the gas and liquid densities due to the thermodynamic changes and dissolution are expressed using the following state laws:

$$\begin{aligned} \text{for gas:} \quad d\rho_{\gamma} &= \partial_p \rho_{\gamma} dp + \partial_T \rho_{\gamma} dT; \\ \text{for liquid:} \quad d\rho_{\lambda} &= \partial_p \rho_{\lambda} dp + \partial_T \rho_{\lambda} dT + \partial_c \rho_{\lambda} dc. \end{aligned} \tag{3.27}$$

The liquid state law assumes that the brine is fully saturated with salt at any time. The effect of the dissolved gas as well as the temperature changes on the density are confined to the body force term of the momentum equation. The λ-phase equation of state becomes,

$$\varepsilon_{\lambda} = \frac{\rho_{\lambda}}{\rho_{\lambda 0}} = 1 + \beta(c - c_0) - \chi_{p\lambda}(T_{\lambda} - T_{\lambda 0}), \tag{3.28}$$

where values of the constant β can be found in literature (Yan, Huang, and Stenby, 2011), and $\rho_{\lambda 0}$ is the initial brine density.

3.3.1.3 Cavern thermodynamics

To simulate a uniform thermodynamic state within the cavern gas space, the system of Eqs 3.10 is used again. The only difference concerns $\bar{\pi}_g^{\gamma}$ that describes the mass rate of gas dissolution in the brine. The system of Eqs 3.10 can be cast in a non-dimensional form by defining the following non-dimensional quantities:

$$\tilde{T}_{\gamma} = \frac{T_{\gamma} - T_{\gamma 0}}{T_{\gamma 0}}; \quad \tilde{p}_{\gamma} = \frac{p_{\gamma}}{p_{\gamma 0}}; \quad \text{and} \quad \tilde{\rho}_{\gamma} = \frac{\rho_{\gamma}}{\rho_{\gamma 0}(T_{\gamma 0},\, p_{\gamma 0})}, \tag{3.29}$$

with $T_{\gamma 0}$ being the initial gas temperature, $p_{\gamma 0}$ the initial gas pressure, and $\rho_{\gamma 0}$ the initial gas density. These definitions imply that:

$$\tilde{\chi}_{T\gamma} = \chi_{T\gamma}\, p_{\gamma 0}; \quad \text{and,} \quad \tilde{\chi}_{p\gamma} = \chi_{p\gamma}\, T_{\gamma 0}, \tag{3.30}$$

where $\tilde{\chi}_{T\gamma}$ is the non-dimensional gas isothermal compressibility and $\tilde{\chi}_{p\gamma}$ is the non-dimensional gas isobaric thermal expansivity. The system of Eqs 3.10 then becomes:

$$\begin{aligned} \text{mass balance:} \quad -\tilde{\chi}_{T\gamma}\,\dot{\tilde{T}}_{\gamma} + \tilde{\chi}_{p\gamma}\dot{\tilde{p}}_{\gamma} &= \frac{Q_e\, L^2}{\mathcal{M}_{\gamma}\, D} - \frac{\bar{\pi}_g^{\gamma}\, L^2}{\mathcal{M}_{\gamma}\, D}; \\ \text{energy balance:} \quad \dot{\tilde{T}}_{\gamma} + A\frac{\tilde{\chi}_{T\gamma}(\tilde{T}+1)}{\tilde{\rho}_{\gamma}}\,\dot{\tilde{p}}_{\gamma} &= \frac{Q_e^{+}\, L^2}{\mathcal{M}_{\gamma}\, D}(\tilde{T}_{\gamma}^{\text{inj}} - \tilde{T}_{\gamma}) - B\tilde{\Psi}, \end{aligned} \tag{3.31}$$

with $A = p_{\gamma 0}/(T_{\gamma 0}\,\rho_{\gamma 0}\,C_{p\gamma})$, $B = 1/(\tilde{\mathcal{V}}_\gamma\,\tilde{\rho}_\gamma)$ with $\tilde{\mathcal{V}}_\gamma$ being the non-dimensional gas volume, and L being the characteristic length (see Eq. 3.33 below). The non-dimensional injection temperature $\tilde{T}_\gamma^{\text{inj}}$ is scaled with respect to $T_{\gamma 0}$ as indicated in Eq. 3.29.

3.3.1.4 Mass balance of the liquid phase

The mass changes of the λ-phase are attributed to the gas dissolution:

$$\rho_\lambda \partial_t c + \rho_\lambda \boldsymbol{v}_\lambda \cdot \boldsymbol{\nabla} c - \boldsymbol{\nabla} \cdot (\rho_\lambda D \boldsymbol{\nabla} c) = 0; \quad \text{with,} \quad \dot{\rho}_\lambda + \rho_\lambda \boldsymbol{\nabla} \cdot \boldsymbol{v}_\lambda = 0. \tag{3.32}$$

Taking L as the dimension of the cavern, L^2/D, D/L, and $\rho_{\lambda 0} D^2/L^2$, as scale factors for length, time, velocity, and pressure, the following non-dimensional quantities and operators are defined:

$$\tilde{t} = t\,\frac{D}{L^2}; \quad \tilde{\boldsymbol{v}}_\lambda = \boldsymbol{v}_\lambda\,\frac{L}{D}; \quad \tilde{P}_\lambda = P_\lambda\,\frac{L^2}{\rho_{\lambda 0} D^2}; \quad \text{and,} \quad \tilde{\nabla}\varphi = \nabla\varphi\, L. \tag{3.33}$$

The mass concentration is normalized with respect to the saturation concentration of the liquid phase c_{sat}, i.e. $\tilde{c} = c/c_{\text{sat}}$. Using the non-dimensional definitions along with Eq. 3.28, the non-dimensional form of Eq. 3.32 can be found:

$$\varepsilon_\lambda \partial_{\tilde{t}} \tilde{c} + \varepsilon_\lambda \tilde{\boldsymbol{v}}_\lambda \cdot \tilde{\boldsymbol{\nabla}} \tilde{c} - \tilde{\boldsymbol{\nabla}} \cdot (\varepsilon_\lambda \tilde{\boldsymbol{\nabla}} \tilde{c}) = 0; \quad \text{with,} \quad \partial_{\tilde{t}} \varepsilon_\lambda + \tilde{\boldsymbol{\nabla}} \cdot (\varepsilon_\lambda \tilde{\boldsymbol{v}}_\lambda) = 0. \tag{3.34}$$

3.3.1.5 Momentum balance of the liquid phase

The momentum balance equation for the liquid phase can be written as,

$$\rho_\lambda \partial_t \boldsymbol{v}_\lambda + \rho_\lambda \boldsymbol{v}_\lambda \cdot \underline{\underline{\boldsymbol{\nabla}}} \boldsymbol{v}_\lambda = -\boldsymbol{\nabla} P_\lambda + \boldsymbol{\nabla} \cdot \underline{\underline{\boldsymbol{\zeta}}} + (\rho_\lambda - \rho_{\lambda 0})\mathfrak{g}, \tag{3.35}$$

with $\underline{\underline{\boldsymbol{\zeta}}}$ being the viscous stress tensor, i.e. $\underline{\underline{\boldsymbol{\zeta}}} = \mu_\lambda \left(\underline{\underline{\boldsymbol{\nabla}}} \boldsymbol{v}_\lambda + \underline{\underline{\boldsymbol{\nabla}}} \boldsymbol{v}_\lambda^{\mathrm{T}}\right) - (2/3)\mu_\lambda \left(\boldsymbol{\nabla} \cdot \boldsymbol{v}_\lambda\right) \underline{\underline{\boldsymbol{\delta}}}$, the brine dynamic viscosity is μ_λ, and $\underline{\underline{\boldsymbol{\delta}}}$ is the second-order Kronecker delta. The λ-phase pressure P_λ is calculated with respect to the gas pressure and to the initial hydrostatic pressure ($p_{\lambda H} = -\rho_{\lambda 0}\mathfrak{g}z$), i.e. $P_\lambda = p_\lambda - p_\gamma - p_{\lambda H}$. At the brine interface, $P_\lambda(t) = 0$ and $p_\lambda(t) = p_\gamma(t)$. Initially in the brine domain, $p_{\lambda 0} = p_{\gamma 0} + p_{\lambda H}$ and $P_{\lambda 0} = 0$.

The non-dimensional form of Eq. 3.35 can be written as,

$$\varepsilon_\lambda \partial_{\tilde{t}} \tilde{\boldsymbol{v}}_\lambda + \varepsilon_\lambda \tilde{\boldsymbol{v}}_\lambda \cdot \underline{\underline{\tilde{\boldsymbol{\nabla}}}} \tilde{\boldsymbol{v}}_\lambda = -\tilde{\boldsymbol{\nabla}} \tilde{P}_\lambda + \mathrm{Pr} \tilde{\boldsymbol{\nabla}} \cdot \underline{\underline{\tilde{\boldsymbol{\zeta}}}} + \mathrm{RaPr}\, \boldsymbol{e}_z, \tag{3.36}$$

with $\underline{\underline{\tilde{\boldsymbol{\zeta}}}} = \underline{\underline{\tilde{\boldsymbol{\nabla}}}} \tilde{\boldsymbol{v}}_\lambda + \underline{\underline{\tilde{\boldsymbol{\nabla}}}} \tilde{\boldsymbol{v}}_\lambda^{\mathrm{T}} - (2/3)\,\tilde{\boldsymbol{\nabla}} \cdot \tilde{\boldsymbol{v}}_\lambda \underline{\underline{\boldsymbol{\delta}}}$ and $\tilde{P}_\lambda$ being the λ-phase non-dimensional pressure. The brine dynamic viscosity is assumed constant. Therefore, the Prandtl number of the natural convection problem is defined as,

$$\mathrm{Pr} = \frac{\mu_\lambda}{\rho_{\lambda 0}\, D}, \quad \text{and the Rayleigh number is } \mathrm{Ra} = \frac{\mathfrak{g}(\varepsilon_\lambda - 1)\rho_{\lambda 0} L^3}{D \mu_\lambda}. \tag{3.37}$$

Since the intrinsic diffusion coefficient of CO_2 in brine is very small, the simulations lead to high values of the Parndtl number ($\mathrm{Pr} \gg 1$). This indicates the dominance of the momentum diffusivity over the chemical/Fickian diffusivity (Busse and Whitehead, 1971). On the other hand, the Rayleigh number characterizes the regime of the gas flow in the brine phase. When the Rayleigh number is small (typically $\mathrm{Ra} < 10^3$), natural convection is negligible. Besides, a turbulent model is necessary to fully describe the velocity field when Buoyancy forces are considerably high, i.e. $\mathrm{Ra} > 10^8$ (Sankar et al., 2011). This research numerical model accounts

only for laminar flow, the Rayleigh number is expected to fall within its range, i.e. $10^3 < \mathrm{Ra} < 10^8$.

3.3.1.6 Energy balance of the liquid phase

The energy equation of the λ-phase can be cast in the following form,

$$\rho_\lambda C_{p\lambda} \partial_t T_\lambda + \rho_\lambda C_{p\lambda} \boldsymbol{v}_\lambda \cdot \boldsymbol{\nabla} T_\lambda - \boldsymbol{\nabla} \cdot (\Lambda_\lambda \boldsymbol{\nabla} T_\lambda) = 0, \tag{3.38}$$

with $C_{p\lambda}$ being the brine heat capacity, and Λ_λ is the brine thermal conductivity. If the non-dimensional brine temperature is defined as $\tilde{T}_\lambda = (T_\lambda - T_{\lambda 0})/T_{\lambda 0}$, and its heat capacity is assumed constant, the non-dimensional form of Eq. 3.38 is written as,

$$\varepsilon_\lambda \partial_{\tilde{t}} \tilde{T}_\lambda + \varepsilon_\lambda \tilde{\boldsymbol{v}}_\lambda \cdot \tilde{\boldsymbol{\nabla}} \tilde{T}_\lambda - \tilde{\boldsymbol{\nabla}} \cdot \left(\frac{\mathcal{K}_\lambda}{D} \tilde{\boldsymbol{\nabla}} \tilde{T}_\lambda \right) = 0, \tag{3.39}$$

the brine thermal diffusivity $\mathcal{K}_\lambda = \Lambda_\lambda / \rho_{\lambda 0} C_{p\lambda}$ is assumed constant.

3.3.1.7 Energy balance of the solid phase

To solve for heat exchange between the fluid phases and the rock domain, the energy equation of the σ-phase is required,

$$\rho_\sigma C_{p\sigma} \partial_t T_\sigma - \boldsymbol{\nabla} \cdot (\Lambda_\sigma \boldsymbol{\nabla} T_\sigma) = 0, \tag{3.40}$$

with $C_{p\sigma}$ being the rock salt heat capacity, and Λ_σ is the rock salt thermal conductivity. Keeping in mind that $\tilde{T}_\sigma = (T_\sigma - T_{\sigma 0})/T_{\sigma 0}$, the non-dimensional form of this equation is,

$$\partial_{\tilde{t}} \tilde{T}_\sigma - \tilde{\boldsymbol{\nabla}} \cdot \left(\frac{\mathcal{K}_\sigma}{D} \tilde{\boldsymbol{\nabla}} \tilde{T}_\sigma \right) = 0, \tag{3.41}$$

where the rock salt thermal diffusivity is $\mathcal{K}_\sigma = \Lambda_\sigma / \rho_\sigma C_{p\sigma}$.

The exchanged power Ψ (Eq. 3.10) has two parts,

$$\Psi = \underbrace{\int_{\mathcal{S}_{\gamma\sigma}} -\Lambda_\sigma \boldsymbol{\nabla} T_\sigma \cdot \boldsymbol{n} \, d\mathcal{A}_{\gamma\sigma}}_{\text{exchanged with rock}} + \underbrace{\int_{\mathcal{S}_{\gamma\lambda}} -\Lambda_\lambda \boldsymbol{\nabla} T_\lambda \cdot \boldsymbol{n} \, d\mathcal{A}_{\gamma\lambda}}_{\text{exchanged with brine}}, \tag{3.42}$$

where the unit normal outward vector is $\boldsymbol{n}$. The surface integrations are calculated over the gas-solid interface $\mathcal{S}_{\gamma\sigma}$ with its area $\mathcal{A}_{\gamma\sigma}$, and the gas-liquid interface $\mathcal{S}_{\gamma\lambda}$ with its area $\mathcal{A}_{\gamma\lambda}$. The non-dimensional exchanged power (Eq. 3.31) is defined as,

$$\tilde{\Psi} = \int_{\tilde{\mathcal{S}}_{\gamma\sigma}} -w_\sigma \tilde{\boldsymbol{\nabla}} \tilde{T}_\sigma \cdot \boldsymbol{n} \, d\tilde{\mathcal{A}}_{\gamma\sigma} + \int_{\tilde{\mathcal{S}}_{\gamma\lambda}} -w_\lambda \tilde{\boldsymbol{\nabla}} \tilde{T}_\lambda \cdot \boldsymbol{n} \, d\tilde{\mathcal{A}}_{\gamma\lambda}, \tag{3.43}$$

with $w_\sigma = (T_{\sigma 0}/T_{\gamma 0}) \left[\Lambda_\sigma / (\rho_{\gamma 0} \, C_{p\gamma} \, D) \right]$ and $w_\lambda = (T_{\lambda 0}/T_{\gamma 0}) \left[\Lambda_\lambda / (\rho_{\gamma 0} \, C_{p\gamma} \, D) \right]$, where $\tilde{S}_{\gamma\sigma}$ and $\tilde{S}_{\gamma\lambda}$ are the non-dimensional interfaces as well as $\tilde{A}_{\gamma\sigma}$ and $\tilde{A}_{\gamma\lambda}$ are their non-dimensional areas.

Since the model is non-dimensional, once validated by the laboratory measurements, it can be applied to other scales. Experimental work is required, some of it considered in this research, in order to establish the key model parameters. Such experiments should be performed under conditions similar to the geological storage, in terms of pressure and temperature.

3.3.2 Initial and boundary conditions

In this section the initial and boundary conditions for the gas dissolution problem, both at the laboratory and at the cavern scales, are defined.

3.3.2.1 Initial conditions

The temperature is controlled at the laboratory scale (Sect. 3.3.3) by placing the dissolution cell in a temperature-controlled basin. Consequently, the temperature of all phases is maintained at T_0. At the cavern scale (Sect. 3.3.5), all phases are initially assumed to be in thermal equilibrium which corresponds to the geothermal gradient. Temperature is non-dimensionalized with respect to an initial T_0.

The gas pressure in the laboratory cell is initially equal to the vapor pressure[3]. However, at the cavern scale, it is determined by the cavern working conditions, i.e. the cavern depth. The initial brine pressure is $P_{\lambda 0} = 0$ because $p_{\lambda 0} = p_{\gamma 0} + p_{\lambda H}$. Subsequent changes in the brine pressure are generated by gas dissolution.

3.3.2.2 Boundary conditions

At the gas-liquid interface, gas can dissolve into or exsolve from the brine phase as a function of the gas pressure. The brine and gas also exchange heat based on the cycling program. There is also heat exchange between these two phases and the surrounding rock domain. At the interface $\mathcal{S}_{\gamma\lambda}$, the following definitions are employed:

- the gas mass concentration is $c = p_\gamma / H$. Its non-dimensional form is $\tilde{c} = c / c_{\text{sat}}$;
- the flow of gas into the λ-phase is expressed as $\boldsymbol{J} \cdot \boldsymbol{n} = K(c - p_\gamma / H)$, with K being an experimental mass transfer coefficient. In a non-dimensional form, this expression becomes $\tilde{\boldsymbol{J}} \cdot \boldsymbol{n} = \tilde{K}(\tilde{c} - p_\gamma / (H\, c_{\text{sat}}))$, with $\tilde{\boldsymbol{J}} = -\boldsymbol{\nabla}\tilde{c}$ and $\tilde{K} = K\,(L/D)$;
- the non-dimensional λ-phase velocity at the interface $\mathcal{S}_{\gamma\lambda}$ takes the following form $\tilde{\boldsymbol{v}}_\lambda = \tilde{\boldsymbol{J}} / (1/c_{\text{sat}} - \tilde{c})$. This is equivalent to $\tilde{\boldsymbol{v}}_\lambda \cdot \boldsymbol{n} = \tilde{K}(\tilde{c} - p_\gamma / (H\, c_{\text{sat}}))/(1/c_{\text{sat}} - \tilde{c})$;
- the mass rate of the dissolved gas is $\bar{\pi}_g^\gamma = -\int_{\mathcal{S}_{\gamma\lambda}} \rho_\lambda \boldsymbol{v}_\lambda \cdot \boldsymbol{n}\, d\mathcal{A}_{\gamma\lambda}$, with $\boldsymbol{n}$ being the normal outward vector. In a non-dimensional form, the following definition is reached,

$$\frac{\bar{\pi}_g^\gamma\, L^2}{\mathcal{M}_\gamma\, D} = \frac{-\int_{\tilde{\mathcal{S}}_{\gamma\lambda}} \varepsilon_\lambda \tilde{\boldsymbol{v}}_\lambda \cdot \boldsymbol{n}\, d\tilde{\mathcal{A}}_{\gamma\lambda}}{\tilde{\mathcal{V}}_\gamma\, \varepsilon_{\gamma\lambda}} = \frac{-\int_{\tilde{\mathcal{S}}_{\gamma\lambda}} \varepsilon_\lambda \left[\dfrac{\tilde{K}(\tilde{c} - p_\gamma / (H\, c_{\text{sat}}))}{1/c_{\text{sat}} - \tilde{c}}\right] d\tilde{\mathcal{A}}_{\gamma\lambda}}{\tilde{\mathcal{V}}_\gamma\, \varepsilon_{\gamma\lambda}}, \tag{3.44}$$

  with $\varepsilon_{\gamma\lambda} = \rho_\gamma / \rho_{\lambda 0}$. During cycling or dissolution, the gas density evolves. Therefore, a gas state law is used to trace the gas density as a function of pressure and temperature (Kunz et al., 2007), i.e. $\rho_\gamma = \rho_\gamma\left(\tilde{p}_\gamma p_{\gamma 0},\, [(\tilde{T}_\gamma T_{\gamma 0}) + T_{\gamma 0}]\right)$;
- the conditions $p_\gamma(t) = p_\lambda(t)$ and $\tilde{P}_\lambda(t) = 0$ are set at time t.

The following other boundary conditions are needed:

- the temperature boundary condition between the brine and the rock phases is defined such that $\tilde{T}_\lambda(t) = \tilde{T}_\sigma(t)$ at any time t;
- between the gas and the rock phases, temperature continuity is assumed, i.e. $\tilde{T}_\gamma(t) = \tilde{T}_\sigma(t)$ at any time t;

[3] The cell is vacuumed and brine is injected into it prior to the gas introduction.

– between the gas and the brine phases, a heat transfer coefficient $h_{\gamma\lambda}$ is introduced, leading to the following non-dimensional heat exchange formula: $-\tilde{\boldsymbol{\nabla}}\tilde{T}_\lambda.\boldsymbol{n} = \tilde{h}_{\gamma\lambda}\left(\tilde{T}_\gamma - \tilde{T}_\lambda\right)$ and $\tilde{h}_{\gamma\lambda} = h_{\gamma\lambda}\left(L/\Lambda_\lambda\right)$;

– an appreciably large rock domain is considered in our modelling to avoid the effect of far-field boundaries. The far-field temperatures are set equal to the geothermal gradient all the time.

The model parameters β and D can be found in literature (Yan, Huang, and Stenby, 2011; Tayeb et al., 2023). The mass transfer coefficient K needs to be adjusted experimentally so that the experimental data and the simulation curves would have the same initiation behavior. The same values of these parameters are used on any scale. However, if such parameters have units, once the equations are worked out in a non-dimensional form, they get scaled by their equivalent scale factors (see Tables 3.2 and 3.3). All the non-dimensionalization details can be found in AbuAisha et al. (2023).

3.3.3 CO_2 dissolution at the laboratory scale scale

Before applying the non-dimensional model at the cavern scale, experimental validation is needed. Laboratory experiments are performed based on a pressure decay test using a PVT (Pressure-Volume-Temperature) cell. In this setup, the CO_2 gas is injected from a tank into the cell that is partially filled with saturated brine. The cell temperature is controlled by placing it into a temperature-controlled basin (Fig. 3.17). Once gas is injected, it starts dissolving in the liquid phase.

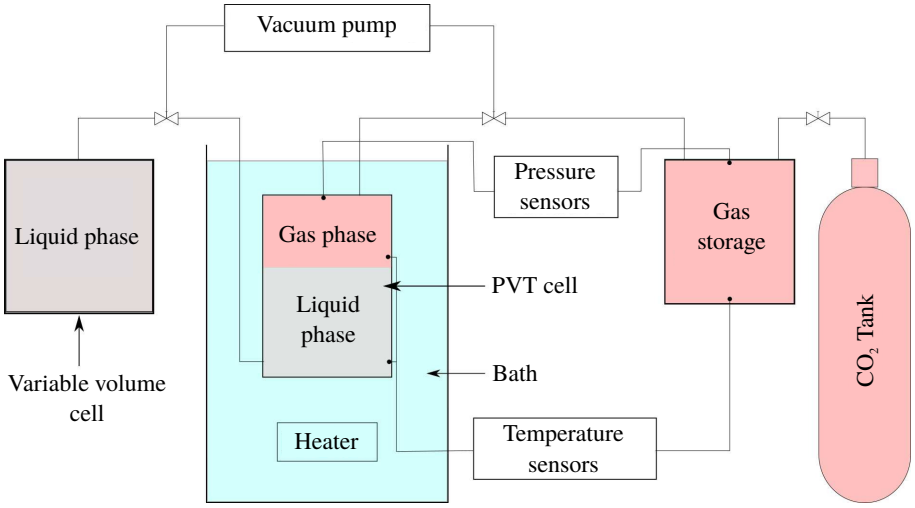

FIGURE 3.17: Schematic representation of the pressure decay PVT cell used to study the CO_2 dissolution in the brine, and to validate the mathematical model.

The PVT cell has a volume of 131.64 cm^3 and a diameter of 4 cm. Two dissolution tests are carried out. In the two tests, the cell is initially filled with saturated brine[4] to a 26.32 cm^3 volume. Gas is subsequently injected at initial pressures that correspond to the geological storage conditions, with the basin temperature set equal to 40 °C.

Table 3.2 shows the test conditions and model parameters of the two PVT cell experiments. The table presents the values as given to a typical dimensional model and as fed to the non-dimensional model of this research. The characteristic length is chosen to be equal to the model radius $L = R = 0.02$ m. It is used along with the intrinsic diffusion coefficient D to calculate the scale factors of Eq. 3.33. The β parameter gives an idea about how the brine density changes

[4]The salt mass represented 22.5% of the solution mass.

TABLE 3.2: Test conditions and model parameters of the two PVT experiments. References: 1. (Tayeb et al., 2023); 2. (Yan, Huang, and Stenby, 2011); 3. (Chabab et al., 2019).

As given to a typical dimensional model							
	$p_{\gamma 0}$ (MPa)	D (m^2/s)	$L = R$ (m)	c_0	β	H (MPa)	K (m/s)
Test 1	12.90	6.5×10^{-9}	0.02	0.01123	0.212	550	2.52×10^{-5}
Test 2	16.87	6.5×10^{-9}	0.02	0.01389	0.212	726	2.52×10^{-5}
Reference	–	[1]	–	Calculated	[2]	[3]	Adjusted
As given to the non-dimensional model							
	$\tilde{p}_{\gamma 0}$		$\tilde{R}$	$\tilde{c}_0$	β	$\tilde{H}$	$\tilde{K}$
Test 1	1.0		1	0.60	0.212	42.64	77.54
Test 2	1.0		1	0.74	0.212	43.03	77.54

[1] The initial brine density is $\rho_{\lambda 0} = 1200$ kg/m^3 and its viscosity is $\mu_\lambda = 3.6 \times 10^{-3}$ Pa s
[2] The scaling of the gas pressure and the Henry coefficient values is done using $p_{\gamma 0} = 12.90$ MPa for test 1 and $p_{\gamma 0} = 16.87$ MPa for test 2
[3] The CO_2 concentrations are scaled with respect to $c_{\text{sat}} = 0.0188$
[4] $\tilde{K} = K\,(L/D)$

as a function of the dissolution. It is already non-dimensional and does not vary between the two approaches. The model parameter K is adjusted experimentally such that the initiation of the numerical response correlates with the experimental data. A real gas behavior is considered in the simulations. A high accuracy state equation is used as described in Kunz et al. (2007). Since the cell is placed in the basin all the time, an isothermal condition is prevailing. Equations 3.34 and 3.36 are only solved for in the brine domain. As an interface boundary condition, the first part of the gas Eq. 3.31 is used without the thermal contribution, and it is completed with Eq. 3.44 to account for the mass exchange. Although the initial CO_2 concentration of the brine should be zero, the fast injection to high pressure has evidently caused some CO_2 to dissolve in the brine during the filling phase. The CO_2 concentration in the brine is normalized with respect to the saturation value ($c_{\text{sat}} = 0.0188$) at $p_\gamma = 14$ MPa and temperature $T_\gamma = 40$ °C. The initial concentrations are calculated by inverse mass calculations between the final and the initial tests statuses (Yang and Gu, 2006). Figure 3.18 shows how our numerical model correlates to the experimental data. The pressure histories are normalized with respect to the initial gas pressure indicated on each figure.

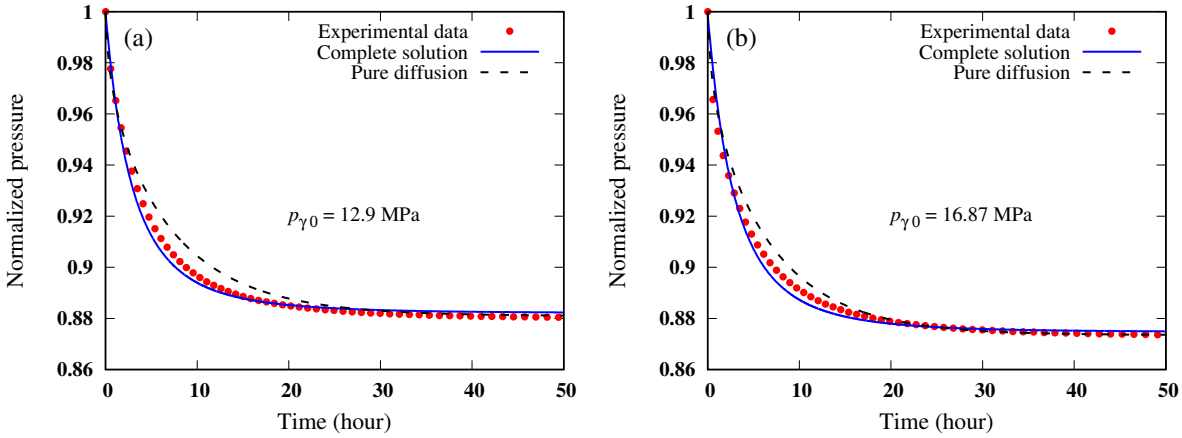

FIGURE 3.18: A comparison between the numerical and the experimental pressure histories for the two laboratory tests: (a) $p_{\gamma 0} = 12.9$ MPa; and (b) $p_{\gamma 0} = 16.87$ MPa. The black curves represent the numerical solutions while considering only pure diffusion ($D_{\text{app}} = 8.6 \times 10^{-8}$ m^2/s).

The black curves (Fig. 3.18) represent the numerical solutions while considering only the diffusion phenomenon, i.e. only Eq. 3.34 in the brine domain. For these solutions to correlate to the experimental data, the diffusion coefficient needs to be enhanced. The method adopted in this research is based on increasing the intrinsic diffusion coefficient gradually until a match is reached between the numerical solution and the experimental data. The match value of the diffusion coefficient is then saved and called an apparent diffusion coefficient D_{app}. Figure 3.18 shows that an apparent diffusion with value $D_{\text{app}} = 8.6 \times 10^{-8}$ m^2/s is sufficient to represent the effect of the convection process.

3.3.4 Thermal effects on the kinetics of dissolution

Although our numerical model reproduces the kinetics of CO_2 dissolution in brine, upscaling it to the cavern scale is arduous. Difficulties stem from the use of the Navier-Stokes equation (3.36). As the model dimension is increased, the body forces represented by the term (Ra Pr) intensify by a power of three. There is a limiting characteristic length after which the numerical convergence becomes exceedingly slow. In this vein, when the two terms ($\tilde{\boldsymbol{\nabla}}\tilde{P}_\lambda$ and Ra Pr $\boldsymbol{e}_z$) are of the same order of magnitude, the simulations run correctly. The use of an apparent diffusion to represent the complex effects of convection (Fig. 3.18) seems to be the solution. However, at the cavern scale, this approach is impractical for two main reasons:

1. in addition to tuning the apparent D parameter, the apparent mass transfer coefficient K also requires tuning, since both of these apparent parameters depend upon the scale of the problem;

2. the cavern brine is characterized by a geothermal gradient, while the gas cycling within the cavern drives significant thermal changes on the brine surface. These thermal effects cannot be neglected at the cavern scale.

The mathematical model developed in Sect. 3.3.1 is general; it accounts for thermal changes effects on the kinetics of dissolution. Equation 3.28 highlights the importance of thermal changes on the natural convection due to density alteration. AbuAisha et al. (2023) have numerically investigated the effect of applying a temperature gradient on the kinetics of dissolution. Different numerical simulations have been conducted while applying different temperature gradients over the laboratory cell (Sect. 3.3.3). It is observed that the dissolution kinetics increases substantially as a function of the temperature gradient. The brine may occupy up to 11% of the cavern volume (Chromik and Korzeniowski, 2021) and will generally be characterized by a linear thermal gradient. Taken together with the cycling effects, it is clear that thermal effects play a significant role for the dissolution process.

3.3.5 CO_2 dissolution at the cavern scale

This section presents the CO_2 dissolution at the cavern scale. To highlight the importance of considering the kinetics of dissolution, two scenarios are considered: namely while accounting for kinetics by coupling the cavern thermodynamics with the dissolution; and while neglecting kinetics and calculating the saturation concentration in a post-treatment strategy. The results of the two scenarios are compared systematically.

3.3.5.1 The numerical model

The numerical model represents a cylindrical cavern of volume $\mathcal{V} = 42412$ m^3 in an infinite rock salt domain (Fig. 3.19). The cavern brine occupies almost 11% of the volume over a height of 1.5 m. The cavern is assumed to be initially full of real CO_2 at a pressure of 16 MPa. The cavern and its brine are in thermal equilibrium with the surrounding rock domain. The geothermal

gradient gives a cavern volume averaged temperature of 44 °C and a temperature difference of 0.045 °C over the brine height.

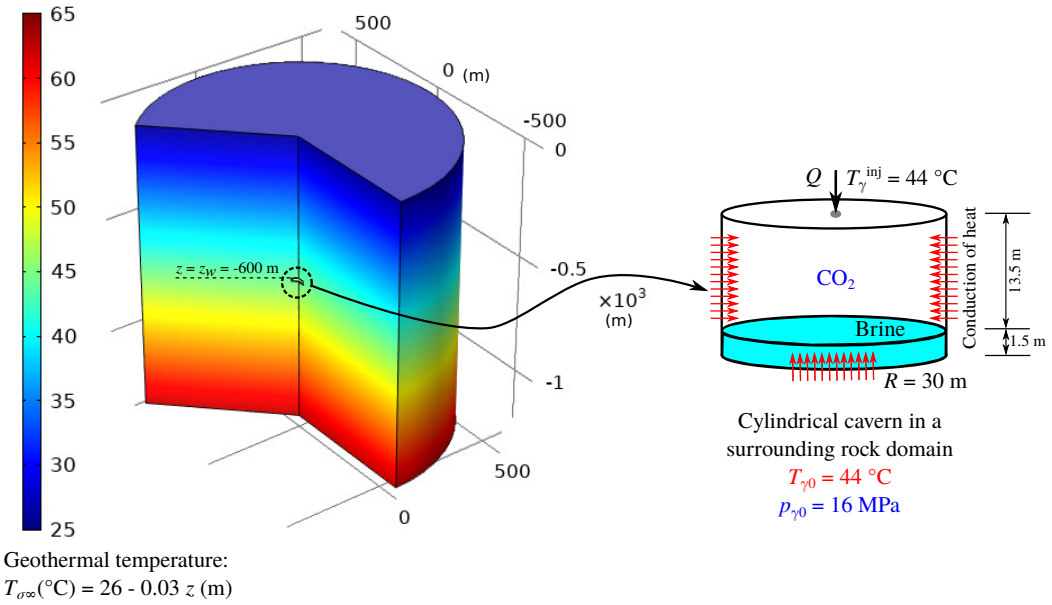

FIGURE 3.19: Schematic diagram of the boundary value problem: it represents a cylindrical cavern created at a depth of 600 m in a surrounding rock salt domain. The geothermal gradient gives a cavern volume averaged temperature of 44 °C. The cavern is assumed initially full of real CO_2 at a pressure of 16 MPa. This figure is presented in the dimensional form.

For simplicity, a homogeneous thermodynamic state is assumed within the cavern. The cavern thermodynamics (Eq. 3.31) is used simply as boundary conditions for heat transfer with the rock domain, and for heat and mass transfer with the brine (Fig. 3.20).

Figure 3.20 shows a two-dimensional axisymmetric discretization of the boundary value problem of Fig. 3.19. The figure represents the model used with the COMSOL software, shown in a non-dimensional form. A typical geothermal gradient of 3 °C/100 m is defined. The far-field boundary conditions are assumed to be of the Dirichlet type. A temperature continuity is assumed between the cavern gas and the rock domain, and between the cavern brine and the rock domain. A heat transfer coefficient $h_{\gamma\lambda} = 12$ (W/m^2/K) is chosen to account for thermal changes between the gas and the brine (Bourne-Webb, Bodas Freitas, and da Costa Gonçalves, 2016). A pressure continuity on the surface $\mathcal{S}_{\gamma\lambda}$ is assured between the two phases all the time. Therefore, initially, $p_\lambda(\boldsymbol{x}, 0) = p_{\gamma 0} + p_{\lambda H}(\boldsymbol{x})$ and $P_{\lambda 0} = \tilde{P}_{\lambda 0} = 0$ every where in the brine domain.

The characteristic length is taken equal to the brine height, i.e. $L = 1.5$ m. The CO_2 concentration is normalized with regard to the saturation value $c_{\text{sat}} = 0.0188$ for an average cycling pressure of $\langle p_\gamma \rangle = 14$ MPa. To account for the effect of the filling phase, the brine is assumed to have an initial CO_2 concentration of $c_0 = 0.0023$ (almost 12% of the saturation value). The Henry coefficient is assumed to be a function of the fluctuating gas pressure during cycling (Chabab et al., 2019). The same values of the model parameters (β, D, and K) of Table 3.2 are used at the cavern scale. Yet, the scale factors of Eq. 3.33 are calculated with respect to the new characteristic length. Table 3.3 presents the non-dimensional model parameters as given to the COMSOL software. The temperatures of the cavern three phases are normalized with respect to $T_0 = 44$ °C. Brine thermo-physical properties are assigned the following values (Gevantman and Lorenz, 1981): $\Lambda_\lambda = 0.51$ (W/m/K); $C_{p\lambda} = 3300$ (J/kg/K); and $\chi_{p\lambda} = 45 \times 10^{-5}$ (1/K).

The operation cycling program for this research is presented in Fig. 3.21. A withdrawal phase is firstly recognized, where the relative mass changes $(\mathcal{M}_\gamma/\mathcal{M}_{\gamma 0} - 1) \times 100\%$ are decreased to -2.5%. Cycling starts subsequently where four cycles are accounted for. This cycling program demonstrates a weekly utilization of the cavern where changes spread out over

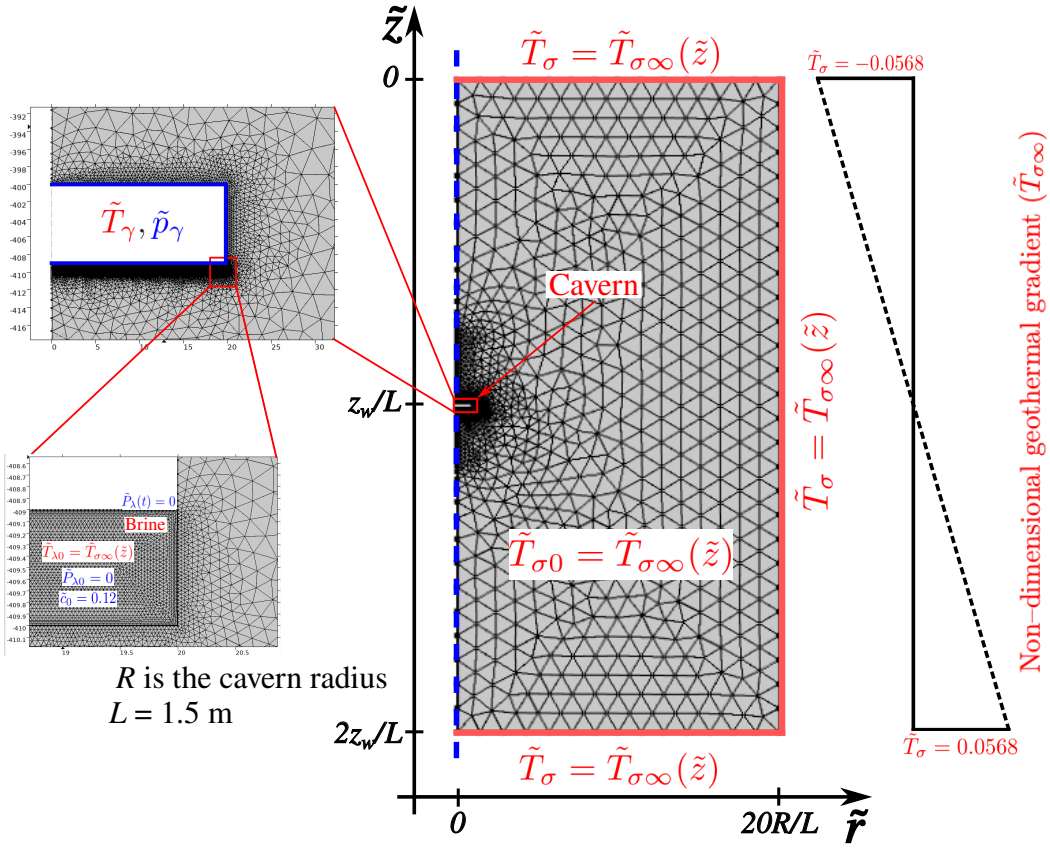

FIGURE 3.20: Two-dimensional axisymmetric discretization of the boundary value problem of Fig. 3.19. A surrounding rock volume of $\tilde{r} = 20R/L$ is chosen around the cavern to avoid the effect of far-field boundaries. The gas domain is not considered in modeling, and only the brine domain is discretized. The cavern thermodynamics ($\tilde{p}_\gamma$, $\tilde{T}_\gamma$) is used as boundary conditions for heat transfer with the rock domain, and heat and mass transfer with the brine. The mesh is heavily refined close to the cavern to account for the abrupt changes taking place close to it. The mesh contains 144665 elements, of which 9183 are quadrilateral boundary elements.

TABLE 3.3: Non-dimansionaml model parameters at the cavern scale. Reference: 1. (Chabab et al., 2019).

$L = H$ (m) (Brine height)	$\tilde{R}$	$\tilde{c}_0$	β	$\tilde{H} = f(\tilde{p}_\gamma)$	$\tilde{K}$	$\tilde{h}_{\gamma\lambda}$
1.5	20	0.12	0.212	Evolving [1]	5815.38	35.29

[1] $D = 6.5 \times 10^{-9}$ m^2/s, $\rho_{\lambda 0} = 1200$ kg/m^3, and $\mu_\lambda = 3.6 \times 10^{-3}$ Pa s
[2] The CO_2 saturation concentration is $c_{\text{sat}} = 0.0188$
[3] $\tilde{K} = K\,(L/D)$, and $\tilde{h}_{\gamma\lambda} = h_{\gamma\lambda}(L/\Lambda_\lambda)$

a period of ∼28 days. Only the first four cycles are presented, however, this program can be repeated over long periods of time.

3.3.5.2 Results and discussion

Two scenarios are adopted to present the results of CO_2 dissolution at the cavern scale. In the first scenario, the kinetics of dissolution is neglected. Hence, the CO_2 saturation concentration c_{sat} is calculated as a function of the cavern thermodynamics (p_γ and T_γ). In this scenario, only the cavern thermodynamics is solved whilst considering heat exchange with the rock and the brine domains. In the second scenario, the cavern thermodynamics is coupled with dissolution in the brine domain, and the entire problem is solved. This enables comparison between simulations of the two scenarios, and consequently insights into the importance of considering the

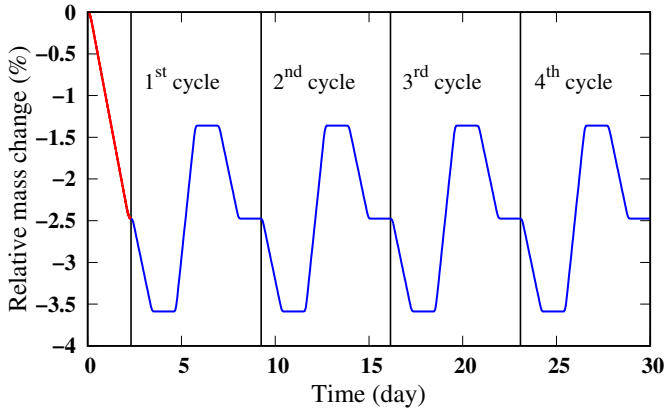

FIGURE 3.21: The cycling program envisaged for this research: a weekly utilization of the cavern with four cycles spreading over ∼28 days. Cycling leads to reasonable mass variations where the cycled CO_2 stays always in its supercritical state.

kinetics of dissolution to periodically calculate the dissolved gas mass.

During the first scenario, the cycling program of Fig. 3.21 is repeated over a period of 2 years. The saturation concentration is subsequently calculated in a post-treatment approach, where such values are found abundantly in the literature. For instance, Fig. 3.22 shows the saturation concentration of CO_2 in brine as a function of temperature and pressure for the range used in this paper (Chabab et al., 2019).

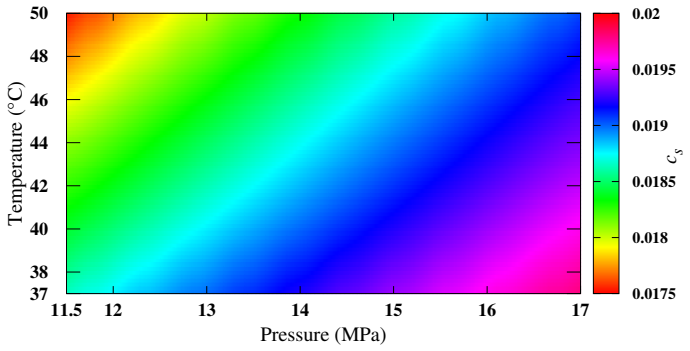

FIGURE 3.22: Saturation concentration of CO_2 in brine as a function of pressure and temperature (Chabab et al., 2019).

Figures 3.23(a, b) show the evolution of the cavern pressure and temperature as a function of cycling over two years. The cavern thermodynamics is used in a post-treatment strategy to calculate the CO_2 saturation concentration in brine as a function of the relative mass variations (Fig. 3.23(c)).

Following Fig. 3.23(b) one can see clearly the effect of heat exchange with the rock and the brine domains on the cavern temperature. This effect is reflected by the cavern pressure, which shows evolving behavior during cycling (Fig. 3.23(a)). The brine CO_2 saturation concentration varies slightly ($c_{\text{sat}} \in [0.0187, 0.0192]$) for the temperature and pressure ranges considered in this research (Fig. 3.23(c)). This saturation concentration can be converted into dissolved CO_2 mass. Knowing the brine volume $\mathcal{V}_\lambda$ and its average density ($\langle\rho_\lambda\rangle = 1158$ kg/m^3), the dissolved CO_2 mass is calculated as $\mathcal{M}_{\gamma\lambda} = c_{\text{sat}}\langle\rho_\lambda\rangle\mathcal{V}_\lambda$. For the CO_2 saturation concentration variations observed in this research, the maximum dissolved mass is expected to be $\mathcal{M}_{\gamma\lambda} \in [91.8, 94.3]$ tons. The initial CO_2 stored mass in the cavern is equal to 29283.8 tons. Therefore, the mass lost due to dissolution is approximately 0.32% of the initial stored mass.

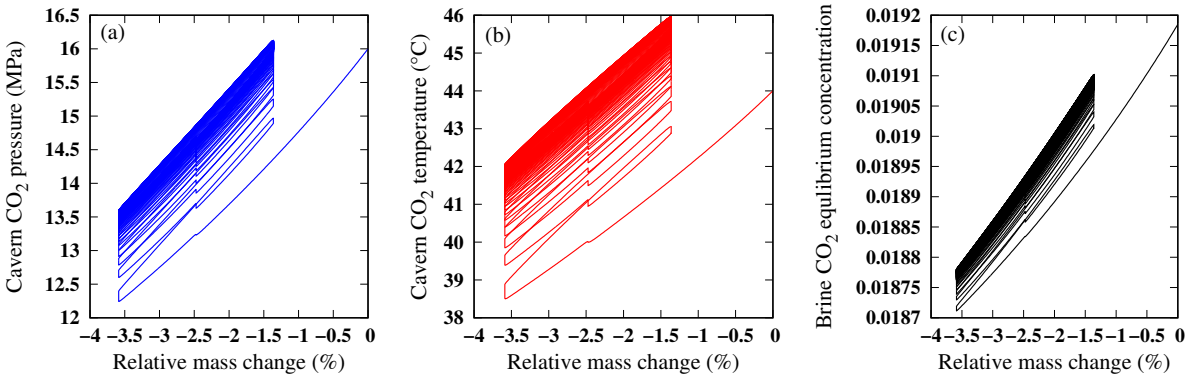

FIGURE 3.23: Cavern CO_2 pressure (a) and temperature (b) as a function of the relative mass variations during 2 years. The cavern thermodynamics is used in a post-treatment approach to calculate the CO_2 saturation concentration in the brine (c).

In the next simulations, the kinetics of dissolution is studied and quantified. To do so, the cavern thermodynamics is coupled with dissolution in the brine domain, and the entire problem is solved numerically. This necessitates solving the Navier-Stockes equation in the brine domain, along with convection due to mass transfer and thermal changes. Such simulations require extended computational time; for 6.5 months of cycling presented in this research the simulations required 3.5 months calculation time. Figure 3.24 shows the cavern thermodynamics as well as the brine CO_2 volume averaged concentration as a function of cycling. Figure 3.24(c) shows how the brine CO_2 concentration increases linearly due to cycling. The figure also demonstrates the kinetics of dissolution where concentration increases from the initial value to almost 37% the saturation value in 6.5 months.

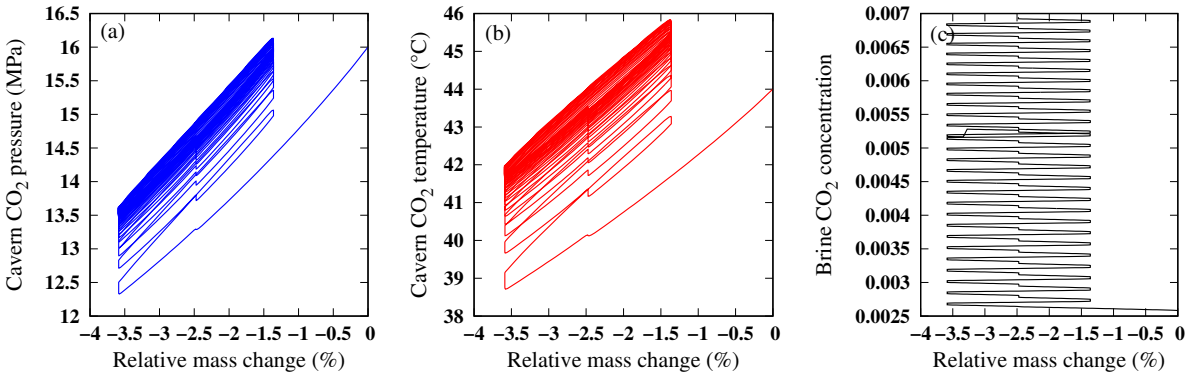

FIGURE 3.24: Cavern CO_2 pressure (a) and temperature (b) as a function of the relative mass variations during 6.5 months. The CO_2 volume averaged concentration in the brine (c) is increasing linearly showing clearly the kinetics of dissolution.

Figure 3.25(b) shows the brine CO_2 concentration averaged over its surface and volume. As for the relatively short time period of simulations (6.5 months), most of the concentration changes take place close to the surface. Therefore, the two responses give almost the same values. However, the surface averaged concentration shows obviously the effect of cycling. The volume averaged concentration is not showing the cycling effect as cycling is taking place very fast compared to the characteristic time of the dissolution problem.

Figure 3.25(a) shows how the brine volume averaged temperature is impacted by cycling. The first withdrawal phase causes a decrease in the brine temperature, before it starts to heat up again following a heating trend similar to that of the cavern (Fig. 3.24(b)). Such temperature changes are expected to alter the brine density and to play a significant role in the dissolution process by natural convection. The small irregularity observed at $t \approx 4$ months is a known

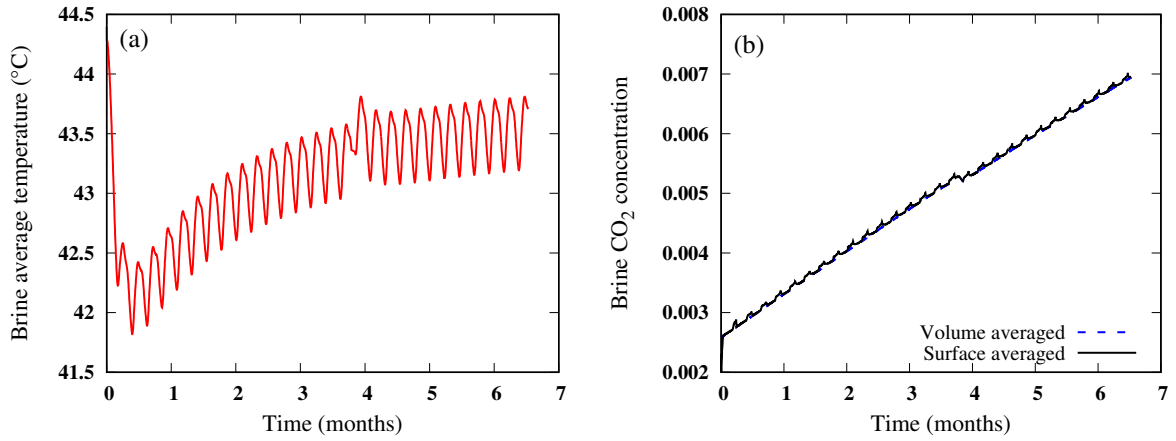

FIGURE 3.25: (a) The evolution of the brine average temperature during the CO_2 cycling. (b) The brine CO_2 concentration averaged over its surface and volume. The surface averaged concentration shows clearly the effects of cycling.

artifact of stopping and restarting the simulation. The software used here could not recover the numerical solution without this perturbation.

The evolution of the CO_2 dissolved mass can be calculated using Eq. 3.44. A total mass of 22.11 tons is dissolved during the 6.5 months of cycling. This mass is 0.076% of the initial stored mass.

Figure 3.26 shows the contours of the velocity, the concentration difference, the temperature, and the pressure fields at 10 days of the cycling. It is observed that even-though the velocity field is generated by convection (mass and thermal), it has values that are not far from $\sim$1 cm/s. The concentration, temperature, and pressure fields follow the trends of the velocity evolution. The values of any pressure perturbations attributed to the dissolution or the thermal effects do not exceed a maximum limit of 1.0 Pascal.

3.3.6 Conclusion

Gas stored in underground salt caverns, and their residual brine, are subjected to geothermal gradients. Such gradients create thermal convection that has important effects on the dissolution process of the stored gases. These effects are enhanced when gas undergoes cycling during storage. As the brine thermal expansivity is relatively high, even small temperature changes lead to significant density variations, highlighting the significance of considering thermal convection when simulating gas dissolution in the context of underground gas storage. In this research, two strategies for the kinetics of dissolution are used in order to predict the ultimate dissolved mass of CO_2. Simulations demonstrate that the ultimate total dissolved mass is approximately 0.32% of the initial stored mass. Although this loss may seem insignificant, the quantification of this loss, during cycling becomes important when other loss mechanisms are studied.

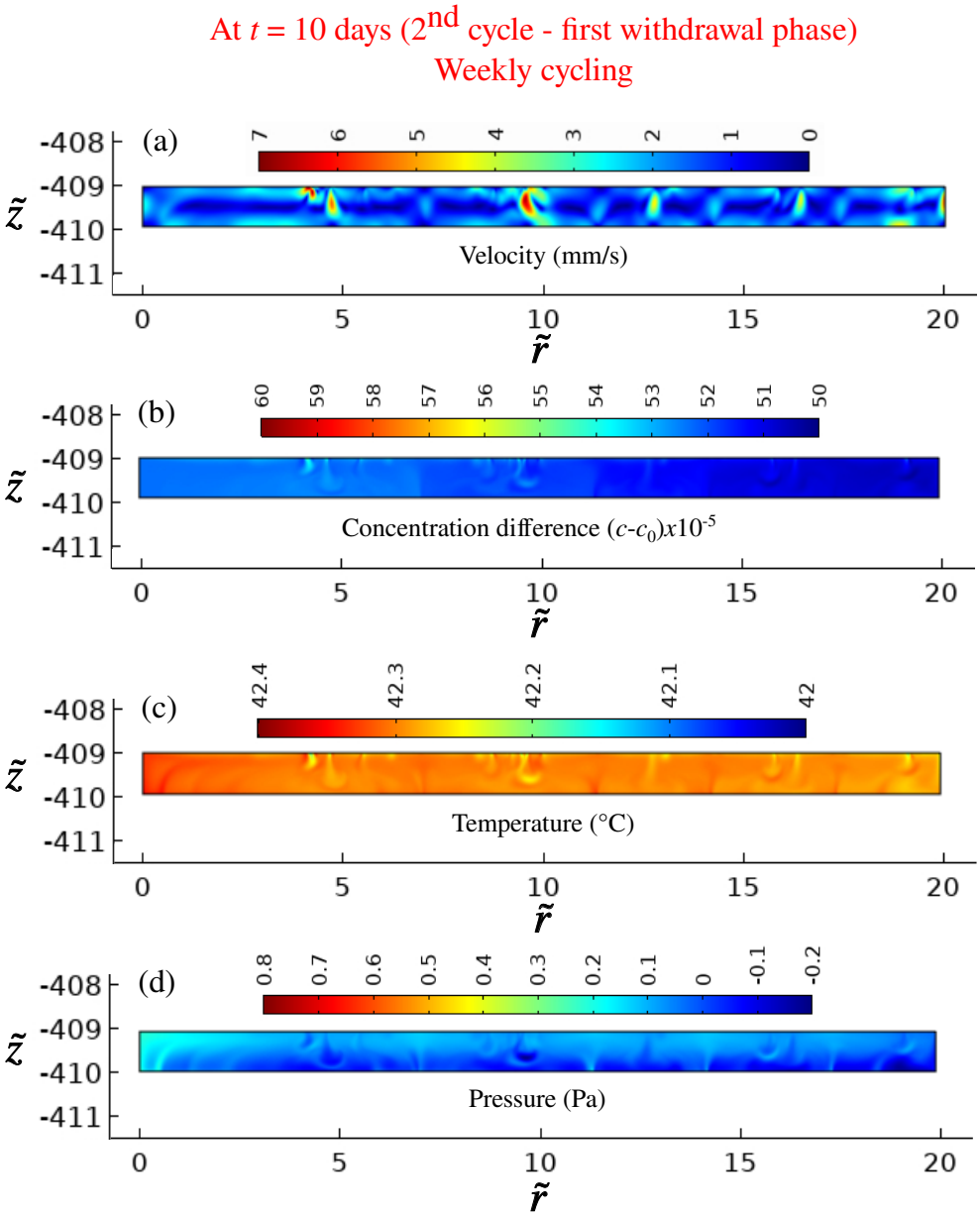

FIGURE 3.26: Contours at 10 days of weekly cycling of: (a) the velocity; (b) the concentration difference ($c - c_0$); (c) the temperature; and (d) the pressure fields. It is clear that the changes in the velocity field are the driving force for any evolution in the other fields.

3.4 Humidification kinetics of the cavern gas

During cycling in salt caverns, gas pressure and temperature evolve. The thermodynamics of the residual brine is also changing. The evaporation of water into the cavern gas (Flux F_1 of Fig. 3.1) is expected to take place due to these changes. The kinetics of evaporation must be studied to estimate the water content in the gas at each moment of cycling. The presence of water vapor may change the thermodynamic behavior of the stored gas, leading to a misestimation of the cavern thermal inventory as well as the cycled gas quantities. Humidity of withdrawn gas creates hydrates that clog pipes and prevents the direct use of gas, leading to additional costs related to dehumidification. This research includes the development of a numerical model that couples the gas thermodynamics with the evaporation mechanisms from the brine. A laboratory gas storage pilot is used to validate the numerical model while considering a fast cycling scenario. Once the numerical model is validated at the laboratory scale, it can be used for *in situ*

applications. This work helps understand why the cavern sump brine remains colder than the surrounding rock, even decades after the cavern is created (Bérest and Louvet, 2020)

3.4.1 Mechanism of evaporation

Evaporation takes place when the molecules of a liquid near its surface absorb enough energy to break the intermolecular bonds and overcome the vapor pressure. This energy removed from the liquid phase reduces its temperature, resulting in evaporative cooling. Evaporation continues until an equilibrium is reached when liquid evaporation is equal to its condensation. Actually, the escaping molecules accumulate as a vapor above the liquid. Many of these molecules return to the liquid, with returning molecules becoming more frequent as the vapor pressure increases. When the process of escape and return reaches an equilibrium, the vapor is said to be *saturated*. For a system consisting of vapor and liquid of a pure substance[5], this equilibrium state is directly related to the vapor pressure of the substance, as given by the Clausius–Clapeyron relation,

$$\ln\left(\frac{p_1}{p_2}\right) = -\frac{\Delta h}{R}\left(\frac{1}{T_2} - \frac{1}{T_1}\right), \tag{3.45}$$

where p_1, p_2 are the vapor pressures at temperatures T_1, T_2 respectively, Δh is the enthalpy of evaporation, and R is the universal gas constant. This relation assumes that water vapor behaves like an ideal gas. If a liquid is heated, when the vapor pressure reaches the ambient pressure the liquid boils.

3.4.2 The mathematical model

There is abundant literature that addresses the problem of gas-water or gas-brine equilibria. Valtz et al. (2004) reported experimental volume liquid equilibria data for the CO_2-water binary systems over a wide temperature ranging from 278.2 to 318.2 K and pressures up to 8 MPa. Salari et al. (2008) have estimated the vapor content of CO_2 in equilibrium with brine. Feistel et al. (2010) developed a sophisticated model for the thermodynamic behavior of humid sea air. Their model is, nevertheless, valid at low pressure values up to 5 MPa maximum, which do not correspond to the underground storage range. Other works focused on studying phase equilibria of energy vectors, for instance Roa Pinto et al. (2021) studied phase equilibrium of hydrogen and natural gas in brine with applications related to storage in salt caverns. Bérest and Louvet (2020) provided a comparative study on the thermodynamic behavior of underground caverns in the presence of vapor.

To present the model of this study, let us assume a mixture of dry gas d and pure water w. The dry gas is assumed to be in the gaseous phase all the time. However, water changes phase, therefore the mixture can contain water vapor v or suspended liquid water l (fog). The dissolution of dry gas in the liquid phase of water is assumed negligible, i.e. the liquid phase of the mixture is only formed of water. The total mass occupying a volume $\mathcal{V}$ of this mixture is $\mathcal{M} = \mathcal{M}_k$, $k = (d, v, l)$. By introducing the mass fractions $d = \mathcal{M}_d/(\mathcal{M}_d + \mathcal{M}_v)$ and $\mathrm{c} = \mathcal{M}_\mathrm{d}/\mathcal{M}$, the composition $\boldsymbol{c} = (c_d, c_v, c_l)$ of the mixture is expressed as:

$$c_d = c; \quad c_v = c/d - c; \quad \text{and}, \quad c_l = 1 - c/d. \tag{3.46}$$

The composition vector of the mixture $\boldsymbol{c}$ becomes a function of a single independent mass fraction which is the dry gas concentration c. The mas fractions c_v and c_l are functions of state (Sect. 1.2), the inequality $c \leq d$ must be satisfied for these fractions to remain positive. Moreover, the equality $d(p, T, c) = c$ describes the saturation of the mixture (dry air, water vapor) where any additional water appears only in the liquid form.

[5] A pure substance is defined as a substance having a constant and uniform chemical composition. A homogeneous mixture of gases which do not react with one another may, therefore, be considered a pure substance.

Based on the approach provided by Rouabhi (2019), in case of phase change of water, the volume $\mathcal{V}$ is the sum of a volume $\mathcal{V}_{dv}$ occupied by the dry gas and water vapor, and a volume $\mathcal{V}_l$ occupied by liquid water, such that $\mathcal{V} = \mathcal{V}_{dv} + \mathcal{V}_l$. Therefore, the specific volumes v_k are defined:

$$v_d = \mathcal{V}_{dv}/\mathcal{M}_d; \quad v_v = \mathcal{V}_{dv}/\mathcal{M}_v; \quad \text{and,} \quad v_l = \mathcal{V}_l/\mathcal{M}_l, \tag{3.47}$$

giving rise to the mixture specific volume which takes the following form,

$$v = c_l v_l + c_d v_d = c_l v_l + c_v v_v. \tag{3.48}$$

A simple model to construct the thermodynamic potential $g(p,T,c)$ is to consider that the partial functions $g_k(p,T,c)$ are those of the pure constituents of mixture $g_k^\circ(p_k,T)$ where p_k is a partial pressure depending on the state (p,T,c),

$$g(p,T,c) = \sum c_k g_k(p,T,c) = \sum c_k g_k^\circ(p_k(p,T,c),T). \tag{3.49}$$

The mechanical and thermodynamic equilibrium equations are needed. Such equilibrium equations ensure the introduction of entropy and the equality of the total pressure to the pressure of the liquid phase. Therefore, in terms of partial pressures (p_d, p_v, p_l), the problem comes down to solving the following system:

$$\begin{array}{lrcl} \text{thermodynamic equilibrium:} & g_v^\circ & = & g_l^\circ; \quad \text{and,} \\ \text{mechanical equilibrium:} & p_d + p_v & = & p_l, \end{array} \tag{3.50}$$

with the following condition on the total pressure and the specific volumes:

$$\begin{array}{lcl} p_l & = & p; \quad \text{and,} \\ c(1 - v_d/v_v)v_d + (1-c)v_l & = & v. \end{array} \tag{3.51}$$

Being among the most precise state laws, the GERG-2004 (Kunz et al., 2007) and GERG-2008 (Kunz and Wagner, 2012) equations are used in this work. The free energy is divided into two parts: an ideal part that describes the behavior of an ideal gas, and a residual part that accounts for deviations from this ideal behavior,

$$f(\rho,T) = f^i(\rho,T) + f^r(\rho,T), \tag{3.52}$$

that when density is low ($\lim_{\rho\to 0} f(\rho,T) = f^i(\rho \to 0, T)$), the behavior of the ideal gas is retrieved. The general form of the GERG model is expressed as:

$$\begin{array}{rcl} f^i(\rho,T) & = & \ln \varrho + a_1 + a_2\mathcal{T} + a_3 \ln(\mathcal{T}) + a_4 \ln\left(1 - e^{-b_4\mathcal{T}}\right); \\ f^r(\rho,T) & = & \displaystyle\sum_{i=1}^{N_1} n_i \mathcal{T}^{t_i} \varrho^{d_i} + \sum_{i=N_1+1}^{N_2} n_i \mathcal{T}^{t_i} \varrho^{d_i} e^{-\varrho^{c_i}}, \end{array} \tag{3.53}$$

with $\varrho = \rho/\rho_c$ and $\mathcal{T} = T_c/T$. The critical point of the fluid is defined by the coordinates (ρ_c, T_c). For each substance, the constants a_i, b_i, c_i, d_i, n_i, and t_i are known. The thermodynamic potential, free enthalpy, becomes,

$$g(p,T,c) = f(p,T,c) + p\partial_p g(p,T,c). \tag{3.54}$$

The behavior of the mixture is described by the mass density ρ, the barycentric velocity $\boldsymbol{v} = \sum c_k \boldsymbol{v}_k$, the temperature T, and the gas concentration c. The balance laws that govern the

evolution of these fields can be expressed by the following field equations:

$$\begin{array}{lrcl} \text{total mass balance:} & \dot{\rho} + \rho\,\boldsymbol{\nabla}\cdot\boldsymbol{v} & = & 0; \\ \text{momentum balance:} & \rho\,\dot{\boldsymbol{v}} - \boldsymbol{\nabla}\cdot\underline{\underline{\boldsymbol{\sigma}}} & = & \rho\,\mathfrak{g}; \\ \text{energy balance:} & \rho\,\dot{u} + \boldsymbol{\nabla}\cdot\boldsymbol{\Psi}_u & = & \underline{\underline{\boldsymbol{\sigma}}} : \underline{\underline{\boldsymbol{\nabla}}}\boldsymbol{v}; \\ \text{gas mass balance:} & \rho\dot{c} + \boldsymbol{\nabla}\cdot(\rho\boldsymbol{J}) & = & \pi^{\gamma}, \end{array} \tag{3.55}$$

with $\bar{\pi}_w^{\gamma}$ being the mass rate of water exchanged through the gas-liquid interface $\mathcal{S}_{\gamma\lambda}$ due to phase change. The internal energy flux $\boldsymbol{\Psi}_u$ is thus written as,

$$\boldsymbol{\Psi}_u = \boldsymbol{\psi} + \rho\partial_c h(p,T,c)\boldsymbol{J}. \tag{3.56}$$

Other quantities are as defined in Sect. 3.1. The derivative of enthalpy with respect to the gas concentration is,

$$\frac{\partial h(p,T,c)}{\partial c} = T\frac{\partial s(p,T,c)}{\partial c}, \tag{3.57}$$

with,

$$\frac{\partial s(p,T,c)}{\partial c} = \left(s_v^{\circ} - s_l^{\circ}\right)\left[1 + \frac{\rho_v}{\rho_d}\right] - s_v^{\circ} + s_d^{\circ}, \tag{3.58}$$

therefore,

$$\frac{\partial h(p,T,c)}{\partial c} = \left(h_v^{\circ} - h_l^{\circ}\right)\left[1 + \frac{\rho_v}{\rho_d}\right] - h_v^{\circ} + h_d^{\circ}. \tag{3.59}$$

The heat capacity of the mixture can be written as (Rouabhi, 2019),

$$C_p(p,T,c) = \partial_T h(p,T,c) = \sum c_k C_{pk} + \left[\left(c_v\partial_{pv}h_v^{\circ} - c_d\partial_{pd}h_d^{\circ}\right)/(\nu_v T) - \partial_T c_l\right](h_v^{\circ} - h_l^{\circ}). \tag{3.60}$$

The dynamic viscosity and the thermal conductivity of the mixture are defined as (Tsilingiris, 2008; Zhang, Gupta, and Baker, 2007),

$$\mu = \sum_{i=d,v,l} \frac{c_i\mu_i}{\sum_{j=d,v,l} c_j\vartheta_{ij}} \tag{3.61}$$

with,

$$\vartheta_{ij} = \frac{\left[1 + \left(\frac{\mu_i}{\mu_j}\right)^{1/2} + \left(\frac{M_{wj}}{M_{wi}}\right)^{1/4}\right]^2}{\left[8\left(1 + \frac{M_{wi}}{M_{wj}}\right)\right]^{1/2}}, \tag{3.62}$$

M_w is the molecular weight and μ_d, μ_v, and μ_l are the dynamic viscosities of the dry gas, the steam, and the liquid water respectively, and,

$$\Lambda = \sum_{i=d,v,l} \frac{c_i\Lambda_i}{\sum_{j=d,v,l} c_j\vartheta_{ij}}, \tag{3.63}$$

with Λ_d, Λ_v, and Λ_l being the thermal conductivities of the dry gas, the steam, and the liquid water respectively.

The mechanical behavior of the rock mass around the cavern is neglected. For a time-dependent problem, the temperature field in the surrounding rock mass verifies the following form of the heat equation,

$$\partial_t T_\sigma = \mathcal{K}_\sigma \boldsymbol{\nabla} \cdot (\boldsymbol{\nabla} T_\sigma). \tag{3.64}$$

3.4.3 Modeling of the brine domain

The residual brine of the cavern is expected to undergo thermal changes due to the geothermal gradient over its height and gas cycling. As in indicated in Sect. 3.3, these thermal changes result in density changes. To describe the velocity field generated by natural convection due to density changes, both the Navier-Stokes equation as well the energy equation in the liquid phase are needed. Considering a computational fluid dynamics framework in the brine domain considerably complicates the numerical calculations. As a simplification, a convectively enhanced conductivity is used in the liquid energy equation to substitute for the effect of the velocity field. This permits us to modelize correctly the heat transfer in the liquid phase while using only the energy equation. Hence, the energy equation in the liquid domain takes the form,

$$\rho_\lambda C_{p\lambda} \partial_t T_\lambda + \boldsymbol{\nabla} \cdot \boldsymbol{\psi}_\lambda = Q_w, \tag{3.65}$$

where Q_w is the heat source attributed to the phase change of the liquid phase, and $\boldsymbol{\psi} = -\Lambda \mathrm{Nu} \boldsymbol{\nabla} T_\lambda$ with Nu being the Nusselt number. Values of the Nusselt number for similar applications can be found in the works of Calcagni, Marsili, and Paroncini (2005) and Hasnaoui, Bilgen, and Vasseur (1992). The heat source related to the phase change of the liquid phase is calculated using the latent heat $\Delta \bar{h}_w$ (Sect. 1.3.2), such that,

$$Q_w = -\bar{\pi}_w^\gamma \Delta \bar{h}_w, \quad \text{with,} \quad \Delta \bar{h}_w = \bar{h}_v - \bar{h}_l. \tag{3.66}$$

At the gas-liquid interface, as a function of cycling, molecules escape the liquid phase. However, many of them return to the liquid until saturation is reached. The material flux between the two phases is expressed as,

$$\boldsymbol{J} \cdot \boldsymbol{n} = K((1 - c) - c_{\mathrm{sat}}), \tag{3.67}$$

therefore it is concluded that,

$$\bar{\pi}_w^\gamma = \frac{1}{\mathcal{V}} \int_{\mathcal{S}_{\gamma\lambda}} \rho \, K(c_{\mathrm{sat}} - (1 - c)) \, d\mathcal{A}_{\gamma\lambda}, \tag{3.68}$$

where K is the mass transfer coefficient (calibrated). The vapor saturation concentration is calculated as $c_{\mathrm{sat}} = 1 - \rho_d / \rho$ (at saturation).

3.4.4 Laboratory gas storage pilot

Gas humidification kinetics at the laboratory scale is presented in this section. The laboratory model consists of a cylindrical high-pressure stainless steel vessel (Fig. 3.27), with dimensions: height ($L = 50$ cm) and radius ($R = 9$ cm) with a volume $\mathcal{V} = 12.3$ l. The model is equipped with a heating system to allow for the generation of natural convection resulting from thermal gradients.

The temperature at the model base is controlled by a circulating fluid, the top temperature can be controlled by a heating collar or left equal to the room temperature. Sides are isolated by an isolating jacket that is wrapped around the system, and the temperature gradient is left to develop naturally by the applied bottom and top temperatures. The objective is to develop a temperature difference over the model height that resembles the geothermal gradients that salt caverns undergo. The pilot is equipped with 15 temperature probes to measure the temperature spatial variations during cycling. Humidity is also measured by 7 sensors that are distributed over the pilot volume.

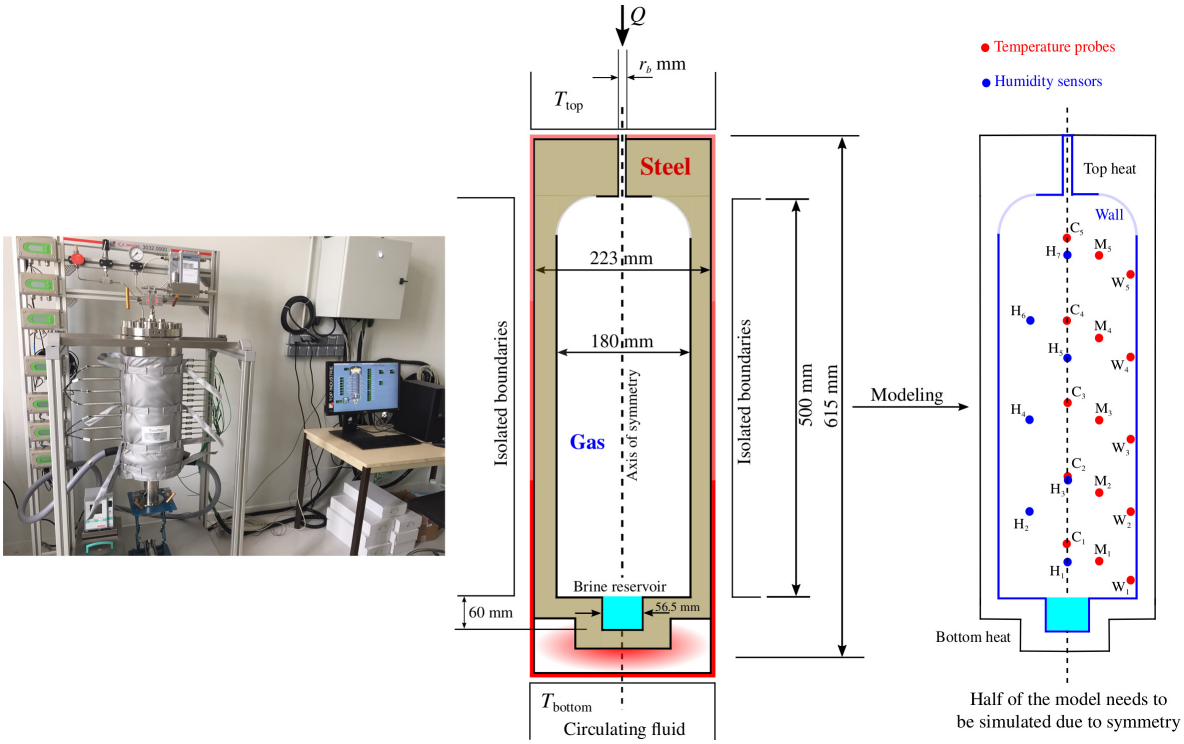

FIGURE 3.27: Schematic diagram of the laboratory model used to reproduce the underground cavern thermodynamic behavior. The figure shows the axes where the vertical temperature profiles are measured, five sensors over each vertical axis: sensors C (86 mm off wall), M (46 mm off wall), and W (6 mm of wall). Sensors are separated by a vertical distance of 28 mm. Humidity is also measured by 7 sensors H_1 to H_7: these sensors are either arranged axially or at 46 mm off the wall and separated vertically by 56 mm distance.

The injection tube has a diameter of 3 mm. A brine reservoir is placed at the model base to study the effect of vapor saturation on the thermodynamic behavior of stored gas during cycling. The reservoir brine height is measured precisely during tests to estimate the quantity of the evaporated water. The pilot steel thermal diffusivity is $\mathcal{K}_\sigma = 3.038 \times 10^{-6}$ m^2/s. This thermal diffusivity allows for a characteristic time along the wall thickness equal to $t = l^2/\mathcal{K}_\sigma = (21.5 \times 10^{-3})^2/3.038 \times 10^{-6} \simeq 152$ s.

3.4.4.1 Laboratory cycling tests

Two laboratory tests, with and without brine in the reservoir, are carried out, with helium used as the storage gas. The objective is to quantify the effect of humidity on the thermodynamic behavior of helium. Tests are performed following this procedure:

- in the humid test the reservoir is filled with saturated brine to a height of 6.15087 cm. In the dry test the reservoir is left empty;
- a helium flush is done to chase out air inside the pilot;
- the top and bottom temperatures of the model are set equal 46 °C and 43 °C respectively, and sides are isolated;
- a filling phase is done where helium pressure within the pilot is increased from atmospheric to 12 MPa;
- the system is left to reach equilibrium during 2.5 days;
- the mass variation program (Fig. 3.28) is fed to the acquisition system to start cycling.

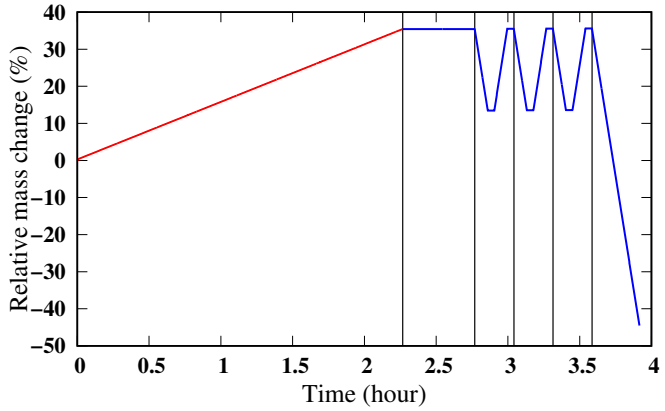

FIGURE 3.28: The program begins with a slow filling phase of ∼2.26 hours followed by a rest phase of ∼0.5 hour. Cycling begins after this rest phase and includes three cycles. Each cycle extends over ∼0.27 hour where withdrawal and injection last for ∼0.09 hour each, and the rest phases last only for ∼0.04 hour each. Cycling is followed by an intense withdrawal phase which extends over ∼0.33 hour. This cycling leads to relative mass changes of ∼[35.43% à -44.51%].

Figure 3.29(a) shows the evolution of the average Relative Humidity (RH) (averaged over the seven sensors) during the stabilization phase. It is observed that saturation (at 85%) is attained after approximately one day. Cycling begins after the stabilization phase (2.5 days). RH is seen to decrease during cycling (Fig. 3.29(b)); a RH of ∼40% is recorded after ∼4 hours. This reduction of humidity is attributed to the injection of dry helium and withdrawal of wet gas.

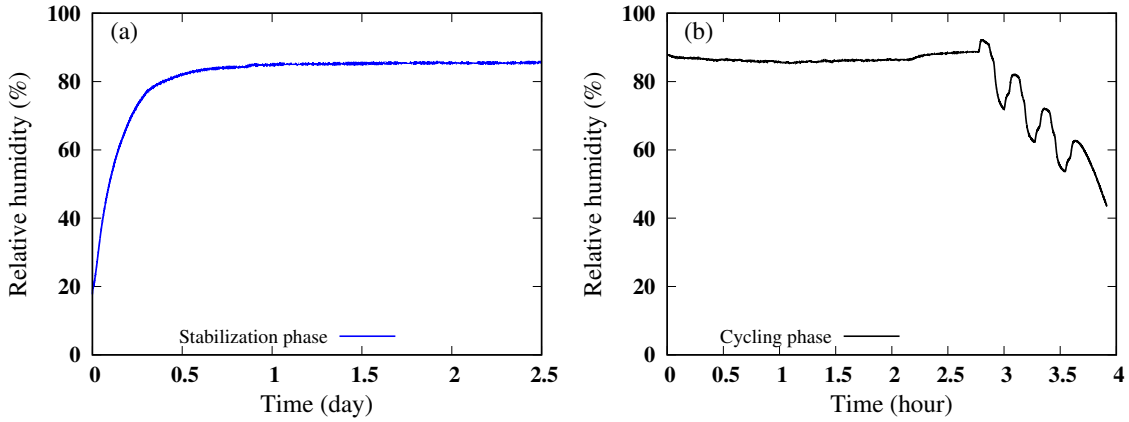

FIGURE 3.29: (a) Evolution of the average RH during the stabilization phase of 2.5 days, and (b) during cycling.

Figure 3.30(a) shows the evolution of the helium pressure during the two cycling tests, wet and dry. The two histories correlate well and any observed differences are minimal. Figure 3.30(b) shows the average temperature histories (averaged over the 15 sensors) during the dry and wet tests, the discrepancies do not exceed ∼0.7 °C.

Figures 3.31, 3.32, and 3.33 show the temperature histories by the wall (W sensors), at middle of the model (M sensors), and axially (C sensors). The experimental results of the wet and dry tests are comparable and differences are minor. The differences are more obvious at the top of the model which is less influenced by the heating source at the bottom (Figs 3.31(b), 3.32(b), and 3.33(b)).

Figure 3.34 shows the RH histories at sensors H_1 (bottom) and H_7 (top) during the dry and wet tests. It is obvious that RH is negligible during the dry test. The H_1 sensor always measures

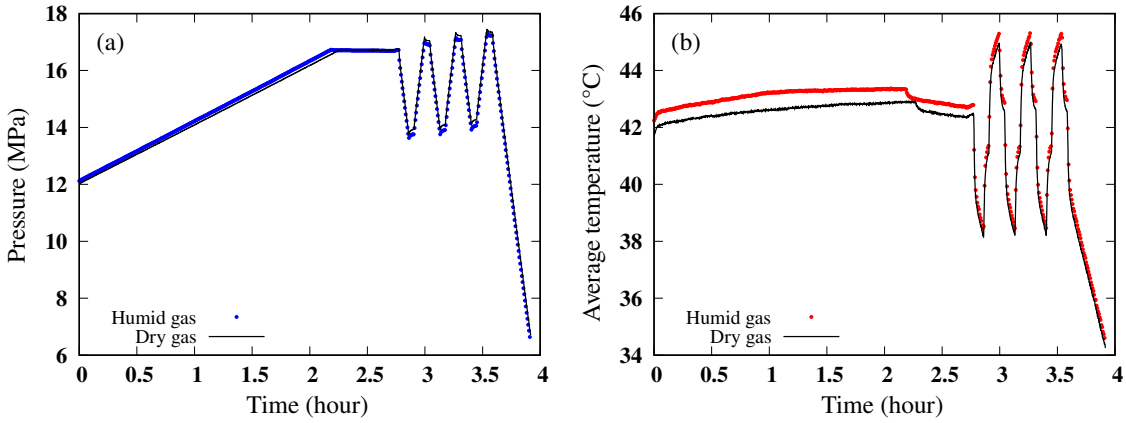

FIGURE 3.30: Pressure (a) and average temperature (b) histories during the two cycling tests of dry and humid helium.

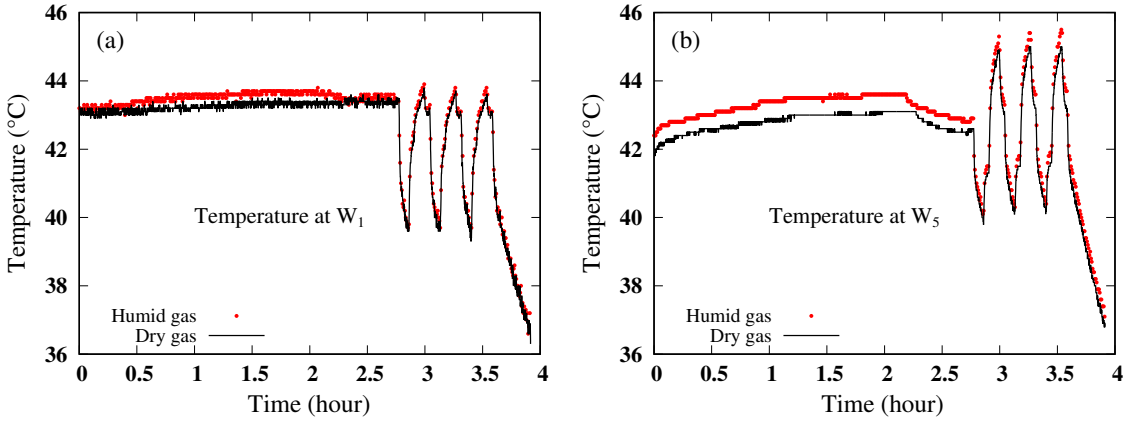

FIGURE 3.31: Wall temperature histories: (a) at the W_1 sensor (bottom) and (b) at the W_5 sensor (top). The figures compare the results of the dry test (continuous lines), and the wet test (dots).

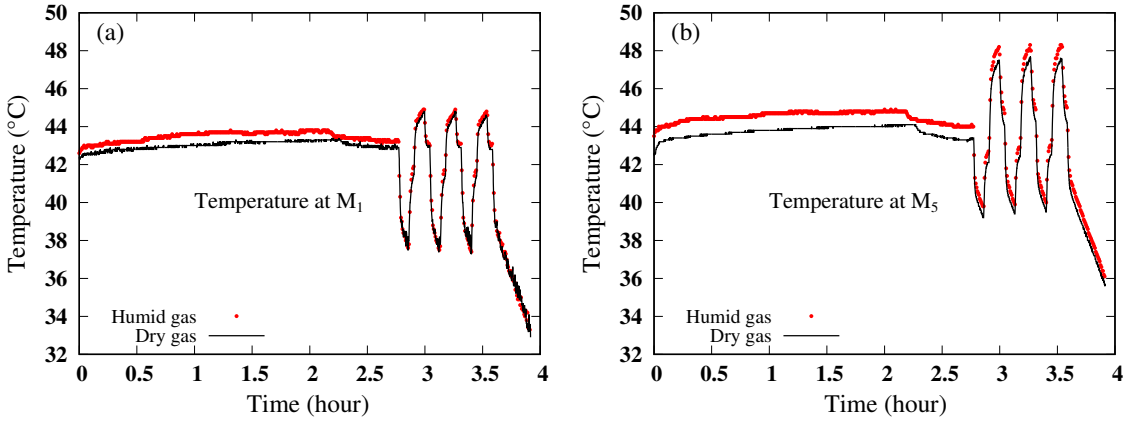

FIGURE 3.32: Temperature histories at middle of the pilot: (a) at the M_1 sensor (bottom) and (b) at the M_5 sensor (top).

a more humid level of gas as it is closer to the reservoir. Nevertheless, RH is more affected by cycling at the sensor H_7.

3.4.4.2 Numerical simulations

The numerical simulation results of the wet test are presented in this section. Simulations of this particular laboratory test are performed by implementing the same boundary and initial

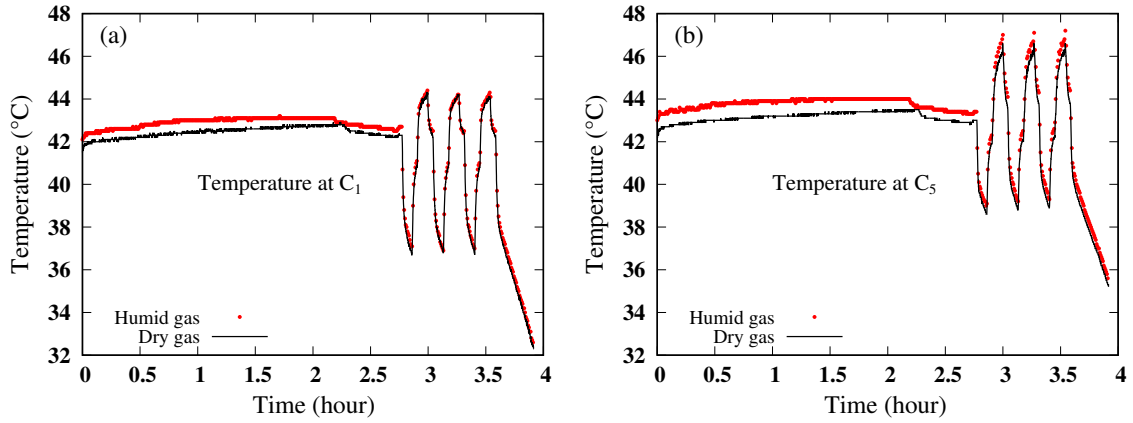

FIGURE 3.33: Axial temperature histories: (a) at the C_1 sensor (bottom) and (b) at the C_5 sensor (top).

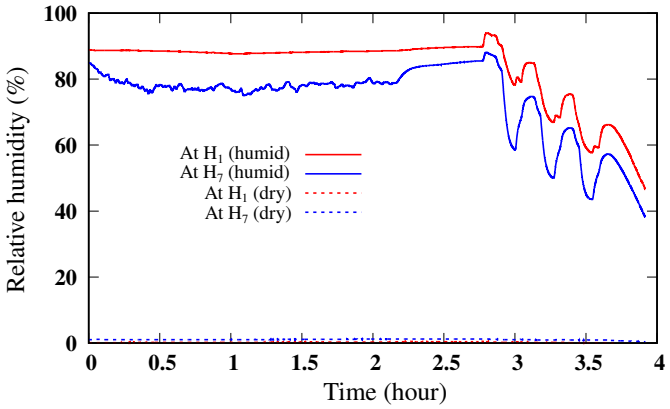

FIGURE 3.34: Evolution of RH at the sensors H_1 (bottom) et H_7 (top) during the dry and wet tests. Humidity is negligible during the dry test.

conditions as in Sect. 3.4.4.1. Only half of the model is simulated due to its two-dimensional axisymmetry. As to abide to COMSOL accuracy requirements for conjugate heat transfer, the k-ϵ turbulent flow, and heat convection (Sect. 3.1), the mesh includes 52554 elements of which 1566 quadrilateral boundary elements (Fig. 3.35).

Vapor diffusion in helium depends on temperature, for this study an average value $D = 1.011 \times 10^{-4}$ m^2/s is used (Schwertz and Brow, 1951). The mass transfer coefficient is parametrized during the stabilization phase to $K = 3.8 \times 10^{-4}$ m/s. Brine thermo-physical properties are presented in Sect. 3.2. COMSOL gives analytical expressions for the evolution of the dynamic viscosity and thermal conductivity of pure water and helium as a function of temperature.

Figure 3.36 shows the evolution of pressure and average temperature during the stabilization phase of 2.5 days. The figure compares the experimental data with the numerical results. Numerical average temperature is averaged over the model volume, however, experimentally, it is averaged over the 15 sensors.

Figure 3.37(a) shows the evolution of average relative humidity during the stabilization phase. It is averaged over the model volume numerically, however, it is averaged over the 7 sensors experimentally. The brine temperature is measured experimentally at the middle of the reservoir (Fig. 3.37(b)), nevertheless, it is averaged over the brine domain numerically. The mass transfer coefficient is the only parameter adjusted numerically, it is value is chosen such that the kinetics of humidification, both experimentally and numerically, best-fit (Fig. 3.37(a)).

Figure 3.38 shows the evolution of the gas pressure and its average temperature in the pilot during cycling. Experimental data and numerical responses are satisfactorily comparable.

(a) Laboratory set-up

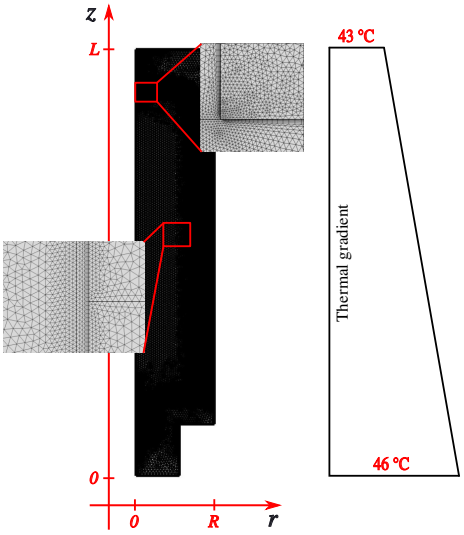

(b) 2-D axisymmetric descritization

FIGURE 3.35: (a) The laboratory set-up: bottom and top temperatures are set equal 46 °C and 43 °C respectively. The model sides are isolated, helium is injected to establish a pressure of 12 MPa, and temperature gradient is left to develop over the model. (b) Two-dimensional axisymmetric discretization of COMSOL.

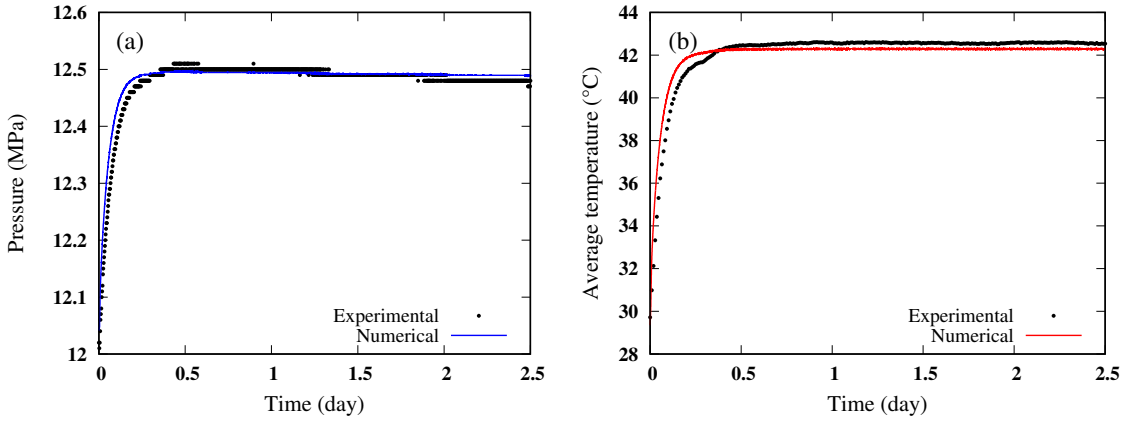

FIGURE 3.36: Evolution of pressure (a) and average temperature (b) in the pilot during the stabilization phase.

However, in case of RH (Fig. 3.39(a)), an important deviation between experimental data and numerical results is observed. This is supposedly attributed to the mass transfer coefficient that is calibrated during the stabilization phase yet never updated during cycling. It is expected that the value of this coefficient to be a function of the gas velocity close to the brine surface. Comparing the numerical results of the brine average temperature to the experimental data (Fig. 3.39(b)), it is noticed that the experimental temperature is changing significantly during the slow filling phase where the pilot RH is relatively not changing, this behavior needs more investigation. Although, the numerical results are stable during the slow filling phase, during cycling they show a slow heating trend that is consistent with the experimental data.

3.4.5 Humidification kinetics at the cavern scale

Studying humidification kinetics while running CFD calculations is numerically expensive. It requires extensive calculation time and memory. In an exploitation context where cycling within

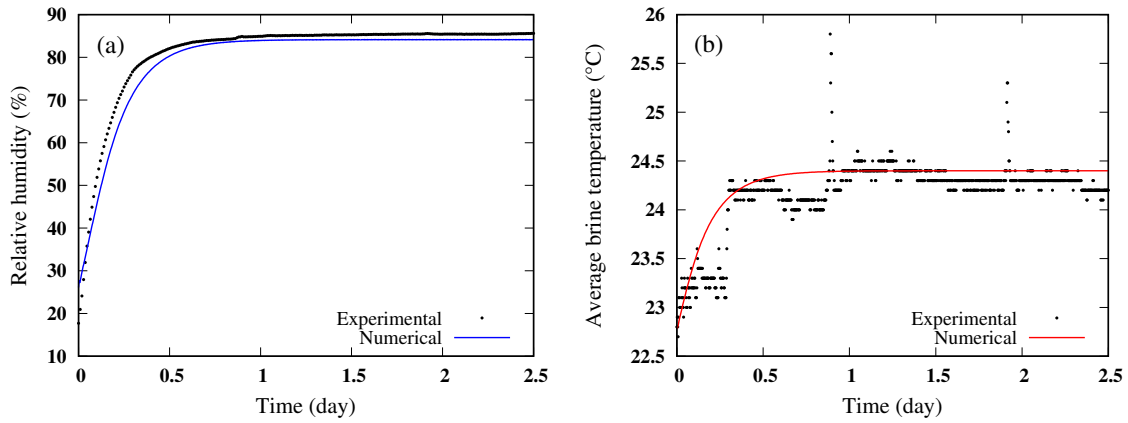

FIGURE 3.37: Evolution of average RH (a) and average brine temperature (b) during the stabilization phase.

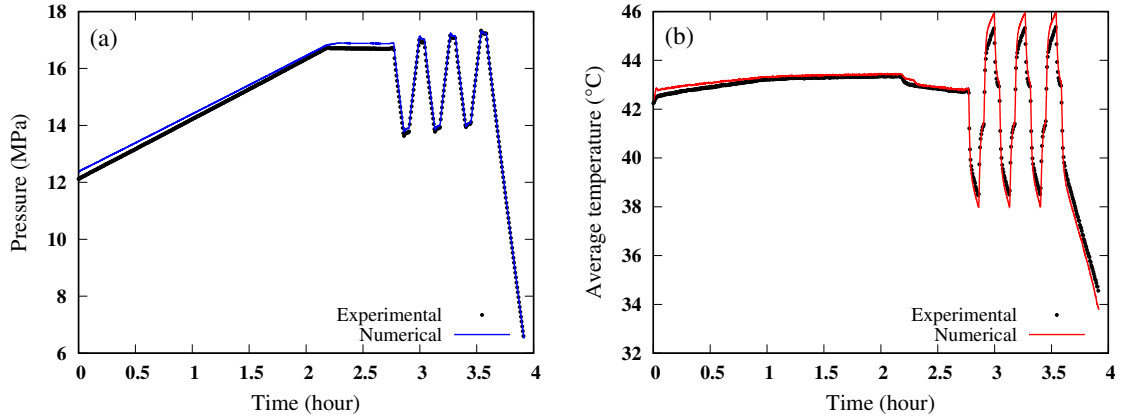

FIGURE 3.38: Evolution of pressure (a) and average temperature (b) in the pilot during cycling.

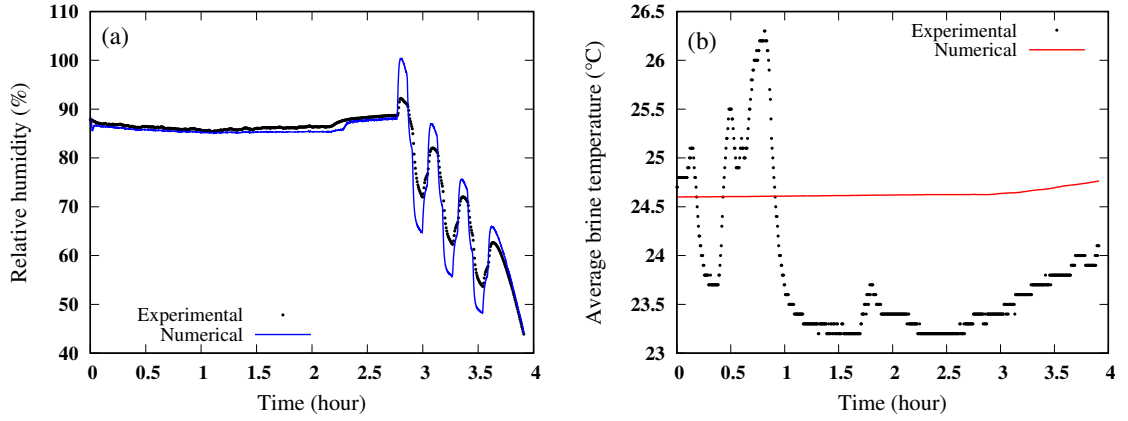

FIGURE 3.39: Evolution of average RH (a) and average brine temperature (b) during cycling.

the cavern expands over its lifetime (30 to 40 years), it is necessary to study the humidification kinetics while assuming a cavern uniform thermodynamic state (Sect. 3.1).

3.4.5.1 Humidification kinetics in a uniform thermodynamic state

In a uniform thermodynamic framework, the system of equations (3.55) becomes:

$$\begin{array}{lccl} \text{total mass balance:} & \mathcal{M}\left(-\chi_p \dot{T} + \chi_T \dot{p} + \beta \dot{c}\right) & = & Q_e; \\ \text{energy balance:} & \mathcal{M} C_p \dot{T} - \mathcal{V}\chi_p T \dot{p} + \mathcal{M} T \partial_c s & = & Q_e^+ (h_t^w - h^c) - \Psi; \\ \text{gas mass balance:} & \tau \dot{c} & = & (1-c) - c_{\text{sat}}, \end{array} \tag{3.69}$$

with $\beta = \nu \partial_c \rho|_{p,T}$, and the humidification characteristic time is τ. Other quantities are as defined previously. The characteristic time is a function of cycling and needs to be calibrated based on field or experimental data. The parameter β can be found using the following expression,

$$\beta = -\rho \left[\frac{1}{\rho_d} \left(1 - \frac{\rho_v}{\rho_l} \right) - \frac{1}{\rho_l} \right]. \tag{3.70}$$

3.4.5.2 A post-treatment approach for humidification kinetics

The objective of this section is to know if the average RH of Fig. 3.29(b) can be reproduced knowing the evolution of gas pressure and its average temperature (Fig. 3.30). To do so, vapor concentration at saturation needs to be calculated for each pressure and temperature value. Therefore, the following equation for humidification kinetics can be used:

$$\dot{c} = \begin{cases} \dfrac{1}{\tau_1} \left[(1-c) - c_{\text{sat}} \right], & (1-c) \geq c_{\text{sat}}; \\ \dfrac{1}{\tau_2} \left[-(1-c) + c_{\text{sat}} \right], & (1-c) < c_{\text{sat}}. \end{cases} \tag{3.71}$$

The two characteristic times are calibrated to $\tau_1 = 85$ s and $\tau_2 = 2500$ s, these two values best-fit the experimental data as shown in Fig. 3.40.

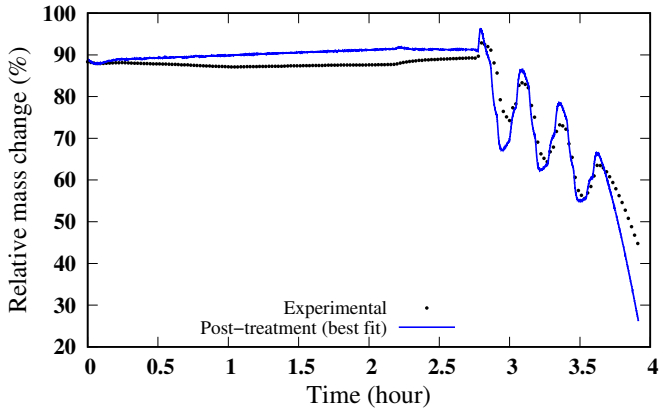

FIGURE 3.40: Evolution of experimental average RH correlated with numerical values calculated using the humid gas state law in a post-treatment approach.

Even-though there are some differences, depending on the application, they can be be accepted, and the kinetics itself is reproduced.

3.4.6 Discussion and conclusion

This work demonstrates that its feasible to reproduce at the laboratory scale thermodynamic evolutions that resemble those of real scale caverns. Such evolutions include the gas pressure,

its temperature, and its vapor content. To focus on the gas humidification kinetics during cycling, this study provides a mathematical model based on the free enthalpy. The laboratory measurements show that the gas pressure and temperature do not change significantly due to the presence of water vapor. However, the presence of the RH itself is important. Depending on the cycling frequency, RH within the cavern changes, with a tendency to decrease in case of fast cycling. The presence of RH in the withdrawn gas is harmful, it clogs conduits and requires additional costs related to dehumidification (wet gas can not be used directly). Still, some simulations need to be performed at the cavern scale while considering several cycling scenarios to have an idea about the effect of cycling on the humidification kinetics, and to estimate the humidification characteristic time at the cavern scale.

Review and perspectives

This document presents the knowledge I acquired over a time-course of 14 years while working on the exploitation of underground energy resources by fluid circulation. I began as a modeler when I developed my skills in the field of the finite element coding of complex physics. During my research at the University of Calgary, I was a part of the microseismic industry consortium, where I got familiarized with the industrial problems and had access to field data. Once I started working at MINES Paris, applied research became essential. At that point, I understood that one can get satisfied by treating each industrial problem using a specific engineering tackle, or delve into the fineness of physics to develop general approaches. In this work, I tried to construct the mathematical and physical models based on thermodynamics. I adopted simplifying approaches in a next step, while quantifying at the same time their effect and range of validity.

This research is characterized by conducting validations at the laboratory scale, and by transferring techniques to communicate it with the real scale applications. The skills I gained through this knowledge are interdependent and multidisciplinary, they fit in the general research axis defined by our team at the Center of Geosciences of MINES Paris for the coming five years. They help me mount or participate in mounting private and industrial projects, and contribute to teaching activities of the University PSL. Recently, we got the funding for a European project (FrHyGe) that concerns large-scale demonstration of underground hydrogen storage.

Specifically, I would further work on the following aspects:

- while gas storage in salt caverns represents a solution to the intermittency problem coherent to renewable energy, cycling is expected to take place rapidly (weekly or daily). An emergency need appears with regard to the FEM codes used to reproduce the stored gas thermodynamics. While the CFD simulations may be precise, conducting them over the cavern lifetime is unfeasible. Future research will focus on exploiting the storage pilot (Sect. 3.4) to enhance the existing FEM codes that assume a uniform thermodynamic state. The pilot experimental results can be reproduced by performing simplified simulations while using a heat transfer coefficient over the pilot wall. This coefficient can be a function of the well velocity or the treatment rate, and it aims at recreating the effect of the velocity field. Once validated, this approach can be generalized to the cavern scale, it can be also enhanced if *in situ* measurements are available from these caverns;

- fast solicitations of salt caverns definitely affects the mechanical integrity of the rock salt surrounding them. The developed mathematical model (Sect. 3.2) does not take into account the mechanical deformation of the rock salt. We are currently conducting research to evaluate the evolution of the rock salt hydraulic properties due to mechanical loading. The results of such a research can be implemented in the current framework to study their effects on the total amount of gas lost into the rock domain;

- basically, this research focuses on CO_2 dissolution in brine. However, future research will include the development of a dissolution cell dedicated to studying hydrogen dissolution kinetics, particularly due to thermal gradients, and for different volume ratios of gas and brine. Hydrogen production is still expensive and available caverns might be large. For a small quantity of hydrogen and to keep a minimum cavern working pressure, caverns

might be half (or more) filled with brine. Geothermal gradients can not be negligible over considerable brine volumes, nor can be the dissolved mass of hydrogen. This illustrates the need to study hydrogen dissolution kinetics in such conditions;

- the storage pilot will be used to study hydrogen humidification kinetics under common storage conditions. The presence of water vapor is observed to have a little effect on helium thermodynamics, however, water vapor diffusion in hydrogen is more important. Thus, this conclusion needs to be verified in the case of hydrogen. The numerical model has to be enhanced with regard to the used mass transfer coefficient on the wet surface. An evolving value as a function of cycling is expected to better reproduce the relative humidity experimental curves;
- as *in situ* data with regard to methane cycling in a real cavern are available, the humid gas model of this study can be used to investigate the cooling effects close to the brine surface. This study demonstrates that, due to evaporation, brine stays colder than the cycled gas. This will help estimate the buffer zone size above the cavern brine during cycling.

These activities will help me acquire new skills and establish new research axis/axes. For instance, I would like to deploy the artificial intelligence technology in the field of induced seismicity due to fluid injection. I proposed an inter-team PhD project concerning the non-diffusive seismicity triggering fronts in a thermo-hydromechanical framework. The results of this project will show how seismic interpretations can improve simulation models and, reciprocally, how fully coupled physics-based modeling can add to earthquake data interpretations in analysis of induced seismic sequences. Outcomes will be valued in terms of publications in peer-reviewed journals.

Appendix A

Detailed Curriculum Vitæ (CV)

Murad AbuAisha Ph.D.

2 Bis Avenue du Général de Gaulle, 77210 Avon, France
murad.abuaisha@minesparis.psl.eu | +33615808952 | 36 years old |

EDUCATION

University of Grenoble, Grenoble, France — March 2011 | May 2014
Ph.D. degree in Geomechanics
Thesis: Enhanced Geothermal Systems (EGS): Hydraulic fracturing in a thermo-poloelastic framework

University of Joseph Fourier, Grenoble, France — September 2009 | July 2010
Master's degree in Mechanics of Solid Materials
Thesis: Digital image correlation: Strain localization and landfill clay barrier reinforcement

University IUG, Gaza, Palestinian Territories — September 2004 | February 2009
Bachelor's degree in Civil Engineering
Graduation project: Design of an artificial island

PROFESSIONAL EXPERIENCE

MINES Paris — Paris, France
Researcher-Teacher (Assistant professor) — May 2017 | Present
Projects: Participating in and mounting several projects with industrial partners: STORENGY, GEOSTOCK, TEREGA, TOTAL, AIRLIQUIDE. Academic partners include other members of the PSL university, and the university of Lorraine

- Uniformity of thermodynamic state of gas stored in underground salt caverns, particularly hydrogen
- Computational Fluid Dynamics (CFD) modeling with turbulent flows
- Conjugate hate transfer and the boundary layer theory
- Mass exchanges between cavern phases: Gas, residual brine, and rock salt
- Non-isothermal two-phase hydrogen permeation in the saturated rock salt
- Geothermal effects on the gas dissolution kinetics in the cavern residual brine during cycling
- Gas humidification kinetics as a function of cycling frequency
- Carbon dioxide sequestration in geological media and induced seismicity
- AI-driven geothermal exploration (new research theme)

University of Calgary — Calgary, Canada
Postdoctoral researcher — November 2014 | May 2017

Project: Modeling and simulating Hydraulic Fracturing (HF) for petroleum industry using continuum/discontinuum approaches and related induced seismicity

- The finite and the discrete element methods to describe linear/nonlinear deformations as well as fracturing of rock formations
- Darcian flow and fluid compressibility law for fluid diffusion in the reservoirs and fracture leakoff
- Tracking and simulating the induced hydraulic fracturing seismicity due to fault activation either by dynamic effects or by fluid pressure changes
- Parallel programming using C++ on a Linux environment and High Performance Computing (HPC) simulations
- Two years of teamwork experience at the department of Geoscience, University of Calgary

CNRS Grenoble, France
Ph.D. researcher March 2011 | March 2014
Project: Enhanced Geothermal Systems (EGS)

- Hot Dry Rock (HDR) reservoir enhancement by Hydraulic Fracturing (HF), in terms of production, impedance, and efficiency of thermal recovery
- Developing a fully coupled HF thermo-poroelastic framework with all the required partial differential equations
- Writing a finite element FORTRAN 90 code to simulate fluid circulation and heat transfer in enhanced large-scale geothermal systems
- Several finite element meshing approaches and implicit time integration schemes for stable solutions of fluid flow and heat transfer
- Navier-Stokes equation for complex flow, fluid Newtonian/non-Newtonian characteristic and Darcian/non-Darcian nature of flow
- Fair knowledge of the physics of fluid flow in dual-porosity media and possible phase changes
- Experience with physically coupled phenomena and numerically challenging stabilization techniques, i.e. heat convection
- ABAQUS and COMSOL expertise, analytical solutions and field data treatment for validation of the numerical approaches
- Three-year experience of teamwork at the Laboratoire 3SR, Grenoble, France

Laboratory 3SR Grenoble, France
Master's internship in material mechanics February 2010 | July 2010
Project: Tensile strength of clays: Applications to landfill clay barriers

- Clay reinforcement by fibers
- Strain localization phenomenon
- Laboratory tests
- Validations using the 3-dimensional digital image correlation

SKILLS

Competencies

- Reservoir geomechanical modeling
- Finite and discrete element methods
- Fluid thermodynamics
- Dissolution kinetics of gas in the aqueous phases
- Kinetics of gas humidification

- Non-isothermal two-phase flows
- Partial differential equations
- Coupled physical phenomena
- Fluid flow mechanics in fractured media and tight reservoirs
- Parallel coding in C++ Linux
- FORTRAN 90, Matlab and Python languages
- **Training in "Supervising Ph.D. students" (PSL)**
- **Training in "Choose teaching methods adapted to the targeted learning" (PSL)**
- **Training in "How do I make sure that the way I teach is appropriate?" (PSL)**
- **Training in "Design an educational slideshow" (PSL)**
- Courses in "Interpersonal communications and relations of work"
- Courses in "Time management and personal organization of work"
- Commercial numerical software: ABAQUS and COMSOL

Language Skills

- Fluent in written and spoken English
- Fluent in written and spoken French
- Fluent in written and spoken Arabic, Hebrew, and Aramaic

SUPERVISING AND COLLABORATION ACTIVITIES

Graduate students
Ph.D. students

- Khashayar Khezri: Dynamic fracturing in a THM framework: Upscaling applications to geo-energy production and induced seismicity
  Co-supervising at 30% November 2023 | November 2026
- Firas Tayeb: Thermodynamics of underground gas storage: From laboratory to salt caverns
  Co-supervising at 60% November 2019 | February 2024

Collaboration with PostDocs

- Angeline Defay: Numerical modeling of hydrogen permeation in the rock salt
  Collaboration at 50% November 2023 | September 2024

Master's internships

- Parth Nigam: Numerical modelling of rock dynamic fracture and study of fluid-driven fracture: FEM and XFEM framework
  Co-supervising at 50% February 2018 | July 2018

Undergraduate students:

- Mini-project UE-14 (five students of MINES Paris). Title: Tightness of underground salt caverns to hydrogen
  Supervising at 100% September 2022 | December 2022
- Option student of ground and underground applications. Title: Energy storage by compressing CO_2 using hydraulic pumps
  Co-supervising at 50% June 2021 | September 2021
- Foreigner option student from the university Mohammed VI polytechnic. Title: Mining through high pressure water jetting: Definition of the pilot testing campaign of SABRE 2020 field tests
  Co-supervising at 50% June 2020 | September 2020

TEACHING ACTIVITIES

At MINES Paris (2017-2023) - Since I started working at the school of mines (MINES Paris), my teaching load was around 35 hours/year:

- November 2023: Courses in the MIG (Métier de l'Ingénieur Généraliste). Title: Prospective study of a strategic resource: Underground gypsum exploitation in Maurienne. Students delivered a report at the end of this option.
- September 2022 - November 2022: Mini-project UE-14. Title: Tightness of underground salt caverns to hydrogen
- September 2021 (one week): Geology field internship for second year students. Title: Geosciences in urban context - Ile de France region
- November 2018 (one week): Courses in the MIG (Métier de l'Ingénieur Généraliste). Title: Hydrogen storage in salt caverns. Students delivered a report at the end of this option.
- September 2017 (one week): Geology field internship for second year students. Geological lecture on rock fracturing - Sisteron region

Invited lecturer at the university of Calgary - Alberta - Canada (2014-2017):

- Introduction to induced seismicity
- Structural engineering

RESEARCH PROJECTS

At MINES Paris (2017-2023) - My history since 2017 of participating in and mounting projects can be listed in the following points:

- February 2024 for 5 years: **Contribution** to the FrHyGe Horizon European project: Full qualification in France of large-scale Hydrogen underground storage and replication from Germany to all European countries.
- October 2023: **Participating in mounting** a Horizon Europe project. Title: G-AIDANCE: Geothermal AI-driven advisory network for comprehensive exploration. *Project was well classified but it was not retained*.
- November 2023 for 10 months: **Contribution** to the project InterCarnot H2toSALTCAV in collaboration with the laboratory GeoRessources of Lorraine university. Title: Hydrogen storage in salt caverns for energy transition. This project helped fund the PostDoc of Angeline Defay listed above.
- September 2023 for 3 years: **Participating in mounting** a Marie-Curie doctoral proposal through the SMILE network (https://smile-msca-dn.eu/). This proposal was accepted and gave rise to the Ph.D. of Khashayar Khezri listed above.
- January 2023 for 2 years in two phases: **Piloting** a CITEPH project concerning tightness of salt caverns to the stored hydrogen. In this project we are working with many industrial partners including: TOTALENERGIES; STORENGY; TEREGA; and GEOSTOCK.
- September 2019 to September 2020: **Contribution** to the HyTREND project (Hydrogen for a carbon-free energy transition). It is a Power to X unifying project from the Carnot M.I.N.E.S institute, funded by the ANR.
- September 2018 to August 2020: **Contribution** to the STOPIL project. Title: Development of an industrial pilot for hydrogen storage in a salt caverns in France. Phase 1: feasibility study. This project included working with many industrial partners especially, STORENGY, GEOSTOCK, AIRLIQUIDE, INERIS, and BRGM.
- May 2017 to April 2020: **Contribution** to the ROSTOCK-H project. Title: Risks and opportunities of geological hydrogen storage in salt caverns in France and Europe. This project was held by AIRLIQUIDE, it had another industrial partners including: INERIS, GEOSTOCK, and University of Lorraine.

At the university of Calgary:
Since I enrolled in my PostDoc, I was a member of the Microseismic Industry Consortium (URL). It is a novel applied-research geophysical initiative dedicated to the advancement of research, education and technological innovations in microseismic methods and their practical applications for resource development. This consortium is a team of industry partners, government agencies, and faculty members.

PUBLICATIONS

Papers in peer reviewed journals:

1. **AbuAisha M.**, & **Tayeb F.** (2024). Gas humidification kinetics during cycling in underground salt caverns: A case study of Helium and Methane. *Paper is under preparation*
2. **Tayeb F.**, Rouabhi A., & **AbuAisha M.** (2024). Effect of cycling frequency on kinetics of hydrogen humidification in salt caverns. *Paper is under preparation*
3. **AbuAisha M.**, Rouabhi A., Hadj-Hassen F., Eaton D., **Tayeb F.**, & Valtz A. (2023). Geothermal effects on CO_2 dissolution kinetics in brine: A non-dimensional model for underground storage in salt caverns. Journal of Natural Gas Science and Engineering **(IF 5.3)**, 117, 205076. https://doi.org/10.1016/j.jgsce.2023.205076
4. **Tayeb F.**, Rouabhi A., **AbuAisha M.**, & Valtz A. (2023). Kinetics of CO_2 dissolution for underground applications. Geoenergy Science and Engineering **(IF 5.4)**, 230, 212061. https://doi.org/10.1016/j.geoen.2023.212061
5. **AbuAisha M.**, Rouabhi A., Billiotte J., & Hadj-Hassen F. (2021). Non-isothermal two-phase hydrogen transport in rock salt during cycling in underground caverns. International Journal of Hydrogen Energy **(IF 7.2)**, 46(9): 6632-6647. https://doi.org/10.1016/j.ijhydene.2020.11.152
6. **AbuAisha M.**, & Billiotte J. (2021). A discussion on hydrogen migration in rock salt for tight underground storage with an insight into a laboratory setup. Journal of Energy Storage **(IF 8.9)**, 38, 102589. https://doi.org/10.1016/j.est.2021.102589
7. **AbuAisha M.**, & Rouabhi A. (2019). On the validity of the uniform thermodynamic state approach for underground caverns during fast and slow cycling. International Journal of Heat and Mass Transfer **(IF 5.4)**, 142, 118424. https://doi.org/10.1016/j.ijheatmasstransfer.2019.07.074
8. **AbuAisha M.**, Eaton D., Priest J., Wong R., Loret B., & Kent A.H. (2018). Fully coupled hydro-mechanical controls on non-diffusive seismicity triggering front driven by hydraulic fracturing. Journal of Seismology **(IF 1.6)**, 23, 109-121. https://doi.org/10.1007/s10950-018-9795-0
9. **AbuAisha M.**, Eaton D., Priest J., & Wong R. (2017). Hydro-mechanically coupled FDEM framework to investigate near-wellbore hydraulic fracturing in homogeneous and fractured rock formations. Journal of Petroleum Science and Engineering **(IF 5.4)**, 154, 100-113. https://doi.org/10.1016/j.petrol.2017.04.018
10. **AbuAisha M.**, Loret B., & Eaton D. (2016). Enhanced Geothermal Systems (EGS): Hydraulic fracturing in a thermo-poroelastic framework. Journal of Petroleum Science and Engineering **(IF 5.4)**, 146, 1179-1191. https://doi.org/10.1016/j.petrol.2016.07.027
11. **AbuAisha M.**, & Loret B. (2016). Influence of hydraulic fracturing on impedance and efficiency of thermal recovery from HDR reservoirs. Geomechanics for Energy and the Environment **(IF 5.1)**, 7, 10-25. https://doi.org/10.1016/j.gete.2016.02.001
12. **AbuAisha M.**, & Loret B. (2016). Stabilization of Forced Heat Convection: Applications to Enhanced Geothermal Systems (EGS). Transport in Porous Media **(IF 2.9)**, 112, 229-252. https://doi.org/10.1007/s11242-016-0642-x
13. Plé O., Tourabi A., & **AbuAisha M.**. (2013). 3-Dimensional digital image correlation for strains determination in clayey soil. Applied Mechanics and Materials, 353-356, 463-466.

https://doi.org/10.4028/www.scientific.net/ AMM.353-356.463
14. Plé O., Ha Le T.N., & **AbuAisha M.**. (2011). Landfill clay barrier: fibre reinforcement technique. Advanced Materials Research, 378-379, 780-784. https://doi.org/10.4028/www.scientific.net/AMR.378-379.780

Conferences:

1. **AbuAisha M.**, Rouabhi A., Hadj-Hassen F., Eaton D., **Tayeb F.**, & Valtz A. (2023). Thermal effects on the kinetics of gas dissolution in brine: A case study of CO_2 storage in salt caverns (a non-dimensional model). DECOVALEX 2023, November 2023, Troyes, France.
2. **AbuAisha M.**, Rouabhi A., Billiotte J., & Hadj-Hassen F. (2022). Hydrogen migration in rock salt during cycling in underground caverns. CouFrac2022, November 2022, Berkeley, United States.
3. **AbuAisha M.**, & Rouabhi A. (2022). Is the hypothesis of a uniform thermodynamic state still valid in hydrogen underground caverns during fast cycling? CouFrac2022, November 2022, Berkeley, United States.
4. Hytrend, un projet power to X de l'Institut Carnot M.I.N.E.S. Christian Beauger, Pascaline Pre, Alain Thorel, Anthony Chesnaud, Charly Lemoine, **AbuAisha M.** et al. Énergie renouvelable et ressources, les enjeux de demain : de l'ingénierie aux territoires, Institut Mines-télécom, Avril 2021, France.
5. **AbuAisha M.**, Eaton D., Priest J., & Wong R. (2016). Simulating HF using FDEM: Effects of pre-existing joints, induced microseismicity and fluid diffusion. Seismological Society of America - Annual meeting, April 2016, Reno, United States.
6. **AbuAisha M.**, Eaton D., Priest J., & Wong R. (2016). Simulating hydraulic fracturing using finite-discrete element method (FDEM): Effects of pre-existing joints and lateral stress gradient, Geoconvention 2016, March 2016, Calgary, Canada.
7. **AbuAisha M.**, Eaton D., Priest J., & Wong R. (2015). Review of hybrid continuum / discontinuum methods for geomechanical modelling of hydraulic fracture growth. Geoconvention 2015, May 2015, Calgary, Canada.
8. **AbuAisha M.**, & Loret B. (2016). Stimulation of Geothermal Reservoirs: Impedance and Efficiency of Thermal Recovery. The 40^{th} Workshop on Geothermal Reservoir Engineering, January 2015, Stanford, CA, United States.
9. **AbuAisha M.**, & Loret B. (2014). Permeability enhancement of HDR reservoirs by hydraulic fracturing. The 14^{th} International Conference of the International Association for Computer Methods and Advances in Geomechanics, September 2014, Kyoto, Japan.

Invited communications:

1. **AbuAisha M.** (2019). Hydraulic fracturing for geothermal and petroleum applications: Continuum/ discontinuum approaches. Seminar at the Karlsruhe Institute of Technology - KIT, May 2019, Karlsruhe, Germany.
2. **AbuAisha M.** (2014). Enhanced Geothermal Systems (EGS): Permeability Stimulation Through Hydraulic Fracturing in a Thermo-Poroelastic Framework. Seminar at the University of Seoul, August 2014, Seoul, South Korea.

Books and book chapters:

1. **AbuAisha M.** (2017). Geothermal reservoir stimulation using the finite element method. Éditions Universitaires Européennes, 978-3330872134.
2. **AbuAisha M.**, Eaton D., Priest J., & Wong R. (2016). Finite discrete element framework for investigating the effect of temperature-dependent dynamic viscosity on hydraulic fracturing. Microseismic Industry Consortium: Annual Research Report, Volume 7.
3. **AbuAisha M.**, Eaton D., Priest J., & Wong R. (2016). Hydraulic fracture growth and migration of induced microseismicity: Application of a fully coupled hydromechanical FDEM approach. Microseismic Industry Consortium: Annual Research Report, Volume 7.

4. **AbuAisha M.**, Eaton D., Priest J., & Wong R. (2016). Simulating hydraulic fracturing using Finite-Discrete Element Method (FDEM): Effects of pre-existing joints and induced seismicity. Microseismic Industry Consortium: Annual Research Report, Volume 6.
5. Eaton D., Mason Mackay, Anton Biryukov, & **AbuAisha M.** (2016). Identifying critically stressed faults without triggering slip: A discussion. Microseismic Industry Consortium: Annual Research Report, Volume 6.
6. **AbuAisha M.**, Eaton D., Priest J., & Wong R. (2015). Finite/Discrete Element Method (FDEM) by Y-Geo: An overview. Microseismic Industry Consortium: Annual Research Report, Volume 5.
7. **AbuAisha M.**, Eaton D., Priest J., & Wong R. (2015). Hydraulic fracture simulation using the GEOS code. Microseismic Industry Consortium: Annual Research Report, Volume 5.

Bibliography

AbuAisha, M. (2014). "Enhanced Geothermal Systems: Permeability stimulation through hydraulic fracturing in a thermo-poroelastic framework". PhD dissertation. Grenoble, France: Université de Grenoble.

AbuAisha, M. and J. Billiotte (2021). "A discussion on hydrogen migration in rock salt for tight underground storage with an insight into a laboratory setup". In: *Journal of Energy Storage* 38, p. 102589. ISSN: 2352-152X. DOI: https://doi.org/10.1016/j.est.2021.102589.

AbuAisha, M. and B. Loret (2016a). "Influence of hydraulic fracturing on impedance and efficiency of thermal recovery from HDR reservoirs". In: *Geomechanics for Energy and the Environment* 7, pp. 10–25. ISSN: 2352-3808. DOI: https://doi.org/10.1016/j.gete.2016.02.001.

— (2016b). "Stabilization of Forced Heat Convection: Applications to Enhanced Geothermal Systems (EGS)". In: *Transport in Porous Media* 112.1, 229–252. DOI: https://doi.org/10.1007/s11242-016-0642-x.

AbuAisha, M., B. Loret, and D. Eaton (2016). "Enhanced Geothermal Systems (EGS): Hydraulic fracturing in a thermo-poroelastic framework". In: *Journal of Petroleum Science and Engineering* 146, pp. 1179–1191. ISSN: 0920-4105. DOI: https://doi.org/10.1016/j.petrol.2016.07.027.

AbuAisha, M. and A. Rouabhi (2019). "On the validity of the uniform thermodynamic state approach for underground caverns during fast and slow cycling". In: *International Journal of Heat and Mass Transfer* 142, p. 118424. ISSN: 0017-9310. DOI: https://doi.org/10.1016/j.ijheatmasstransfer.2019.07.074.

AbuAisha, M. et al. (2017). "Hydro-mechanically coupled FDEM framework to investigate near–wellbore hydraulic fracturing in homogeneous and fractured rock formations". In: *Journal of Petroleum Science and Engineering* 154, pp. 100–113. ISSN: 0920-4105. DOI: https://doi.org/10.1016/j.petrol.2017.04.018.

AbuAisha, M. et al. (2019). "Fully coupled hydro-mechanical controls on non-diffusive seismicity triggering front driven by hydraulic fracturing". In: *Journal of Seismology* 23.1, pp. 109–121. ISSN: 1573-157X. DOI: https://doi.org/10.1007/s10950-018-9795-0.

AbuAisha, M. et al. (2021). "Non-isothermal two-phase hydrogen transport in rock salt during cycling in underground caverns". In: *International Journal of Hydrogen Energy* 46.9, pp. 6632–6647. ISSN: 0360-3199. DOI: https://doi.org/10.1016/j.ijhydene.2020.11.152.

AbuAisha, M. et al. (2023). "Geothermal effects on CO2 dissolution kinetics in brine: A non-dimensional model for underground storage in salt caverns". In: *Gas Science and Engineering* 117, p. 205076. ISSN: 2949-9089. DOI: https://doi.org/10.1016/j.jgsce.2023.205076.

Adachi, J. et al. (2007). "Computer simulation of hydraulic fractures". In: *International Journal of Rock Mechanics and Mining Sciences* 44.5, pp. 739–757. ISSN: 1365-1609. DOI: https://doi.org/10.1016/j.ijrmms.2006.11.006.

Atkinson, B. K. (1991). *Fracture Mechanics of Rock*. Second edition. London, Great Britain: Academic Press Limited.

Bannach, A. et al. (2005). *Technology enhancement for (1) inventory assessment and mechanical integrity testing of gas-filled solution mined caverns and (2) mechanical integrity tests of solution mines and liquid storage caverns*. Tech. rep. GRI–05/0175 project final report, prepared for Gas Research Institute.

Barenblatt, G. I. (1962). "The Mathematical Theory of Equilibrium Cracks in Brittle Fracture". In: ed. by H.L. Dryden et al. Vol. 7. Advances in Applied Mechanics. Elsevier, pp. 55–129. DOI: https://doi.org/10.1016/S0065-2156(08)70121-2.

Baria, R. et al. (2000). "Progress at the European HDR project at Soultz-sous-Forêts: Preliminary results from the deepening of the well GPK2 to 5000 m". In: *Proceedings World Geothermal Congress 2000*. Kyushu, Tohoku, Japan.

Battistelli, A., C. Calore, and K. Pruess (1997). "The simulator TOUGH2/EWASG for modelling geothermal reservoirs with brines and non-condensible gas". In: *Geothermics* 26.4, 437 – 464. DOI: https://doi.org/10.1016/S0375-6505(97)00007-2.

Baumgärtner, J. et al. (1996). "The European HDR project at Soultz-sous-Forêts: Stimulation of the second deep well and first circulation experiment". In: *Proceedings of the 21th Workshop on Geothermal Reservoir Engineering*. Stanford, California: Stanford University.

Bear, J. (1972). *Dynamics of fluids in porous media*. American Elsevier Publishing Company, Inc.

Boroumand, N. and D. W. Eaton (2015). "Energy-based hydraulic fracture numerical simulation: Parameter selection and model validation using microseismicity". In: *Geophysics* 80.5, W33–W44. DOI: https://doi.org/10.1190/geo2014-0091.1.

Bourne-Webb, P. J., T. M. Bodas Freitas, and R. A. da Costa Gonçalves (2016). "Thermal and mechanical aspects of the response of embedded retaining walls used as shallow geothermal heat exchangers". In: *Energy and Buildings* 125, pp. 130–141. ISSN: 0378-7788. DOI: https://doi.org/10.1016/j.enbuild.2016.04.075.

Bradley, J. S. (1975). "ABNORMAL FORMATION PRESSURE". In: *AAPG Bulletin (American Association of Petroleum Geologists)* 59.6, pp. 957–973.

Brooks, Alexander N. and Thomas J.R. Hughes (1982). "Streamline upwind/Petrov-Galerkin formulations for convection dominated flows with particular emphasis on the incompressible Navier-Stokes equations". In: *Computer Methods in Applied Mechanics and Engineering* 32.1, pp. 199–259. ISSN: 0045-7825. DOI: https://doi.org/10.1016/0045-7825(82)90071-8.

Bruel, D. (1995a). "Heat extraction modelling from forced fluid flow through stimulated fractured rock masses: application to the Rosemanowes hot dry rock reservoir". In: *Geothermics* 24.3. Hot Dry Rock (HDR) Reservoir Modelling Activities within Europe, pp. 361–374. ISSN: 0375-6505. DOI: https://doi.org/10.1016/0375-6505(95)00014-H.

— (1995b). "Modelling heat extraction from forced fluid flow through stimulated fractured rock masses: evaluation of the soultz-sous-forets site potential". In: *Geothermics* 24.3. Hot Dry Rock (HDR) Reservoir Modelling Activities within Europe, pp. 439–450. ISSN: 0375-6505. DOI: https://doi.org/10.1016/0375-6505(95)00019-M.

— (2007). "Using the migration of the induced seismicity as a constraint for fractured Hot Dry Rock reservoir modelling". In: *International Journal of Rock Mechanics and Mining Sciences* 44.8, pp. 1106–1117. ISSN: 1365-1609. DOI: https://doi.org/10.1016/j.ijrmms.2007.07.001.

Burger, J., P. Sourieau, and M. Combarnous (1985). *Thermal methods of oil recovery*. Paris: Editions Technip.

Busse, F. H. and J. A. Whitehead (1971). "Instabilities of convection rolls in a high Prandtl number fluid". In: *Journal of Fluid Mechanics* 47.2, pp. 305–320. DOI: https://doi.org/10.1017/S0022112071001071.

Bérest, P. and F. Louvet (2020). "Aspects of the thermodynamic behavior of salt caverns used for gas storage". In: *Oil & Gas Science and Technology–Revue d'IFP Energies nouvelles* 75, p. 57.

Caglayan, D. G. et al. (2020). "Technical potential of salt caverns for hydrogen storage in Europe". In: *International Journal of Hydrogen Energy* 45.11, pp. 6793–6805. ISSN: 0360-3199. DOI: https://doi.org/10.1016/j.ijhydene.2019.12.161.

Calcagni, B., F. Marsili, and M. Paroncini (2005). "Natural convective heat transfer in square enclosures heated from below". In: *Applied thermal engineering* 25.16, pp. 2522–2531. DOI: https://doi.org/10.1016/j.applthermaleng.2004.11.032.

Chabab, S. et al. (2019). "Thermodynamic study of the CO2-H2O-NaCl system: Measurements of CO2 solubility and modeling of phase equilibria using Soreide and Whitson, electrolyte CPA and SIT models". In: *International Journal of Greenhouse Gas Control* 91, p. 102825. ISSN: 1750-5836. DOI: https://doi.org/10.1016/j.ijggc.2019.102825.

Charnavel, Y., D. Leca, and F. Poulain (1999). "Advanced geometrical modelling of salt dissolution during cavern leaching – illustration with a case study". In: The SMRI Meeting. Las Vegas, Nevada, USA.

Chen, Y., C. Zhou, and Y. Sheng (2007). "Formulation of strain-dependent hydraulic conductivity for a fractured rock mass". In: *International Journal of Rock Mechanics and Mining Sciences* 44.7, pp. 981–996. ISSN: 1365-1609. DOI: https://doi.org/10.1016/j.ijrmms.2006.12.004.

Chen, Z., G. Huan, and Y. Ma (2006). *Computational Methods for Multiphase Flows in Porous Media*. SIAM.

Chou, Q., J. Gao, and M. Somerwil (Jan. 2011). "Analysis of Geomechanical Data for Horn River Basin Gas Shales, NE British Columbia, Canada". In: vol. All Days. SPE Middle East Unconventional Resources Conference and Exhibition, SPE–142498–MS.

Chromik, M. and W. Korzeniowski (2021). "A Method to Increase the Leaching Progress of Salt Caverns with the Use of the Hydro-Jet Technique". In: *Energies* 14.18. ISSN: 1996-1073. DOI: https://doi.org/10.3390/en14185833.

Class, H., R. Helmig, and P. Bastian (2002). "Numerical simulation of non-isothermal multiphase multicomponent processes in porous media.: 1. An efficient solution technique". In: *Advances in Water Resources* 25.5, pp. 533–550. ISSN: 0309-1708. DOI: https://doi.org/10.1016/S0309-1708(02)00014-3.

Cornet, F. H. (Feb. 2000). "Comment on 'Large-scale in situ permeability tensor of rocks from induced microseismicity' by S. A. Shapiro, P. Audigane and J.-J. Royer". In: *Geophysical Journal International* 140.2, pp. 465–469. ISSN: 0956-540X. DOI: https://doi.org/10.1046/j.1365-246x.2000.00018.x.

Cornet, F.H., Th. Bérard, and S. Bourouis (2007). "How close to failure is a granite rock mass at a 5km depth?" In: *International Journal of Rock Mechanics and Mining Sciences* 44.1, pp. 47–66. ISSN: 1365-1609. DOI: https://doi.org/10.1016/j.ijrmms.2006.04.008.

Cosenza, Ph. et al. (1999). "In situ rock salt permeability measurement for long term safety assessment of storage". In: *International Journal of Rock Mechanics and Mining Sciences* 36.4, pp. 509–526. ISSN: 1365-1609. DOI: https://doi.org/10.1016/S0148-9062(99)00017-0.

Crozier, T. E. and S. Yamamoto (1974). "Solubility of hydrogen in water, sea water, and sodium chloride solutions". In: *Journal of Chemical and Engineering Data* 19.3, pp. 242–244.

Côté, J. and J. M. Konrad (2005). "A generalized thermal conductivity model for soils and construction materials". In: *Canadian Geotechnical Journal* 42.2, pp. 443–458. DOI: https://doi.org/10.1139/t04-106.

Damjanac, B. and P. Cundall (2016). "Application of distinct element methods to simulation of hydraulic fracturing in naturally fractured reservoirs". In: *Computers and Geotechnics* 71, pp. 283–294. ISSN: 0266-352X. DOI: https://doi.org/10.1016/j.compgeo.2015.06.007.

Dinske, C. and Shapiro S. A. Rutledge J. T. (2010). "Interpretation of Microseismicity Resulting from Gel and Water Fracturing of Tight Gas Reservoirs". In: *Pure and Applied Geophysic* 167.1, pp. 169–182. DOI: https://doi.org/10.1007/s00024-009-0003-6.

Duan, K., C. Kwok, and W. Wu (2018). "DEM modeling of hydraulic fracturing in permeable rock: influence of viscosity, injection rate and in situ states". In: *Acta Geotechnica* 13, pp. 1187–1202. ISSN: 1861-1133. DOI: https://doi.org/10.1007/s11440-018-0627-8.

Eaton, D. W. et al. (2014). "Breakdown of the Gutenberg-Richter relation for microearthquakes induced by hydraulic fracturing: influence of stratabound fractures". In: *Geophysical Prospecting* 62.4, pp. 806–818. DOI: https://doi.org/10.1111/1365-2478.12128.

Evans, K. et al. (2009). *Studies and Support for the EGS Reservoirs at Soultz-sous-Forêts*. Tech. rep. University of Neuchâtel: Centre for Geothermal Research - CREGE.

Everett, D. H. (1975). "Thermodynamics of multiphase fluids in porous media". In: *Journal of Colloid and Interface Science* 52.1, pp. 189–198. ISSN: 0021-9797. DOI: https://doi.org/10.1016/0021-9797(75)90316-1.

Feistel, R. et al. (2010). "Thermodynamic properties of sea air". In: *Ocean Science* 6.1, pp. 91–141. DOI: https://doi.org/10.5194/os-6-91-2010.

Fer, F. (1970). *Thermodynamique macroscopique, Tome I: systèmes fermés*. Gordon and Breach, Science Publishers Ltd.

— (1971). *Thermodynamique macroscopique, Tome II: systèmes ouverts*. Gordon and Breach, Science Publishers Ltd.

Fjaer, E. et al. (2008). *Petroleum related rock mechanics*. Second edition. Radarweg 29, 1000 AE Amsterdam, The Netherlands: Elsevier B.V.

Forsyth, P. A. and R. B. Simpson (2012). "A two-phase, two-component model for natural convection in a porous medium". In: *International Journal for Numerical Methods in Fluids* 12.7, pp. 655–682. DOI: https://doi.org/10.1002/fld.1650120705.

Francke, H. and M. Thorade (2010). "Density and viscosity of brine: An overview from a process engineers perspective". In: *Geochemistry* 70. Geoenergy: From Visions to Solutions, pp. 23–32. ISSN: 0009-2819. DOI: https://doi.org/10.1016/j.chemer.2010.05.015.

Fries, T. P. and H. G. Matthies (2004). "A Review of Petrov-Galerkin Stabilization Approaches and an Extension to Meshfree Methods". In: *Informatikbericht Nr. 2004-01. Technische Universitaet Braunschweig*. Braunschweig, Germany.

Fu, P., S. M. Johnson, and C. R. Carrigan (2013). "An explicitly coupled hydro-geomechanical model for simulating hydraulic fracturing in arbitrary discrete fracture networks". In: *International Journal for Numerical and Analytical Methods in Geomechanics* 37.14, pp. 2278–2300. DOI: https://doi.org/10.1002/nag.2135.

Gelet, R., B. Loret, and N. Khalili (2012a). "A thermo-hydro-mechanical coupled model in local thermal non-equilibrium for fractured HDR reservoir with double porosity". In: *Journal of Geophysical Research: Solid Earth* 117.B7, B07205. DOI: https://doi.org/10.1029/2012JB009161.

— (2012b). "Borehole stability analysis in a thermoporoelastic dual-porosity medium". In: *International Journal of Rock Mechanics and Mining Sciences* 50, pp. 65–76. ISSN: 1365-1609. DOI: https://doi.org/10.1016/j.ijrmms.2011.12.003.

— (2013). "Thermal recovery from a fractured medium in local thermal non-equilibrium". In: *International Journal for Numerical and Analytical Methods in Geomechanics* 37.15, pp. 2471–2501. DOI: https://doi.org/10.1002/nag.2145.

Gevantman, L. H. and J. Lorenz (1981). *Physical properties data for rock salt*. Vol. 167. US Department of Commerce, National Bureau of Standards.

Grathwohl, P. (2012). *Diffusion in Natural Porous Media: Contaminant Transport, Sorption/Desorption and Dissolution Kinetics*. Topics in Environmental Fluid Mechanics. Springer US. ISBN: 9781461556831.

Gray, W. G. and C. T. Miller (2014). *Introduction to the Thermodynamically Constrained Averaging Theory for Porous Medium Systems*. Springer.

Grecksch, G. et al. (2003). "Hydraulic fracturing at the European HDR/HFR test site Soultz-sous-Forêts (France) a conceptual model". In: *Proceedings of the European Geothermal Conference*. Leibniz Institute for Applied Geosciences, Germany.

Guo, C. et al. (2017). "Numerical investigation of a joint approach to thermal energy storage and compressed air energy storage in aquifers". In: *Applied Energy* 203, pp. 948–958. ISSN: 0306-2619. DOI: https://doi.org/10.1016/j.apenergy.2017.06.030.

Harari, I. (2004). "Stability of semidiscrete formulations for parabolic problems at small time steps". In: *Computer Methods in Applied Mechanics and Engineering* 193.15. Recent Advances in Stabilized and Multiscale Finite Element Methods, pp. 1491–1516. ISSN: 0045-7825. DOI: https://doi.org/10.1016/j.cma.2003.12.035.

Hasnaoui, M., E. Bilgen, and P. Vasseur (1992). "Natural convection heat transfer in rectangular cavities partially heated from below". In: *Journal of Thermophysics and Heat transfer* 6.2, pp. 255–264. DOI: https://doi.org/10.2514/3.353.

Hassanizadeh, M. S. and W. G. Gray (1990). "Mechanics and thermodynamics of multiphase flow in porous media including interphase boundaries". In: *Advances in Water Resources* 13.4, pp. 169–186. ISSN: 0309-1708. DOI: https://doi.org/10.1016/0309-1708(90)90040-B.

Hauke, G., G. Sangalli, and M. H. Doweidar (2007). "COMBINING ADJOINT STABILIZED METHODS FOR THE ADVECTION-DIFFUSION-REACTION PROBLEM". In: *Mathematical Models and Methods in Applied Sciences* 17.02, pp. 305–326. DOI: https://doi.org/10.1142/S0218202507001929.

Hughes, T. J. R. (2000). *The Finite Element Method; Linear Static and Dynamic Finite Element Analysis*. Second edition. Dover, Mineola: Paris: Editions Technip.

Hughes, T. J. R., L. P. Franca, and G. M. Hulbert (1989). "A new finite element formulation for computational fluid dynamics: VIII. The galerkin/least-squares method for advective-diffusive equations". In: *Computer Methods in Applied Mechanics and Engineering* 73.2, pp. 173–189. ISSN: 0045-7825. DOI: https://doi.org/10.1016/0045-7825(89)90111-4.

Jiang, F., L. Luo, and J. Chen (2013). "A novel three-dimensional transient model for subsurface heat exchange in enhanced geothermal systems". In: *International Communications in Heat and Mass Transfer* 41, pp. 57–62. ISSN: 0735-1933. DOI: https://doi.org/10.1016/j.icheatmasstransfer.2012.11.003.

John, V. and P. Knobloch (2007). "On spurious oscillations at layers diminishing (SOLD) methods for convection–diffusion equations: Part I – A review". In: *Computer Methods in Applied Mechanics and Engineering* 196.17, pp. 2197–2215. ISSN: 0045-7825. DOI: https://doi.org/10.1016/j.cma.2006.11.013.

Jupe, A.J. et al. (1995). "Modelling of a european prototype hdr reservoir". In: *Geothermics* 24.3. Hot Dry Rock (HDR) Reservoir Modelling Activities within Europe, pp. 403–419. ISSN: 0375-6505. DOI: https://doi.org/10.1016/0375-6505(95)00017-K.

Karimi-Jafari, M. (2010). "Comportement transitoire des cavités salines profondes". PhD dissertation. Paris, France: Ecole Polytechnique X.

Kaviany, M. (2002). *Principles of Heat Transfer in Porous Media*. Second edition. New York, USA: John Wiley & sons.

Klimczak, C. et al. (2010). "Cubic law with aperture-length correlation: implications for network scale fluid flow". In: *Hydrogeology Journal* 18, pp. 851–862. DOI: https://doi.org/10.1007/s10040-009-0572-6.

Klumpp, F. (2016). "Comparison of pumped hydro, hydrogen storage and compressed air energy storage for integrating high shares of renewable energies-Potential, cost-comparison and ranking". In: *Journal of Energy Storage* 8, pp. 119–128. ISSN: 2352-152X. DOI: https://doi.org/10.1016/j.est.2016.09.012.

Kolditz, O. (1995). "Modelling flow and heat transfer in fractured rocks: dimensional effect of matrix heat diffusion". In: *Geothermics* 24.3. Hot Dry Rock (HDR) Reservoir Modelling Activities within Europe, pp. 421–437. ISSN: 0375-6505. DOI: https://doi.org/10.1016/0375-6505(95)00018-L.

Kolditz, O. et al. (2012). *Thermo-Hydro-Mechanical-Chemical Processes in Porous Media*. Volume 86. Springer.

Kondepudi, D. and I. Prigogine (2014). *Modern Thermodynamics: From Heat Engines to Dissipative Structures*. John Wiley and Sons, Ltd.

Kunz, O. and W. Wagner (2012). "The GERG-2008 wide-range equation of state for natural gases and other mixtures: an expansion of GERG-2004". In: *Journal of chemical & engineering data* 57.11, pp. 3032–3091. DOI: https://doi.org/10.1021/je300655b.

Kunz, O. et al. (2007). *The GERG-2004 wide-range equation of state for natural gases and other mixtures*.

Labaune, P. et al. (2019). "Dilatancy Criteria for Salt Cavern Design: A Comparison Between Stress- and Strain-Based Approaches". In: *Rock Mechanics and Rock Engineering* 51.2, pp. 599–611. ISSN: 1434-453X. DOI: https://doi.org/10.1007/s00603-017-1338-4.

Lacasse, D., E. Turgeon, and D. Pelletier (2004). "On the judicious use of the $k-\epsilon$ model, wall functions and adaptivity". In: *International Journal of Thermal Sciences* 43.10, pp. 925–938. ISSN: 1290-0729. DOI: https://doi.org/10.1016/j.ijthermalsci.2004.03.004.

Lee, S. H. and A. Ghassemi (2010). "Thermo-poroelastic analysis of injection-induced rock deformation and damage evolution". In: *Proceedings of the Thirty-Fifth Workshop on Geothermal Reservoir Engineering*. Stanford, California: Stanford University.

— (2011). "Three-dimensional thermo-poro-mechanical modeling of reservoir stimulation and induced microseismicity in geothermal reservoir". In: *Proceedings of the Thirty-Sixth Workshop on Geothermal Reservoir Engineering*. Stanford, California: Stanford University.

Lenormand, R. et al. (1989). "Flow through porous media: limits of fractal patterns". In: *Proceedings of the Royal Society of London. A. Mathematical and Physical Sciences* 423.1864, pp. 159–168. DOI: https://doi.org/10.1098/rspa.1989.0048.

Likhachev, E.R. (2003). "Dependence of water viscosity on temperature and pressure". In: *Technical Physics* 48.4, 514 – 515. DOI: https://doi.org/10.1134/1.1568496.

Lisjak, A., G. Grasselli, and T. Vietor (2014). "Continuum–discontinuum analysis of failure mechanisms around unsupported circular excavations in anisotropic clay shales". In: *International Journal of Rock Mechanics and Mining Sciences* 65, pp. 96–115. ISSN: 1365-1609. DOI: https://doi.org/10.1016/j.ijrmms.2013.10.006.

Lisjak, A. et al. (2017). "A 2D, fully-coupled, hydro-mechanical, FDEM formulation for modelling fracturing processes in discontinuous, porous rock masses". In: *Computers and Geotechnics* 81, pp. 1–18. ISSN: 0266-352X. DOI: https://doi.org/10.1016/j.compgeo.2016.07.009.

Lopez-Lazaro, C. et al. (2019). "Predicting the phase behavior of hydrogen in NaCl brines by molecular simulation for geological applications". In: *Bulletin de la Société Géologique de France* 190.1.

Loret, B. (2018). *Fluid injection in deformable geological formations: Energy related issues*. Springer.

Loret, B. and F. M. F. Simões (2017). *Biomechanical aspects of soft tissues*. Crc Press.

Lund, J. (2009). "Development and Utilization of Geothermal Resources". In: *Proceedings of ISES World Congress 2007*, Vol. I –Vol. V.

Mahabadi, O. K. et al. (2012). "Y-Geo: New Combined Finite-Discrete Element Numerical Code for Geomechanical Applications". In: *International Journal of Geomechanics* 12.6, pp. 676–688. ISSN: 1365-1609. DOI: https://doi.org/10.1061/(ASCE)GM.1943-5622.0000216.

Mahjoub, M. et al. (2018). "Numerical Study of Callovo-Oxfordian Argillite Expansion due to Gas Injection". In: *International Journal of Geomechanics* 18.1, p. 04017134. DOI: https://doi.org/10.1061/(ASCE)GM.1943-5622.0001050.

Marle, C. M. (1982). "On macroscopic equations governing multiphase flow with diffusion and chemical reactions in porous media". In: *International Journal of Engineering Science* 20.5, pp. 643–662. ISSN: 0020-7225. DOI: https://doi.org/10.1016/0020-7225(82)90118-5.

Matos, C. R., J. F. Carneiro, and P. P. Silva (2019). "Overview of Large-Scale Underground Energy Storage Technologies for Integration of Renewable Energies and Criteria for Reservoir Identification". In: *Journal of Energy Storage* 21, pp. 241–258. ISSN: 2352-152X. DOI: https://doi.org/10.1016/j.est.2018.11.023.

McTigue, D. F. (1986). "Thermoelastic response of fluid-saturated porous rock". In: *Journal of Geophysical Research: Solid Earth* 91.B9, pp. 9533–9542. DOI: https://doi.org/10.1029/JB091iB09p09533.

Mebrahtu, C. et al. (2019). "Chapter 5 - CO2 Methanation: Principles and Challenges". In: *Horizons in Sustainable Industrial Chemistry and Catalysis*. Ed. by Stefania Albonetti, Siglinda

Perathoner, and Elsje Alessandra Quadrelli. Vol. 178. Studies in Surface Science and Catalysis. Elsevier, pp. 85–103. DOI: https://doi.org/10.1016/B978-0-444-64127-4.00005-7.

Mualem, Y. (1978). "Hydraulic conductivity of unsaturated porous media: Generalized macroscopic approach". In: *Water Resources Research* 14.2, pp. 325–334. DOI: https://doi.org/10.1029/WR014i002p00325.

Munjiza, A. (2004). *The Combined Finite-Discrete Element Method*. USA: John Wiley & Sons, Ltd.

Munjiza, A., D. R. Owen, and N. Bićanić (1995). "A combined finite-discrete element method in transient dynamics of fracturing solids". In: *Engineering Computations* 12, pp. 145–174. URL: https://api.semanticscholar.org/CorpusID:120965932.

Murphy, H. et al. (1999). "Hydraulics and well testing of engineered geothermal reservoirs". In: *Geothermics* 28.4, pp. 491–506. ISSN: 0375-6505. DOI: https://doi.org/10.1016/S0375-6505(99)00025-5.

Papanastasiou, P. (1999). "The effective fracture toughness in hydraulic fracturing". In: *International Journal of Fracture* 96.2, 127 – 147. DOI: https://doi.org/10.1023/A:1018676212444.

Papanastasiou, P. and M. Thiercelin (1993). "Influence of inelastic rock behaviour in hydraulic fracturing". In: *International Journal of Rock Mechanics and Mining Sciences & Geomechanics Abstracts* 30.7, pp. 1241–1247. ISSN: 0148-9062. DOI: https://doi.org/10.1016/0148-9062(93)90102-J.

Poppei, J. et al. (2006). "Flooding of an abandoned salt mine modeling two-phase flow in complex mine structures". In: *The proceedings of the TOUGH symposium*. Berkeley, California: Lawrence Berkeley National Laboratory.

Raju, M. and S. K. Khaitan (2012). "Modeling and simulation of compressed air storage in caverns: A case study of the Huntorf plant". In: *Applied Energy* 89.1. Special issue on Thermal Energy Management in the Process Industries, pp. 474–481. ISSN: 0306-2619. DOI: https://doi.org/10.1016/j.apenergy.2011.08.019.

Reynolds, M. M. and D. L. Munn (Feb. 2010). "Development Update for an Emerging Shale Gas Giant Field—Horn River Basin, British Columbia, Canada". In: vol. All Days. SPE Unconventional Resources Conference / Gas Technology Symposium, SPE–130103–MS.

Roa Pinto, J. S. et al. (2021). "Modeling phase equilibrium of hydrogen and natural gas in brines: Application to storage in salt caverns". In: *International Journal of Hydrogen Energy* 46.5, pp. 4229–4240. ISSN: 0360-3199. DOI: https://doi.org/10.1016/j.ijhydene.2020.10.242.

Roche, V. and M. van der Baan (2017). "Modeling of the in situ state of stress in elastic layered rock subject to stress and strain-driven tectonic forces". In: *Solid Earth* 8.2, pp. 479–498. DOI: https://doi.org/10.5194/se-8-479-2017.

Rogers, S. et al. (Oct. 2010). "Understanding Hydraulic Fracture Geometry and Interactions in the Horn River Basin through DFN and Numerical Modeling". In: vol. All Days. SPE Canada Unconventional Resources Conference, SPE–137488–MS.

Rouabhi, A. (2019). "Problèmes de thermodynamique et de thermo-hydro-mécanique associés à l'exploitation du sous-sol". In: *Matériaux et structures en mécanique [physics.class-ph]. Sorbonne Université*.

Rouabhi, A. et al. (2017). "A multiphase multicomponent modeling approach of underground salt cavern storage". In: *Geomechanics for Energy and the Environment* 12, pp. 21–35. ISSN: 2352-3808. DOI: https://doi.org/10.1016/j.gete.2017.08.002.

On Estimating the Water Content of CO2 in Equilibrium with Formation Brine (June 2008). Vol. All Days. PETSOC Canadian International Petroleum Conference, PETSOC–2008–084. DOI: https://doi.org/10.2118/2008-084.

Sankar, M. et al. (2011). "Numerical study of natural convection in a vertical porous annulus with discrete heating". In: *International Journal of Heat and Mass Transfer* 54.7, pp. 1493–1505. ISSN: 0017-9310. DOI: https://doi.org/10.1016/j.ijheatmasstransfer.2010.11.043.

Santoyo, E. et al. (2001). "Rheological property measurement of drilling fluids used in geothermal wells". In: *Applied Thermal Engineering* 21.3, pp. 283–302. ISSN: 1359-4311. DOI: https://doi.org/10.1016/S1359-4311(00)00003-X.

Santoyo-Gutiérrez, S., G. Espinosa, and G. Amaro-Espejo (2005). "Effect of variable rheological properties of drilling muds and cements on the temperature distribution in geothermal wells." In: *Proceedings of World Geothermal Congress 2005*. Turkey, Antalya.

Schulze, O., T. Popp, and H. Kern (2001a). "Development of damage and permeability in deforming rock salt". In: *Engineering Geology* 61.2. Geosciences and Nuclear Waste Disposal, pp. 163–180. ISSN: 0013-7952. DOI: https://doi.org/10.1016/S0013-7952(01)00051-5.

— (2001b). "Development of damage and permeability in deforming rock salt". In: *Engineering Geology* 61.2, pp. 163–180. ISSN: 0013-7952. DOI: https://doi.org/10.1016/S0013-7952(01)00051-5.

Schwertz, F. A. and J. E. Brow (May 1951). "Diffusivity of Water Vapor in Some Common Gases". In: *The Journal of Chemical Physics* 19.5, pp. 640–646. ISSN: 0021-9606. DOI: https://doi.org/10.1063/1.1748306.

Shao, J. F., H. Zhou, and K. T. Chau (2005). "Coupling between anisotropic damage and permeability variation in brittle rocks". In: *International Journal for Numerical and Analytical Methods in Geomechanics* 29.12, pp. 1231–1247. DOI: https://doi.org/10.1002/nag.457.

Shapiro, S. A. and C. Dinske (2009a). "Fluid-induced seismicity: Pressure diffusion and hydraulic fracturing". In: *Geophysical Prospecting* 57.2, pp. 301–310. DOI: https://doi.org/10.1111/j.1365-2478.2008.00770.x.

— (2009b). "Scaling of seismicity induced by nonlinear fluid-rock interaction". In: *Journal of Geophysical Research: Solid Earth* 114.B9. DOI: https://doi.org/10.1029/2008JB006145.

Shapiro, S. A., C. Dinske, and E. Rothert (2006). "Hydraulic-fracturing controlled dynamics of microseismic clouds". In: *Geophysical Research Letters* 33.14. DOI: https://doi.org/10.1029/2006GL026365.

Shapiro, S. A. et al. (Jan. 2002). "Characterization of fluid transport properties of reservoirs using induced microseismicity". In: *Geophysics* 67.1, pp. 212–220. ISSN: 0016-8033. DOI: https://doi.org/10.1190/1.1451597.

Sousani, M. et al. (2015). "Simulation of the hydraulic fracturing process of fractured rocks by the discrete element method". In: *Environmental Earth Sciences* 73, pp. 8451–8469. ISSN: 1866-6299. DOI: https://doi.org/10.1007/s12665-014-4005-z.

Svendsen, B. and K. Hutter (1995). "On the thermodynamics of a mixture of isotropic materials with constraints". In: *International Journal of Engineering Science* 33.14, pp. 2021–2054. ISSN: 0020-7225. DOI: https://doi.org/10.1016/0020-7225(95)00044-X.

Tatone, B. S. A. and G. Grasselli (2015). "A calibration procedure for two-dimensional laboratory-scale hybrid finite–discrete element simulations". In: *International Journal of Rock Mechanics and Mining Sciences* 75, pp. 56–72. ISSN: 1365-1609. DOI: https://doi.org/10.1016/j.ijrmms.2015.01.011.

Tayeb, F. et al. (2023). "Kinetics of CO2 dissolution for underground applications". In: *Geoenergy Science and Engineering* 230, p. 212061. ISSN: 2949-8910. DOI: https://doi.org/10.1016/j.geoen.2023.212061.

Tezduyar, T. E. and Y. J. Park (1986). "Discontinuity-capturing finite element formulations for nonlinear convection-diffusion-reaction equations". In: *Computer Methods in Applied Mechanics and Engineering* 59.3, pp. 307–325. ISSN: 0045-7825. DOI: https://doi.org/10.1016/0045-7825(86)90003-4.

Tsilingiris, P.T. (2008). "Thermophysical and transport properties of humid air at temperature range between 0 and 100°C". In: *Energy Conversion and Management* 49.5, pp. 1098–1110. ISSN: 0196-8904. DOI: https://doi.org/10.1016/j.enconman.2007.09.015.

Turcotte, D. L. and G. Schubert (2002). *Geodynamics*. Second edition. Cambridge, England, UK: Cambridge University Press.

Valtz, A. et al. (2004). "Vapour-liquid equilibria in the carbon dioxide-water system, measurement and modelling from 278.2 to 318.2K". In: *Fluid Phase Equilibria* 226, pp. 333–344. ISSN: 0378-3812. DOI: https://doi.org/10.1016/j.fluid.2004.10.013.

van Genuchten, M. Th. (1980). "A Closed-form Equation for Predicting the Hydraulic Conductivity of Unsaturated Soils". In: *Soil Science Society of America Journal* 44.5, pp. 892–898. DOI: https://doi.org/10.2136/sssaj1980.03615995004400050002x.

Yan, W., S. Huang, and E. H. Stenby (2011). "Measurement and modeling of CO2 solubility in NaCl brine and CO2-saturated NaCl brine density". In: *International Journal of Greenhouse Gas Control* 5.6, pp. 1460–1477. ISSN: 1750-5836. DOI: https://doi.org/10.1016/j.ijggc.2011.08.004.

Yang, C. and Y. Gu (2006). "Accelerated Mass Transfer of CO2 in Reservoir Brine Due to Density-Driven Natural Convection at High Pressures and Elevated Temperatures". In: *Industrial & Engineering Chemistry Research* 45.8, pp. 2430–2436. ISSN: 0888-5885. DOI: https://doi.org/10.1021/ie050497r.

Yew, C. H. and X. Weng (2014). *Mechanics of Hydraulic Fracturing*. Second edition. USA: Gulf Professional Publishing.

Yin, S., M. B. Dusseault, and L. Rothenburg (2009). "Thermal reservoir modeling in petroleum geomechanics". In: *International Journal for Numerical and Analytical Methods in Geomechanics* 33.4, pp. 449–485. DOI: https://doi.org/10.1002/nag.723.

Yortsos, Y. C., B. Xu, and D. Salin (1997). "Phase diagram of fully developed drainage in porous media". In: *Physical Review Letters* 79.23, pp. 4581–4584. DOI: https://doi.org/10.1103/PhysRevLett.79.4581.

Zhang, J., A. Gupta, and J. Baker (2007). "Effect of relative humidity on the prediction of natural convection heat transfer coefficients". In: *Heat transfer engineering* 28.4, pp. 335–342. DOI: https://doi.org/10.1080/01457630601122823.

Zhang, X. et al. (2022). "Large-scale CO2 disposal/storage in bedded rock salt caverns of China: An evaluation of safety and suitability". In: *Energy* 249, p. 123727. ISSN: 0360-5442. DOI: https://doi.org/10.1016/j.energy.2022.123727.